HOKKAIDO UNIVERSITY

Title	Surface Chemistry of Cationic-Ligands-Protected Gold Nanomolecules : Ligand Exchange, Protonation, and Menshutkin Reactions on Au25 Cluster
Author(s)	黄, 仲
Citation	北海道大学. 博士(工学) 甲第13830号
Issue Date	2019-12-25
DOI	10.14943/doctoral.k13830
Doc URL	http://hdl.handle.net/2115/87598
Type	theses (doctoral)
File Information	Zhong_Huang.pdf

Instructions for use

Hokkaido University Collection of Scholarly and Academic Papers : HUSCAP

Surface Chemistry of Cationic-Ligands-Protected Gold Nanomolecules: Ligand Exchange, Protonation, and Menshutkin Reactions on Au_{25} Cluster

Zhong Huang

Graduate School of Engineering

Hokkaido University

December 2019

Surface Chemistry of Cationic-Ligands-Protected Gold Nanomolecules: Ligand Exchange, Protonation, and Menshutkin Reactions on Au_{25} Cluster

Zhong Huang

Laboratory of Novel Hybrid Materials Engineering

Division of Materials Science and Engineering

Faculty of Engineering

Hokkaido University

A dissertation submitted to the Graduate School of Engineering of Hokkaido University in partial fulfilment of the requirements for the degree of Doctor of Philosophy in Materials Science and Engineering

ABSTRACT

Tailoring thiolate ligands (SR) on atomically-precise gold (Au) clusters is of great importance in the functionalization of clusters toward the rational design of their properties and applications. The pendant R-group on cluster surface is exposed to solutions and other phases, and therefore its molecular chemistry determines the molecular-like characteristics of clusters. Regarding the charge state (+1, 0 and –1) of R-group, a vast majority of $Au_n(SR)_m$ clusters have been prepared through the use of neutral and anionic SR ligands, such as phenylethanethiol, methylbenzenethiol, alkanethiols, glutathione, and mercaptocarboxylic acids, among others. There is very rare research concerning the cationic R-group. However, in some special applications, such as biological system, cationic R-groups are incorporated on the cluster surface to cater the long-held belief that these moieties would yield intimate interactions with the negatively-charged contents. Based on this circumstance, this study is to explore the surface chemistry on the cationic-ligands-protected Au clusters.

Chapter One is a general introduction into the noble metal clusters with atomically precision, especially the most-widely researched $Au_{25}(SR)_{18}$. It summarizes the achievements focusing on synthesis, characterization, structure determination, surface engineering and application.

Chapter Two reports the first investigation into the kinetics of cationic-ligand-exchange processes through the reaction of $Au_{25}(SCH_2CH_2Ph)_{18}$ with a cationic thiol $HS(CH_2)_{11}N(CH_3)_3^+$, which resulted in different populations of the two thiolate ligands (SR^0 and SR^+), i.e., $Au_{25}(SR^0)_{18-x}(SR^+)_x$. It reveals that the kinetics of the cationic-ligand-exchange process, which is different from a typical neutral-thiol-to-

neutral-thiol ligand exchange, is strongly dependent on how the SR^+ ligands interact with each other during the ligand-exchange process.

Chapter Three describes the first synthesis of high-purity and high-yield Au_{25} clusters protected by basic pyridyl ethanethiol ($HSCH_2CH_2Py$, 4-PyET and 2-PyET). The as-obtained $[Au_{25}(4\text{-PyET})_{18}]^-\cdot Na^+$ clusters show a structure similar to that known for the phenyl ethanethiolate analog, but with pyridyl-N coordination to Na^+, a more relaxed ligand shell, and a profoundly layered arrangement in the solid state. Because of the pendant Py moiety, the $[Au_{25}(4\text{-PyET})_{18}]^-$ clusters are endowed with a unique (de)protonation equilibria, which results in the formation of positively-charged $-Py\cdot H^+$ moieties on Au cluster surface. In addition, $[Au_{25}(4\text{-PyET})_{18}]^-$ clusters showed an unexpected H^+-dependent solubility that is tunable in aqueous and organic solvents.

Chapter Four investigates the photoluminescence (PL) properties on $Au_{25}(PyET)_{18}$ and $Au_{25}(4\text{-PyET})_{18}$. The results showed that PyET ligand with electron-rich pydidyl-group could significantly enhance the PL emission of Au_{25} clusters. The ligand-to-metal electron transfer is responsible for the PL enhancement on $Au_{25}(PyET)_{18}$. In addition, upon involvement of the proton (H^+), the protonated PyET would reduce the electron-donation, and the emission responses of PyET-capped Au_{25} clusters were found to correlate with the resonance-coupled structure of PyET ligands.

Chapter Five investigates the Menshutkin reaction on $Au_{25}(4\text{-PyET})_{18}$ cluster through the reaction of surface pyridyl moieties with the dimethyl sulfate, which resulted in the formation of consistently-cationized Au_{25} clusters, i.e., $Au_{25}(4\text{-PyET}{-}CH_3^+)_x(4\text{-PyET})_{18-x}$. The results showed that the surface Py moieties amenable to be methylated into $Py{-}CH_3^+$ can easily achieve the methylation modification of PyET-capped Au_{25}

clusters, which opens a facile route to allow the post-assembly of positive charges to metal clusters via interfacial surface modification.

Chapter Six summarizes the research findings, contributions and perspectives of the thesis.

TABLE OF CONTENTS

List of Figures

List of Tables

List of Schemes

List of Abbreviations

Å	angstroms
Abs	absorbance
Ag	silver
Au	gold
B.C.	before Christ
BSA	bovine serum albumin
CD	circular dichroism
COSY	correlation spectroscopy
CTAB	cetyltrimethylammonium bromide
Capt	captopril
Cys	L-cysteine
Cysm	cysteamine
Da	daltons
DPPC	dipalmitoylphosphatidylcholine
DPPG	dipalmitoylphosphatidylglycerole
DMF	dimethylformamide
DCM	dichloromethane
DMSO	dimethyl sulfoxide

e	electron charge
ESI-MS	electrospray ionization mass spectrometry
EDT	2,2´-(ethylenediocy)diethanethiol
h	hour
HOMO	highest occupied molecular orbital
HPLC	high-performance liquid chromatography
ICP	inductivity coupled plasma
LUMO	lowest unoccupied molecular orbital
LEIST	ligand-exchange-induced size/structure transformation
MALDI	matrix assisted laser desorption ionization
mg	milligram
min	minute
mL	milliliter
mm	millimeter
MPC	monolayer protected cluster
MS	mass spectrometry
MB	3-mercapto-2-butanol
MBA	m-mercaptobenzonic acid
MeOH	methanol
MHA	6-mercaptohexanoic acid

MPA	3-mercaptopropionic acid
MetH	2-mercaptoethanol
MR	Menshutkin reaction
NaBH4	sodium borohydride
nm	nanometer
NMR	nuclear magnetic resonance
NP	nanoparticle
NPs	nanoparticles
NC	nanocluster
NCs	nanoclusters
^{o}C	degrees celsius
Oct_4N^+	tetraoctylammonium
PAGE	poly acrylamide gel electrophoresis
PET	4-phenyl ethanethiol
PET*	chirally modified PET, $–SCH_2C^*H(CH_3)Ph$
Pd	palladium
Pt	platinum
PL	photoluminescence
Ph	phenyl group
Py	pyridyl group

PNA	long-chain peptide nucleic acid
***p*-MBA**	*p*-mercaptobenzoic acid
***p*-BBT**	*p*-bromobenzenethiol
QQQ	triple quadripole
QY	quantum yield
ROS	reactive oxygen species
SG	glutathione
SPR	surface plasmon resonance
SR	thiolate
SR^0	neutral thiolate
SR^+	cationic thiolate
SR^-	anionic thiolate
SAMs	self-assembled monolayers
SC-XRD	single-crystal X-ray diffraction
SN_2	bimolecular nucleophilic substitution reaction
T	temperature
THF	tetrahydrofuran
TBBT	4-tert-butylbenzenethiolate
TOAB	tetraoctyl ammonium bromide
TOA	tetraoctyl ammonium

TOF	time of flight
TD-DFT	time-dependent density functional theory calculations
TGA	thermogravimetric analysis
µL	microliter
UV-vis	ultraviolet-visible
2-PyET	2-pyridyl ethylmercaptan
4-PyET	2-(4-pyridinyl)ethanethiol

Chapter 1

General Introduction

1.1 History of noble metal nanoclusters with atom precision

Noble metal nanoparticles (NPs) are the subject of one of the hottest topics of investigation in science, which outputs an exponentially increasing number of papers, especially in the cases of emerging nanoscience and nanotechnology with NPs and self-assembled monolayers (SAMs). They advance the fascinating aspects such as their assembly of multiple types relating to materials science, the behavior of the individual particles, size-related optical (surface plasma resonance), magnetic and electronic properties, and their utilizations in catalysis and biology.[1–5]

The utilization of noble metals, e.g. gold (Au), can date back to the 5th millennium B.C. when the marvelous statue of Toutankhamon (Figure 1.1) was constructed. It is probable that "soluble" gold contents had been used around the 5th or 4th century B.C. in China and Egypt. The modern scientific research on colloidal NPs was thought to be started in 1857,[6] when Faraday presented the preparation of dark red solutions of colloidal Au by phosphorus reduction of an aqueous solution of chloroaurate ($AuCl_4^-$) using CS_2 as a two-phase system. He also studied the optical properties of thin films obtained from the dried colloidal solutions, and observed a reversible color change of as-preapred films (from bluish-purple to green) upon mechanical compression. Then in 1861, the term "colloid", from French *colle*, was coined soon thereafter by Graham.[7] After more than 150 years of scientific researches on metal colloidal NPs, nanochemists had achieved precise control of particle size, shape, composition, and

properties in many publications.[8–11]

Figure 1.1 Statue of Toutankhamon in Egypt. (Source: https://lavillette.com/programmation/toutankhamon_e185)

Although relatively remarkable achievements have been made in colloidal NPs, nanochemists are still frustrated because of the fact that there are no totally same NPs. Therefore, many unclear issues, such as the poorly-understood in terms of surface layer (including organic stabilizers and the inorganic-organic interface), their structure-properties relationships, the mechanisms for shape-controlled synthesis of NPs, and the evolutions of core-shell structures were still unclear.[12–15] To unveil all of these critical issues, colloid chemists are motivated to pursue the NPs of totally same, namely clusters or nanoclusters (NCs) with atom precision, and further determine their total structures, that is, not only the core structure (i.e., the arrangements and shape of metal kernel), but also the shell structure (i.e., the arrangements of ligands and the bonding between the ligands and the metal kernel).

1.2 The story of $Au_{25}SR_{18}$ nanoclusters

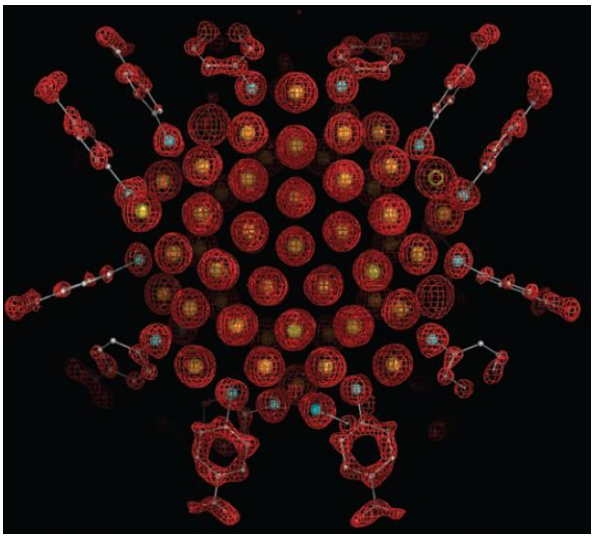

Figure 1.2 X-ray crystal structure determination of the Au_{102}(*p*-MBA)$_{44}$ NCs. Reproduced from ref. (19) with permission from American Association for the Advancement of Science, copyright 2018.

Among many groups of metal NPs capped by various ligands, the gold-thiolate (SR) system can be seen as a model one due to its extraordinary robustness. Gold-thiol chemistry started to bloom in the 1980s because of the researches in SAMs of thiols on bulk gold surfaces.[16,17] In the basis of SAMs work, researchers began to use thiols for the functionalization and preparation of gold NPs since 1990s. The most common method for Au NPs synthesis is the "Brust-Schriffin method" published in 1994,[18,19] which was the first report of using thiol as a capping ligand for stabilizing Au NPs. Since then, atomically precise $Au_m(SR)_n$ NCs had been widely prepared in molecular purity, and thus more focuses on their special properties, such as atom precision, superatom-like structure, and many physicochemical properties resulting from quantum-confinement effects. This high-quality $Au_m(SR)_n$ NCs had also paved the

way for their crystallization works, and the subsequent analysis of their total structures by single crystal X-ray diffraction (SC-XRD).

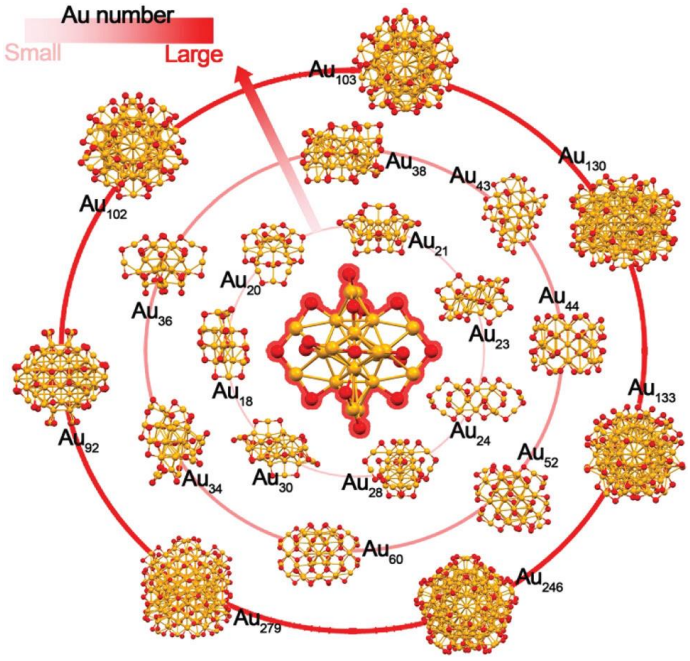

Scheme 1.1 Selected $Au_m(SR)_n$ NCs with atomically precise structures. Legand: orange, Au atoms; red, S atoms; the C, H and other atoms are removed for clarity. Reproduced from ref. (20) with permission from The Royal Society of Chemistry, copyright 2018.

In 2007, the first determined structure of metal cluster was that of the decahedral Au_{102}(*p*-MBA)$_{44}$ NCs (*p*-MBA*: p*-mercaptobenzoic acid; Figure 1.2), reported by the Kornberg's group.[19] Then the development of Au NCs appears to have a high-speed increasing tendency. To date, around 40 species of thiolate-capped Au NCs with atomically precise structure have been resolved, such as Au_{15}, Au_{23}, Au_{24}, Au_{25}, Au_{30}, Au_{36}, Au_{38}, Au_{44}, Au_{55}, Au_{64}, Au_{67}, Au_{99}, Au_{102}, Au_{130}, Au_{246}, Au_{279} and so on.[20–40] (Scheme 1.1) In addition, several $Au_m(SR)_n$ NCs also have been synthesized in high

purity, but the crystal structures were not yet obtained. All in all, the past decade has witnessed a significant progress in this field.

Among these NCs, $Au_{25}(SR)_{18}$ and its several derivatives hold a very special place in the NCs field because of the initial discovery, easy preparation in high- stability and yield, and thus for easy researches on functionalization and application. The construction of $Au_{25}(SR)_{18}$ exhibits an icosahedral Au_{13} kernel, which is further wrapped by six $Au_2(SR)_3$ staple motifs. (Figure 1.3) Through many years of efforts and developments, the physicochemical properties of $Au_{25}(SR)_{18}$ has been fully researched, including catalytic, optical, electrochemical, chiral, and magnetic properties. Furthermore, benefiting from the high biocompatibility, good photostability, and low toxicity, Au_{25} nanoclusters are highly promising for application in the biological field, namely, cell labelling, phototherapy, and biosensing.

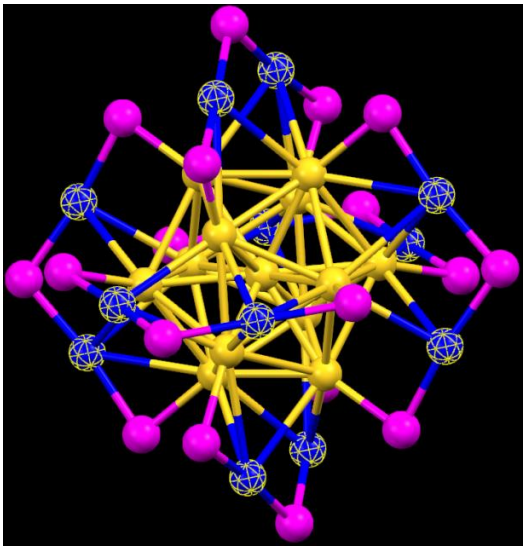

Figure 1.3 Crystal structure of $Au_{25}(SR)_{18}$ NCs. Legand: yellow, kernel Au atoms; blue, staple Au atoms; magenta, S atoms; the C, H and other atoms are omitted for clarity).

1.3 Synthetic method

For investigating the $Au_{25}(SR)_{18}$ cluster at a deeper level and promoting the wider application of the nanocluster, there is the need for methods to prepare the $Au_{25}(SR)_{18}$ NCs with high-yield and high-purity. Extensive efforts have therefore been made toward the syntheses and purifications of $Au_{25}(SR)_{18}$ nanoclusters.

In 1994, Brust et al.[18] presented the preparation of gold NPs using a two-phase liquid–liquid system, which led to more homogeneous NPs relative to the previously reported ones. The "Brust–Schiffrin" method involves two steps where the first step involves the phase transfer of gold salt by using a phase transfer agent (tetraoctyl ammonium bromide, TOAB) and subsequently the Au(I)–SR precursor was reduced by $NaBH_4$ to form NPs. On the basis of the "Brust" method or its modified synthetic procedures, early works (before 2007) by Whetten,[41] Murray,[42] and Tsukuda[43] groups released many reports focusing on controlling particle size and monodispersity of Au NCs. Unfortunately, the earlier synthetic works generally produced polydispersed Au NCs. The modern isolation techniques, like polyacrylamide gel electrophoresis (PAGE)[43] and high-performance liquid chromatography (HPLC)[44] were necessarily applied to separate the discrete cluster species. Thus, the yields of individual NCs should be very low, which was apparently not content with the further researches on crystallizations and utilizations.

The major synthetic breakthrough has been done, especially that two systematic ways: size-focusing method[15] and ligand exchange reaction were established since 2007.[45] These methods allowed the systematic size-controlled preparation of various $Au_m(SR)_n$ NCs in high-purity and high-yield.

1.3.1 Size-focusing method

The fundamental principle of the size-focusing method is the essential stabilities of the initially polydispersed $Au_m(SR)_n$ NCs, and the different stabilities result in the survival of the most robust one, reminiscent of "survival of the fittest" in natural selection. The size-focusing method is not simply the as-reported "Brust–Schiffrin" method, because the key for size-focusing is to build a comfortable environment for only one monodispersed NC, which can simultaneously eliminate other NCs species. Control over the size-focusing method is significantly relied on the kinetic control, and the controlled parameters including solvent types, reducing agent, temperature, reactant ratio, and so on.

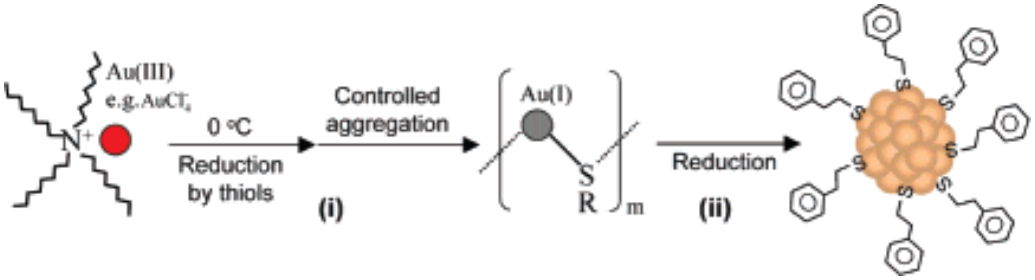

Scheme 1.2 Schematic illustration of the formation of the $Au_{25}(PET)_{18}$ clusters via the kinetically controlled strategy. Reproduced from ref. (46) with permission from The American Chemical Society, copyright 2007.

In 2007, the Jin group firstly reported a kinetically-controlled strategy for Au_{25} NCs synthesis (Scheme 1.2).[46] This procedure had two main modifications on the basis of the previous "Brust–Schiffrin" method. (i) During the addition of HSC_2H_4Ph (PET) into Au(III)-TOA (toluene solution), a very low stirring speed ~30 rpm and a temperature of 0°C (ice bath) were modified for the formation of Au(I)-SR precursors. (ii) the freshly-made aq. $NaBH_4$ dissolved in water was immediately injected into above solution under the vigorous stirring (~1100 rpm). These two changes are

critical on the formation of monodisperse Au(I)–SR precursors as well as the final $Au_{25}(PET)_{18}$ NCs. The UV-vis absorption of the purified product exhibited an obvious peak at 670 nm and two shoulder peaks at 400 and 450 nm. This was the first report that $Au_{25}(PET)_{18}$ clusters could be prepared in high-purity and high-yield (~40%, based on Au atoms).

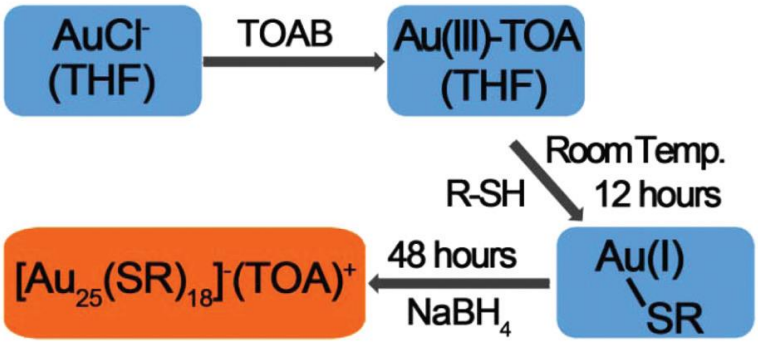

Scheme 1.3 Schematic illustration of the formation of the $Au_{25}(PET)_{18}$ clusters by the one-phase in situ synthetic method. Reproduced from ref. (20) with permission from The Royal Society of Chemistry, copyright 2018.

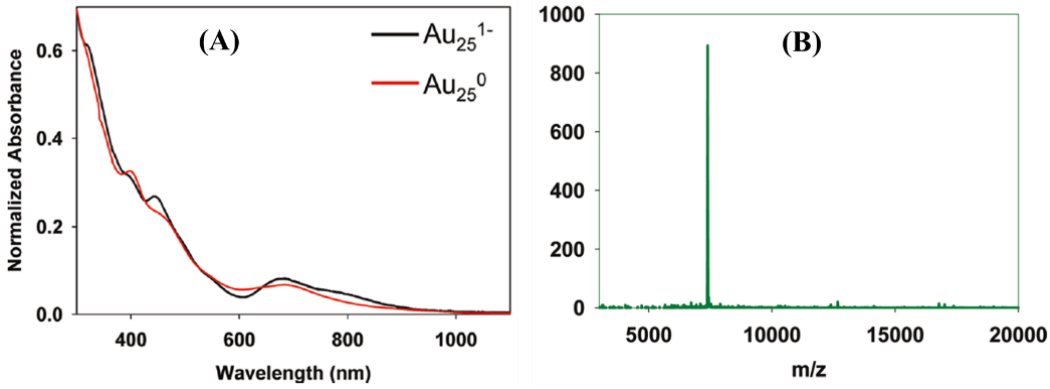

Figure 1.4 (A) UV-vis spectra in CH_2Cl_2 of $Au_{25}(PET)_{18}$ with –1 core charge (indicated by black curve) and 0 core charge (indicated by red curve). (B) Matrix-assisted laser desorption ionization (MALDI) MS of pure $[TOA]^+[Au_{25}(PET)_{18}]^-$. Reproduced from ref. (47) with permission from The American Chemical Society, copyright 2010.

The kinetically controlled strategy was further optimized into a one-phase synthetic method by the Murray group in 2010.[47] In this method (Scheme 1.3), $HAuCl_4$ and TOAB with 1:1.2 of molar ratio were firstly added to the tetrahydrofuran (THF) solvent and stirred for 15 min. PET was then added at room temperature (the mole ratio of PET to Au was 1:5). The solution was stirred for overnight, and it would become completely transparent. The $NaBH_4$ powders (the mole ratio of $NaBH_4$ to Au was 1:5) dissolved in ice-cold water and then stirred for around 1 hour under 0°C (ice bath). After that, the aq. $NaBH_4$ was rapidly injected under a vigorous stirring. The reaction would be allowed to quietly stir for more than 48 h, and then the obtained solution was purified to get the pure $[TOA]^+[Au_{25}(PET)_{18}]^-$. Figure 1.4A shows the characteristic optical peaks of $Au_{25}(PET)_{18}$ located at ~670, 450, and 400 nm regardless of core charge (0 or –1), and Figure 1.4B presents that the MALDI-MS detected only one peak that corresponds to the $Au_{25}(PET)_{18}$ NCs. In this case, the synthetic yield could be achieved at ~52% based on Au atom. They also synthesized several other species of Au_{25} NCs capped by different thiols (i.e., $HS(CH_2)_5CH_3$, $HSCH_2CH(CH_3)_2$, and $HS(CH_2)_{11}CH_3$) using the same procedure.

Aside from the above two famous examples, recently, the Xie group developed a NaOH-mediated $NaBH_4$ reduction method for Au_{25} NC synthesis (Scheme 1.4).[48] In this case, instead of toluene or THF, water was used as the reaction medium, and the additional NaOH solution was added to tune the formation kinetics by decreasing the reducing capability of $NaBH_4$, and simultaneously enhancing the etching capability of thiol. It is noting that the use of NaOH could greatly reduce the etching time into less than 3 h. They also report a kinetically controlled method by using carbon monoxide (CO) as the reductant, aiming to the synthesis of $Au_{25}(SR)_{18}$ by slow growth, which was fit for the study on the growth mechanism of Au NCs.[49,50]

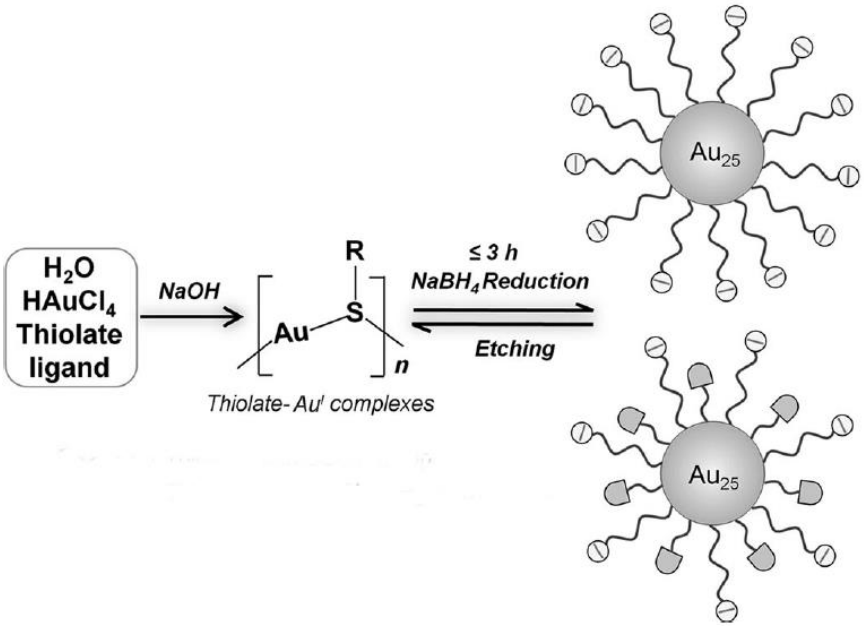

Scheme 1.4 Schematic illustration of the formation of the $Au_{25}(SR)_{18}$ clusters by the NaOH-mediated $NaBH_4$ reduction method. Reproduced from ref. (48) with permission from Wiley-VCH, copyright 2014.

In the past decade, the size-focusing method had been extended to the successful syntheses of molecularly-pure Au NCs, such as $Au_{38}(SR)_{24}$,[51] and $Au_{64}(SR)_{32}$,[52] $Au_{99}(SR)_{42}$,[53] and $Au_{144}(SR)_{60}$.[54] Given all of these successful syntheses, the size-focusing method is remarkable and paves a key route toward the rational synthesis of atomically-precise metal clusters.

1.3.2 Ligand-exchange reaction

Regarding $Au_m(SR)_n$ NCs, the SR are used to cap on the surface by Au-S affinity, in terms of "monolayer protected clusters" (MPCs). Ligand-exchange method is not only capable of obtaining the NCs with new capped ligands or bi- (or tri-) thiolated ligands, but also provides a platform for thoroughly studying the intermolecular reaction process on the NCs surface. In addition, the substituent R-group can magically affect the sizes and structures of NCs during ligand-exchange, which offers

an opportunity to create the new NCs (which have not yet obtained by the size-focusing method) through a ligand-exchange-induced size/structure transformation (LEIST) process.[45]

1.3.2.1. ligand exchange with preserving the structure template

In 2007, the Murray group[55,56] reported the ligand-exchange reaction of $Au_{25}(PET)_{18}$ with several different thiol ligands, such as −SPh, $-SC_6H_{13}$, and −SPhCOOH ligands. The results suggest that only the partial surface PET ligands could be ligand-exchanged to generate the bi-thiolated $Au_{25}(PET)_{18-x}(SR')_x$ NCs (SR′ represents the incoming thiolate ligand). By contrast, the $-SC_6H_{13}$ ligands can substitute all PET ligands in the surface of $Au_{25}(PET)_{18}$ clusters, and thus obtain the mono-thiolated $Au_{25}(SC_6H_{13})_{18}$ NCs (Figure 1.5A).[56] In 2010, the bi-thiolated $Au_{25}(PET)_{18-x}(SR')_x$ NCs were also obtained via the ligand-exchange between $Au_{25}(PET)_{18}$ NCs and electron-withdrawing SR′ (−SPh-*p*-X, X = Br or NO_3), and ^{1}H-NMR was first used to monitor the ligand-exchange process.[57] In the same year, they exchanged the $Au_{25}(PET)_{18}$ with toluene-3,4-dithiol ($CH_3Ph(SH)_2$), and the ESI-QQQ mass spectrum revealed the formation of $Au_{25}(CH_3Ph(S^-)_2)_x(CH_3Ph(SH)(S^-))_y$ $(PET)_{18-2x-y}$ NCs (Figure 1.5B), which could be termed the tri-thiolated $Au_{25}(SR)_{18}$.[58]

The mechanism of ligand-exchange has also widely researched. Based on the results of ^{1}H-NMR, the Murray group reported the distinctions of the second-order rate constants on ligand-exchange reaction of Au_{25} NCs with different core charge (+1, $\sim 1.9 \times 10^{-5}$ $M^{-1}\cdot s^{-1}$ against −1, $\sim 1.2 \times 10^{-4}$ $M^{-1}\cdot s^{-1}$), indicating that the partial charge transfers between the NCs and ligands determine the ligand-exchange rate.[59] The aforementioned works shows that the surface ligands of Au_{25} NCs were difficult to completely exchanged by the incoming ligand. This indicates that each ligand at the

different sites should hold different activity in exchange reaction. The Ackerson group successfully prepared the crystal of $Au_{25}(SC_6H_{12})_{16}$(*p*-BBT)$_2$ by ligand exchange of $Au_{25}(SC_6H_{12})_{18}$ NCs with *p*-bromobenzenethiol (*p*-BBT).[60] The X-ray crystallography results illustrated that the surface ligand, that bond to the most solvent -exposed Au atom, is easier to be exchanged by incoming thiols. (Figure 1.6) Very recently, the Bürgi group investigated the ligand-exchange of the $Au_{25}(PET)_{18}$ NCs with butanethiol and phenyl mercaptan, and unveiled that the thiolate monolayer in Au_{25} NCs shows a dynamic nature.[61]

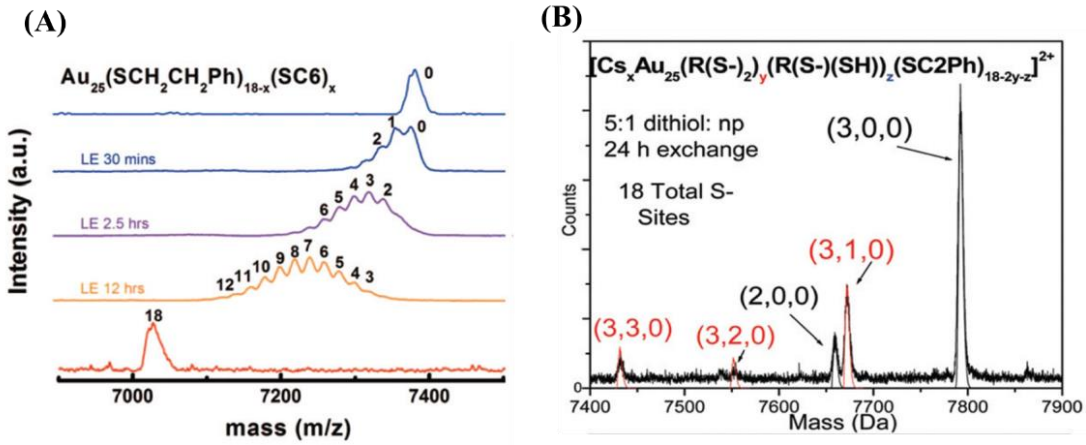

Figure 1.5 (A) MALDI-TOF-MS spectrum to detect the number of exchanged $-SC_6H_{13}$ ligands on the $Au_{25}(PET)_{18}$ surface. Reproduced from ref. (56) with permission from American Chemical Society, copyright 2008. (B) ESI-QQQ mass spectrum to detect the number of exchanged ligands including monothiol and dithiol. Reproduced from ref. (58) with permission from American Chemical Society, copyright 2010.

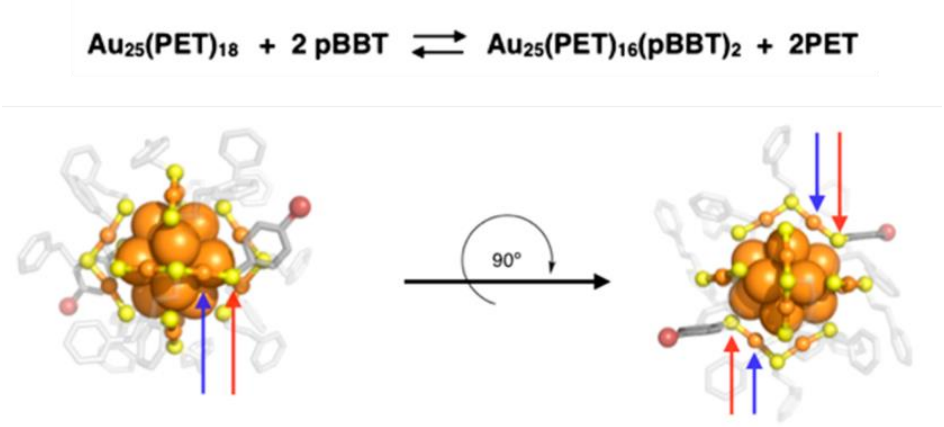

Figure 1.6 Crystal structure of $Au_{25}(PET)_{16}(pBBT)_2$ NCs. Blue arrows point to the most solvent-exposed Au atoms, and red arrows to the S atoms of the *p*-BBT ligands. Reproduced from ref. (60) with permission from American Chemical Society, copyright 2014.

1.3.2.2 ligand-exchange with structure transformation

In the above conventional ligand-exchange reactions, they were typically conducted by using low concentrations of incoming thiol ligands at room temperature. Recently, some reports[45] released that when the ligand-exchange reaction were carried out under the harsh conditions, i.e. a large excess of incoming thiol and high temperature, the ligand-exchange process can not only lead to the completely exchange of surface ligands, but also re-operate the etching process and general a new kind of monodispersed NCs in high-purity and high-yield.

The ligand-exchange-induced size/structure transformation (LEIST) was first proposed by the Jin group. Through the LEIST process, they reported four notable examplesof the transformations of $Au_{25}(PET)_{18}$ to $Au_{28}(TBBT)_{20}$ or $Au_{20}(TBBT)_{16}$,[62,63] $Au_{38}(PET)_{24}$ to $Au_{36}(TBBT)_{24}$,[64] and $Au_{144}(PET)_{60}$ to $Au_{133}(TBBT)_{52}$,[65] where TBBT is the abbreviation of 4-tert-butylbenzenethiolate. As an example presented here, the starting $Au_{25}(PET)_{18}$ NCs, by ligand-exchange with a

large excess of TBBT at 80°C, resulted in the formation of $Au_{28}(TBBT)_{20}$ after ~2 h reaction. The yield of $Au_{28}(TBBT)_{20}$ NCs was unexpectedly as high as >90% (based on Au atoms), and the product was molecularly-pure, as indicated by the ESI-MS spectrum (Figure 1.7).[62] What is more, by just changing the reaction temperature to 40°C, 8 hours of thermal reaction of $Au_{25}(PET)_{18}$ with excess TBBT could produce another new NC, $Au_{20}(TBBT)_{16}$.[63]

The LEIST process is also remarkable because it resembles the organic transformation chemistry, in which one type of molecule can be transformed into a new type.[15] It is developed from size-focusing method, but allows us to synthesize new NCs that are normally hard to obtain by the direct synthesis.

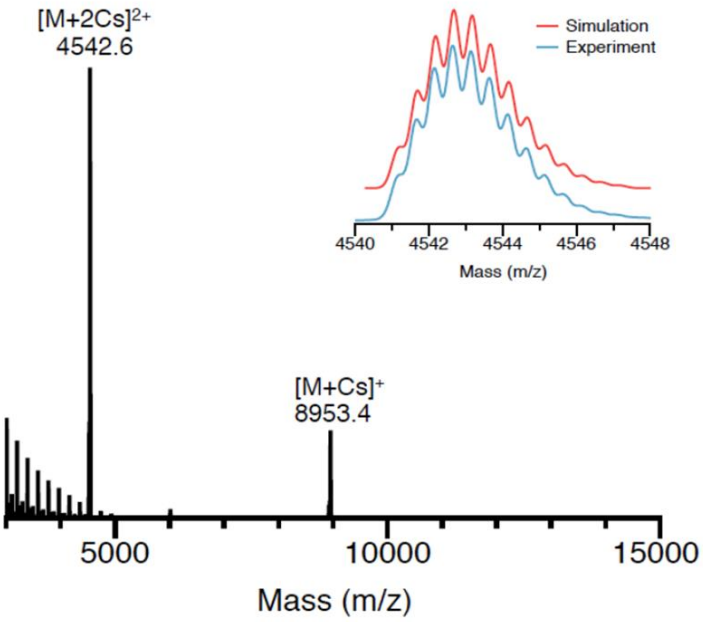

Figure 1.7 ESI-MS spectrum of the $Au_{28}(TBBT)_{20}$ NCs. CsOAc was used to form Cs^+-contained adducts. The inset shows the simulated and observed isotope patterns of the m/z 4542.6 peak. Reproduced from ref. (62) with permission from American Chemical Society, copyright 2014.

1.4 Ligand engineering on $Au_{25}SR_{18}$

The significance of the ligand effect has been highlighted in many researches such as size-focusing synthesis and property regulations of metal NCs. Through engineering the steric hindrance, acid-base, charge-state or other properties of the capped SR ligands, researchers can tailor the properties of Au_{25} NCs, such as solubility, chiral, and optical properties. Synthesizing the Au NCs with the same magic size, but protected by diverse ligands, not only results in the rational designs of NCs with similar structures, but also allows insight into the structure–property relationship.

1.4.1 Water-solubility of $Au_{25}SR_{18}$

The early works for thiolate-protected NCs with molecularly pure had been mainly focused on the organic-soluble ligands; as a result, the as-capped NCs are only organic-soluble. However, water-soluble NCs are advantageous of their good photostability, low toxicity, and high biocompatibility, which lead to their use in cell labelling, phototherapy, biosensing and so on. The water-soluble NCs are thus highly desirable in many applications.

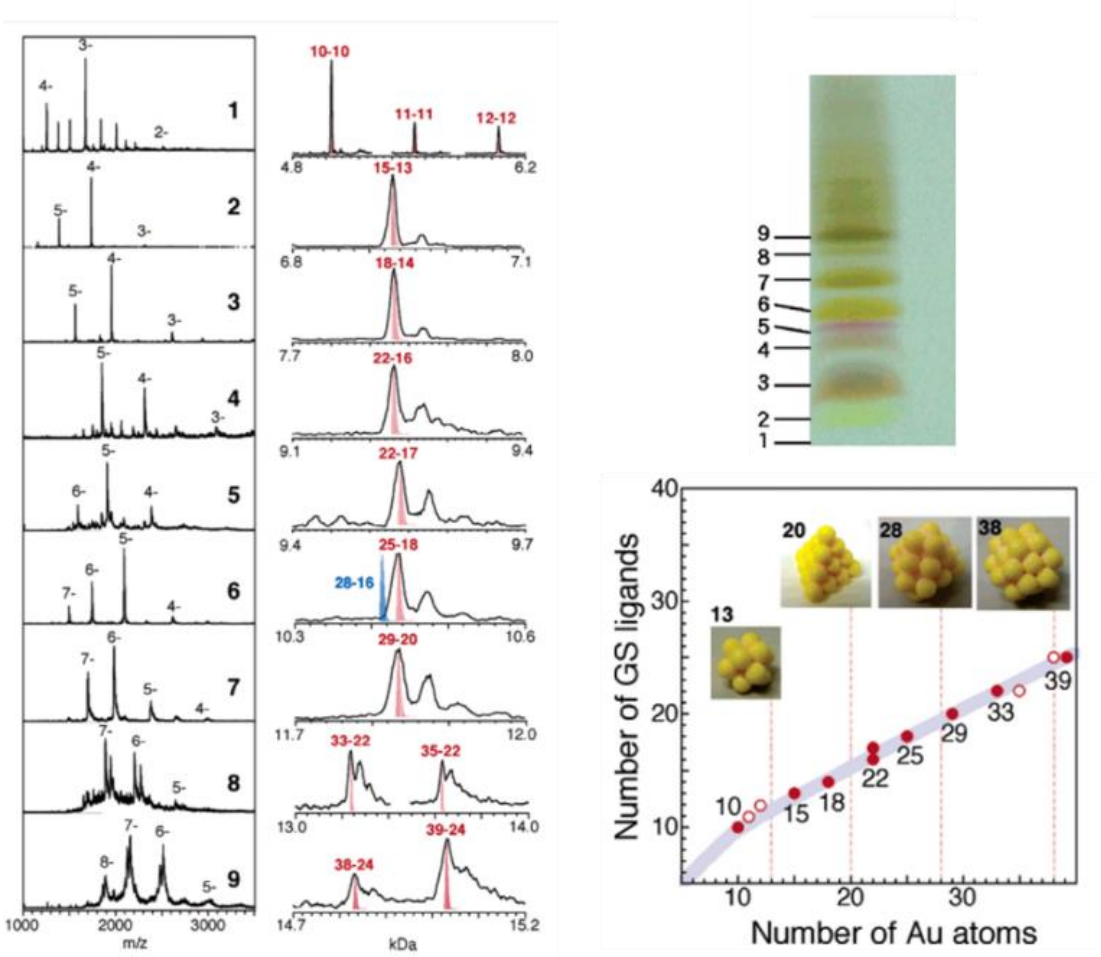

Figure 1.8 Low-resolution ESI-MS of the PAGE results on the ploydispersed $Au_m(SG)_n$ NCs, and a plot of the chemical compositions of 1–9 against the number of Au atoms and GS ligands. Reproduced from ref. (69) with permission from American Chemical Society, copyright 2005.

In earlier work, the Whetten and Tsukuda groups separately carried out a series of synthetic works of Au NCs by using the glutathione (GSH), which is well-soluble in water.[66–69] Whetten et al.[66] prepared the GS-capped Au NCs with molecular weights of 4.3, 5.6, 8.2 and 10.4 kDa. Among them, the NCs with the molecular weight of 10.4 kDa was successfully separated by PAGE. Tsukuda et al.[69] also conducted PAGE on the polydispersed $Au_m(SG)_n$ NCs, and a series of relatively pure products, $Au_{10}(SG)_{10}$/$Au_{11}(SG)_{11}$/$Au_{12}(SG)_{12}$, $Au_{15}(SG)_{13}$, $Au_{18}(SG)_{14}$, $Au_{22}(SG)_{16}$/$Au_{22}(SG)_{17}$,

$Au_{25}(SG)_{18}$, $Au_{29}(SG)_{20}$, $Au_{33}(SG)_{22}/Au_{35}(SG)_{22}$, and $Au_{38}(SG)_{24}/Au_{39}(SG)_{24}$, respectively were separated and characterized in detail. (Figure 1.8).

In 2012, Yuan et al.[70] showed the fast synthesis of Au_{25} NCs capped by cysteine (Cys for short) NCs. They used a surfactant molecule (cetyltrimethylammonium bromide, CTAB) to protect Cys-Au(I) precursors during reduction. The water-soluble $Au_{25}(Cys)_{18}$ was obtained after as short as 10 min reaction. The water-soluble $Au_{25}(Capt)_{18}$ (Capt represents captopril) NCs was synthesized by the Jin group.[71] It showed that the $Au_{25}(Capt)_{18}$ NCs hold the better thermal stability over $Au_{25}(SG)_{18}$ NCs because of the enhanced ligand stability of captopril relative to GSH (Figure 1.9). Shivhare et al.[72] reported the synthesis of Au_{25} NCs capped by 11-mercaptoundecanoic acid and 16-mercaptohexadecanoic acid, separately, and their yields of the syntheses were ~15%.

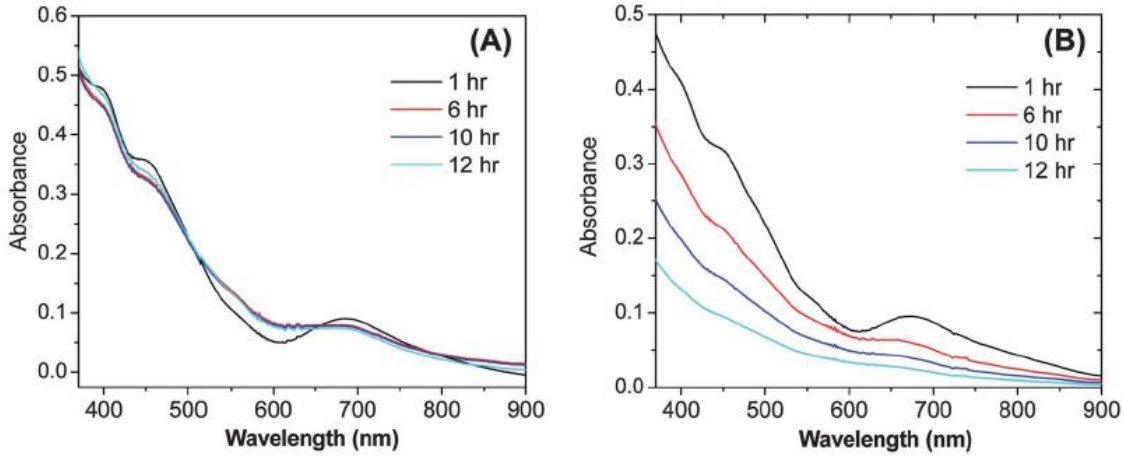

Figure 1.9 The stability comparisons of (A) $Au_{25}(Capt)_{18}$, and (B) $Au_{25}(SG)_{18}$ at 80 ℃. Reproduced from ref. (72) with permission from The Royal Society of Chemistry, copyright 2012.

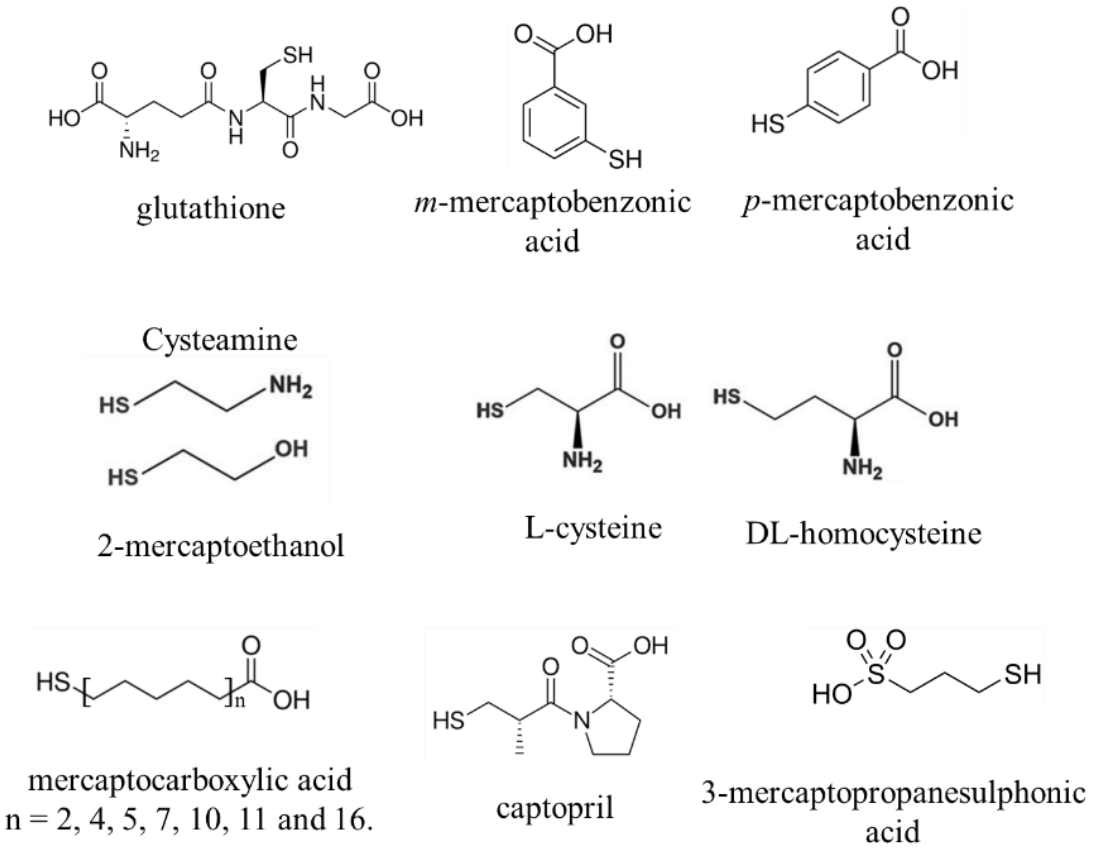

Scheme 1.5 The SR ligands used for the syntheses of water-soluble Au_{25} clusters.

The Xie group proposed a NaOH-mediated $NaBH_4$ reduction method (see the section 1.2.1), by which they achieved the gram-scale syntheses of several kinds of water-soluble Au_{25} NCs, such as the ones protected by $HSC_nH_{2n}COOH$ (n = 2, 7, 10).[48] Lee et al.[73,74] report the synthesis of a new water-soluble Au_{25} NCs capped by (3-mercaptopropyl)sulfonate. The ligand-exchange method can also be applied to prepare water-soluble metal clusters. For example, the Pradeep group exchanged the $Au_{25}(SG)_{18}$ NCs with the 3-mercapto-2-butanol (MB) ligand, and the excitation spectrum of the MB-exchanged Au_{25} was completely different from these of the acetyl- or formyl-exchanged Au_{25} products.[75]

High-purity and -yield synthesis of these water-soluble nanoclusters is fundamental for further characterizations and applications. After years of research, many kinds of SR ligands-protected Au_{25} NCs have been synthesized, as summarized in Scheme 1.5.

1.4.2 Chirality of $Au_{25}SR_{18}$

Chirality is a universal phenomenon in nature, meaning an object and its mirror-symmetrical counterpart cannot be perfectly superimposed. It has been extensively researched in the field of organic chemistry, and plays a critical role in scientific research and real applications, such as chiral catalysis and drug development. Because the atomically precise structure of metal NCs more resemble the molecule or "superatom", many researches have been focused on the chirality of NCs recently. The origins of the chirality in the NCs can be ascribed to the following three reasons: (a) chiral arrangements of the metallic core; (b) asymmetric arrangements of the capped ligands; (c) chiral carbon tails in the surface ligands. As shown in Figure 1.3, Au_{25} NCs consist by the symmetric Au_{13} kernel and six of Au_2S_3 motifs, which also show the highly symmetrical arrangement on the Au_{13} kernel. Thus, only the strategy (c) is possible to be used for endowing chiral properties to $Au_{25}(SR)_{18}$ NCs.

In 2011, Zhu et al.[76,77] prepared the *R*- or *S*-$Au_{25}(PET^*)_{18}$ NCs (PET* represents chirally modified PET, $–SCH_2C^*H(CH_3)Ph$) by the size-focusing method (see the section 1.2.1). The as-obtained $Au_{25}(PET^*)_{18}$ NCs had the obvious circular dichroism (CD) responses at ~275, 325, 375, 430 and 490 nm (Figure 1.10A), while no such response was detected in the $Au_{25}(PET)_{18}$ NCs. Subsequently, Jin et al.[71] synthesized the water-soluble $Au_{25}(Capt)_{18}$ clusters (Capt is short for Captopril), which also showed the chiral properties (Figure 1.10B). In addition, ligand-exchange is also a facile method for introducing a chiral ligand into achiral metal NCs, thus endowing

the exchanged NCs with the chiroptical response. For instance, Bürgi et al.[78,79] conducted the ligand exchange to convert the achiral $Au_{25}(PET)_{18}$ to obtain chiral properties by introducing the R/S-BINAS or NILC/NIDC ligands. The BINAS-Au_{25} NCs showed chiroptical responses at ~300, 350, 400 and 500 nm (Figure 1.10C). These works all unveiled the critical role of pendant ligands in the CD responses of metal NCs.

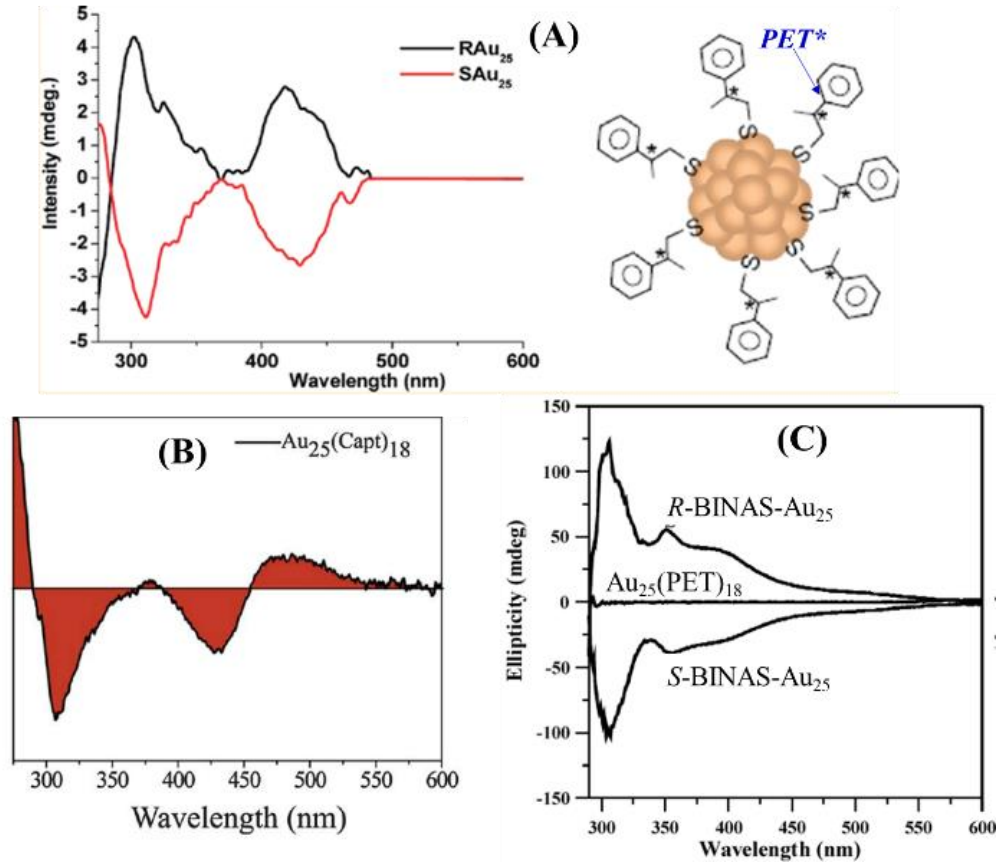

Figure 1.10 Circular dichroism (CD) spectra of (A) $Au_{25}(PET^*)_{18}$ NCs. Reproduced from ref. (76) with permission from American Chemical Society, copyright 2011. (B) $Au_{25}(Capt)_{18}$ NCs. Reproduced from ref. (71) with permission from The Royal Society of Chemistry, copyright 2012. (C) $Au_{25}(PET)_{18}$ NCs and its *R*/*S*-BINAS ligand-exchange products. Reproduced from ref. (78) with permission from American

Chemical Society, copyright 2009.

1.4.3 Optical properties of $Au_{25}SR_{18}$

When the size of Au NPs ranges in nano-scale (normally 5–20 nm), the surface plasmon resonance (SPR) bands dominate in the optical absorption located at ~520 nm. Along with the size decrease of Au NPs, this absorption peak will gradually blue-shifts and finally disappears. Owing to the discrete energy levels of small-sized NPs (with size < ~2 nm, in terms of nanoclusters), other optical absorption peaks occur instead.

In 2008, for the first time, the Jin group[33] conducted the time-dependent density functional theory (TD-DFT) calculations on the model compound of $Au_{25}(SH)_{18}$, which was simplified based on the crystal structure of $[Au_{25}(PET)_{18}]^{-}\cdot(TOA)^{+}$ (Figure 1.11A). The $Au_{25}(SR)_{18}$ NCs in the solution state have three obvious absorption peaks at ~400, 450 and 670 nm, and several shoulder peaks at ~350, 560 and 800 nm (Figure 1.11B). The major absorption peaks (a, b and c) match well between the observed ones (Figure 1.11b) and the calculated ones (Figure 1.11c). Based on the orbital energy level, the UV-vis signal at ~670 nm (~1.82 eV, peak a) corresponds to the transition between the HOMO and LUMO gap, which is essentially the interband transition (*sp*←*sp*). The peak at ~450 nm (~2.75 eV, peak b) is consisted by the interband *sp*←*sp* and intraband *d*←*sp* transitions. Regarding the peak of ~400 nm (~3.10 eV, peak c), the transition mode is an intraband transition (*d*←*sp*), arising from the other occupied HOMO to the *d* band. In addition, the optical absorptions of $Au_{25}(PET)_{18}$ with different charge states (–1, 0, +1 charge states) were found to be distinctive (Figure 1.12), arising from the increasing HOMO–LUMO transitions.[15,20] The alternation of Au_{25} core charge state from –1 to 0 (or +1) would eliminate one (or

two) electron, which lead to a larger splitting of 1P orbitals, and therefore the highest energy 1P orbital would become unoccupied.[80]

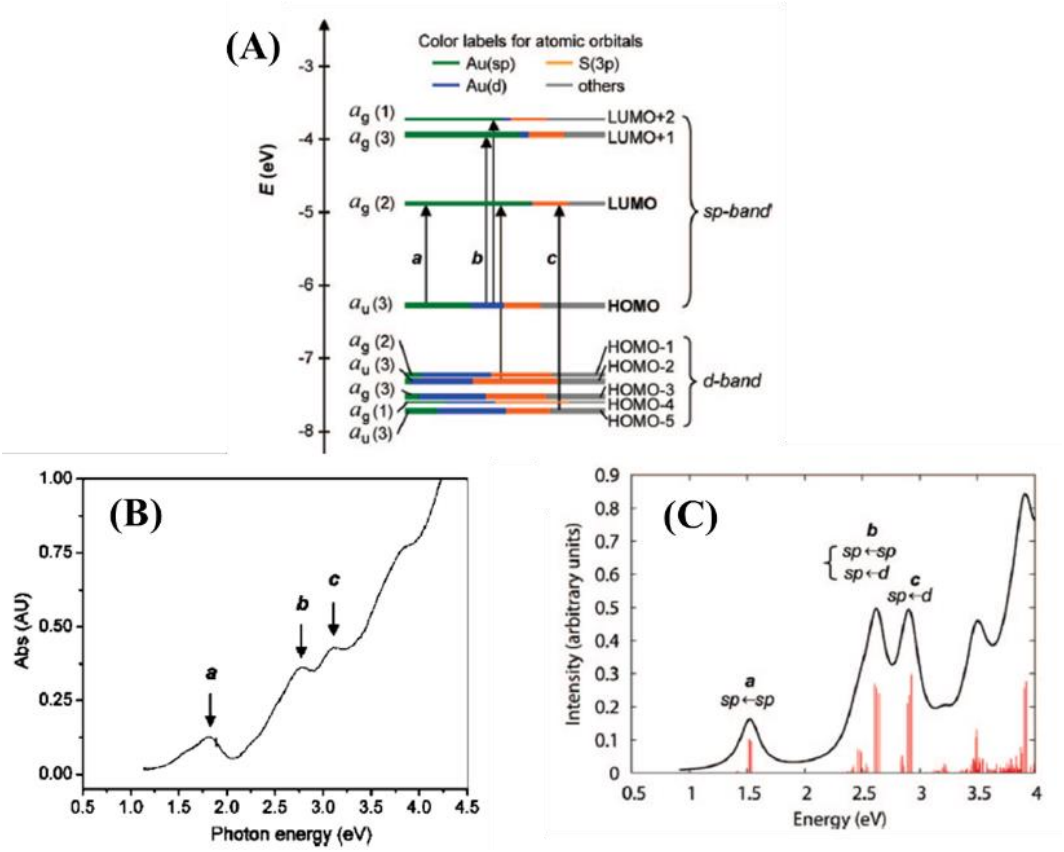

Figure 1.11 (A) Kohn-Sham orbital energy level diagram for a model compound $Au_{25}(SH)_{18}$; (B) the experimental absorption spectrum of $[Au_{25}(PET)_{18}]$ NCs; (C) the theoretical absorption spectrum of $Au_{25}(SH)_{18}$. Peak *a* corresponds to 1.8 eV, peak *b* corresponds to 2.75 eV, and peak *c* corresponds to 3.1 eV. Reproduced from ref. (33) with permission from American Chemical Society, copyright 2008.

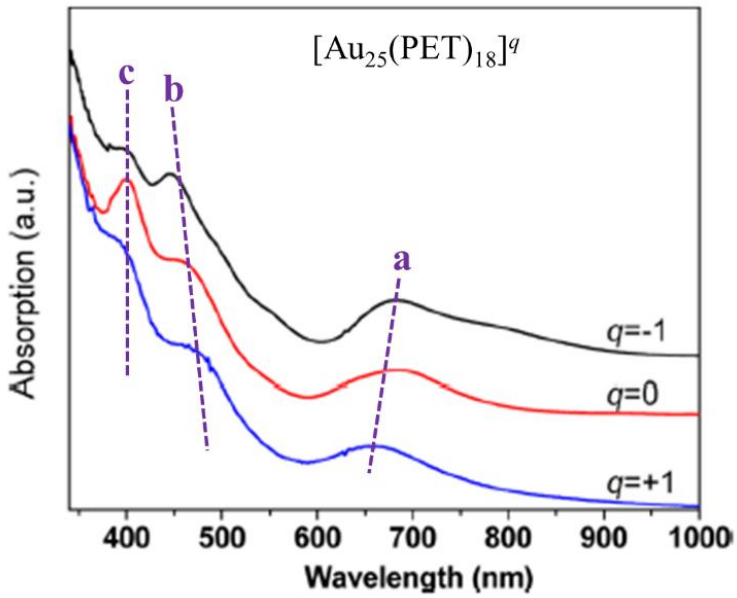

Figure 1.12 UV-vis absorption spectra of $Au_{25}(PET)_{18}$ clusters with charge states of –1, 0, and +1. Reproduced from ref. (15) with permission from American Chemical Society, copyright 2016.

Recently, the Xie group[48] synthesized a series of water-soluble Au_{25} NCs by the NaOH-mediated $NaBH_4$ reduction method. Through controlling the positively or neutrally charge of SR ligands (Figure1.13A), the shapes of absorption spectra shows the distinctive changes among them.[81] As shown in Figure 1.13B, two abnormal characteristic optical absorptions at 780 and 980 nm were observed when the Au_{25} surface was mainly capped by the negatively charged SR ligands. They proposed that the charge anisotropy, induced by the interactions between the charged SR ligands, could result in the structural distortions of the $Au_{25}(SR)_{18}$, which simultaneously result in the occurrence of the above abnormal absorption peaks.

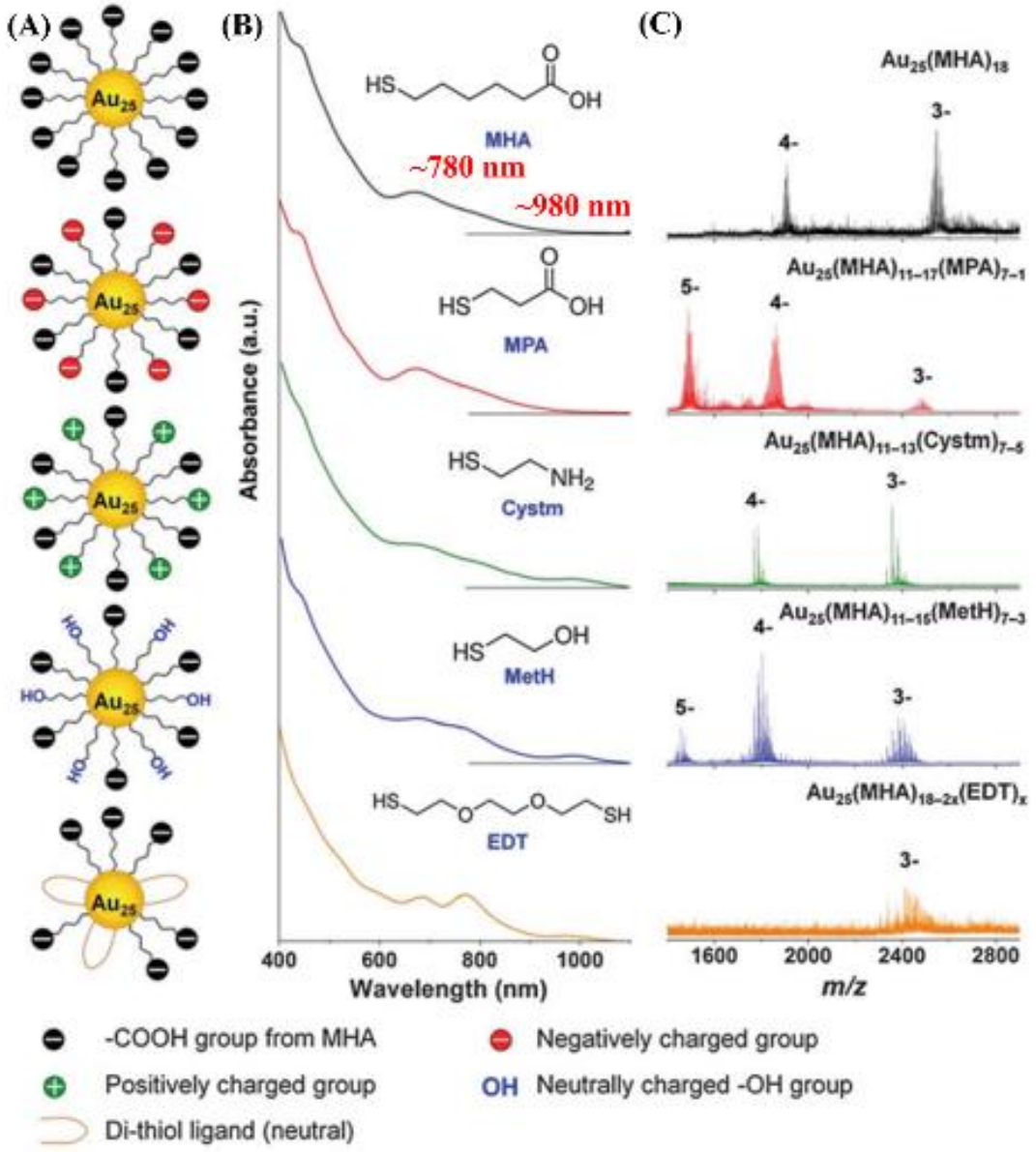

Figure 1.13 (A) Illustrations, (B) UV-vis absorptions, and (C) ESI-MS of the mono/bi-thiolate protected Au_{25} clusters. Reproduced from ref. (81) with permission from The Royal Society of Chemistry, copyright 2016.

Photoluminescence is one of the most fascinating properties of nanomaterials, which has attracted wide research interest in the chemical sensing and bioimaging fields. Among these fluorescent nanomaterials, nanoclusters have emerged as a prominent member with the advantages of monodisperse size and the atomically accurate

structure, and thus the mechanism of the PL could be reasonably proposed. In 2009, the Xie group[82] synthesized a fluorescent Au_{25} NCs stabilized by a common protein (bovine serum albumin), and its quantum yield (QY) was about 6% under excitation at 640 nm. Noted that this Au_{25} NCs has been widely applied in the ion detection and bioimaging fields in their following works.[83–85] In addition, the kind of Au_{25} NCs hold a long fluorescence lifetime, and thus show a polarization behaviour, which can be used for time-gated detection in imaging and microscopy.

The Jin group[86] reported the ligand effect for the PL of $Au_{25}(SR)_{18}$ clusters. As presented in Figure 1.14A, the PL intensity follows the order $[Au_{25}(SG)_{18}]^{-}$ >> $[Au_{25}(PET)_{18}]^{-}$ > $[Au_{25}(SC_{12}H_{25})_{18}]^{-}$ > $[Au_{25}(SC_6H_{13})_{18}]^{-}$. Because all $Au_{25}(SR)_{18}$ NCs should share a typical Au_{12}/Au_{13} shell-core structure regardless of the SR ligands (Figure 1.3), it indicated that the PL property cannot be solely ascribed to the quantization effect of Au atoms. This is, the ligand effect also acts an important role on the PL of metal clusters. In addition, the PL intensities of $Au_{25}(PET)_{18}$ with different charges are also different, following the trend: $-1 < 0 < +1 < +2$ (Figure 1.14B). Based on these, it was concluded that the electron-donation from surface SR ligands to metal core should be reasoned for the different PL intensities when the Au_{25} NCs were capped by different ligands. Therefore, they proposed three strategies for enhancing the PL performance of metal NCs: (1) to use SR ligands with the strong electron donation capability; (2) to use SR ligands containing electron-rich atoms or groups; (3) to increase the electropositivity of the metal core. On the basis of these guidance, when the $Au_{25}(SG)_{18}$ NCs were ligand-exchanged with a long-chain peptide nucleic acid (PNA, containing the electron-rich N and O atoms, Figure 1.14C), the PL intensity could be enhanced by 1.8 times, as show in Figure 1.14D. Recently, Wu et al.[87] studied the PL intensities of $MAg_{24}(SR)_{18}$ NCs, which show a sequence of

$PdAg_{24}(SR)_{18}$ < $Ag_{25}(SR)_{18}$ < $PtAg_{24}(SR)_{18}$ < $AuAg_{24}(SR)_{18}$, and such an order is matched well with the electron affinity order of Au_{13} core. This results also hints that the charge transfer of delocalized electrons contributes to the emission intensity of these clusters.

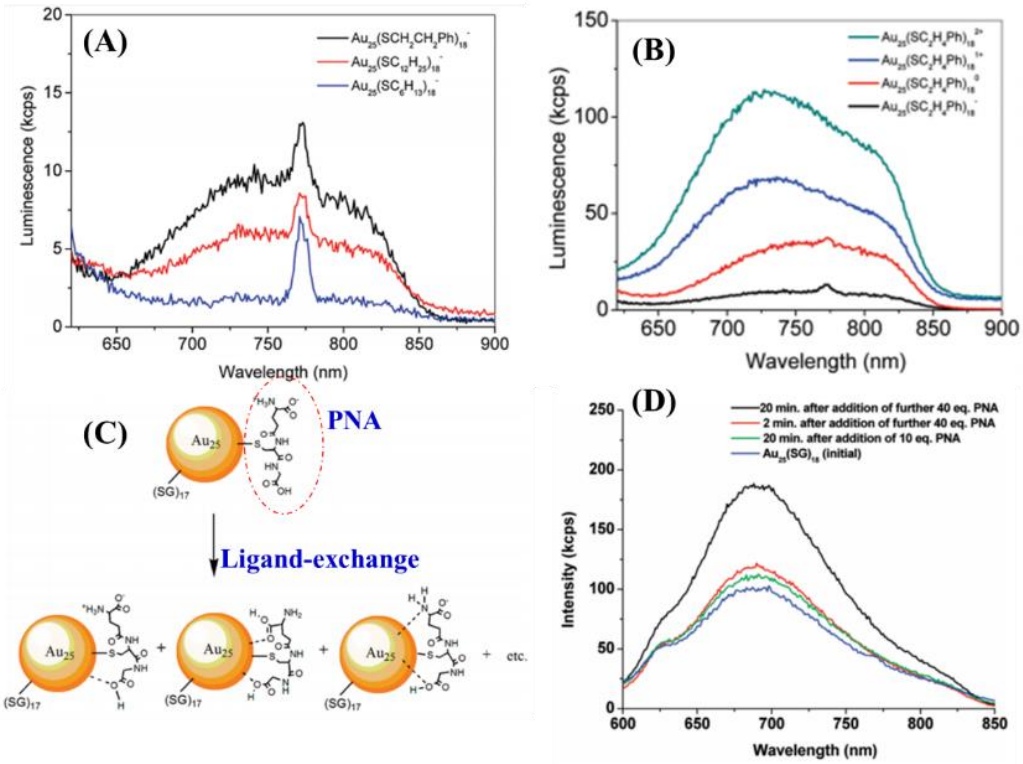

Figure 1.14 (A) PL spectra of Au_{25} NCs capped by different ligands. (B) PL spectra of $Au_{25}(PET)_{18}$ nanoclusters with different charge states. (C) Illustration of ligand-exchange of $Au_{25}(SG)_{18}$ with PNA. (D) PL spectra of $Au_{25}(SG)_{18}$ NCs before and after being exchanged by PNA. Reproduced from ref. (86) with permission from American Chemical Society, copyright 2010.

1.5 Applications of cationic-ligand-protected Au nanoparticle/nanocluster

Owing to the intriguing optical properties, noble metal nanoparticles have been widely utilized in environmental monitoring, chemical sensing, drug delivery, cancer therapy, bioimaging, biolabeling, nanomedicine, and photodynamic therapy.[1–5,8–11,15,17,20] A complex task because the metal NPs are in diverse environments with a plethora of potential interactions with the host, that limit their practical uses. Especially in some special fields, such as biological signalling, cellular toxicity, particle transportation, and environmental impact, endowing the positively charged ligands to metal NPs with respect to their behaviors at the nano–bio interface can offer the great advantages.[88–92] Thus, tuning the surface charge of metal NPs is a particularly important role in rational design of their real applications.

1.5.1 Cationic-ligand-protected Au nanoparticles

Metal NPs are often functionalized with the long hydrocarbon chains possessing diverse functional groups, such as sulfonates, alcohols, amines, and carboxylate.[88] These charged NPs will therefore show good interaction with other charged species in the targeted contents, resulting in the designed utilizations of NPs.

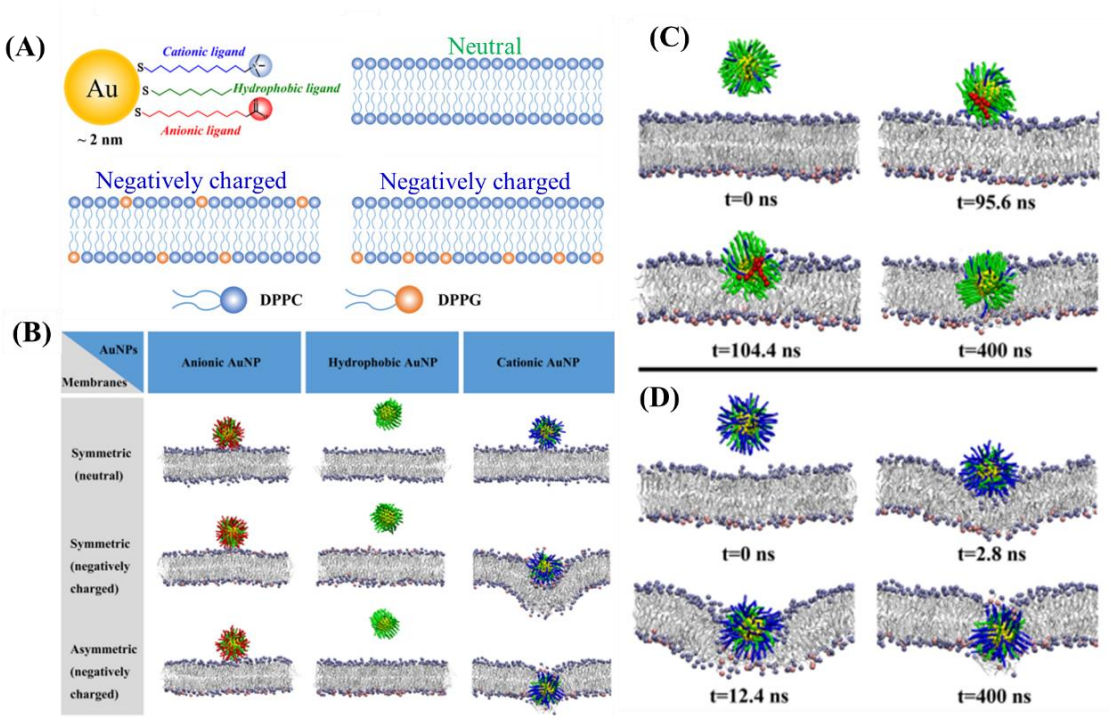

Figure 1.15 (A) Schematic illustration of the models of AuNPs decorated with different ligands, the symmetric lipid membrane (neutral), the symmetric lipid membrane (negatively charged), and the asymmetric lipid membrane (negatively charged). (B) Representative snapshots of equilibrated states for AuNPs with different signs of charge interacting with the three kinds of lipid membranes. (C) AuNP with 10% surface charge density, and (D) AuNP with 70% surface charge density. Reproduced from ref. (93) with permission from American Chemical Society, copyright 2017.

By using the computational simulations, Quan et al.[93] studied the role of ligand charge during Au NPs penetration through the liquid bilayers, as illuminated in Figure 1.15A. Figure 1.15B shows the hydrophobic (or neutral) Au NPs do not adsorb into all three kinds of membranes. Although the anionic Au NPs attached to both neutral or negatively charged membranes, no driving force is formed for these Au NPs to further penetrate the symmetric or asymmetric bilayers. By comparison, cationic Au NPs

have the strong affinities to the all types of membranes, but the penetration of cationic Au NPs through the membrane only occur for the negatively charged membranes, indicating the strong electrostatic attractions between the surface ligands on AuNPs and the charged groups in membranes. In addition, the simulations for cationic Au NPs with 10% and 70% surface charge density were also carried out (Figure 1.15 C and D), illustrating how important of electrostatic interactions for the Au NPs penetration mechanism.

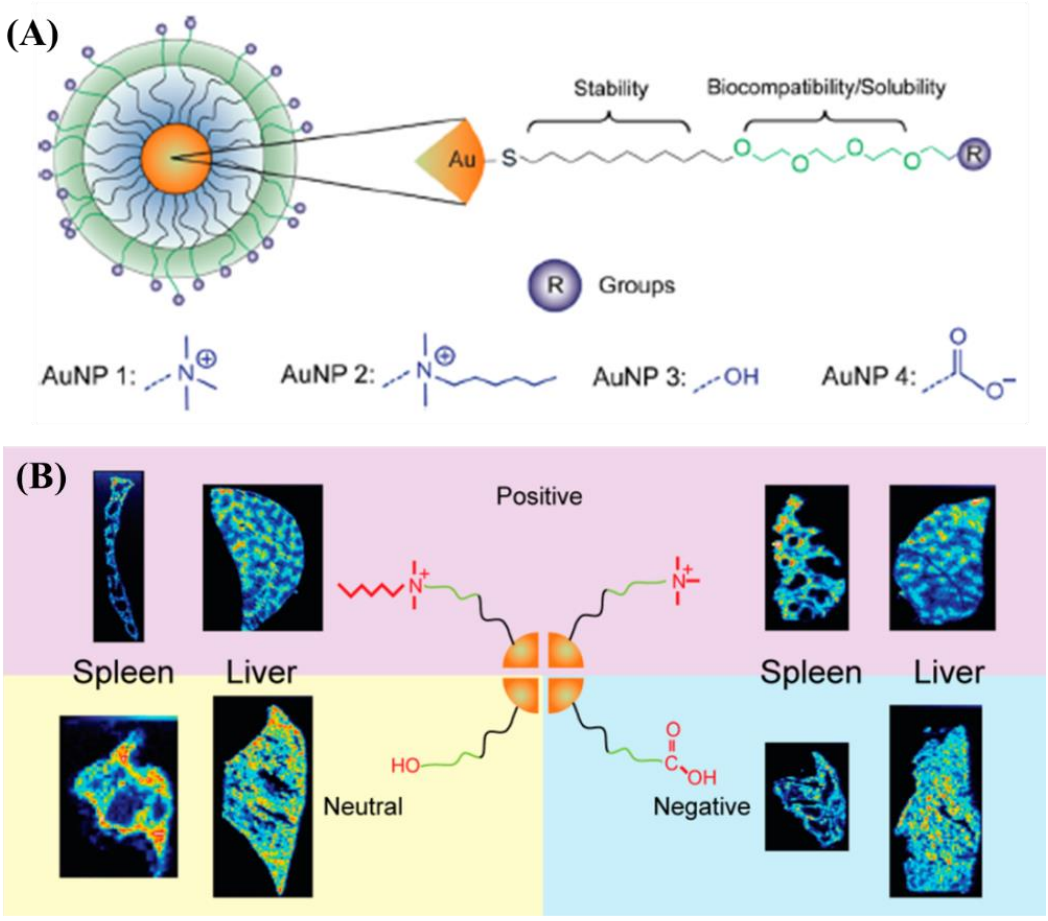

Figure 1.16 (A) Design and structure of the Au NPs. (B) Laser ablation ICP-MS results of the biodistribution of Au NPs in the spleen and liver tissues. Reproduced from ref. (94) with permission from American Chemical Society, copyright 2016.

Elci et al.[94] investigated how surface-ligand charge affects the biodistribution of 2-nm Au NPs *in vivo*, The Au NPs were first functionalized with different charged ligands (Figure 1.16A). The charges were shown by the identity of the headgroup in each of the AuNPs, which were either a positively-charged amine (Au NP1 and 2), a neutral alcohol group (Au NP3), or a negatively-charged carboxylate group (Au NP4). To investigate the sub-organ distribution, the authors used the laser ablation ICP-MS (LAICP-MS), which could capture the images including the quantifiable data of gold amount. Figure 1.16B shows the images on the distribution of the Au NPs in the spleen and liver. As for the biodistribution in spleen, it showed that all of the Au NPs accumulated in the cleans blood. But the Au NP3 and Au NP4 accumulated in the host immune system and the transition area (where the matter moves from the cleans blood to host immune system), while the Au NPs1 and 2 showed only a little presence in these areas. Regarding the biodistribution in liver, the the Au NPs1 and 2 ended up in the endothelium and hepatocytes, with very little ending up in Kupffer cells. On the other hand, the Au NP3 and Au NP4 had more accumulation in Kupffer cells, but were generally more broadly-distributed throughout the whole organ. These different accumulations indicated that the cationic-ligand-protected AuNPs (1 and 2) are more quickly filtered by the body than the neutral or anionic ones. This understanding of surface-charge effects on Au NPs distribution in the sub-organ is benefit to the rational design of metal NPs used in specific nanotherapeutic utilizations.

1.5.2 Cationic-ligand-protected Au nanoclusters

Cationic ligands incorporated on the NCs surface cater the long-held belief that these animo-groups (like $-NH_2$, $-N(CH_3)_2$, positive in solution) would provide the intimate interactions on negatively-charged cell wall, which thus damages the bacterial

membrane, and subsequently results in a better antimicrobial efficacy.[88–91] However, only a few works have been focused on the applications of cationic-ligand-protected Au NCs because of the infrequent synthetic works for the cationic-ligand-protected Au NCs.

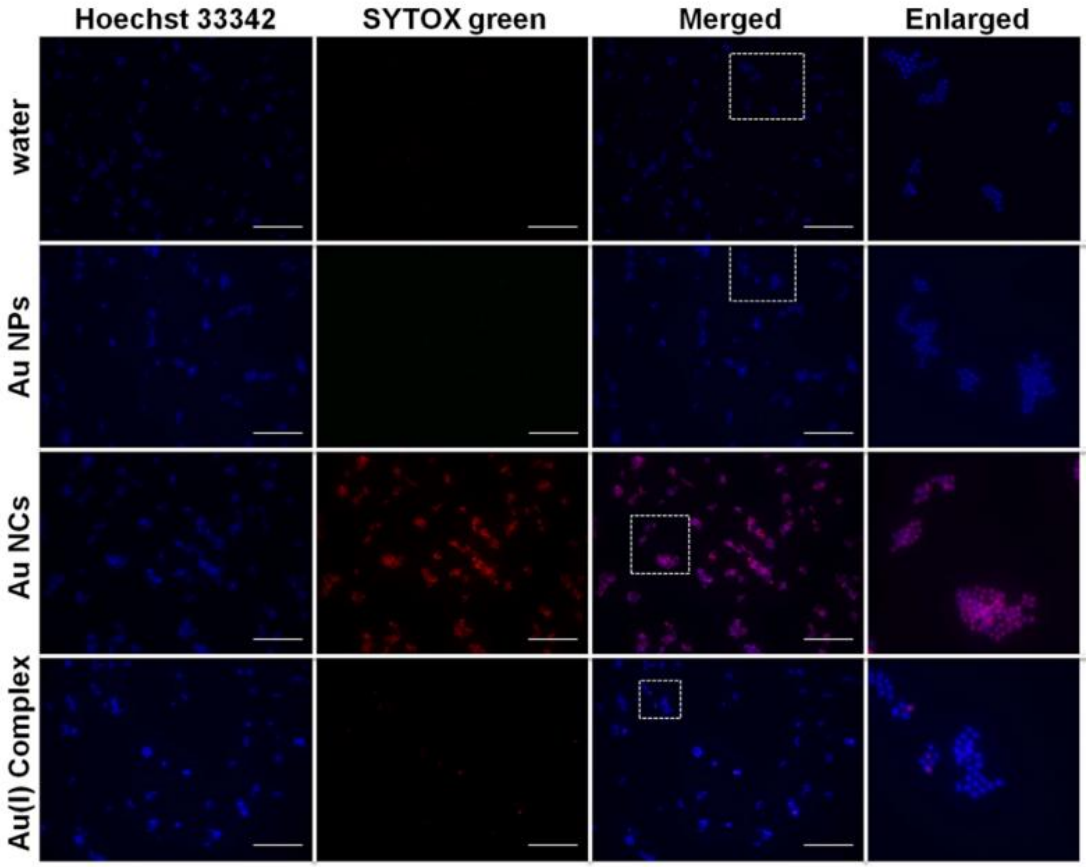

Figure 1.17 Representative fluorescence images of the S. aureus treated with water, Au NPs, Au_{25} NCs and Au(I) complex. The dead cells were visualized by SYTOX green (false color: red), whereas the Hoechst 33342 (blue) helped to identify all cells. Scale bar is 25 μm. Reproduced from ref. (95) with permission from American Chemical Society, copyright 2017.

Recently, the Xie group[95] reported that it was possible to use $Au_{25}(MHA)_{18}$ (MHA short for 6-mercaptohexanoic acid) NCs to kill both Gram-positive and Gram-negative bacteria. As shown in Figure 1.17, compared with the Au NPs and Au(I)

complexes, the Au_{25} NCs hold the better killing efficiency on the *S. aureus*. The antimicrobial mechanism of Au_{25} NCs lies on the internalization of NCs, inducing a metabolic imbalance in bacterial cells, which lead to an increase of intracellular reactive oxygen species (ROS) generation that kills bacteria consequently. Furthermore, considering the role of surface ligands in regulating the NPs' interaction to bacterial cells, the Xie et al.[96] hypothesized that it could control the Au NCs' antimicrobial properties through tuning its surface ligands' charges. Figures 1.18A and D show that $Au_{25}(MHA)_{18}$, $Au_{25}(MBA)_{18}$ and $Au_{25}(Cys)_{18}$ NCs effectively killed ~95%, ~93% and ~15% of *S. aureus*, respectively, indicating the types of surface ligands (or charge states) could affect the antimicrobial ability of Au_{25} NCs. Figures 1.18B and D shows that $Au_{25}Cystm_xMHA_{18-x}$, ~91 to 28 and ~16% with the number of $-NH_2$ groups on the Au_{25} clusters, increase from 0−2 to 1−4 and 6−9, respectively, suggesting an inverse relationship between the number of $-NH_2$ groups and their antimicrobial efficacy. Figures 1.18C and D show that $Au_{25}MetH_xMHA_{18-x}$, ~92%, 90% and ~38% at x = 0−2, 1−5, 7−10, respectively, suggesting the higher ratio of −COOH group led to the better antimicrobial ability of Au_{25} NCs. All these results proposed that the surface charge in Au_{25} NCs could affect the ROS generation ability of bacteria, and more ROS interfere the metabolism enzyme of bacteria, disturb their normal metabolism, and kill the bacteria in the end.

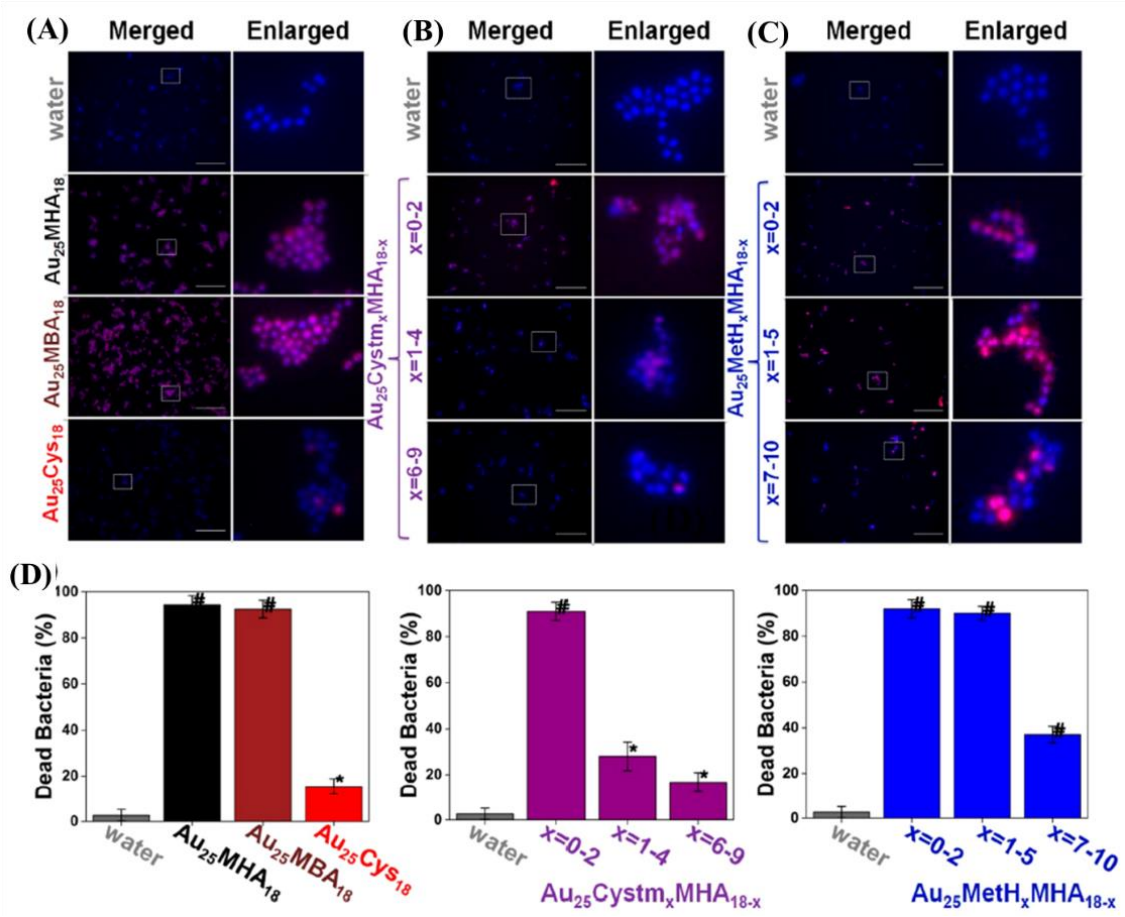

Figure 1.18 (A−C) Merged and enlarged representative fluorescence images of the *S. aureus* after treatment of Au_{25} NCs. The dead cells were stained by SYTOX green (false color: red), whereas the total cells were stained by Hoechst 33342 (blue). Scale bar is 25 μm. (D) Percentage of the dead *S. aureus* after treated with different ligand-protected Au_{25} NCs. MHA short for 6-mercaptohexanoic acid; MBA short for *m*-mercaptobenzonic acid; Cys short for L-cysteine; Cysm short for cysteamine; MetH short for 2-mercaptoethanol. (See Scheme 1.5) Reproduced from ref. (96) with permission from American Chemical Society, copyright 2018.

1.6 Summary and Perspective

To date, Au_mSR_n NCs have been extensively studied due to their excellent stabilities and intriguing physicochemical properties, such as $Au_{25}(SR)_{18}$, $Au_{38}(SR)_{24}$, $Au_{67}(SR)_{35}$, $Au_{102}(SR)_{44}$, $Au_{130}(SR)_{50}$, and $Au_{144}(SR)_{60}$ can be easily synthesized. However, $Au_m(SR)_n$ NCs are mainly prepared through the use of neutral and anionic SR (or acidic ones, which possess the negative charge in solution) ligands, as summarized in Table 1.1.

Table 1.1 The summary of SR ligands used for the syntheses of Au NCs with atomic precision.

Types	Thiolate ligands (SR)
Neutral	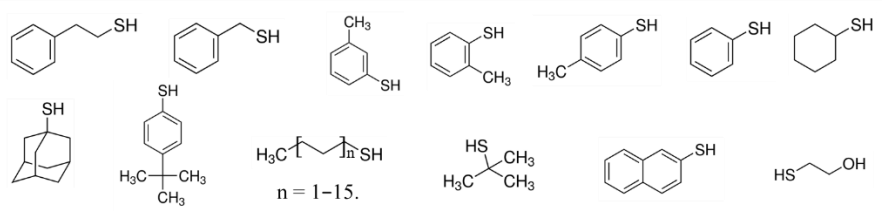
Anionic (or acidic)	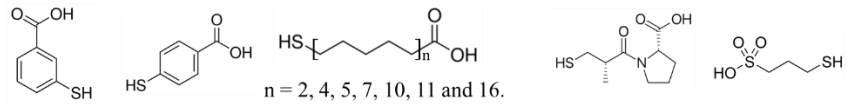
Cationic (or basic)	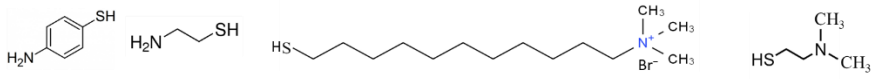
Ones containing both acidic and basic groups	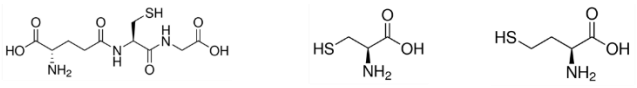

To the best of my knowledge, there are only four reports for the cationic SR (or basic ones, which possess the positive charge in solution). In 2012, Au_{25} NCs stabilized by 4-aminothiophenol ($HSPhNH_2$) was prepared but its molecular formula was accidentally assigned as $Au_{25}(SPhNH_2)_{17}$.[97] Recently, the Xie group[48,95,96] developed a

NaOH-mediated $NaBH_4$ reduction method for Au_{25} NCs synthesis using cystamine ($HSCH_2CH_2NH_2$). However, cystamine should associate with the mercaptocarboxylic acids for stabilizing Au_{25} NCs. Recently, Ishida et al.[98,99] modified the Burst method at optimized reduction rate, resulting in the successful synthesis of a Au_{25}NCs using a SR ligand with the pendant quaternary-ammonium group ($-[N(CH_3)_3]^+$).The latest reports by the Whetten group[100,101] only reported the evidence of polydisperse captamine ($HS(CH_2)_2N(CH_3)_2$)-protected Au NCs with sizes ranging from 25–144. These few works seem to follow a categorically state mention 2005: "Small positively charged ligands do not support the production of the monolayer protected clusters (MPCs) in the Brust synthesis."[68] However, in some special areas, such as biological signalling, particle transportation, cellular toxicity, and environmental impact, cationic-ligands-protected NCs can be indispensable due to the good affinity of the cationic ligand for the biomaterial. Accordingly, there is an emergency need for methods to synthesize the cationic-ligand-protected NCs with high-yield and high-purity, and researching their physicochemical properties.

1.7 Objective of the study

This study is to pursue the exploration of the surface chemistry on the cationic-ligand-protected Au NCs.

(1) To understand the kinetics of cationic-ligand-exchange reactions in Au_{25} NCs.

(2) To synthesize the pyridyl ethanethiol ($HSCH_2CH_2Py$)-protected Au_{25} NCs in high-purity and high-yield.

(3) To research the unique (de)protonation reaction on the $Au_{25}(SCH_2CH_2Py)_{18}$ NCs.

(4) To evaluate the photoluminescent property of the pyridyl-thiolated Au_{25} NCs;

(5) To investigate the Menshutkin reaction on the $Au_{25}(SCH_2CH_2Py)_{18}$ NCs.

1.8 References

(1) Daniel, M. C.; Astruc, D. Gold nanoparticles: assembly, supramolecular chemistry, quantum-size-related properties, and applications toward biology, catalysis, and nanotechnology. *Chem. Rev.* **2004,** *104*, 293–346.

(2) Jain, P. K.; El-Sayed, I. H.; El-Sayed, M. A. Au nanoparticles target cancer. *Nano Today*, **2007**, *2*, 18–29.

(3) Saha, K.; Agasti, S. S.; Kim, C.; Li, X.; Rotello, V. M. Gold nanoparticles in chemical and biological sensing. *Chem. Rev.* **2012**, *112*, 2739–2779.

(4) Sperling, R. A.; Gil, P. R.; Zhang, F.; Zanella, M.; Parak, W. J. Biological applications of gold nanoparticles. *Chem. Soc. Rev.* **2008**, *37*, 1896–1908.

(5) Fedlheim, D. L.; Foss, C. A. *Metal nanoparticles: synthesis, characterization, and applications*. 2001, CRC press.

(6) Faraday, M. The bakerian lecture: experimental relations of gold (and other metals) to Light. *Philos. Trans. R. Soc. London* **1857**, *147*, 145−181.

(7) Graham, T. X. Liquid diffusion applied to analysis. *Philos. Trans. R. Soc. London* **1861**, *151*, 183–224.

(8) Crooks, R. M.; Zhao, M.; Sun, L.; Chechik, V.; Yeung, L. K. Dendrimer-encapsulated metal nanoparticles: synthesis, characterization, and applications to catalysis. *Acc. Chem. Res.* **2001**, *34*, 181–190.

(9) Liu, L.; Corma, A. Metal catalysts for heterogeneous catalysis: from single atoms to nanoclusters and nanoparticles. *Chem. Rev.* **2018**, *118*, 4981–5079.

(10) Chakraborty, I.; Pradeep, T. Atomically precise clusters of noble metals: emerging link between atoms and nanoparticles. *Chem. Rev.* **2017**, *117*, 8208–8271.

(11) Kang, H.; Buchman, J. T.; Rodriguez, R. S.; Ring, H. L.; He, J.; Bantz, K. C.;

Haynes, C. L. Stabilization of silver and gold nanoparticles: preservation and improvement of plasmonic functionalities. *Chem. Rev.* **2018**, *119*, 664–699.

(12) Jin, R.; Cao, Y. C.; Hao, E.; Metraux, G. S.; Schatz, G. C.; Mirkin, C. A. Controlling anisotropic nanoparticle growth through plasmon excitation. *Nature* **2003**, *425*, 487−490.

(13) Wang, Y.; Zheng, Y.; Huang, C. Z.; Xia, Y. Synthesis of Ag nanocubes 18−32 nm in edge length: the effects of polyol on reduction kinetics, size control, and reproducibility. *J. Am. Chem. Soc.* **2013**, *135*, 1941−1951.

(14) Jin, R. Atomically precise metal nanoclusters: stable sizes and optical properties. *Nanoscale* **2015**, *7*, 1549−1565.

(15) Jin, R.; Zeng, C.; Zhou, M.; Chen, Y. Atomically precise colloidal metal nanoclusters and nanoparticles: fundamentals and opportunities. *Chem. Rev.* **2016**, *116*, 10346–10413.

(16) Bain, C. D.; Troughton, E. B.; Tao, Y. T.; Evall, J.; Whitesides, G. M.; Nuzzo, R. G. Formation of monolayer films by the spontaneous assembly of organic thiols from solution onto gold. *J. Am. Chem. Soc.* **1989**, *111*, 321–335.

(17) Rosi, N. L.; Mirkin, C. A. Nanostructures in biodiagnostics. *Chem. Rev.* **2005**, *105*, 1547–1562.

(18) Brust, M.; Walker, M.; Bethell, D.; Schiffrin, D. J.; Whyman, R. Synthesis of thiol-derivatised gold nanoparticles in a two-phase liquid–liquid system. *J. Am. Chem. Soc. Chem. Commun.* **1994**, *7*, 801–802.

(19) Jadzinsky, P. D.; Calero, G.; Ackerson, C. J.; Bushnell, D. A.; Kornberg, R. D. Structure of a thiol monolayer-protected gold nanoparticle at 1.1 Å resolution. *Science* **2007**, *318*, 430–433.

(20) Kang, X.; Chong, H.; Zhu, M. $Au_{25}(SR)_{18}$: the captain of the great

nanocluster ship. *Nanoscale* **2018**, *10*, 10758–10834.

(21) Kang, X.; Zhu, M. Tailoring the photoluminescence of atomically precise nanoclusters. *Chem. Soc. Rev.* **2019**, *48*, 2422–2457.

(22) Xu, W. W.; Zeng, X. C.; Gao, Y. Application of electronic counting rules for ligand-protected gold nanoclusters. *Acc. Chem. Res.* **2018**, *51*, 2739–2747.

(23) Yao, Q.; Chen, T.; Yuan, X.; Xie, J. Toward total synthesis of thiolate-protected metal nanoclusters. *Acc. Chem. Res.* **2018**, *51*, 1338–1348.

(24) Sakthivel, N. A.; Dass, A. Aromatic thiolate-protected series of gold nanomolecules and a contrary structural trend in size evolution. *Acc. Chem. Res.* **2018**, *51*, 1774–1783.

(25) Chen, Y.; Zeng, C.; Liu, C.; Kirschbaum, K.; Gayathri, C.; Gil, R. R.; Rosi, N. L; Jin, R. Crystal structure of barrel-shaped chiral Au_{130}(*p*-MBT)$_{50}$ nanocluster. *J. Am. Chem. Soc.* **2015**, *137*32, 10076–10079.

(26) Zeng, C.; Li, T.; Das, A.; Rosi, N. L.; Jin, R. Chiral structure of thiolate-protected 28-gold-atom nanocluster determined by X-ray crystallography. *J. Am. Chem. Soc.* **2013**, *135*, 10011–10013.

(27) Qian, H.; Eckenhoff, W. T.; Zhu, Y.; Pintauer, T.; Jin, R. Total structure determination of thiolate-protected Au_{38} nanoparticles. *J. Am. Chem. Soc.* **2010**, *132*, 8280–8281.

(28) Chen, S.; Wang, S.; Zhong, J.; Song, Y.; Zhang, J.; Sheng, H.; Pei, Y.; Zhu, M. The structure and optical properties of the (Au_{18}(SR)$_{14}$) nanocluster. *Angew. Chem., Int. Ed.* **2015**, *54*, 3145−3149.

(29) Zeng, C.; Qian, H.; Li, T.; Li, G.; Rosi, N. L.; Yoon, B.; Barnett, R. N.; Whetten, R. L.; Landman, U.; Jin, R. Total structure and electronic properties of the gold nanocrystal Au_{36}(SR)$_{24}$. *Angew. Chem., Int. Ed.* **2012**, *51*, 13114−13118.

(30) Das, A.; Li, T.; Nobusada, K.; Zeng, C.; Rosi, N. L.; Jin, R. Nonsuperatomic $[Au_{23}(SC_6H_{11})_{16}]^-$ nanocluster featuring bipyramidal Au_{15} kernel and trimeric $Au_3(SR)_4$ motif. *J. Am. Chem. Soc.* **2013**, *135*, 18264−18267.

(31) Crasto, D.; Barcaro, G.; Stener, M.; Sementa, L.; Fortunelli, A.; Dass, A. $Au_{24}(SAdm)_{16}$nanomolecules: x-ray crystal structure, theoretical analysis, adaptability of adamantane ligands to form $Au_{23}(SAdm)_{16}$ and $Au_{25}(SAdm)_{16}$, and its relation to $Au_{25}(SR)_{18}$. *J. Am. Chem. Soc.* **2014**, *136*, 14933−14940.

(32) Heaven, M. W.; Dass, A.; White, P. S.; Holt, K. M.; Murray, R. W. Crystal structure of the gold nanoparticle $[N(C_8H_{17})_4][Au_{25}(SCH_2CH_2Ph)_{18}]$. *J. Am. Chem. Soc.* **2008**, *130*, 3754−3755.

(33) Zhu, M.; Aikens, C. M.; Hollander, F. J.; Schatz, G. C.; Jin, R. Correlating the crystal structure of a thiol-protected Au_{25} cluster and optical properties. *J. Am. Chem. Soc.* **2008**, *130*, 5883−5885.

(34) Crasto, D.; Malola, S.; Brosofsky, G.; Dass, A.; Häkkinen, H. Single crystal XRD structure and theoretical analysis of the chiral $Au_{30}S(S\text{-}t\text{-}Bu)_{18}$ cluster. *J. Am. Chem. Soc.* **2014**, *136*, 5000−5005.

(35) Zeng, C.; Chen, Y.; Liu, C.; Nobusada, K.; Rosi, N. L.; Jin, R. Gold tetrahedra coil up: Kekulé-like and double helical superstructures. *Sci. Adv.* **2015**, *1*, e1500425.

(36) Zeng, C.; Chen, Y.; Iida, K.; Nobusada, K.; Kirschbaum, K.; Lambright, K. J.; Jin, R. Gold quantum boxes: on the periodicities and the quantum confinement in the Au_{28}, Au_{36}, Au_{44}, and Au_{52} magic series. *J. Am. Chem. Soc.* **2016**, *138*, 3950–3953.

(37) Dass, A.; Theivendran, S.; Nimmala, P. R.; Kumara, C.; Jupally, V. R.; Fortunelli, A.; Sementa, L.; Barcaro, G.; Zuo, X.; Noll, B. C. Au_{133}(SPh-

*t*Bu)$_{52}$nanomolecules: X-ray crystallography, optical, electrochemical, and theoretical analysis. *J. Am. Chem. Soc.* **2015**, *137*, 4610−4613.

(38) Higaki, T.; Zhou, M.; Lambright, K. J.; Kirschbaum, K.; Sfeir, M. Y.; Jin, R. Sharp transition from nonmetallic Au_{246} to metallic Au_{279} with nascent surface Plasmon resonance. *J. Am. Chem. Soc.* **2018**, *140*, 5691–5695.

(39) Sakthivel, N. A.; Dass, A. Aromatic thiolate-protected series of gold nanomolecules and a contrary structural trend in size evolution. *Acc. Chem. Res.* **2018**, *51*, 1774–1783.

(40) Zhou, M.; Higaki, T.; Hu, G.; Sfeir, M. Y.; Chen, Y.; Jiang, D. E.; Jin, R. Three-orders-of-magnitude variation of carrier lifetimes with crystal phase of gold nanoclusters. *Science* **2019**, *364*, 279–282.

(41) Schaaff, T. G.; Shafigullin, M. N.; Khoury, J. T.; Vezmar, I.; Whetten, R. L.; Cullen, W. G.; First, P. N.; Gutierrez-Wing, C.; Ascensio, J.; Jose-Yacaman, M. J. Isolation of smaller nanocrystal Au molecules: robust quantum effects in optical spectra. *J. Phys. Chem. B* **1997**, *101*, 7885−7891.

(42) Tracy, J. B.; Crowe, M. C.; Parker, J. F.; Hampe, O.; Fields- Zinna, C. A.; Dass, A.; Murray, R. W. Electrospray ionization mass spectrometry of uniform and mixed monolayer nanoparticles: $Au_{25}[S(CH_2)_2Ph]_{18}$ and $Au_{25}[S(CH_2)_2Ph]_{18-x}(SR)_x$. *J. Am. Chem. Soc.* **2007**, *129*, 16209−16215.

(43) Negishi, Y.; Nobusada, K.; Tsukuda, T. Glutathione-protected gold clusters revisited: bridging the gap between gold(I)−thiolate complexes and thiolate-protected gold nanocrystals. *J. Am. Chem. Soc.* **2005**, *127*, 5261−5270.

(44) Donkers, R. L.; Lee, D.; Murray, R. W. Synthesis and isolation of the molecule-like cluster $Au_{38}(PhCH_2CH_2S)_{24}$. *Langmuir* **2004**, *20*, 1945−1952.

(45) Zeng, C.; Chen, Y.; Das, A.; Jin, R. Transformation chemistry of gold

nanoclusters: From one stable size to another. *J. Phys. Chem. Lett.* **2015**, *6*, 2976–2986.

(46) Zhu, M.; Lanni, E.; Garg, N.; Bier, M. E.; Jin, R. Kinetically controlled, high-yield synthesis of Au_{25} clusters. *J. Am. Chem. Soc.* **2008**, *130*, 1138−1139.

(47) Parker, J. F.; Weaver, J. E.; McCallum, F.; Fields-Zinna, C. A.; Murray, R. W. Synthesis of monodisperse $[Oct_4N^+][Au_{25}(SR)_{18}^-]$ nanoparticles, with some mechanistic observations. *Langmuir* **2010**, *26*, 13650–13654.

(48) Yuan, X.; Zhang, B.; Luo, Z.; Yao, Q.; Leong, D. T.; Yan, N.; Xie, J. Balancing the rate of cluster growth and etching for gram-scale synthesis of thiolate-protected Au_{25} nanoclusters with atomic precision. *Angew. Chem., Int. Ed.* **2014**, *53*, 4623–4627.

(49) Luo, Z.; Nachammai, V.; Zhang, B.; Yan, N.; Leong, D. T.; Jiang, D. E.; Xie, J. Toward understanding the growth mechanism: tracing all stable intermediate species from reduction of Au (I)–thiolate complexes to evolution of Au_{25} nanoclusters. *J. Am. Chem. Soc.* **2014**, *136*, 10577–10580.

(50) Yao, Q.; Chen, T.; Yuan, X.; Xie, J. Toward total synthesis of thiolate-protected metal nanoclusters. *Acc. Chem. Res.* **2018**, *51*, 1338–1348.

(51) Qian, H.; Zhu, Y.; Jin, R. Size-focusing synthesis, optical and electrochemical properties of monodisperse $Au_{38}(SC_2H_4Ph)_{24}$ nanoclusters. *ACS Nano* **2009**, *3*, 3795–3803.

(52) Zeng, C.; Chen, Y.; Li, G.; Jin, R. Magic size Au64 $(S\text{-}c\text{-}C_6H_{11})_{32}$ nanocluster protected by cyclohexanethiolate. *Chem. Mater.* **2014**,*26*, 2635–2641.

(53) Li, G.; Zeng, C.; Jin, R. Thermally robust $Au_{99}(SPh)_{42}$ nanoclusters for chemoselective hydrogenation of nitrobenzaldehyde derivatives in water. *J. Am. Chem. Soc.* **2014**, *136*, 3673–3679.

(54) Qian, H.; Jin, R. Ambient synthesis of $Au_{144}(SR)_{60}$ nanoclusters in methanol. *Chem. Mater.* **2011**, *23*, 2209–2217.

(55) Tracy, J. B.; Crowe, M. C.; Parker, J. F.; Hampe, O.; Fields-Zinna, C. A.; Dass, A.; Murray, R. W. Electrospray ionization mass spectrometry of uniform and mixed monolayer nanoparticles: $Au_{25}[S(CH_2)_2Ph]_{18}$ and $Au_{25}[S(CH_2)_2Ph]_{18-x}(SR)_x$. *J. Am. Chem. Soc.* **2007**, *129*, 16209–16215.

(56) Dass, A.; Stevenson, A.; Dubay, G. R.; Tracy, J. B.; Murray, R. W. Nanoparticle MALDI-TOF mass spectrometry without fragmentation: $Au_{25}(SCH_2CH_2Ph)_{18}$ and mixed monolayer $Au_{25}(SCH_2CH_2Ph)_{18-x}(L)_x$. *J. Am. Chem. Soc.* **2008**, *130*, 5940–5946.

(57) Parker, J. F.; Kacprzak, K. A.; Lopez-Acevedo, O.; Häkkinen, H.; Murray, R. W. Experimental and density functional theory analysis of serial introductions of electron-withdrawing ligands into the ligand shell of a thiolate-protected Au25 nanoparticle. *J. Phys. Chem. C* **2010**, *114*, 8276–8281.

(58) Fields-Zinna, C. A.; Parker, J. F.; Murray, R. W. Mass spectrometry of ligand exchange chelation of the nanoparticle $[Au_{25}(SCH_2CH_2C_6H_5)_{18}]^{1-}$ by $CH_3C_6H_3(SH)_2$. *J. Am. Chem. Soc.* **2010**, *132*, 17193–17198.

(59) Carducci, T. M.; Blackwell, R. E.; Murray, R. W. Charge-transfer effects in ligand exchange reactions of Au_{25} monolayer-protected clusters. *J. Phys. Chem. Lett.* **2015**, *6*, 1299–1302.

(60) Ni, T. W.; Tofanelli, M. A.; Phillips, B. D.; Ackerson, C. J. Structural basis for ligand exchange on $Au_{25}(SR)_{18}$. *Inorg. Chem.* **2014**, *53*, 6500–6502.

(61) Salassa, G.; Sels, A.; Mancin, F.; Bürgi, T. Dynamic nature of thiolate monolayer in $Au_{25}(SR)_{18}$ nanoclusters. *ACS Nano* **2017,** *11*, 12609–12614.

(62) Zeng, C.; Li, T.; Das, A.; Rosi, N. L.; Jin, R. Chiral structure of thiolate-

protected 28-gold-atom nanocluster determined by X-ray crystallography. *J. Am. Chem. Soc.* **2013**, *135*, 10011–10013.

(63) Zeng, C.; Liu, C.; Chen, Y.; Rosi, N. L.; Jin, R. Gold−thiolate ring as a protecting motif in the $Au_{20}(SR)_{16}$ nanocluster and implications. *J. Am. Chem. Soc.* **2014**, *136*, 11922−11925.

(64) Zeng, C.; Liu, C.; Pei, Y.; Jin, R. Thiol ligand-induced transformation of $Au_{38}(SC_2H_4Ph)_{24}$ to Au_{36}(SPh-*t*-Bu)$_{24}$. *ACS Nano* **2013**, *7*, 6138–6145.

(65) Zeng, C.; Chen, Y.; Kirschbaum, K.; Appavoo, K.; Sfeir, M. Y.; Jin, R. Structural patterns at all scales in a nonmetallic chiral $Au_{133}(SR)_{52}$ nanoparticle. *Sci. Adv.* **2015**, *1*, e1500045.

(66) Schaaff, T. G.; Whetten, R. L. Giant gold−glutathione cluster compounds: intense optical activity in metal-based transitions. *J. Phys. Chem. B* **2000**, *104*, 2630–2641.

(67) Negishi, Y.; Takasugi, Y.; Sato, S.; Yao, H.; Kimura, K.; Tsukuda, T. Magic-numbered Au_n clusters protected by glutathione monolayers (n= 18, 21, 25, 28, 32, 39): isolation and spectroscopic characterization. *J. Am. Chem. Soc.* **2004**, *126*, 6518–6519.

(68) Ackerson, C. J.; Jadzinsky, P. D.; Kornberg, R. D. Thiolate ligands for synthesis of water-soluble gold clusters. *J. Am. Chem. Soc.* **2005**, 127, 6550–6551.

(69) Link, S.; El-Sayed, M. A.; Schaaff, T. G.; Whetten, R. L. Transition from nanoparticle to molecular behavior: a femtosecond transient absorption study of a size-selected 28 atom gold cluster. *Chem. Phys. Lett.* **2002**, *356*, 240–246.

(70) Yuan, X.; Yu, Y.; Yao, Q.; Zhang, Q.; Xie, J. Fast synthesis of thiolated Au_{25} nanoclusters via protection–deprotection method. *J. Phys. Chem. Lett.* **2012**, *3*, 2310–2314.

(71) Kumar, S.; Jin, R. Water-soluble $Au_{25}(Capt)_{18}$ nanoclusters: synthesis, thermal stability, and optical properties. *Nanoscale* **2012**, *4*, 4222–4227.

(72) Shivhare, A.; Wang, L.; Scott, R. W. Isolation of carboxylic acid-protected Au_{25} clusters using a borohydride purification strategy. *Langmuir* **2015**, *31*, 1835–1841.

(73) Kwak, K.; Lee, D. Electrochemical characterization of water-soluble Au_{25} nanoclusters enabled by phase-transfer reaction *J. Phys. Chem. Lett.* **2012**, *3*, 2476–2481.

(74) Kwak, K.; Kumar, S. S.; Pyo, K.; Lee, D. Ionic liquid of a gold nanocluster: a versatile matrix for electrochemical biosensors. *ACS Nano* **2013**, *8*, 671–679.

(75) Shibu, E. S.; Muhammed, M. H.; Tsukuda, T.; Pradeep, T. Ligand exchange of $Au_{25}SG_{18}$ leading to functionalized gold clusters: spectroscopy, kinetics, and luminescence. *J. Phys. Chem. C* **2008**, *112*, 12168–12176.

(76) Zhu, M.; Qian, H.; Meng, X.; Jin, S.; Wu, Z.; Jin, R. Chiral Au_{25} nanospheres and nanorods: synthesis and insight into the origin of chirality. *Nano Lett.* **2011**, *11*, 3963–3969.

(77) Qian, H.; Zhu, M.; Gayathri, C.; Gil, R. R.; Jin, R. Chirality in gold nanoclusters probed by NMR spectroscopy. *ACS Nano* **2011**, *5*, 8935–8942.

(78) Si, S.; Gautier, C.; Boudon, J.; Taras, R.; Gladiali, S.; Bürgi, T. Ligand exchange on Au_{25} cluster with chiral thiols. *J. Phys. Chem. C* **2009**. *113*, 12966–12969.

(79) Knoppe, S.; Bürgi, T. The fate of $Au_{25}(SR)_{18}$ clusters upon ligand exchange with binaphthyl-dithiol: interstaple binding vs. decomposition. *Phys. Chem. Chem. Phys.* **2013**, *15*, 15816–15820.

(80) Yao, Q.; Yuan, X.; Fung, V.; Yu, Y.; Leong, D. T.; Jiang, D. E.; Xie, J.

Understanding seed-mediated growth of gold nanoclusters at molecular level. *Nature Commun.* **2017**, *8*, 927.

(81) Yuan, X.; Goswami, N.; Chen, W.; Yao, Q.; Xie, J. Insights into the effect of surface ligands on the optical properties of thiolated Au_{25} nanoclusters. *Chem. Commun.* **2016**, *52*, 5234–5237.

(82) Xie, J., Zheng, Y., Ying, J. Y. Protein-directed synthesis of highly fluorescent gold nanoclusters. *J. Am. Chem. Soc.* **2009**, *131*, 888−889.

(83) Xie, J.; Zheng, Y.; Ying, J. Y. Highly selective and ultrasensitive detection of Hg^{2+} based on fluorescence quenching of Au nanoclusters by Hg^{2+}–Au^{+} interactions. *Chem. Commun.* **2010**,*46*, 961−963.

(84) Pu, K. Y.; Luo, Z.; Li, K.; Xie, J.; Liu, B. Energy transfer between conjugated-oligoelectrolyte-substituted POSS and gold nanocluster for multicolor intracellular detection of mercury ion. *J. Phys. Chem. C* **2011**, *115*, 13069−13075.

(85) Guan, G.; Zhang, S. Y.; Cai, Y.; Liu, S.; Bharathi, M. S.; Low, M.; Yu, Y.; Xie, J.; Zheng, Y.; Zhang. Y. W.; Han, M. Y. Convenient purification of gold clusters by co-precipitation for improved sensing of hydrogen peroxide, mercury ions and pesticides. *Chem. Commun.* **2014**, *50*, 5703−5705.

(86) Wu, Z.; Jin, R. On the Ligand's Role in the Fluorescence of Gold Nanoclusters. *Nano Lett.* **2010**, *10*, 2568–2573.

(87) Liu, X.; Yuan, J.; Yao, C.; Chen, J.; Li, L.; Bao, X.; Yang, J.; Wu, Z. Crystal and solution photoluminescence of $MAg_{24}(SR)_{18}$ (M= Ag/Pd/Pt/Au) nanoclusters and some implications for the photoluminescence mechanisms. *J. Phys. Chem. C* **2017**, *121*, 13848−13853.

(88) Allen, C.; Qiu, T. A.; Pramanik, S.; Buchman, J. T.; Krause, M. O.; Murphy, C. J. Research highlights: investigating the role of nanoparticle surface charge in

nano–bio interactions. *Environ. Sci.: Nano* **2017**, *4*, 741−746.

(89) Albanese, A.; Tang, P. S.; Chan, W. C. The effect of nanoparticle size, shape, and surface chemistry on biological systems. *Annu. Rev. Biomed. Eng.* **2012**, *14*, 1−16.

(90) Fröhlich, E. The role of surface charge in cellular uptake and cytotoxicity of medical nanoparticles. *Int. J. Nanomed.* **2012**, *7*, 5577−5591.

(91) Verma, A.; Stellacci, F. Effect of surface properties on nanoparticle-cell interactions. *Small* **2010**, *6*, 12−21.

(92) Jo, D. H.; Kim, J. H.; Lee, T. G.; Kim, J. H. Size, surface charge, and shape determine therapeutic effects of nanoparticles on brain and retinal diseases. *Nanomed-Nanotechnol.* **2015**, *11*, 1603−1611.

(93) Quan, X.; Peng, C.; Zhao, D.; Li, L.; Fan, J.; Zhou, J. Molecular understanding of the penetration of functionalized gold nanoparticles into asymmetric membranes. *Langmuir* **2016**, *33*, 361−371.

(94) Elci, S. G.; Jiang, Y.; Yan, B.; Kim, S. T.; Saha, K.; Moyano, D. F.; Tonga, G. Y.; Jackson, L. F.; Rotello, V. M.; Vachet, R. W. Surface charge controls the suborgan biodistributions of gold nanoparticles. *ACS Nano*, **2016**, *10*, 5536−5542.

(95) Zheng, K.; Setyawati, M. I.; Leong, D. T.; Xie, J. Antimicrobial gold nanoclusters. ACS Nano **2017**, *11*, 6904−6910.

(96) Zheng, K.; Setyawati, M. I.; Leong, D. T.; Xie, J. Surface ligand chemistry of gold nanoclusters determines their antimicrobial ability. *Chem. Mater.* **2018**, *30*, 2800−2808.

(97) Lavenn, C.; Albrieux, F.; Bergeret, G.; Chiriac, R.; Delichere, P.; Tuel, A.; Demessence, A. Functionalized gold magic clusters: $Au_{25}(SPhNH_2)_{17}$. *Nanoscale* **2012**. *4*, 7334–7337.

(98) Ishida, Y.; Narita, K.; Yonezawa, T.; Whetten, R. L. Fully cationized goldclusters: synthesis of $Au_{25}(SR^{+})_{18}$. *J. Phys. Chem. Lett.* **2016**, *7*, 3718–3722.

(99) Ishida, Y.; Huang, Y. L.; Yonezawa, T.; Narita, K. Charge neutralization strategy: a novel synthetic approach to fully cationized thiolate−protected $Au_{25}(SR^{+})_{18}$ clusters with atomic precision. *ChemNanoMat* **2017**, *3*, 298−302.

(100) Hoque, M. M.; Black, D. M.; Mayer, K. M.; Dass, A.; Whetten, R. L. The base side of noble metal clusters: efficient route to captamino-gold, $Au_n(-S(CH_2)_2N(CH_3)_2)_p$, n= 25–144. *J. Phys. Chem. Lett.* **2019**, *10***,** 3307−3311.

(101) Hoque, M. M.; Dass, A.; Mayer, K. M.; Whetten, R. L. Protein-like large gold clusters based on the ω-amino-thiolate DMAET: precision thermal and reaction control leads to selective formation of cationic gold clusters in the critical size range, n= 130–144 Au atoms. *J. Phys. Chem. C* **2019**, *123*, 14871–14879.

Chapter 2

Kinetics of Cationic-Ligand-Exchange Reactions in Au_{25} Nanoclusters

Abstract

Herein, this chapter reports the first investigation into the kinetics of cationic-ligand-exchange processes through the reaction of $Au_{25}(SCH_2CH_2Ph)_{18}$ with a cationic thiol $HS(CH_2)_{11}N(CH_3)_3^+$, which resulted in different populations of the two thiolate ligands (SR^0 and SR^+), i.e., $Au_{25}(SR^0)_{18-x}(SR^+)_x$. The ligand-exchange process was monitored by electrospray ionization mass spectrometry and the reaction kinetics is discussed in combination with ^{1}H-NMR results; these techniques reveal that the kinetics of the cationic-ligand-exchange process, which is different from a typical neutral-thiol-to-neutral-thiol ligand exchange, is strongly dependent on how the SR^+ ligands interact with each other during the ligand-exchange process .There are two main factors that determine the unique reaction kinetics, namely coulombic repulsions (i) between the attached SR^+ ligands and free ligands in solution that hinder further ligand exchange, and (ii) among the surface SR^+ ligands on the thiolate monolayer, which promotes the thermal decomposition of the nanocluster.

2.1 Introduction

The chemistry and applications of gold (Au) nanoclusters composed of a specific number of metal atoms remains an active research field owing to their atomic precision, superatom-like structures, and physicochemical properties that result from quantum-confinementeffects.[1–5] Such nanoclusters are of intrinsic scientific interest as well as being potentially applicable tocatalysis,[6–8] chemical sensing,[9–11] optical imaging,[12,13] biolabeling,[14,15] and light emitting devices,[16] as examples. Of such nanoclusters, gold nanoclusters protected by thiolate (SR) ligands have been extensively studied due to their excellent stabilities and because specifically stable structures, such as $Au_{25}(SR)_{18}$, $Au_{38}(SR)_{24}$, $Au_{67}(SR)_{35}$, $Au_{102}(SR)_{44}$, $Au_{130}(SR)_{50}$, and $Au_{144}(SR)_{60}$ can be easily synthesized.[17–19] To date, $Au_n(SR)_m$ nanoclusters are mainly prepared through the use of neutral and anionic thiolate ligands, such as 2-phenylethanethiol, methylbenzenethiol, alkanethiols, glutathione, and mercaptocarboxylic acids, among others.[1–21]

However, in some special areas, such as biological signalling, particle transportation, cellular toxicity, and environmental impact, cationic-ligand-protected nanoparticles can be indispensable due to the good affinity of the cationic ligand for the biomaterial.[22–25] For example, Quan et al.[24] used computational simulations to investigate the role of ligand charge during Au-nanoparticle penetration through a liquid bilayer; these nanoparticles only penetrated through asymmetric bilayers (negatively charged 1,2-dipalmitoylphosphatidylglycerol) when the surfaces of the Au nanoparticles were positively charged. Elci et al.[25] studied how surface-ligand charge affects the biodistribution of 2-nm Au nanoparticles *in vivo*, and showed that the liver and the spleen accumulated higher levels of positively charged Au nanoparticles than

neutral or negatively charged ones. This knowledge is important for the intentional design of nanoclusters protected by cationic ligands that are suited to specific nano-biological applications.

Nowadays, the ideal method for the synthesis of atomically precise Au nanoclusters involves a "size-focusing" step, which leads to the formation of thermally metastable structures that are typically referred to as "magic–number" nanoclusters.[1,5] In the case of cationic-ligand-protected Au cluster synthesis, the "size-focusing" methodology has two limitations:[26] i) coulombic attractions between the anionic $AuCl_4^-$ and the cationic thiol (SR^+) that dramatically affect the solubilities of the Au(I)–SR^+ complexes in solution and further restrict homogeneous reduction and Au-nanocluster growth, and ii) coulombic repulsions induced by the densely populated cationic ligands on the small Au cluster surface that promote thermal nanocluster decomposition. In my lab's recent reports,[26,27] "size-focusing" at optimized reduction and etching rates resulted in the first successful synthesis of a pure $Au_{25}(SR^+)_{18}$ cluster in 47% yield (Au basis).

Ligand exchange between different ligand-stabilized nanoclusters has been widely applied to the synthesis and functionalization of nanoclusters without any change in core structure.[28–34] For example, Zhu et al.[28] reported the synthesis of a selenophenolate-capped Au_{25} cluster by the ligand exchange of a $PhCH_2CH_2S$-capped Au_{25} cluster. Murray et al.[29] reported a mass-spectrometric study of ligand-exchange reactions on $Au_{25}(SCH_2CH_2Ph)_{18}$with hexanethiol and thiophenol and found partially exchanged Au_{25}nanoclusters using both of these ligands. Ackerson et al.[30] reported a single-crystal structure of $Au_{25}(SCH_2CH_2Ph)_{16}$(*p*–BBT)$_2$ (*p*–BBT = *para*-bromobenzenethiol) that was obtained following ligand exchange of

$Au_{25}(SCH_2CH_2Ph)_{18}$ with the incoming *p*–BBT ligand. Thus, exchanging initially present thiols, partially or wholly, by ligand-exchange reactions has provided ways of functionalizing nanoclusters.

In the present work, ligand-exchange reaction of $Au_{25}(SCH_2CH_2Ph)_{18}$ nanoclusters with a cationic thiol, ((11-mercaptoundecyl)-*N*,*N*,*N*-trimethylammonium (SR^+)) was investigated for the first time. Mass spectrometry provides the advantage of quantitatively determining the ligand populations of nanoclusters, whereby nanoclusters with a variety of molar ratios of two ligands on their surfaces can be identified.[35,36] In this study, the ligand-exchange process was qualitatively monitored by electrospray-ionization (ESI) mass spectrometry and the kinetics of the reaction is discussed together with ^{1}H-NMR results that determined the average population percentages of the two thiolate ligands.

2.2 Experimental section

2.2.1 Chemicals

Hydrogen tetrachloroaurate (III) ($HAuCl_4 \cdot 4H_2O$, >99.99%, Wako Pure Chemical Industries), 2-phenylethanethiol (PET, 99%, Wako Pure Chemical Industries), (11-mercaptoundecyl)-*N*,*N*,*N*-trimethylammonium bromide ($SR^+ \cdot Br^-$, 99%, Aldrich), tetra-*n*-octylammonium bromide (TOAB, >98%, Wako Pure Chemical Industries), potassium hexafluorophosphate(KPF_6, 99%, Wako Pure Chemical Industries), sodium borohydride ($NaBH_4$, 99%, Wako Pure Chemical Industries) and iodine (I_2, 99%, Wako Pure Chemical Industries) were used as received without further purification. HPLC-grade solvents such as tetrahydrofuran (THF), acetone, toluene, and methanol were purchased from Kanto Chemical. Deionized pure water (>18.2 MΩ) was

prepared by an Organo/ELGA purelab system.

Scheme 2.1 Schematic representation of the ligand-exchange reaction (PET: 2-phenylethanethiol; SR^+: (11-mercaptoundecyl)-*N*,*N*,*N*-trimethylammonium).

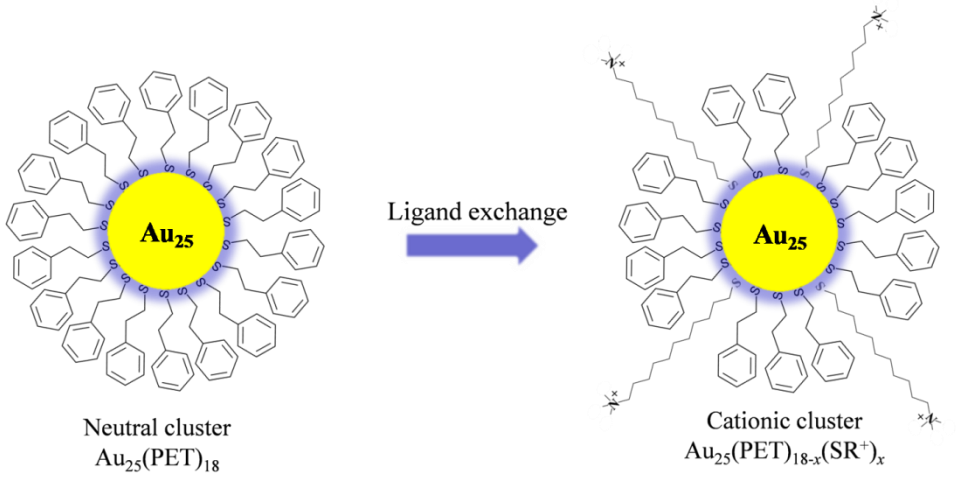

2.2.2 Ligand-exchange reaction

The synthesis of $[TOA^+][Au_{25}(PET)_{18}^-]$ (TOA^+: $(C_8H_{17})_4N^+$; PET: SCH_2CH_2Ph) was based on that previously reported by the group of Murray.[37] The UV-vis absorption and negative-mode ESI-MS characterizations of the starting $[Au_{25}(PET)_{18}]^-$ are presented in Figure S2.1 in the Supporting Information. Prior to the ligand-exchange reaction, the Br^- counter anion of the thiolate ligand ((11-mercaptoundecyl)-*N*,*N*,*N*-trimethylammonium, SR^+) was replaced with hexafluorophosphate (PF_6^-). $SR^+ \cdot PF_6^-$ was prepared by dissolving $SR^+ \cdot Br^-$ (82 mg, 0.25 mmol) in pure water, followed by precipitation through the addition of KPF_6 (55 mg, 0.3 mmol). The white precipitate was collected by centrifugation, washed three-times with pure water and dried overnight under vacuum.

In a typical ligand-exchange reaction (Scheme 2.1), a sample of $[TOA^+][Au_{25}(PET)_{18}^-]$ (1 mg, 0.11 μmol) and KPF_6 (3.6 mg, 10 μmol) were dissolved in acetone (1 mL) and

mixed with the incoming cationic thiol ($SR^+ \cdot PF_6^-$, 3.87 mg, 9.9 μmol) in a 1:5 molar ratio (based on the exchangeable surface ligands (18 per cluster) rather than the Au cluster), after which the mixture was stirred for a specified period of time at room temperature. The product was washed with methanol (typically 5 times) to remove excess thiol and by-products. The purified samples were dried under vacuum overnight for further characterization.

2.2.3 Characterization

UV-vis absorption spectra of samples in acetone were recorded using a JASCO V-630 spectrophotometer using a quartz cuvette with a 10-mm optical path. Electrospray-ionization mass spectrometry (ESI-MS) was performed using a Bruker DaltonicsmicrOTOF-HS mass spectrometer. The purified sample was dissolved in toluene (~1 $mg \cdot mL^{-1}$) and diluted by the addition of twice the volume of dry methanol. The sample was directly infused at $4mL \cdot min^{-1}$. For the data shown here, a 50–10000 *m/z* mass-spectrometer acquisition range was used. The nebulizer pressure was set to 1.5 bar, and the sheath gas was set to 4.0 L/min. The dry temperature was kept at 120°C. The electrospray emitter potential was held at 4500 V (positive mode) and –4500 V (negative mode). The capillary exit, skimmer 1, hexapole 1, and skimmer 2 voltage settings were 200, 50, 25, and 28 V, respectively.

^{1}H-NMR analyses were performed on a JMTC-400/54/SS (JEOL) spectrometer operating at 400 MHz. Dimethyl sulfoxide-d_6 (DMSO-d_6, 750 μL) was used as the solvent to dissolve 0.5 mg of the purified nanoclusters. In a typical NMR experiment, the sample collected at the specified reaction time was dissolved in DMSO-d_6 and then I_2 (~1 mg) was added to extract the PET and SR^+ ligands from the Au nanoclusters through the formation of disulfides.[38,39]

2.3 Results and discussions

2.3.1 Optical Absorption Spectroscopy

The ligand-exchange process was first monitored by optical absorption spectroscopy. Note that the Br^- counter anion of the purchased cationic ligand (SR^+) was replaced with PF_6^- by the procedure outline in the Experimental Section, which was found to be very important for further ligand exchange. As shown in Figure S2.2, when the cationic ligand with the Br^- counterion was used, the Au_{25} cluster decomposed rapidly because Br^- oxidized the Au_{25}.[26,27,40]

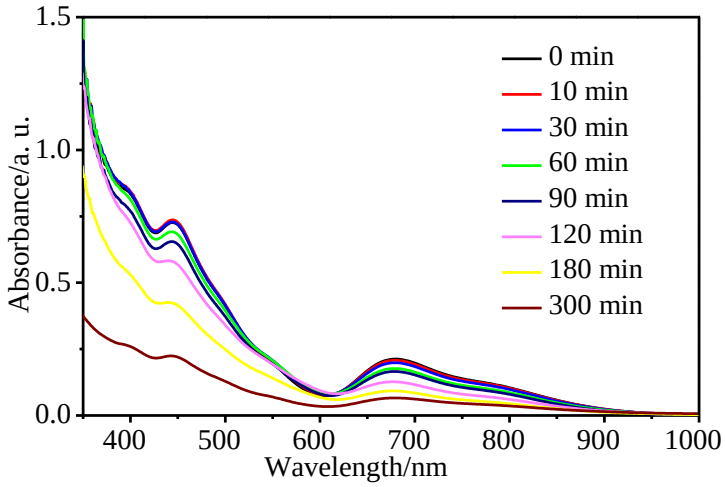

Figure 2.1 UV-vis absorption spectra of Au_{25} during the ligand-exchange reaction.

As presented in Figure 1, the characteristic Au_{25}nanoclusterabsorption peaks located at 400, 450, and 670 nm decreased in intensity with prolonged reaction time. It did not observe any precipitation during ligand exchange; consequently, the observed decrease in absorbance is indicative of the decomposition of the Au_{25} nanoclusters. Judging by the decrease in absorbance at 670 nm (Figure 2.1), the Au_{25} nanoclusters showed no significant decomposition at 10 min. At 30 and 60 min, decreases in absorbance of ~5% and ~10% were observed, respectively. Furthermore, increasing

the reaction time led to dramatic decreases in absorbance. These results indicate that the Au_{25} clusters were not stable during ligand exchange, especially for reaction times in excess of 60 min. This observation is different from the ligand-exchange reactions reported for Au_{25} nanoclusters with neutral thiolate ligands, where absorbances were maintained for long times in high-temperature reactions.[28–34] Based on this observation, the use of a cationic thiol (SR^+) for the incoming ligand strongly affects Au_{25} nanocluster stability, as discussed in my lab's previous report on the synthesis of the fully cationic $Au_{25}(SR^+)_{18}$ cluster using the same cationic thiol.[26] The main reason for the observed decomposition involves coulombic repulsions between the densely populated charged functional groups on the cluster surfaces, as reported by my lab and others.[26,27,41]

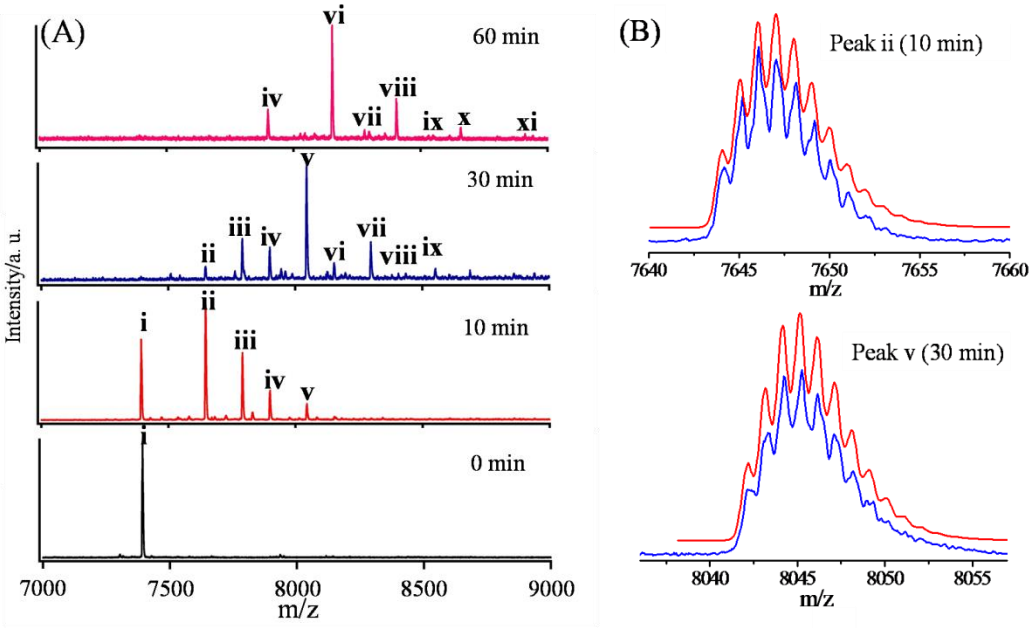

Figure 2.2 (A) Negative-mode ESI mass spectra of samples collected at different times during the ligand-exchange process, and (B) expanded high-resolution ESI mass spectra (blue) and simulated isotope patterns (red) of representative peaks.

2.3.2 ESI-MS

Since the initial $[Au_{25}(PET)_{18}]^-$ is negatively charged, I first monitored the time course of the ligand-exchange reaction between $[Au_{25}(PET)_{18}]^-$ and SR^+ by negative-mode ESI-MS. As shown in Figure 2.1A and Table 2.1, only one peak located at 7394.20 *m/z* was observed in the spectrum of the initial sample, which corresponds to the starting $[Au_{25}(PET)_{18}]^-$ (see details in Figure S2.1 in the Supporting Information). Following the ligand-exchange reaction, the resulting partially cationized Au_{25} nanoclusters, $[Au^{0/-1}{}_{25}(PET)_{18-x}(SR^+)_x(PF_6^-)_{x/x-1}]^-$ ($0 \leq x \leq 18$, theoretically), were observed by negative-mode ESI-MS. At 10 min, the *x* value ranged from 0 to 3, noting that starting material was still present. At 30 min, *x* was distributed between 1 and 5, suggesting that all initial nanoclusters had been consumed; *x* further increased to 2–6 after 60 min. The *x* values at longer reaction times (90, 120, and 180 min) were also determined by negative-mode ESI-MS, as shown in Figure S2.3 and Table S2.1. The ESI-MS results in Figure S2.3 reveal that *x* continues to increase with increasing reaction time, however specific impurity peaks were also observed, as predicted on the basis of the decrease in absorption intensity due to Au_{25} nanocluster decomposition. Expanded ESI mass spectra of the two representative peaks, Au_{25}^- $^1PET_{17}(SR^+)_1\bullet(PF_6^-)_1$ (peak ii) and $Au_{25}{}^{-1}PET_{16}(SR^+)_2\bullet(PF_6^-)_3$ (peak v), are shown in Figure 2.2B, along with the simulated isotope patterns (in red); the observed isotope patterns are well matched to those simulated. The expanded ESI mass spectra of the remaining observed peaks are summarized in Figure S4 in the Supporting Information.

Figure 2.3 displays positive-mode ESI mass spectra of the ligand-exchange reaction between $[Au_{25}(PET)_{18}]^-$ and SR^+. The full spectrum in Figure 2.3A displays prominent groups of peaks for +1 (group I, 7000–8000 *m/z*), +2 (group II, 3600–4600

m/z), and +3 (group III, 2000–3000 *m/z*) charged states; the corresponding expanded spectra and detailed assignments are presented in Figures 2.3B–D and Table 2.2, respectively. The cationized Au_{25}nanoclusters, $[Au^{0/\pm1}_{25}(PET)_{18-x}(SR^+)_x(PF_6^-)_y]^{x-y\pm1}$ ($0 \leq x \leq 18$, $y < x$) were successfully characterized by positive-mode ESI-MS. The x value was observed to increase with time; x = 0–3, 1–5, and 2–6 at 10, 30, and 60 min, respectively. When the reaction was further prolonged to 90, 120, and 180 min, x further increased to 2–9, 3–11, and 3–12, respectively, as summarized in Figure S2.5 and Table S2.2. Again, reaction times in excess of 90 min resulted in spectra that contained peaks corresponding impurities that arise from the decomposition of the Au_{25} nanoclusters, and un-assignable peaks were observed in the spectra of these samples at 90–180 min, as shown in Figure S2.5.

Moreover, well-known $Au_{21}SR_{14}$ fragments[42,43] (in the form of $Au_{21}PET_{14-m}(SR^+)_m(PF_6^-)_n$, with one fragment in the form of $Au_{21}PET_{12}(SR^+)_3(PF_6^-)_2$) with different quantities of exchanged SR^+ were also detected, as shown in Figure 2.3E (a list of assignments for fragmentation peaks *Fa–Ff* is found in Table 2.2). The observed spectra for two representative peaks, $Au_{25}^{-1}PET_{14}(SR^+)_4\bullet(PF_6^-)_1$ (peak j) and $Au_{25}^{-1}PET_{12}(SR^+)_6\bullet(PF_6^-)_2$ (peak o) are well matched with the simulated isotope patterns shown in Figure 2.3F (the remaining expanded spectra are displayed in Figure S2.4). Noted that the negative-mode and positive-mode results revealed different populations of x values, which is ascribable to the requirement for all cations to be neutralized with PF_6^-in the former case; hence highly charged clusters would be difficult to detect. Consequently, by combing the negative-mode and positive-mode ESI–MS results, the minimum and maximum number of exchanged cationic ligands (x values) were successfully determined at different reaction times, respectively.

These results will be discussed later together with the ^{1}H-NMR spectroscopy results.

Table 2.1 Structural and charge assignments of negative-mode ESI-MS in Figure 2.2.

Peak	Assignment[a]	Charge (e)	10 min m/z (obs.)	30 min m/z (obs.)	60 min m/z (obs.)	m/z (calc.)
i	$Au_{25}^{-1}PET_{18}$	–1	7394.20	—	—	7394.19
ii	$Au_{25}^{-1}PET_{17}(SR^{+})_{1}\bullet(PF_{6}^{-})_{1}$	–1	7647.41	7647.49	—	7647.40
iii	$Au_{25}^{0}PET_{17}(SR^{+})_{1}\bullet(PF_{6}^{-})_{2}$	–1	7792.37	7792.32	—	7792.36
iv	$Au_{25}^{-1}PET_{16}(SR^{+})_{2}\bullet(PF_{6}^{-})_{2}$	–1	7900.61	7900.65	7900.66	7900.61
v	$Au_{25}^{0}PET_{16}(SR^{+})_{2}\bullet(PF_{6}^{-})_{3}$	–1	8045.53	8045.51	—	8045.57
vi	$Au_{25}^{-1}PET_{15}(SR^{+})_{3}\bullet(PF_{6}^{-})_{3}$	–1	—	8153.82	8153.79	8153.82
vii	$Au_{25}^{0}PET_{15}(SR^{+})_{3}\bullet(PF_{6}^{-})_{4}$	–1	—	8298.75	8298.76	8298.78
viii	$Au_{25}^{-1}PET_{14}(SR^{+})_{4}\bullet(PF_{6}^{-})_{4}$	–1	—	8407.03	8407.02	8407.03
ix	$Au_{25}^{0}PET_{14}(SR^{+})_{4}\bullet(PF_{6}^{-})_{5}$	–1	—	8552.02	8551.93	8551.99
x	$Au_{25}^{-1}PET_{13}(SR^{+})_{5}\bullet(PF_{6}^{-})_{5}$	–1	—	—	8660.15	8660.24
xi	$Au_{25}^{-1}PET_{12}(SR^{+})_{6}\bullet(PF_{6}^{-})_{6}$	–1	—	—	8913.40	8913.45

[a] SR^{+} represents $S(CH_2)_{11}N(CH_3)_3^{+}$ ligand, and PET represents $S(CH_2)_2(C_6H_5)$ ligand.

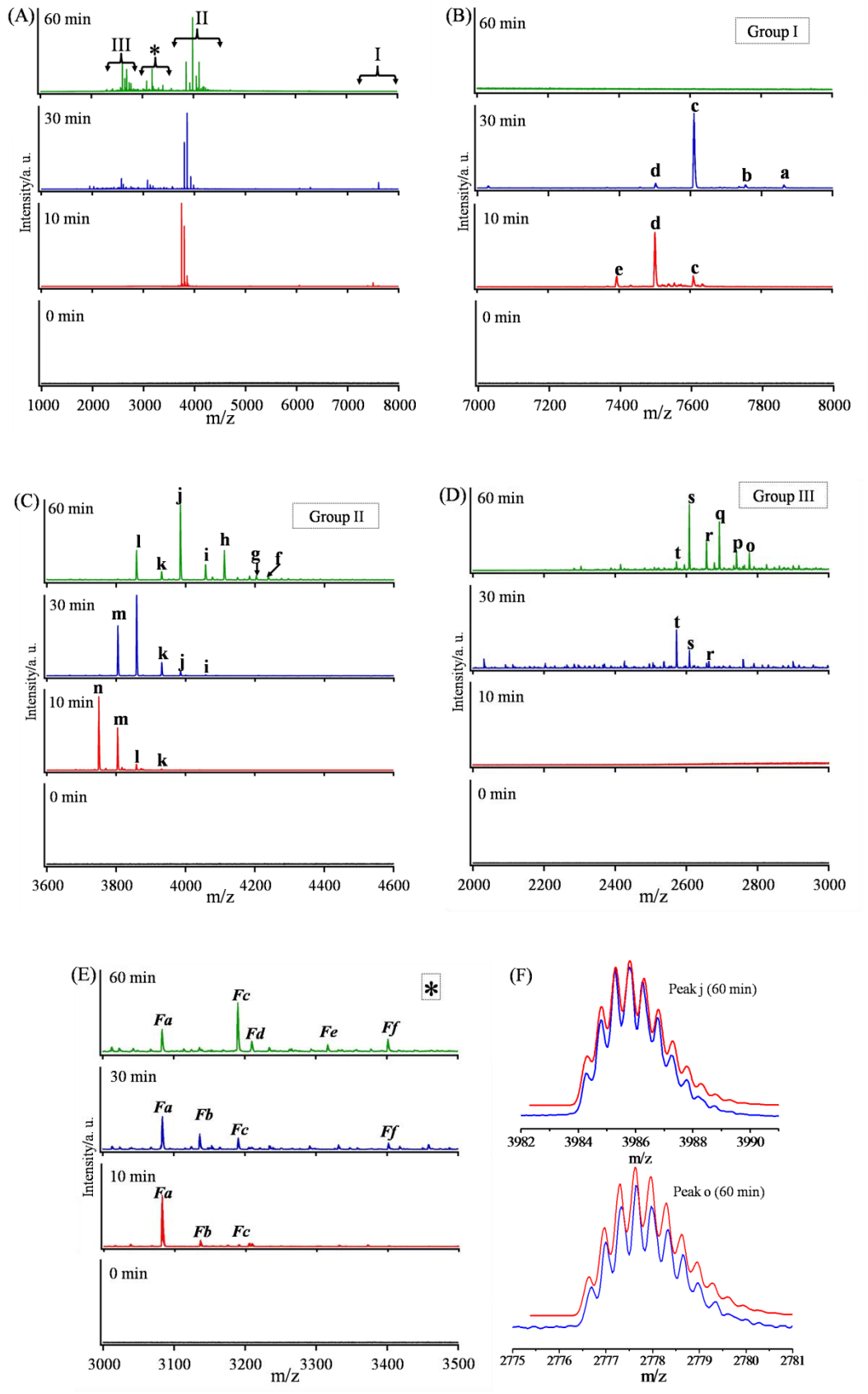

Figure 2.3 (A) Positive-mode ESI mass spectra of samples collected at different times

during the ligand exchange process. (B–D) Expanded spectra of the regions indicated in(A). (B) Group I (7000–8000 *m/z*), (C) group II (3600–4600 *m/z*), (D) group III (2000–3000 *m/z*), and (E) fragments* (3000–3500 *m/z*). (F) Expanded high-resolution ESI mass spectra (blue) and the simulated isotope patterns (red) of representative peaks.

2.3.3 ^{1}H-NMR Spectroscopy

The populations of different types of ligand on nanoclusters or nanoparticles are often determined by the NMR technique, which provides average percentages of mixed ligands per particle.[29,44–47] In the present work, each sample was treated with I_2in order to extract PET and SR^+ from the resultant cationized Au nanoclusters through the formation of disulfides. Figure S2.6 displays ^{1}H-NMR spectra of pure PET and SR^+, and the 10min samples with and without I_2 treatment, in DMSO-d_6. Signals corresponding to PET (7.18 ppm and 2.64 ppm) and SR^+ (2.98 ppm and 1.22 ppm) were clearly observable in the spectrum of the sample following I_2 treatment, but were absent in that of the untreated sample. ^{1}H-NMR spectra of the I_2-treated samples for all reaction times are presented in Figure S2.7. By integrating clearly isolated signals at 7.18 and 2.64 ppm for PET, and 2.98 and 1.22 ppm for SR^+, we successfully determined the average percentages of SR^+ and PET on the resultant Au nanoclusters, as summarized in Table S2.3. Using these data, average SR^+-exchange numbers were calculated, as presented in Figure 2.4A. The initial rapid rate of exchange began to slow at around 50 min.

Table 2.2 Structural and charge assignments of positive-mode ESI-MS in Figure 2.3.

Group	Peak	Assignment	Charge (e)	10 min m/z (obs.)	30 min m/z (obs.)	60 min m/z (obs.)	m/z (calc.)
	a	$Au_{25}^{-1}PET_{15}(SR^+)_3\bullet(PF_6^-)_1$		—	7863.88	—	7863.89
	b	$Au_{25}^{0}PET_{16}(SR^+)_2\bullet(PF_6^-)_1$		—	7755.68	—	7755.64
I	**c**	$Au_{25}^{-1}PET_{16}(SR^+)_2\bullet(PF_6^-)_0$	**+1**	7610.71	7610.67	—	7610.68
	d	$Au_{25}^{0}PET_{17}(SR^+)_1\bullet(PF_6^-)_0$		7502.44	7502.47	—	7502.43
	e	$Au_{25}^{+1}PET_{18}(SR^+)_0\bullet(PF_6^-)_0$		7394.17	—	—	7394.19
	f	$Au_{25}^{-1}PET_{12}(SR^+)_6\bullet(PF_6^-)_3$		—	—	4239.26	4239.28
	g	$Au_{25}^{0}PET_{13}(SR^+)_5\bullet(PF_6^-)_3$		—	—	4185.17	4185.16
	h	$Au_{25}^{-1}PET_{13}(SR^+)_5\bullet(PF_6^-)_2$		—	—	4112.70	4112.67
	i	$Au_{25}^{0}PET_{14}(SR^+)_4\bullet(PF_6^-)_2$		—	4058.52	4058.58	4058.55
II	**j**	$Au_{25}^{-1}PET_{14}(SR^+)_4\bullet(PF_6^-)_1$	**+2**	—	3986.09	3986.10	3986.07
	k	$Au_{25}^{0}PET_{15}(SR^+)_3\bullet(PF_6^-)_1$		3932.01	3931.97	3930.92	3931.95
	l	$Au_{25}^{-1}PET_{15}(SR^+)_3\bullet(PF_6^-)_0$		3859.51	3859.47	3859.48	3859.46
	m	$Au_{25}^{0}PET_{16}(SR^+)_2\bullet(PF_6^-)_0$		3805.34	3805.38	—	3805.34
	n	$Au_{25}^{+1}PET_{17}(SR^+)_1\bullet(PF_6^-)_0$		3751.24	—	—	3751.22
	o	$Au_{25}^{-1}PET_{12}(SR^+)_6\bullet(PF_6^-)_2$		—	—	2777.98	2777.96
	p	$Au_{25}^{0}PET_{13}(SR^+)_5\bullet(PF_6^-)_2$		—	—	2741.78	2741.78
III	**q**	$Au_{25}^{-1}PET_{13}(SR^+)_5\bullet(PF_6^-)_1$	**+3**	—	—	2693.50	2693.46
	r	$Au_{25}^{0}PET_{14}(SR^+)_4\bullet(PF_6^-)_1$		—	2657.37	2657.36	2657.38
	s	$Au_{25}^{-1}PET_{14}(SR^+)_4\bullet(PF_6^-)_0$		—	2609.08	2609.07	2609.06

	t	$Au_{25}^{0}PET_{15}(SR^{+})_3\bullet(PF_6^{-})_0$		—	2573.02	2573.01	2572.97
			Fragments				
	Fa	$Au_{21}^{+1}PET_{13}(SR^{+})_1\bullet(PF_6^{-})_0$		3082.85	3082.84	3082.83	3082.84
	Fb	$Au_{21}^{0}PET_{12}(SR^{+})_2\bullet(PF_6^{-})_0$		3136.99	3137.01	—	3136.96
	Fc	$Au_{21}^{-1}PET_{11}(SR^{+})_3\bullet(PF_6^{-})_0$		3191.07	3191.10	3191.09	3191.08
*	***Fd***	$Au_{21}^{+1}PET_{12}(SR^{+})_2\bullet(PF_6^{-})_1$	**+2**	3209.43	—	3209.41	3209.44
	Fe	$Au_{21}^{+1}PET_{11}(SR^{+})_3\bullet(PF_6^{-})_2$		—	—	3336.06	3336.04
	Ff	$Au_{21}^{+1}PET_{12}(SR^{+})_3\bullet(PF_6^{-})_2$		—	3404.66	3404.70	3404.66

2.3.4 Kinetics of the Cationic-Ligand-Exchange Reaction

Figure 2.4B displays the pseudo-first-order rate plot based on Figure 2.4A. The reaction can be analyzed as a biphasic process; a rapid first-order process (–0.0043 min^{-1}, Phase I) which transitions to a slower process (–0.0026 min^{-1}, Phase II). These results indicate that the cationic-ligand-exchange process is different to those previously reported[48,49] for neutral-thiol-to-neutral-thiol ligand exchanges on Au_{25}, in which the kinetic rate is constant under the similar experimental conditions of the two thiolate ligands at room temperature.

We further discuss the kinetics of the ligand exchange reaction using the actual ligand-population distributions determined by ESI-MS. In the neutral-thiol-to-neutral-thiol ligand-exchange reaction, the difference in *m/z* corresponds to the difference in the molecular weights of the two thiols used; hence the ESI-MS peaks appear in very similar mass regions.[28–34,44] Therefore, the populations of the components of each cluster, with varying thiol ratios, are reliably discussed by comparing the relative intensities of the MS signals. By contrast, the distributions of the various ligand-exchange products in the cationized Au nanoclusters studied in this work cannot be directly determined due to the multiple possible structures that correspond to$[Au^{0/\pm1}_{25}(PET)_{18-x}(SR^{+})_x(PF_6^{-})_y]^{x-y\pm1}$, where different PF_6^- adducts (and the Au_{25}-core charge) result in multiple charged states. It is therefore difficult to directly determine the amplitude distributions (or relative contents) by the relative intensities of the ESI-MS signals. Therefore, in the present work, only the minimum, maximum (determined by negative- and positive-mode ESI-MS), and average *x* values (1.4, 2.5, 3.8, 5.0, and 6.0 at 10, 30, 60, 90, and 120 min, respectively, determined by ^{1}H-NMR spectroscopy) are used to discuss the kinetics of the ligand-exchange process, as

shown in Figure 2.5. The inverse triangles in Figure 2.5 indicate average SR^+ numbers (max: 18) determined by ^{1}H-NMR spectroscopy, double-headed vertical arrows indicate SR^+ distributions (min. and max. values) determined by ESI-MS, and horizontal bars indicate the center of the ESI-MS distributions.

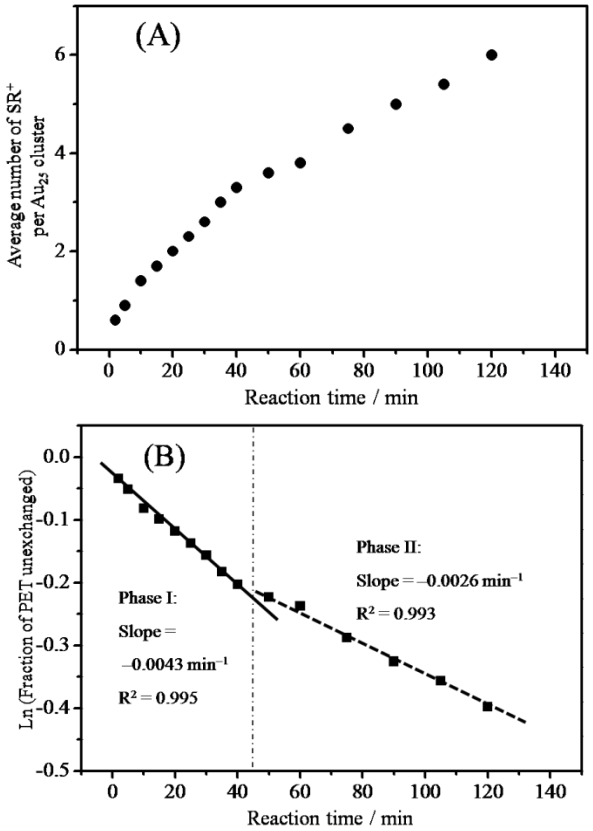

Figure 2.4 (A) Average number of SR^+ ligands per cluster (max: 18) on the cluster surface during the ligand-exchange reaction as determined by ^{1}H-NMR spectroscopy. (B) Ln(Fraction of unexchanged PET on the cluster surface) for the ligand-exchange reaction with SR^+ as a function of reaction time. The two lines in (b) are the lines of best fit at 0–40 min (Phase I) and 50–120 min (Phase II), respectively.

As reported previously,[29,44] the ligand populations following neutral-thiol-to-neutral-thiol ligand exchanges are generally binomially distributed, in which the average exchanged-ligand number (by ^{1}H-NMR integration) is equal to the most abundant

species (detected by MS). In the present work, the results at 10 and 30 min (Figure 2.5) reveal that the central exchange position of each range corresponds well to the ^{1}H-NMR-determined average exchange number (x). When combined with the constant reaction rate observed during Phase I in Figure 2.4B, it is conclude that the cationic-ligand-exchange reaction still obeys similar kinetics to the neutral-thiol-to-neutral-thiol exchange in these cases.[28–34,44–47] In contrast, at longer reaction times (> 30 min) the average SR^{+} numbers do not correspond to the centers of the observed exchange ranges, and were observed to shift to smaller x values, as expressed by the black arrows in Figure 2.5; the difference becomes larger at longer reaction times. These observations suggest that the distributions of the resultant Au nanoclusters in these cases do not match the previously reported Gaussian distributions[28–34,44–47] after ligand exchange for more than 30 min.

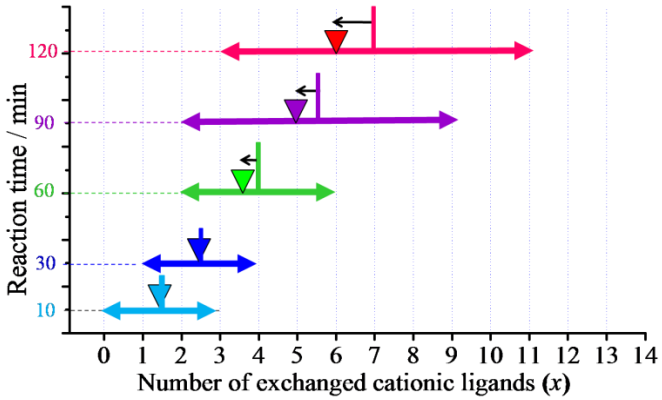

Figure 2.5 Distributions of SR^{+} numbers on Au_{25} clusters at different reaction times. Inverse triangles: average SR^{+} number (max: 18) determined by ^{1}H-NMRspectroscopy; double-headed vertical arrows: SR^{+} distributions determined by ESI-MS; horizontal bars: ESI-MS-distribution centers; and black arrows: differences between the average numbers determined by ^{1}H-NMR spectroscopy and observed center determined by ESI-MS.

Thiol-ligand bulkiness[29,44,50] is a factor that may possibly control the kinetics of the thiol-exchange process in a neutral-thiol-to-neutral-thiol ligand-exchange reaction. When the incoming thiol is clearly of different bulkiness to the original thiol ligand, collision processes may dictate the ratio of initial to incoming ligand, leading to an enriched species with a shifted *x* value. Hence, the distributions of the populations of the two thiol ligands in such a system does not always fit the standard Gaussian shape, as was observed in this study. In the present experiment, with SR^+ as the incoming thiol, the mismatch of cluster distributions (with shifts to lower *x* values) cannot be ascribed to the difference in the bulkiness of the two thiol ligands because the ligand-exchange process involving PET and a normal alkylthiol has been already been demonstrated to be Gaussian distributed.[29,44] Based on this discussion and the kinetic profile shown in Figure 2.4, it is hypothesized that the kinetic process for cationic-ligand exchange is different to that involved in the exchange of neutral ligands, and is significantly affected by how the SR^+ ligands interact with each other during the exchange process.

There are two types of coulombic repulsions that operate in the current system, namely (i) between the surface SR^+ and the free SR^+ in solution, and (ii) among the SR^+ ligands on the cluster surface, as shown in Figure 2.6. In the first case (i), when a PET on the cluster surface becomes detached with the concomitant coupling of SR^+ to the Au_{25} surface, repulsions between the attached SR^+ and those free in solution hinder further ligand exchange, as observed by the significant decrease in reaction rate during Phase II of the reaction (Figure 2.4B) and the non-binomial distribution of $Au_{25}(PET)_{18-x}(SR^+)_x$ at times in excess of 30 min (Figure 2.5). In the second case (ii), cationic groups densely populated on the surface of a Au_{25} cluster experience strong

coulombic repulsions. A higher number of cationic ligands strongly decreases the thermal stability of the Au_{25} structure, consistent with my lab's previous TG-DTA data that indicate that a fully cationized $Au_{25}(SR^+)_{18}$ cluster exhibits a lower decomposition temperature.[27] Similar ligand-induced instability was also reported for anionic $Au_{25}(S(CH_2)_nCOOH)_{18}$ nanoclusters.[41]

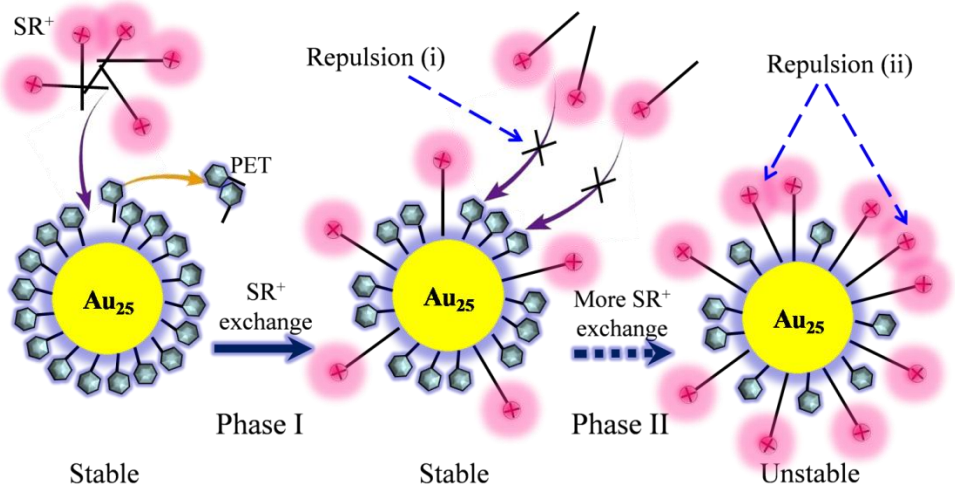

Figure 2.6 Schematic representation of various coulombic repulsions during cationic-ligand exchange: (i) between the surface SR^+ and the free SR^+ in solution, and (ii) between the SR^+ ligands on the cluster surface (PET: 2-phenylethanethiol; SR^+: (11-mercaptoundecyl)-*N*,*N*,*N*-trimethylammonium).

The decreases in absorbance shown in Figure 1 are due to cluster decomposition; hence the effect of (ii) is crucial to the discussion of the kinetics of the cationic-ligand-exchange process. The decomposition of Au_{25} clusters with high levels of exchanged SR^+ (larger *x* values), which are less stable than clusters that are less exchanged (smaller *x*), may be responsible for the observed shifts in the center positions of the distributions to lower values. Hence, the mismatches in the center positions displayed in Figure 2.5 are not only due to the surface SR^+ and the free SR^+

in solution (repulsion (i)), but also due to repulsion (ii). From this, we conclude that synergism between the two types of coulombic repulsion, namely (i) and (ii), result in the mismatch observed in Figure 2.5, but the former dominates.

2.4 Conclusions

The kinetics of cationic-ligand-exchange process of neutral PET ligands on Au_{25} clusters by cationic SR^+ ligands was investigated by ^{1}H-NMR spectroscopy and ESI-MS. The ^{1}H-NMR results revealed that the exchange reaction is initially a rapid first-order process, which transitions to a slower process. The average SR^+ numbers (determined by ^{1}H-NMR spectroscopy) compared with the actual SR^+ distribution ranges (determined by ESI-MS) also showed that the mixed ligand distributions in these Au_{25} nanoclusters are first binomial, which is well-recognized for neutral ligand-exchange process, and then changes to anon-binomial distribution. These results clearly demonstrate that the kinetics of the cationic-ligand-exchange process is different to that of the neutral-thiol-to-neutral-thiol ligand exchange, and is significantly controlled by the cationic-ligand-induced interactions between SR^+ ligands. This result provides a deeper understanding of the physicochemical properties of cationic thiolate monolayers and their interactions, which is beneficial for the precise and controlled functionalization of gold nanoclusters.

2.5 References

(1) Jin, R.; Zeng, C.; Zhou, M.; Chen, Y. Atomically Precise Colloidal Metal Nanoclusters and Nanoparticles: Fundamentals and Opportunities. *Chem. Rev.* **2016**, *116*, 10346−10413.

(2) Qian, H.; Zhu, M.; Wu, Z.; Jin, R. Quantum Sized Gold Nanoclusters with Atomic Precision. *Acc. Chem. Res.* **2012**, *45*, 1470−1479.

(3) Jin, R. Atomically Precise Metal Nanoclusters: Stable Sizes and Optical Properties. *Nanoscale* **2015**, *7*, 1549−1565.

(4) Murray, R. W. Nanoelectrochemistry: Metal Nanoparticles, Nanoelectrodes, and Nanopores. *Chem. Rev.* **2008**, *108*, 2688−2720.

(5) Tsukuda, T.; Hakkinen, H. *Protected Metal Clusters: From Fundamental to Applications*; Elsevier: Amsterdam, **2015**.

(6) Jin, R. The Impacts of Nanotechnology on Catalysis by Precious Metal Nanoparticles. *Nanotechnol. Rev.* **2012**, *1*, 31−56.

(7) Li, G.; Jin, R. Atomically Precise Gold Nanoclusters as New Model Catalysts. *Acc. Chem. Res.* **2013**, *46*, 1749−1758.

(8) Liu, Y.; Tsunoyama, H.; Akita, T.; Tsukuda, T. Efficient and Selective Epoxidation of Styrene with TBHP Catalyzed by Au_{25}Clusters on Hydroxyapatite. *Chem. Commun.* **2010**, *46*, 550−552.

(9) Mathew, A.; Sajanlal, P. R.; Pradeep, T. Selective Visual Detection of TNT at the Sub−Zeptomole Level. *Angew. Chem. Int. Ed.* **2012**, *51*, 9596−9600.

(10) Guan, G.; Zhang, S. Y.; Cai, Y.; Liu, S.; Bharathi, M. S.; Low, M.; Yu, Y.; Xie, J.; Zheng, Y.; Zhang, Y. W; Han, M. Y. Convenient Purification of Gold Clusters by

Co–Precipitation for Improved Sensing of Hydrogen Peroxide, Mercury Ions and Pesticides. *Chem. Commun.* **2014**, *50*, 5703−5705.

(11) Wu, Z.; Wang, M.; Yang, J.; Zheng, X.; Cai, W.; Meng, G.; Qian, H.; Wang, H.; Jin, R. Fluorescent Probes: Well−Defined Nanoclusters as Fluorescent Nanosensors: A Case Study on $Au_{25}(SG)_{18}$. *Small* **2012**, *8*, 2028−2035.

(12) Polavarapu, L.; Manna, M.; Xu, Q. H. Biocompatible Glutathione Capped Gold Clusters as One−and Two−Photon Excitation Fluorescence Contrast Agents for Live Cells Imaging. *Nanoscale* **2011**, *3*, 429−434.

(13) Ramakrishna, G.; Varnavski, O.; Kim, J.; Lee, D.; Goodson, T. Quantum−Sized Gold Clusters as Efficient Two−Photon Absorbers. *J. Am. Chem. Soc.* **2008**, *130*, 5032−5033.

(14) Yuan, X.; Luo, Z.; Yu, Y.; Yao, Q.; Xie, J. Luminescent Noble Metal Nanoclusters as an Emerging Optical Probe for Sensor Development. *Chem. Asian J.* **2013**, *8*, 858−871.

(15) Tan, X.; Jin, R. Ultrasmall Metal Nanoclusters for Bio−Related Applications. *WIREs Nanomed. Nanobiotechnol.* **2013**, *5*, 569−581.

(16) Koh, T. W.; Hiszpanski, A.; Sezen, M.; Naim, A.; Galfsky, T.; Trivedi, A.; Loo, Y. L.; Menon, V.; Rand, B. Metal Nanocluster Light−Emitting Devices with Suppressed Parasitic Emission and Improved Efficiency: Exploring the Impact of Photophysical Properties. *Nanoscale* **2015**, *7*, 9140−9146.

(17) Häkkinen, H. The Gold−Sulfur Interface at the Nanoscale. *Nat. Chem.* **2012**, *4*, 443−455.

(18) Bürgi, T. Properties of the Gold−Sulphur Interface: From Self−Assembled Monolayers to Clusters. *Nanoscale* **2015**, *7*, 15553−15567.

(19) Dass, A. Nano−scaling Law: Geometric Foundation of Thiolated Gold Nanomolecules. *Nanoscale* **2012**, *4*, 2260−2263.

(20) Ghosh, A.; Hassinen, J.; Pulkkinen, P.; Tenhu, H.; Ras, R. H.; Pradeep, T. Simple and Efficient Separation of Atomically Precise Noble Metal Clusters. *Anal. Chem.* **2014**, *86*, 12185−12190.

(21) Yuan, X.; Zhang, B.; Luo, Z.; Yao, Q.; Leong, D. T.; Yan, N.; Xie, J. Balancing the Rate of Cluster Growth and Etching for Gram−scale Synthesis of Thiolate−protected Au_{25}Nanoclusters with Atomic Precision. *Angew. Chem. Inter. Ed.* **2014**, *126*, 4711−4715.

(22) Allen, C.; Qiu, T. A.; Pramanik, S.; Buchman, J. T.; Krause, M. O.; Murphy, C. J. Research Highlights: Investigating the Role of Nanoparticle Surface Charge in Nano–bio Interactions. *Environ. Sci. Nano* **2017**, *4*, 741−746.

(23) Ishida, Y.; Corpuz, R. D.; Yonezawa, T. Matrix Sputtering Method: A Novel Physical Approach for Photoluminescent Noble Metal Nanoclusters. *Acc. Chem. Res.* **2017**, *50*, 2986–2995.

(24) Quan, X.; Peng, C.; Zhao, D.; Li, L.; Fan, J.; Zhou, J. Molecular Understanding of the Penetration of Functionalized Gold Nanoparticles into Asymmetric Membranes. *Langmuir* **2016**, *33*, 361−371.

(25) Elci, S. G.; Jiang, Y.; Yan, B.; Kim, S. T.; Saha, K.; Moyano, D. F.; Tonga, G. Y.; Jackson, L. C.; Rotello, V. M.; Vachet, R. W. Surface Charge Controls the Suborgan Biodistributions of Gold Nanoparticles. *ACS Nano* **2016**, 10, 5536−5542.

(26) Ishida, Y.; Narita, K.; Yonezawa, T.; Whetten, R. L. Fully Cationized Gold Clusters: Synthesis of $Au_{25}(SR^{+})_{18}$. *J. Phys. Chem. Lett.* **2016**, *7*, 3718–3722.

(27) Ishida, Y.; Huang, Y. L.; Yonezawa, T.; Narita, K. Charge Neutralization Strategy: A Novel Synthetic Approach to Fully Cationized Thiolate−Protected $Au_{25}(SR^{+})_{18}$ Clusters with Atomic Precision. *ChemNanoMat* **2017**,*3*, 298−302.

(28) Meng, X. G.; Xu, Q.; Wang, S. X.; Zhu, M. Z. Ligand Exchange Synthesis of Selenophenolate–capped Au_{25} Nanoclusters. *Nanoscale* **2012**, *4*, 4161−4165.

(29) Dass, A.; Holt, K.; Parker, J. F.; Feldberg, S. W.; Murray, R. W. Mass Spectrometrically Detected Statistical Aspects of Ligand Populations in Mixed Monolayer $Au_{25}L_{18}$ Nanoparticles. *J. Phys. Chem. C* **2008**, *112*, 20276−20283.

(30) Ni, T. W.; Tofanelli, M. A.; Phillips, B. D.; Ackerson, C. J. Structural Basis for Ligand Exchange on $Au_{25}(SR)_{18}$. *Inorg. Chem.* **2014**, *53*, 6500−6502.

(31) Rambukwella, M.; Burrage, S.; Neubrander, M.; Baseggio, O.; Aprà, E.; Stener, M.; Fortunelli, A.; Dass, A. $Au_{38}(SPh)_{24}$: Au_{38} Protected with Aromatic Thiolate Ligands. *J. Phys. Chem. Lett.* **2017**, *8*, 1530−1537.

(32) Niihori, Y.; Hossain, S.; Kumar, B.; Nair, L. V.; Kurashige, W.; Negishi, Y. Perspective: Exchange Reactions in Thiolate−protected Metal Clusters. *APL Mater.* **2017**, *5*, 053201.

(33) Fernando, A.; Aikens, C. M. Ligand Exchange Mechanism on Thiolate Monolayer Protected $Au_{25}(SR)_{18}$ Nanoclusters. *J. Phys. Chem. C* **2015**, *119*, 20179−20187.

(34) Niihori, Y.; Hossain, S.; Sharma, S.; Kumar, B.; Kurashige, W.; Negishi, Y. Understanding and Practical Use of Ligand and Metal Exchange Reactions in Thiolate−Protected Metal Clusters to Synthesize Controlled Metal Clusters. *Chem. Rec.* **2017**, *17*, 473−484.

(35) Niihori, Y.; Shima, D.; Yoshida, K.; Hamada, K.; Nair, L. V.; Hossain, S.; Kurashige, W.; Negishi, Y. High−performance Liquid Chromatography Mass

Spectrometry of Gold and Alloy Clusters Protected by Hydrophilic Thiolates. *Nanoscale* **2018**, *10*, 1641−1649.

(36) Fields−Zinna, C. A.; Sardar, R.; Beasley, C. A.; Murray, R. W. Electrospray Ionization Mass Spectrometry of Intrinsically Cationized Nanoparticles, $[Au_{144/146}(SC_{11}H_{22}N(CH_2CH_3)_3^+)_x(S(CH_2)_5CH_3)_y]_x^+$. *J. Am. Chem. Soc.* **2009**, *131*, 16266−16271.

(37) Parker, J. F.; Weaver, J. E.; McCallum, F.; Fields−Zinna, C. A.; Murray, R. W. Synthesis of Monodisperse $[Oct_4N^+][Au_{25}(SR)_{18}^-]$ Nanoparticles, with Some Mechanistic Observations. *Langmuir* **2010**, *26*, 13650−13654.

(38) Ishida, Y.; Jirasupangkul, T.; Yonezawa, T. One−pot Preparation of Cationic Charged Pt Nanoparticles by the Autocatalytic Hydrolysis of Acetylthiocholine. *New J. Chem.* **2015**, *39*, 4214−4217.

(39) Templeton, A. C.; Hostetler, M. J.; Warmoth, E. K.; Chen, S.; Hartshorn, C. M.; Krishnamurthy, V. M.; Forbes, M. D.; Murray, R. W. Gateway Reactions to Diverse, Polyfunctional Monolayer−protected Gold Clusters. *J. Am. Chem. Soc.* **1998**, *120*, 4845−4849.

(40) Zhu, M.; Chan, G.; Qian, H.; Jin, R. Unexpected Reactivity of $Au_{25}(SCH_2CH_2Ph)_{18}$ Nanoclusters with Salts. *Nanoscale* **2011**, *3*, 1703−1707.

(41) Yuan, X.; Goswami, N.; Mathews, I.; Yu, Y.; Xie, J. Enhancing Stability Through Ligand−Shell Engineering: a Case Study with $Au_{25}(SR)_{18}$ Nanoclusters. *Nano Res.* **2015**, *8*, 3488−3495.

(42) Dainese, T.; Antonello, S.; Gascón, J. A.; Pan, F.; Perera, N. V.; Ruzzi, M.; Venzo, V.; Zoleo, A.; Rissanen, K.; Maran, F. $Au_{25}(Set)_{18}$, a Nearly Naked Thiolate−protected Au_{25} Cluster: Structural Analysis by Single Crystal X−ray

Crystallography and Electron Nuclear Double Resonance. *ACS Nano* **2014**, *8*, 3904−3912.

(43) Liu, C.; Lin, S.; Pei, Y.; Zeng, X. C. Semiring Chemistry of $Au_{25}(SR)_{18}$: Fragmentation Pathway and Catalytic Active Site. *J. Am. Chem. Soc.* **2013**, *135*, 18067−18079.

(44) Salassa, G.; Sels, A.; Mancin, F.; Bürgi, T. Dynamic Nature of Thiolate Monolayer in $Au_{25}(SR)_{18}$ Nanoclusters. *ACS Nano* **2017**, *11*, 12609−12614.

(45) Song, Y.; Murray, R. W. Dynamics and Extent of Ligand Exchange Depend on Electronic Charge of Metal Nanoparticles. *J. Am. Chem. Soc.* **2002**, *124*, 7096−7102.

(46) Donders, R. L.; Song, Y.; Murray, R. W. Substituent Effects on the Exchange Dynamics of Ligands on 1.6 nm Diameter Gold Nanoparticles. *Langmuir* **2004**, *20*, 4703−4707.

(47) Guo, R.; Song, Y.; Wang, G.; Murray, R. W. Does Core Size Matter in the Kinetics of Ligand Exchange of Monolayer−Protected Au Clusters? *J. Am. Chem. Soc.* **2005**, *127*, 2752−2757.

(48) Shibu, E. S.; Muhammed, M. H.; Tsukuda, T.; Pradeep, T. Ligand Exchange of $Au_{25}SG_{18}$ Leading to Functionalized Gold Clusters: Spectroscopy, Kinetics, and Luminescence. *J. Phys. Chem. C* **2008**, *112*, 12168−12176.

(49) Pengo, P.; Bazzo, C.; Boccalon, M.; Pasquato, L. Differential Reactivity of the Inner and Outer Positions of $Au_{25}(SCH_2CH_2Ph)_{18}$ Dimeric Staples Under Place Exchange Conditions. *Chem. Commun.* **2015**, *51*, 3204−3207.

(50) Chen, Y.; Zeng, C.; Kauffman, D. R.; Jin, R. Tuning the Magic Size of Atomically Precise Gold Nanoclusters via Isomeric Methylbenzenethiols. *Nano Lett.* **2015**, *15*, 3603−3609.

Appendix I: Supporting Information

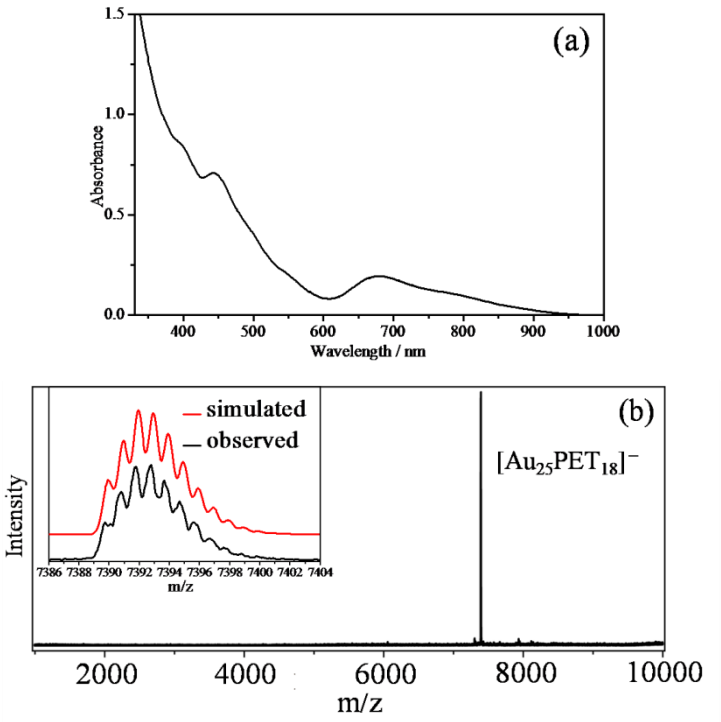

Figure S2.1 UV-vis absorption (a)and negative-mode ESI mass spectra (b) of the starting $Au_{25}(PET)_{18}$.

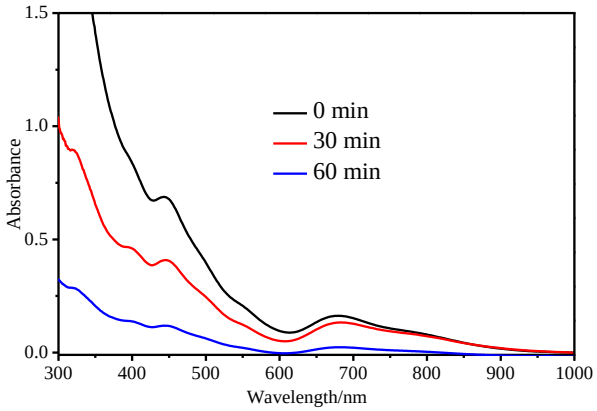

Figure S2.2 UV-vis absorption spectra of samples without ion-exchange process of SR^+ ligand (from Br^- to PF_6^-) during ligand-exchange reaction.

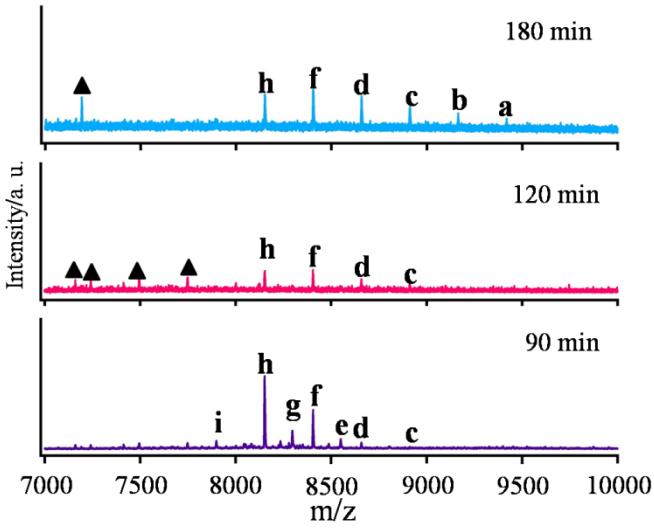

Figure S2.3 Negative-mode ESI mass spectra of samples collected at 90, 120, and 180 min during ligand-exchange process. There have some un-assigned peaks (▲), which may be the decomposition products ofAu_{25} clusters.

Table S2.1 Structural and charge assignments of ESI-MS in Figure S2.3.

Peak	Assignment	Charge I	90 min m/z (obs.)	120 min m/z (obs.)	180 min m/z (obs.)	m/z (calc.)
a	$Au_{25}^{-1}(SR^{+})_8 \bullet (PF_6^{-})_8$	–1	—	—	9419.76	9419.87
b	$Au_{25}^{-1}PET_{11}(SR^{+})_7 \bullet (PF_6^{-})_7$	–1	—	—	9166.63	9166.66
c	$Au_{25}^{-1}PET_{12}(SR^{+})_6 \bullet (PF_6^{-})_6$	–1	8913.40	8913.42	8913.45	8913.45
d	$Au_{25}^{-1}PET_{13}(SR^{+})_5 \bullet (PF_6^{-})_5$	–1	8660.25	8660.30	8660.33	8660.24
e	$Au_{25}^{0}PET_{14}(SR^{+})_4 \bullet (PF_6^{-})_5$	–1	8551.90	—	—	8551.99
f	$Au_{25}^{-1}PET_{14}(SR^{+})_4 \bullet (PF_6^{-})_4$	–1	8406.98	8407.03	8407.02	8407.03
g	$Au_{25}^{0}PET_{15}(SR^{+})_3 \bullet (PF_6^{-})_4$	–1	8298.75	—	—	8298.78
h	$Au_{25}^{-1}PET_{15}(SR^{+})_3 \bullet (PF_6^{-})_3$	–1	8153.99	8153.79	8154.01	8153.82
i	$Au_{25}^{-1}PET_{16}(SR^{+})_2 \bullet (PF_6^{-})_2$	–1	7900.85	—	—	7900.61

In negative-mode ESI-MS shown in Figure 2.2

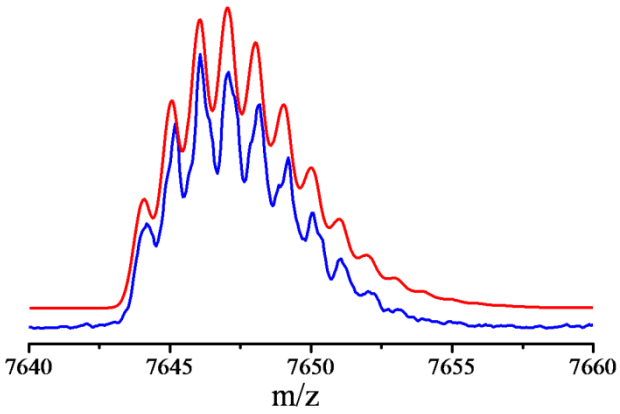

$Au_{25}^{-1}PET_{17}(SR^{+})_1\bullet(PF_6^{-})_1$ (peak ii, 10 min)

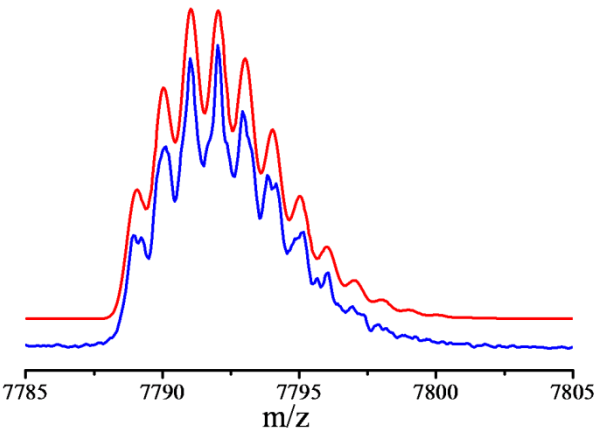

$Au_{25}^{0}PET_{17}(SR^{+})_1\bullet(PF_6^{-})_2$ (peak iii, 10 min)

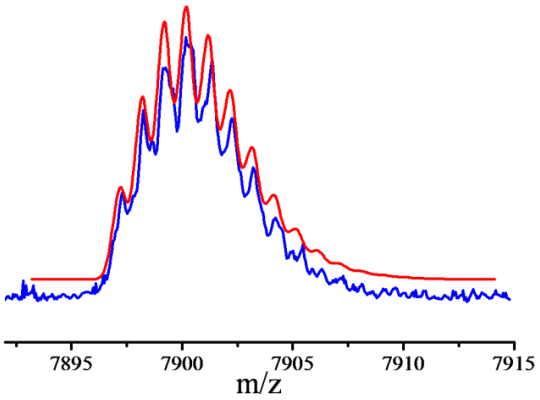

$Au_{25}^{-1}PET_{16}(SR^{+})_2\bullet(PF_6^{-})_2$ (peak vi, 30 min)

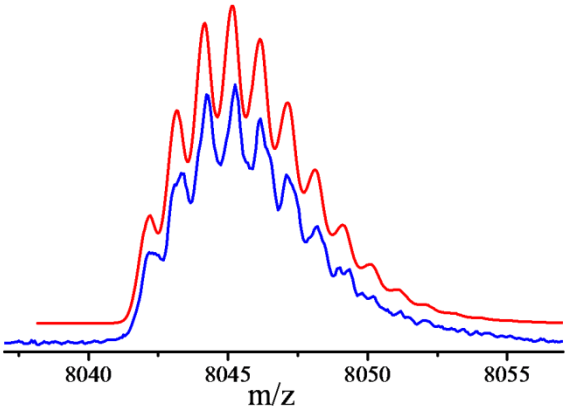

$Au_{25}^{0}PET_{16}(SR^{+})_2\bullet(PF_6^{-})_3$ (peak v, 30 min)

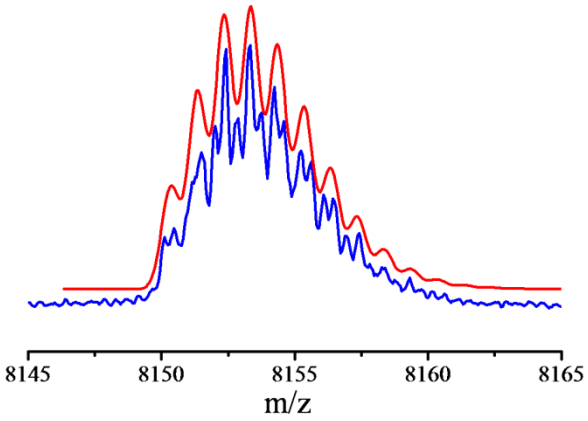

$Au_{25}^{-1}PET_{15}(SR^{+})_3\bullet(PF_6^{-})_3$ (peak vi, 60 min)

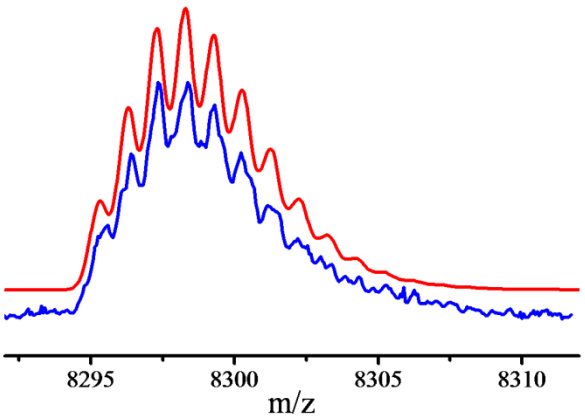

$Au_{25}^{0}PET_{15}(SR^{+})_3\bullet(PF_6^{-})_4$ (peak vii, 30 min)

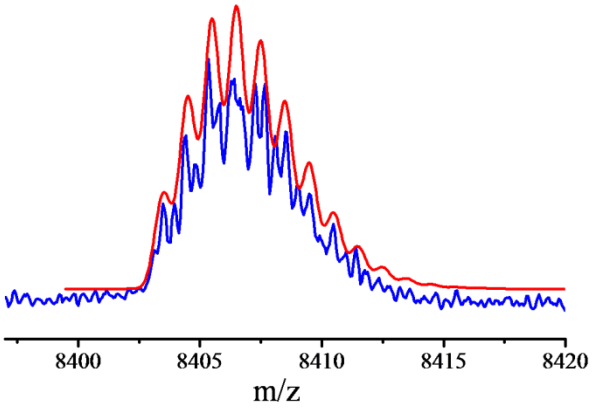

$Au_{25}^{-1}PET_{14}(SR^{+})_4 \bullet (PF_6^{-})_4$ (peak viii, 60 min)

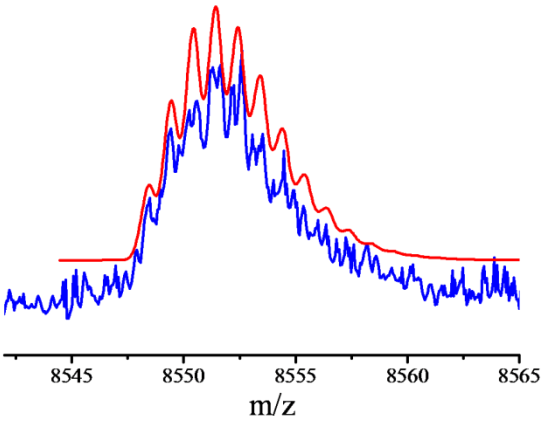

$Au_{25}^{0}PET_{14}(SR^{+})_4 \bullet (PF_6^{-})_5$ (peak ix, 30 min)

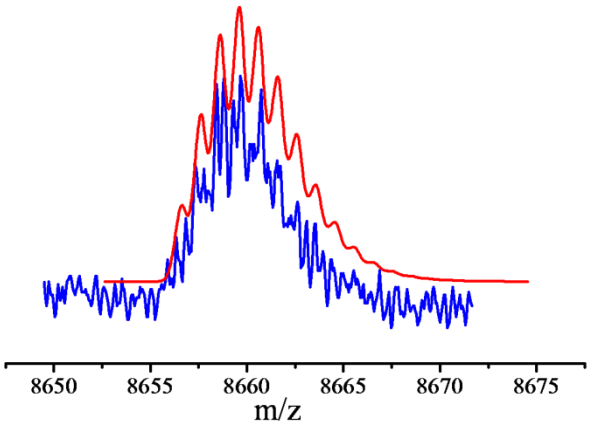

$Au_{25}^{-1}PET_{13}(SR^{+})_5 \bullet (PF_6^{-})_5$ (peak x, 60 min)

In negative-mode ESI-MS shown in Figure S2.3

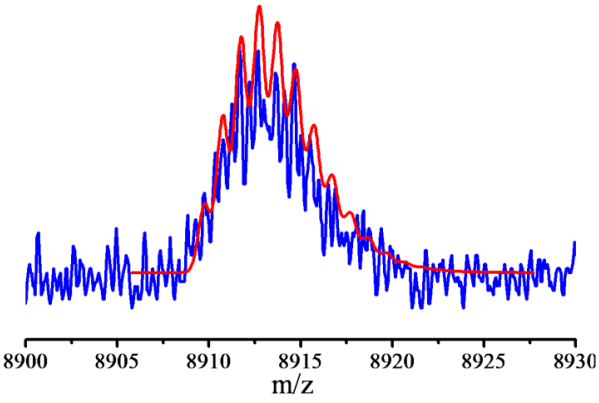

$Au_{25}^{-1}PET_{12}(SR^{+})_6\bullet(PF_6^{-})_6$ (peak c, 180 min)

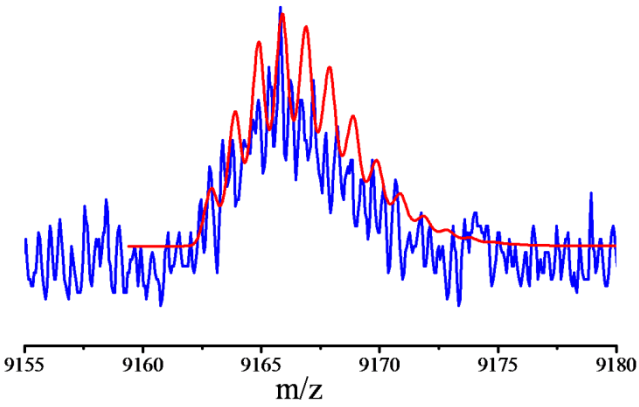

$Au_{25}^{-1}PET_{11}(SR^{+})_7\bullet(PF_6^{-})_7$ (peak b, 180 min)

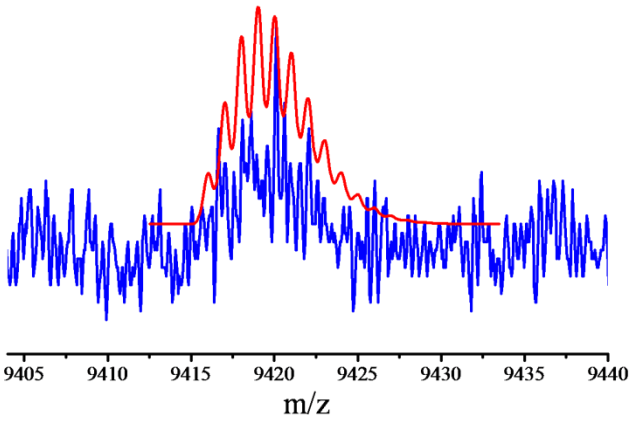

$Au_{25}^{-1}PET_{10}(SR^{+})_8\bullet(PF_6^{-})_8$ (peak a, 180 min)

In positive-mode ESI-MS shown in Figure 2.3

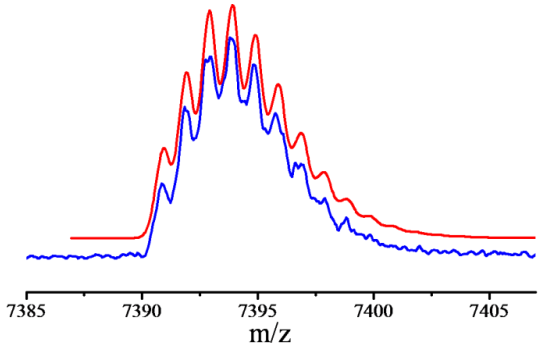

$Au_{25}^{+1}PET_{18}(SR^{+})_0\bullet(PF_6^{-})_0$ (peak e, 10 min)

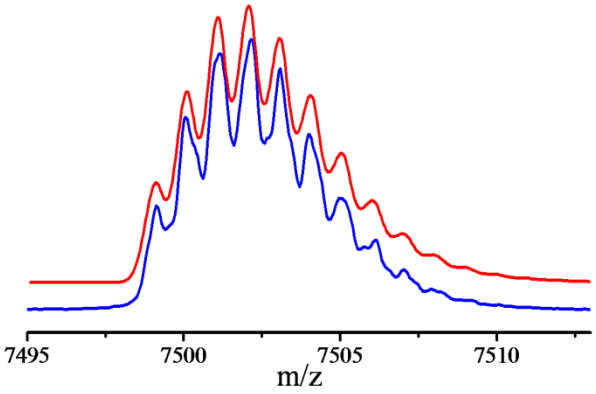

$Au_{25}^{0}PET_{17}(SR^{+})_1\bullet(PF_6^{-})_0$ (peak d, 10 min)

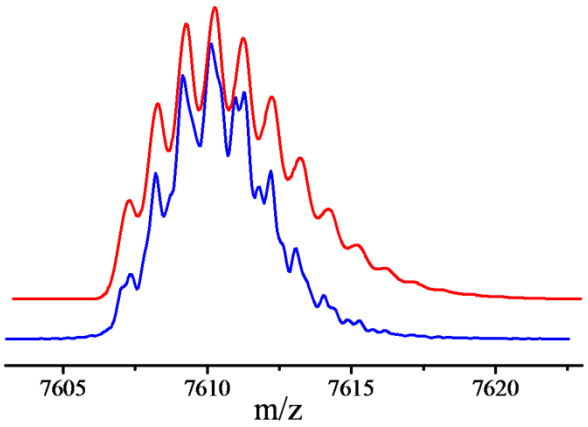

$Au_{25}^{-1}PET_{16}(SR^{+})_2\bullet(PF_6^{-})_0$ (peak c, 30 min)

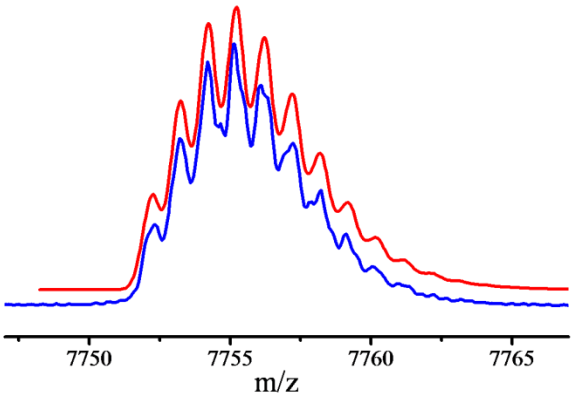

$Au_{25}^{0}PET_{16}(SR^{+})_{2}\bullet(PF_{6}^{-})_{1}$ (peak b, 30 min)

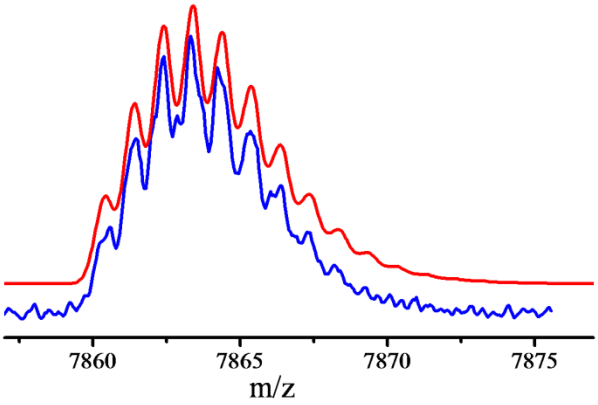

$Au_{25}^{-1}PET_{15}(SR^{+})_{3}\bullet(PF_{6}^{-})_{1}$ (peak a, 30 min)

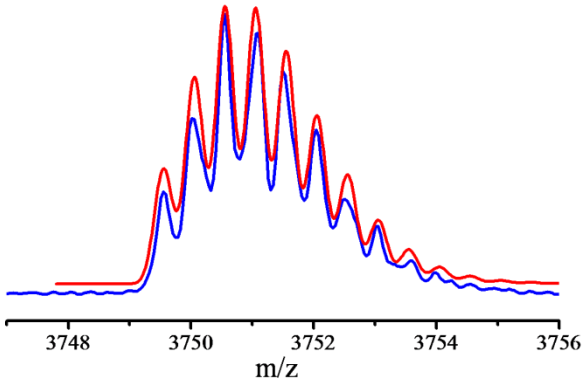

$Au_{25}^{+1}PET_{17}(SR^{+})_{1}\bullet(PF_{6}^{-})_{0}$ (peak n, 10 min)

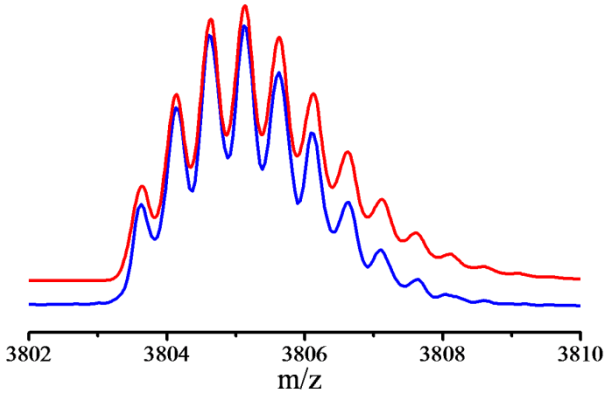

$Au_{25}^{0}PET_{16}(SR^{+})_{2}\bullet(PF_{6}^{-})_{0}$ (peak m, 10 min)

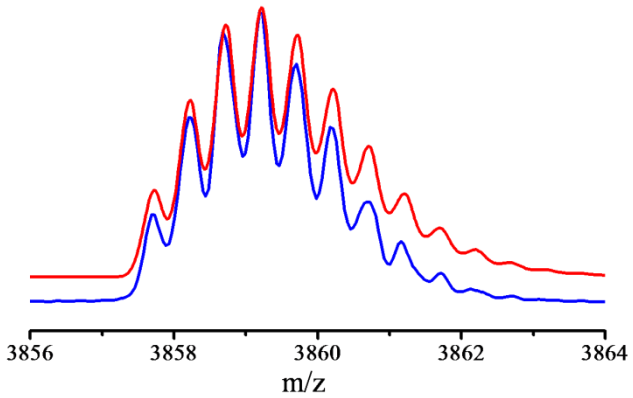

$Au_{25}^{-1}PET_{15}(SR^{+})_{3}\bullet(PF_{6}^{-})_{0}$ (peak l, 30 min)

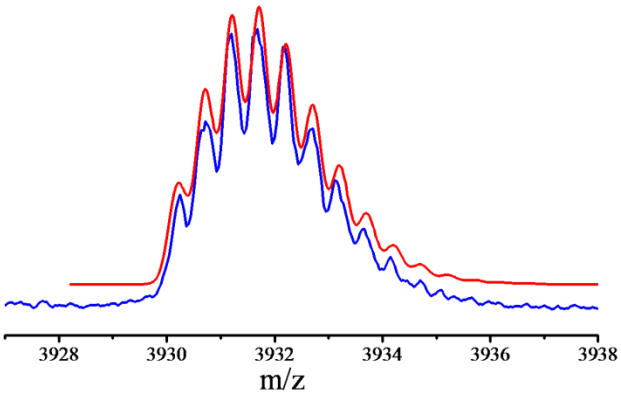

$Au_{25}^{0}PET_{15}(SR^{+})_{3}\bullet(PF_{6}^{-})_{1}$ (peak k, 30 min)

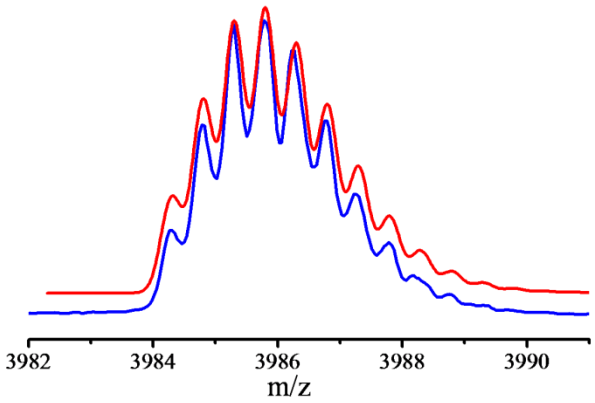

$Au_{25}^{-1}PET_{14}(SR^{+})_4\bullet(PF_6^{-})_1$ (peak j, 60 min)

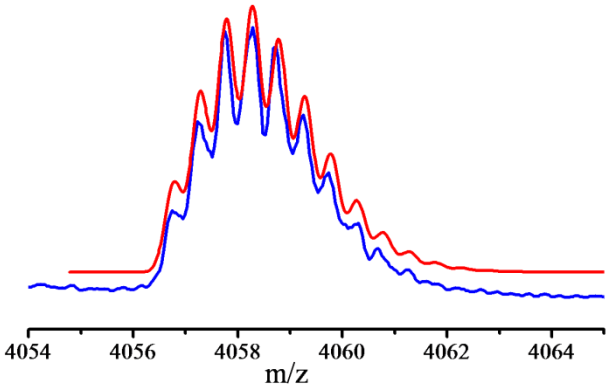

$Au_{25}^{0}PET_{14}(SR^{+})_4\bullet(PF_6^{-})_2$ (peak I, 60 min)

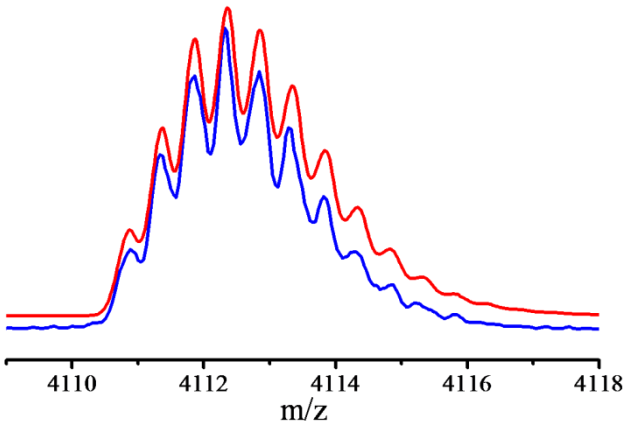

$Au_{25}^{-1}PET_{13}(SR^{+})_5\bullet(PF_6^{-})_2$ (peak h, 60 min)

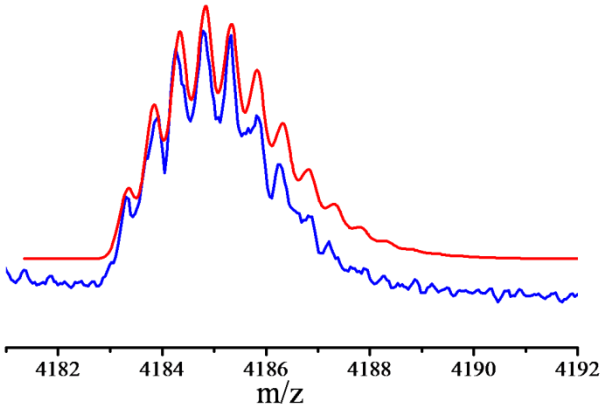

$Au_{25}{}^{0}PET_{13}(SR^{+})_{5}\bullet(PF_{6}{}^{-})_{3}$ (peak g, 60 min)

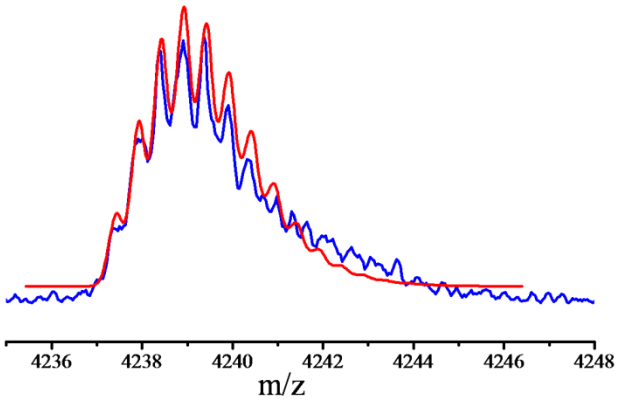

$Au_{25}{}^{-1}PET_{12}(SR^{+})_{6}\bullet(PF_{6}{}^{-})_{3}$ (peak f, 60 min)

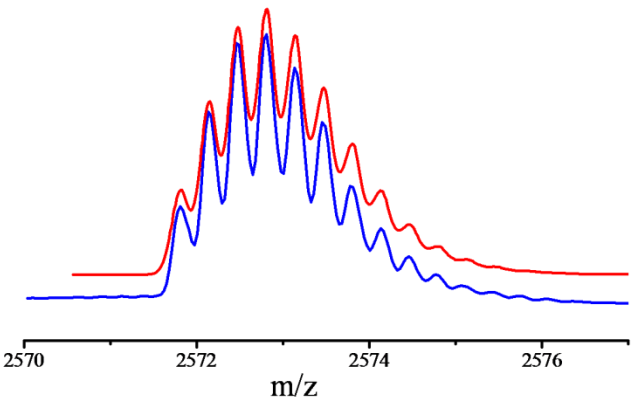

$Au_{25}{}^{0}PET_{15}(SR^{+})_{3}\bullet(PF_{6}{}^{-})_{0}$ (peak t, 30 min)

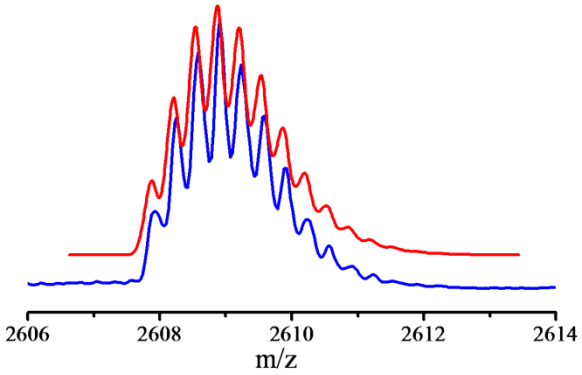

$Au_{25}^{-1}PET_{14}(SR^{+})_{4}\bullet(PF_{6}^{-})_{0}$ (peak s, 60 min)

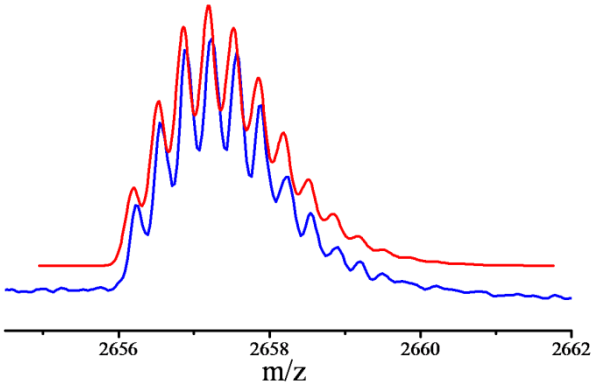

$Au_{25}^{0}PET_{14}(SR^{+})_{4}\bullet(PF_{6}^{-})_{1}$ (peak r, 60 min)

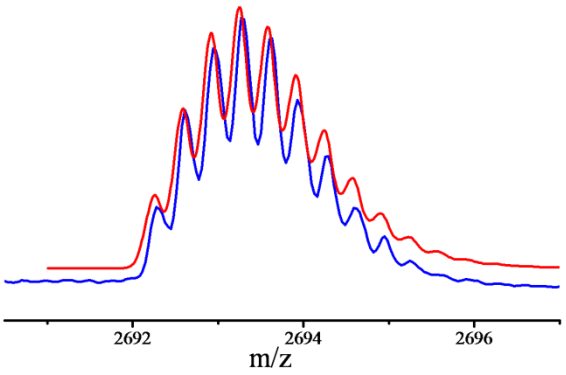

$Au_{25}^{-1}PET_{13}(SR^{+})_{5}\bullet(PF_{6}^{-})_{1}$ (peak q, 60 min)

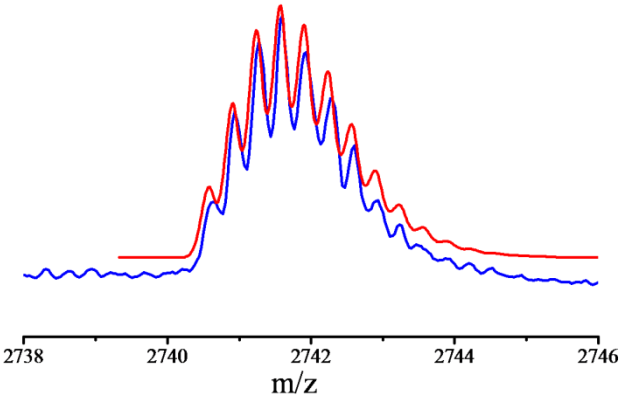

$Au_{25}^{0}PET_{15}(SR^{+})_5\bullet(PF_6^{-})_2$ (peak p, 60 min)

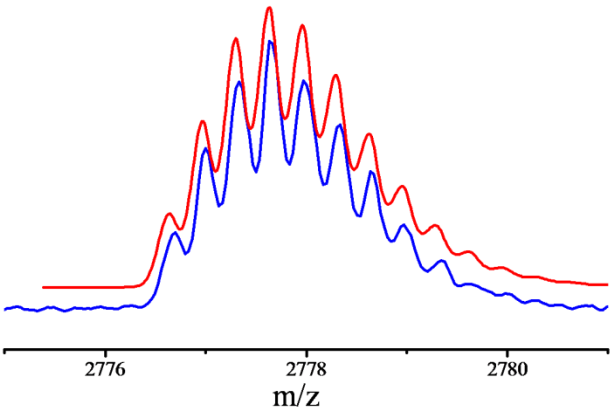

$Au_{25}^{-1}PET_{12}(SR^{+})_6\bullet(PF_6^{-})_2$ (peak o, 60 min)

In positive-mode ESI-MS shown in Figure S2.4

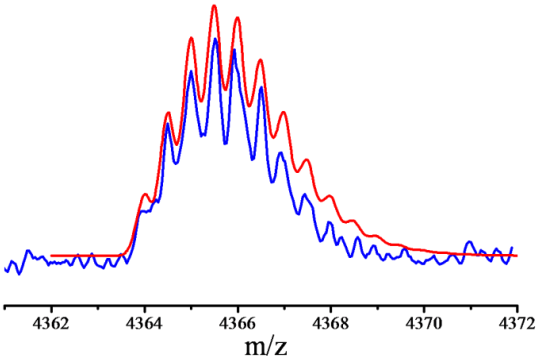

$Au_{25}^{-1}PET_{11}(SR^{+})_7\bullet(PF_6^{-})_4$ (peak a, 180 min)

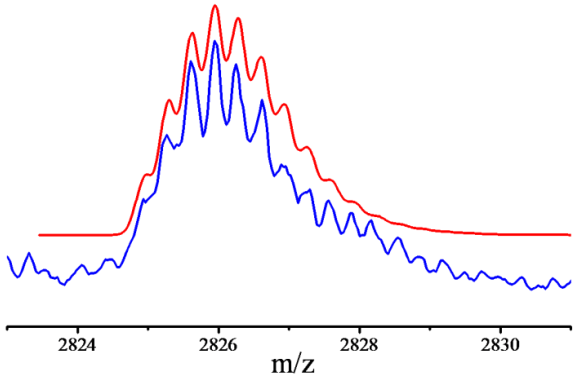

$Au_{25}{}^{0}PET_{12}(SR^{+})_{6}\bullet(PF_{6}{}^{-})_{3}$ (peak n, 120 min)

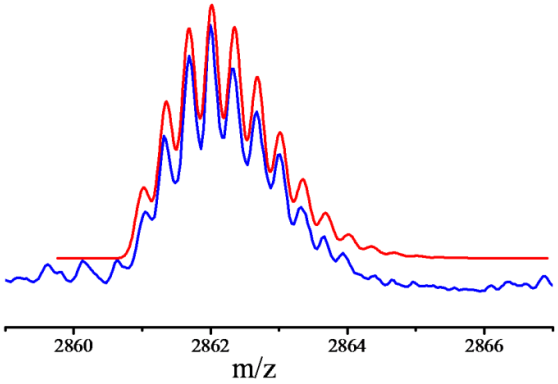

$Au_{25}{}^{-1}PET_{11}(SR^{+})_{7}\bullet(PF_{6}{}^{-})_{3}$ (peak m, 120 min)

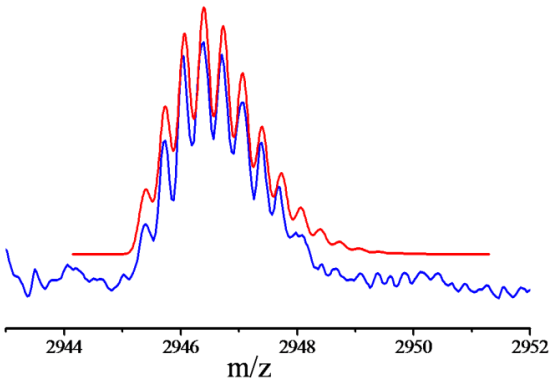

$Au_{25}{}^{0}PET_{10}(SR^{+})_{8}\bullet(PF_{6}{}^{-})_{4}$ (peak l, 180 min)

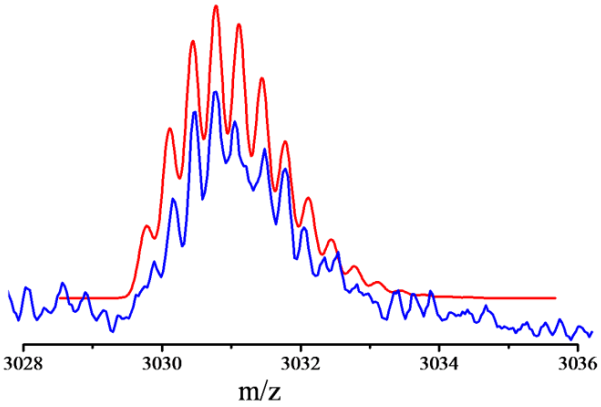

$Au_{25}^{-1}PET_9(SR^+)_9\bullet(PF_6^-)_5$ (peak k, 180 min)

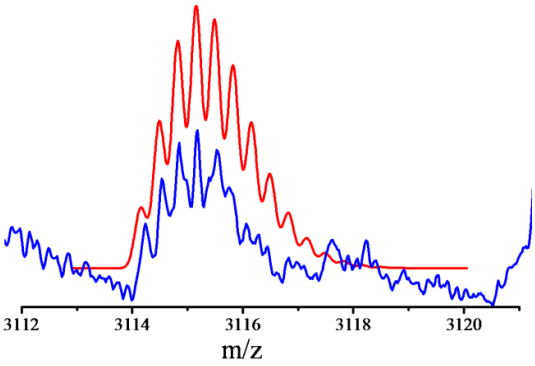

$Au_{25}^{-1}PET_8(SR^+)_{10}\bullet(PF_6^-)_6$ (peak j, 180 min)

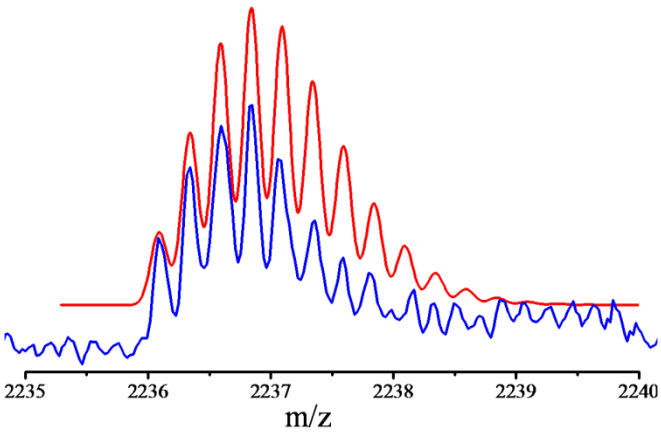

$Au_{25}^{-1}PET_9(SR^+)_9\bullet(PF_6^-)_4$ (peak y, 120 min)

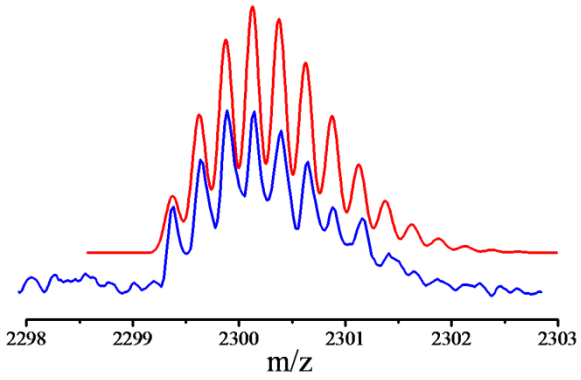

$Au_{25}^{-1}PET_8(SR^+)_{10}\bullet(PF_6^-)_5$ (peak x, 120 min)

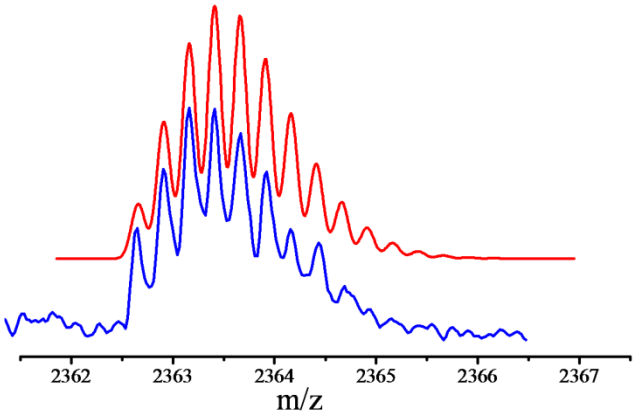

$Au_{25}^{-1}PET_7(SR^+)_{11}\bullet(PF_6^-)_6$ (peak w, 180 min)

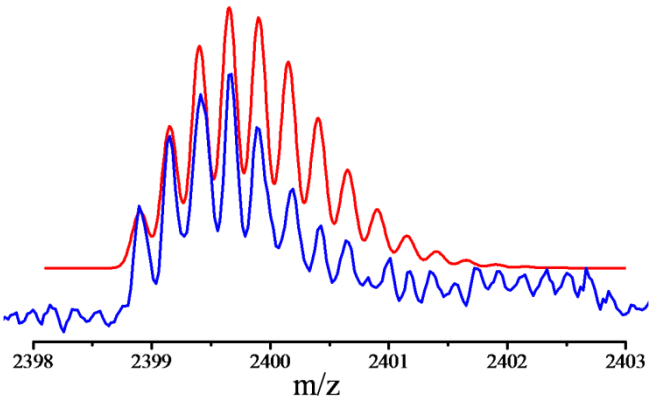

$Au_{25}^{0}PET_7(SR^+)_{11}\bullet(PF_6^-)_7$ (peak v, 180 min)

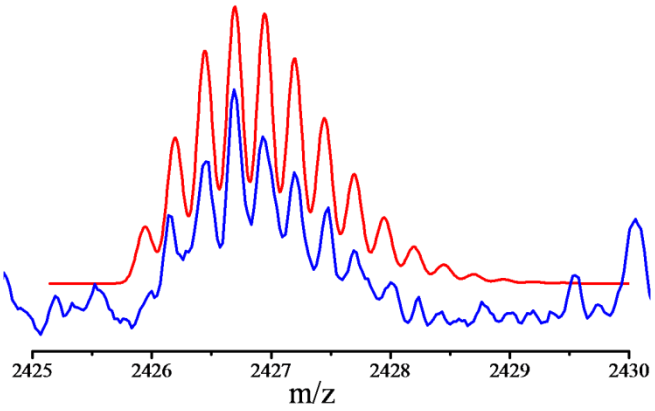

$Au_{25}{}^{0}PET_{6}(SR^{+})_{12}\bullet(PF_{6}{}^{-})_{8}$ (peak u, 180 min)

Fragments shown in Figure 2.3

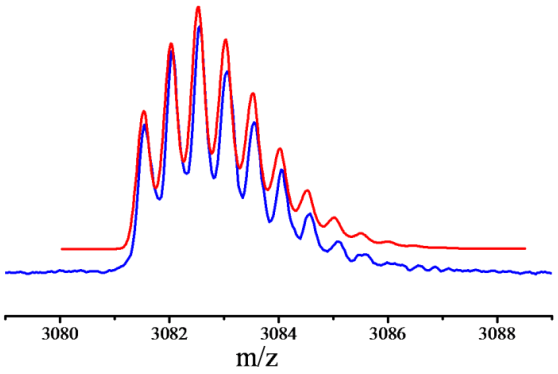

$Au_{21}{}^{+1}PET_{13}(SR^{+})_{1}\bullet(PF_{6}{}^{-})_{0}$ (peak *Fa*, 10 min)

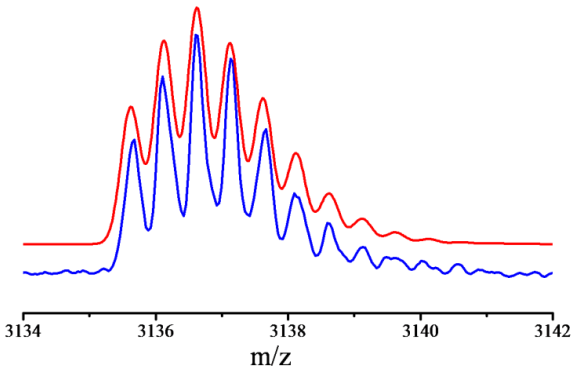

$Au_{21}{}^{0}PET_{12}(SR^{+})_{2}\bullet(PF_{6}{}^{-})_{0}$ (peak *Fb*, 30 min)

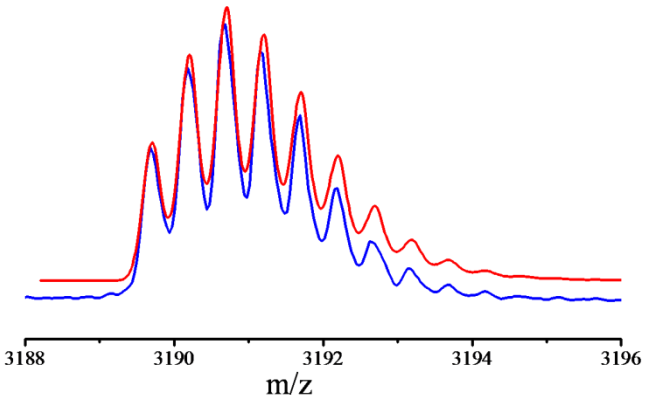

$Au_{21}^{-1}PET_{11}(SR^{+})_3\bullet(PF_6^{-})_0$ (peak *Fc*, 60 min)

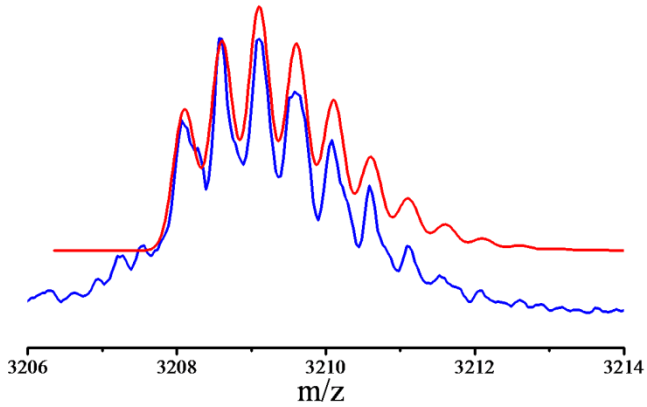

$Au_{21}^{+1}PET_{12}(SR^{+})_2\bullet(PF_6^{-})_1$ (peak *Fd*, 60 min)

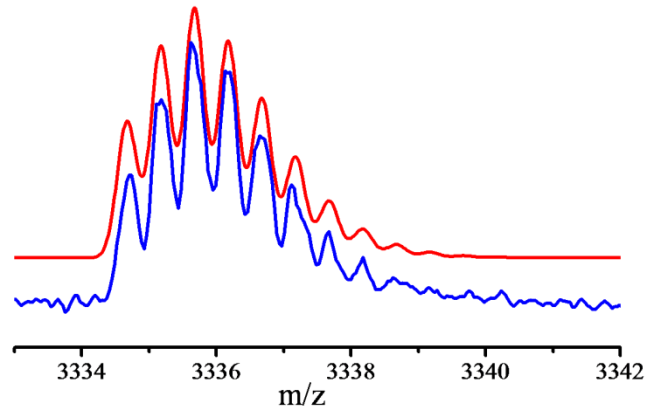

$Au_{21}^{+1}PET_{11}(SR^{+})_3\bullet(PF_6^{-})_2$ (peak *Fe*, 60 min)

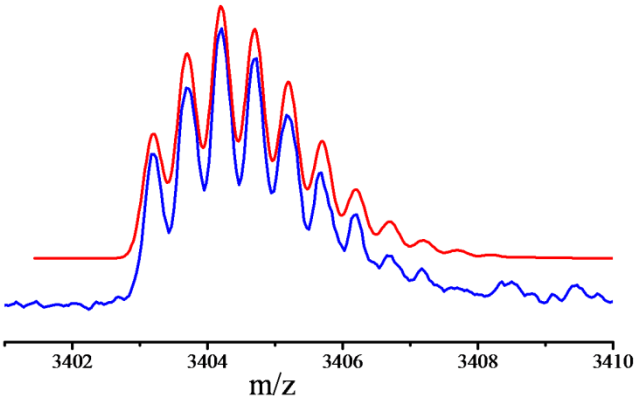

$Au_{21}^{+1}PET_{12}(SR^{+})_3\bullet(PF_6^{-})_2$ (peak *Ff*, 10 min)

Figure S2.4 Isotope patterns of the partially cationic-ligand-protected Au_{25} clusters and Au fragments obtained in Figure 2, 3, S3 and S5. When one cluster has same observed peaks at different reaction time, the strongest one was chosen as a representative example. The expanded high-resolution ESI mass spectrum (blue) and the simulated isotope pattern (red).

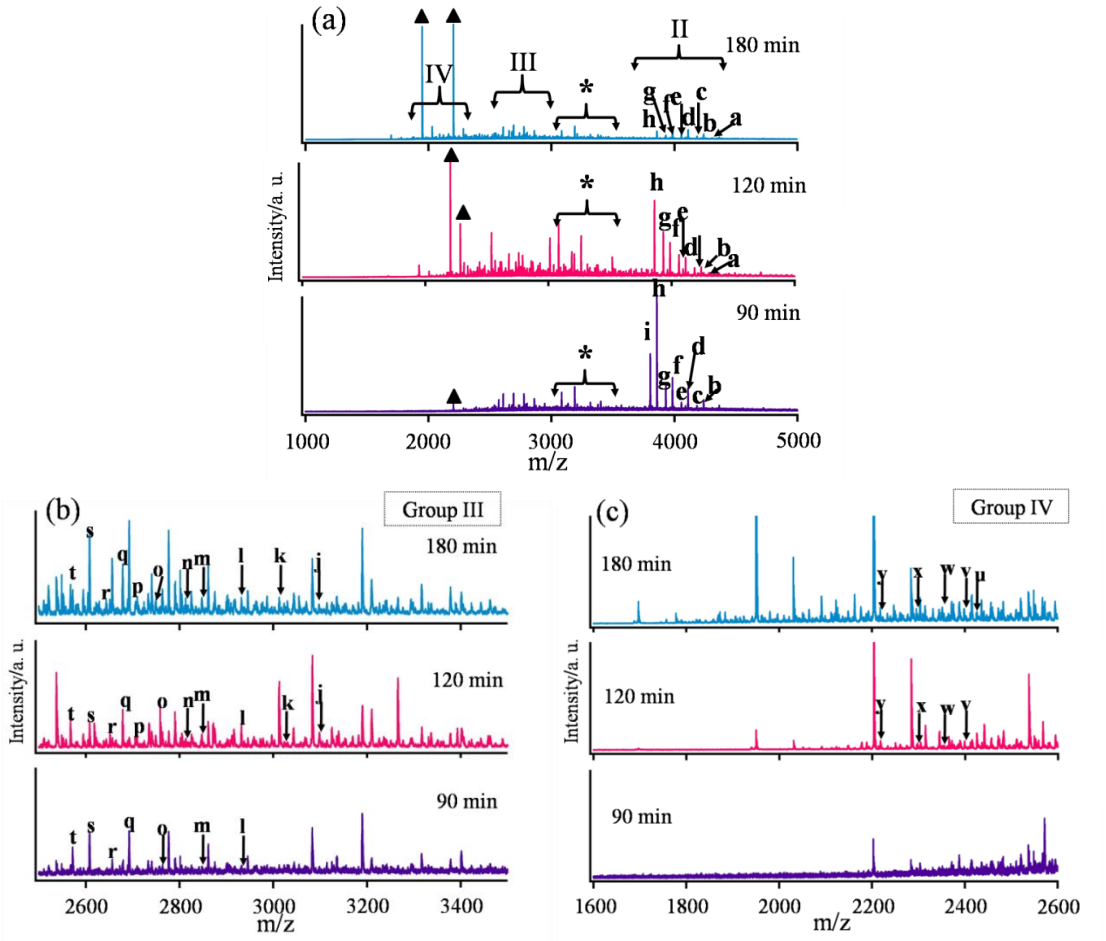

Figure S2.5 (a) Positive-mode ESI mass spectra of samples collected at 90, 120, and 180 min during ligand-exchange process. (b, c) The magnified spectrum of the ranges shown in the Figure (a): b) group III (2500–3500 *m/z*); c) group IV (1600–2600 *m/z*). There have many un-assigned peaks (e. g. ▲), which may be the decomposition products of the Au_{25} clusters.

Table S2.2 Structural and charge assignments of ESI-MS in Figure S2.5.

Group	Peak	Assignment	Charge I	90 min m/z (obs.)	120 min m/z (obs.)	180 min m/z (obs.)	m/z (calc.)
II	a	$Au_{25}^{-1}PET_{11}(SR^{+})_7\bullet(PF_6^{-})_4$	+2	—	4366.82	4366.90	4366.88
	b	$Au_{25}^{-1}PET_{12}(SR^{+})_6\bullet(PF_6^{-})_3$		4239.26	4239.28	4239.47	4239.28
	c	$Au_{25}^{0}PET_{13}(SR^{+})_5\bullet(PF_6^{-})_3$		4185.19	4185.20	4185.14	4185.16
	d	$Au_{25}^{-1}PET_{13}(SR^{+})_5\bullet(PF_6^{-})_2$		4112.64	4112.67	4112.68	4112.67
	e	$Au_{25}^{0}PET_{14}(SR^{+})_4\bullet(PF_6^{-})_2$		4058.61	4058.54	4058.63	4058.55
	f	$Au_{25}^{-1}PET_{14}(SR^{+})_4\bullet(PF_6^{-})_1$		3986.10	3986.12	3986.09	3986.07
	j	$Au_{25}^{0}PET_{15}(SR^{+})_3\bullet(PF_6^{-})_1$		3932.03	3932.07	3932.04	3931.95
	h	$Au_{25}^{-1}PET_{15}(SR^{+})_3\bullet(PF_6^{-})_0$		3859.50	3859.45	3859.55	3859.46
	i	$Au_{25}^{0}PET_{16}(SR^{+})_2\bullet(PF_6^{-})_0$		3805.37	—	—	3805.34
III	j	$Au_{25}^{-1}PET_{8}(SR^{+})_{10}\bullet(PF_6^{-})_6$	+3	—	3115.62	3115.63	3115.65
	k	$Au_{25}^{-1}PET_{9}(SR^{+})_9\bullet(PF_6^{-})_5$		3031.12	3031.10	3031.09	3031.07
	l	$Au_{25}^{-1}PET_{10}(SR^{+})_8\bullet(PF_6^{-})_4$		2946.76	2946.72	2946.69	2946.67
	m	$Au_{25}^{-1}PET_{11}(SR^{+})_7\bullet(PF_6^{-})_3$		2862.24	2862.20	2862.31	2862.27
	n	$Au_{25}^{0}PET_{12}(SR^{+})_6\bullet(PF_6^{-})_3$		—	2826.25	2826.21	2826.18

	o	$Au_{25}^{-1}PET_{12}(SR^{+})_{6}\bullet(PF_{6}^{-})_{2}$		2777.98	2777.97	2777.98	2777.96
	p	$Au_{25}^{0}PET_{13}(SR^{+})_{5}\bullet(PF_{6}^{-})_{2}$		—	2741.80	2741.79	2741.78
	q	$Au_{25}^{-1}PET_{13}(SR^{+})_{5}\bullet(PF_{6}^{-})_{1}$		2693.47	2693.56	2693.49	2693.46
	r	$Au_{25}^{0}PET_{14}(SR^{+})_{4}\bullet(PF_{6}^{-})_{1}$		2657.41	2657.40	2657.36	2657.38
	s	$Au_{25}^{-1}PET_{14}(SR^{+})_{4}\bullet(PF_{6}^{-})_{0}$		2609.09	2609.10	2609.04	2609.06
	t	$Au_{25}^{0}PET_{15}(SR^{+})_{3}\bullet(PF_{6}^{-})_{0}$		2573.03	2573.01	2573.00	2572.97
IV	u	$Au_{25}^{-1}PET_{6}(SR^{+})_{12}\bullet(PF_{6}^{-})_{7}$	+4	—	—	2426.91	2426.97
	v	$Au_{25}^{0}PET_{7}(SR^{+})_{11}\bullet(PF_{6}^{-})_{7}$		—	2399.50	2399.56	2399.51
	w	$Au_{25}^{-1}PET_{7}(SR^{+})_{11}\bullet(PF_{6}^{-})_{6}$		—	2363.59	2363.60	2363.67
	x	$Au_{25}^{-1}PET_{8}(SR^{+})_{10}\bullet(PF_{6}^{-})_{5}$		—	2300.43	2300.42	2300.37
	y	$Au_{25}^{-1}PET_{9}(SR^{+})_{9}\bullet(PF_{6}^{-})_{4}$		—	2237.07	2237.02	2237.07

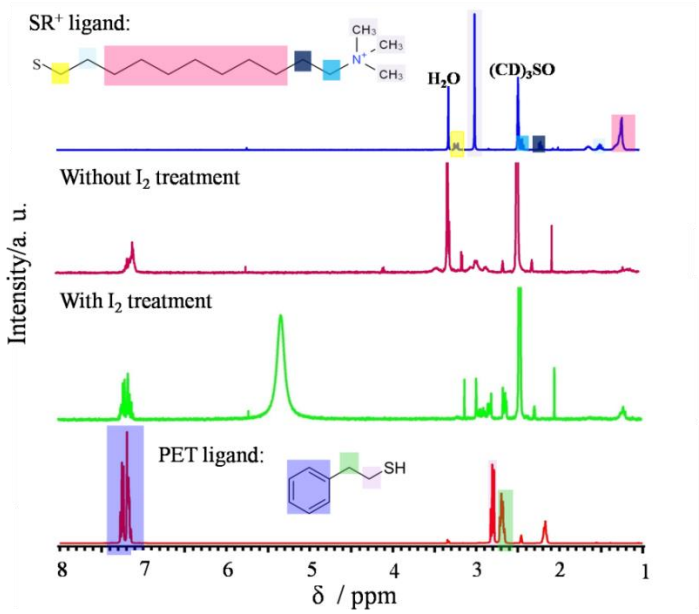

Figure S2.6 ^{1}H-NMR of pure PET, pure $SR^{+}\cdot PF_6^{-}$ and the sample collected at 10 min with & without I_2 treatment in DMSO-d_6 at 400 MHz.

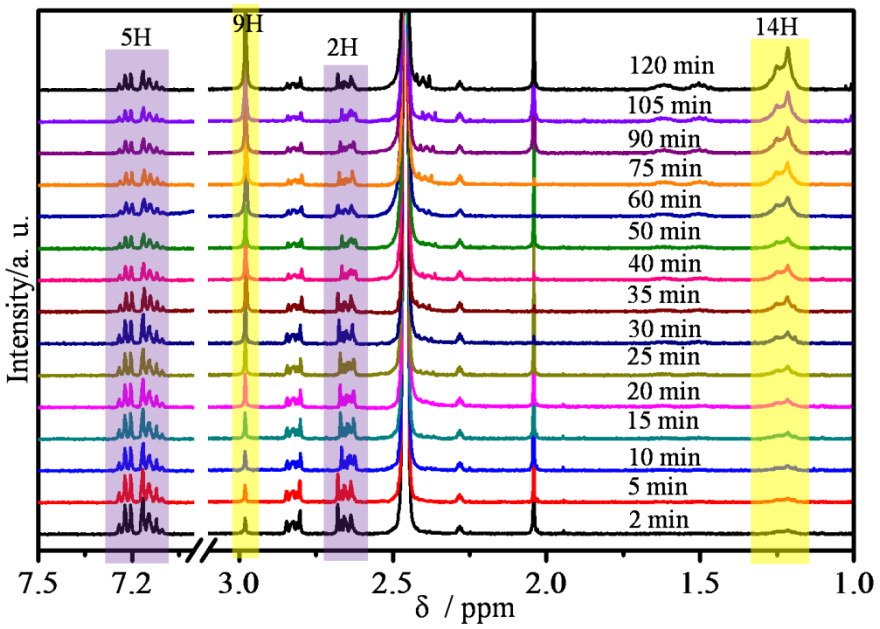

Figure S2.7 ^{1}H-NMR spectra of Au cluster samples in DMSO-d_6 during the ligand-exchange reaction. Highlights denote the representative peaks of PET ligands (7.18 ppm and 2.64 ppm) and SR^{+} (2.98 ppm and 1.22 ppm). The samples were treated with I_2 before ^{1}H–NMR tests.

Table S2.3 The experimental data collected from the ^{1}H-NMR results in Figure S2.7, and base on which, the average ligand-exchange numbers were calculated. (H No.: number of H atoms in each peak, Raw data: normalized integral values of peaks, Each H: integral values of each H atom)

Ligand		**PET**		**Ave.**	**PET No.**	**SR^{+}**		**Ave.**	**SR^{+} No.**
H No.		**5H**	**2H**	**(*a*)^{j}**	**(M)**	**9H**	**14H**	**(*b*)^{j}**	**(N)**
Integral area		**7.30–7.07**	**2.69–2.59**			**3.02–2.94**	**1.35–1.11**		
2 min	Raw data	8.85	4.13			0.62	1		
	Each H^{i}	1.77	2.07	1.92	17.4	0.07	0.07	0.07	0.6
5 min	Raw data	6.37	2.98			0.64	1		
	Each H^{i}	1.27	1.49	1.38	17.1	0.07	0.07	0.07	0.9
10 min	Raw data	3.47	1.87			0.64	1		
	Each H^{i}	0.69	0.94	0.81	16.6	0.07	0.07	0.07	1.4
15 min	Raw data	2.82	1.50			0.61	1		
	Each H^{i}	0.56	0.75	0.66	16.4	0.07	0.07	0.07	1.7
20 min	Raw data	2.53	1.24			0.62	1		
	Each H^{i}	0.51	0.62	0.57	16.0	0.07	0.07	0.07	2.0
25 min	Raw data	2.12	1.12			0.59	1		
	Each H^{i}	0.42	0.56	0.49	15.7	0.07	0.07	0.07	2.3
30 min	Raw data	1.78	0.97			0.6	1		
	Each H^{i}	0.36	0.49	0.43	15.5	0.07	0.07	0.07	2.5
35 min	Raw data	1.49	0.78			0.59	1		
	Each H^{i}	0.30	0.39	0.35	15.0	0.07	0.07	0.07	3.0

40 min	Raw data	1.33	0.69			0.59	1		
	Each H[i]	0.27	0.35	0.31	14.7	0.07	0.07	0.07	3.3
50 min	Raw data	1.15	0.63			0.59	1		
	Each H[i]	0.23	0.32	0.28	14.4	0.07	0.07	0.07	3.6
60 min	Raw data	1.10	0.59			0.61	1		
	Each H[i]	0.22	0.30	0.26	14.2	0.07	0.07	0.07	3.8
75 min	Raw data	0.89	0.47			0.59	1		
	Each H[i]	0.18	0.24	0.21	13.5	0.07	0.07	0.07	4.5
90 min	Raw data	0.78	0.40			0.56	1		
	Each H[i]	0.16	0.20	0.18	13.0	0.06	0.07	0.07	5.0
105 min	Raw data	0.78	0.33			0.60	1		
	Each H[i]	0.16	0.17	0.16	12.6	0.07	0.07	0.07	5.4
120 min	Raw data	0.65	0.29			0.61	1		
	Each H[i]	0.13	0.15	0.14	12.0	0.07	0.07	0.07	6.0

[i]Divided by the number of H atoms, [j]average of two Each H values.

The average ligand-exchange numbers were calculated according to the following equation:

$$\mathrm{M} = \frac{a}{a+b} \times 18 \quad (1)$$

$$\mathrm{N} = \frac{b}{a+b} \times 18 \quad (2)$$

where M and N are the average PET and SR^+ numbers on the Au_{25} surface respectively, *a* and *b* represent the average integrals of PET and SR^+ collected from ^{1}H-NMR, as shown in Table S3.

Chapter 3

Basic $[Au_{25}(SCH_2CH_2Py)_{18}]^{-}\cdot Na^{+}$ Nanomolecules: Synthesis, Layered Crystallographic Arrangement and Unique Surface Protonation

Abstract

Tailoring surface ligands on metal nanoclusters (NCs) ensuring preservation of the structural template is of great importance in the functionalization of NCs toward enhancing their practical utility. This report describes the first synthesis of high-purity and high-yield Au_{25} NCs protected by the basic pyridyl ethanethiol ($HSCH_2CH_2Py$, 4-PyET and 2-PyET). Single-crystal X-ray diffraction of the $[Au_{25}(4\text{-PyET})_{18}]^{-}\cdot Na^{+}$ NCs has revealed a structure similar to that known for the phenyl ethanethiolate analog, but with pyridyl-N coordination to Na^{+}, a more relaxed ligand shell, and a profoundly layered arrangement in the solid state. Because of the pendant Py moiety, the $Au_{25}(PyET)_{18}$ NCs are endowed with a unique (de)protonation equilibria, which has been characterized in detail by UV-vis absorption and ^{1}H-NMR spectroscopy. $Au_{25}(PyET)_{18}$ NCs showed an unexpectedly H^{+}-dependent solubility that is tunable in aqueous and organic solvents. The successful synthesis of the basic Py-terminated thiolate-protected Au_{25} NCs paves the way to realize a new family of metal cluster nanomolecules possessing basic properties.

3.1 Introduction

Thiolate-protected gold nanoclusters ($Au_m(SR)_n$ NCs) with atomic precision and diverse structures have gained increasing attention in research owing to their intriguing physicochemical properties,[1–5] which facilitate their potential application in many contexts such as catalysis,[6–8] sensing,[9–11] and bioapplications.[12–14] SR ligands are used to cap such NCs using surface S-Au bonds to form what are often termed "monolayer protected clusters" (MPCs), in order to prevent Au aggregation and facilitate the isolation of single NCs.

Several studied have highlighted the importance of using SR ligands for metal NCs.[15–30] First, the substituent R-groups can affect the magic size and structure of the as-prepared NCs. For example, Jin et al[15] prepared molecularly pure Au_{130}, Au_{104} and Au_{40} NCs employing isomeric methylbenzenethiols (*para*-, *meta*-, and *ortho*-MBT) under similar size-focusing conditions. They also reported three notable examples[16–18] of ligand-exchange-induced size/structure transformation (LEIST) of Au_{25} to Au_{28}, Au_{38} to Au_{36},and Au_{144} to Au_{133} through the introduction of SR ligands with different R-groups. Furthermore, the pendant R-group on the NC surface is exposed to solutions and other phases and therefore its molecular chemistry determines the molecular-like characteristics of NCs to some extent,[19,20] such as the hydrophobicity/hydrophilicity,[21] chirality,[22,23] catalytic activity,[7,24,25] and optical properties,[26–28] interactions with the hosts.[13,14,29,30] For example, $Au_m(SR)_n$ NCs with carboxyl (−COOH) or amino ($-NH_2$) termini prefer to be hydrophilic,[21] a chiral R-group can endow chirality to NCs with achiral structures,[23] a bulky R-tail significantly promotes the surface reactivity and catalytic properties of NCs,[25] an R-group with an electron-rich atom (like N or O) can largely enhance the photoluminescence of NCs,[26]

and an R-group bearing a positive charge shows good affinity to biomaterials.[14,30] Accordingly, R-group variability on the NCs is of great importance, not only in the "survival of the fittest" of target NC formation, but also in the rational design of their functional properties and applications.

Regarding the acidity/basicity, or the R-group's (de)protonation state in solution, a variety of $Au_n(SR)_m$ NCs have been prepared using SR ligands containing neutral (e.g., 2-phenylethanethiol, benzylmercaptan, methylbenzenethiol, alkanethiols, and adamantanethiolate), acidic (e.g., mercaptocarboxylic acids, mercaptobenzoic acids, and captopril), and both acidic and basic groups (e.g., glutathione, L-cysteine, and DL-homocysteine).[1–5,31] To the best of my knowledge, only three reports have been for basic R-groups. In 2012, Au_{25} NC stabilized by 4-aminothiophenol ($HSPhNH_2$) was prepared but its molecular formula was accidentally assigned as $Au_{25}(SPhNH_2)_{17}$.[32] In 2014, Xie *et al.*[13,14,25,31] developed a NaOH-mediated $NaBH_4$ reduction method for Au_{25} NC synthesis using cystamine ($HSCH_2CH_2NH_2$). However, cystamine interacts with mercaptocarboxylic acids for stabilizing the Au_{25} NCs and therefore pure basic cystamine-capped Au_{25} was not obtained. The latest reports by Whetten *et al.*[33,34] released the earlier evidence of polydisperse captamino ($–S(CH_2)_2N(CH_3)_2$)-capped Au NCs with atom numbers ranging from 25–144. These few works seemed to confirm a statement made in 2005: “Small positively charged ligands do not support the production of MPCs in the Brust synthesis”.[19,35] However, the amino-terminated Au clusters would offer great advantages in (i) “make MPCs behave like proteins”,[33] which envisions the possibility to analyse them using modern standard techniques utilized in molecular biology developed steadily over more than a half-century, and (ii) biological applications in which the amino-moiety incorporated

on nanoparticle surface caters a long-held belief that it yields intimate interactions with the negatively charged contents. In my lab's recent works,[36–39] the modified Brust method at an optimized reduction rate could successfully synthesize Au_{25} NCs utilizing a SR ligand with the pendant quaternary-ammonium group $-[N(CH_3)_3]^+$.

Scheme 3.1 Molecular structure of 4-PyET, 2-PyET, and PET thiols used in this work.

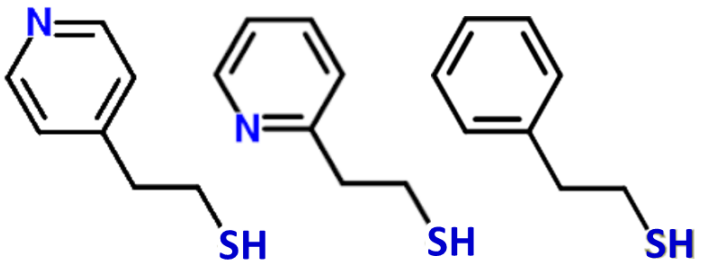

4-PyET **2-PyET** **PET**

In this work, for the first time, this chapter demonstrates that the pyridyl ethanethiol $HSCH_2CH_2C_5H_4N$ (4-PyET or 2-PyET, Scheme 3.1) can be employed in Au NC synthesis. The N center of the Py-group features a lone pair of sp^2electrons; consequently, PyET is basic, similar to the tertiary amine. In particular, I synthesized high-purity $Au_{25}(PyET)_{18}$ NCs using a typical one-pot synthetic strategy, in which synthetic yields of >~30% could be achieved for both $Au_{25}(4\text{-}PyET)_{18}$ and $Au_{25}(2\text{-}PyET)_{18}$ on the basis of Au atoms. Single crystal of $[Au_{25}(4\text{-}PyET)_{18}]^-\cdot Na^+$ could also be successfully prepared and its structure solved. Considering the remarkable achievements of their "cousin", phenyl ethanethiol (PET, Scheme 3.1), it is believed that the use of PyET will ignite the spread of synthesizing the basic metal NCs such as $Au_{38}(PyET)_{24}$, $Au_{67}(PyET)_{35}$, $Au_{144}(PyET)_{60}$, $Ag_{25}(PyET)_{18}$, and their intermetallic (alloy) variations and investigating their basic properties and utilizations. Furthermore, it had been challenging to ionize the neutral-RS capped NCs owing to the lack of

charge on such species.[40] Protonation on the PyET-capped NCs can eliminate the need for special ion-pairing agents during electrospray ionization mass spectrometry (ESI-MS) analysis, which is advantageous for soft ionization toward identification of the accurate composition of NCs.

3.2 Experimental section

3.2.1 Chemicals

Hydrogen tetrachloroaurate (III) ($HAuCl_4 \cdot 4H_2O$, >99.99%, Wako, Japan), 2-(4-pyridinyl)ethanethiol hydrochloride (4-PyET·HCl, >97%, TCI, Japan), 2-pyridyl ethylmercaptan (2-PyET, TRC, Canada), phenyl ethanethiol (PET, 99%, Wako, Japan), tetra-*n*-octylammonium bromide (TOABr, >98%, Wako, Japan), sodium borohydride ($NaBH_4$, 99%, Wako, Japan), sodium hydroxide (NaOH, >97%, Junsei, Japan), hydrochloric acid (HCl, 35−37%, Kanto, Japan), hydrogen chloride–methanol solution (HCl–MeOH, ~1.25 M, Aldrich), acetic acid (CH_3COOH, >99.7%, Junsei, Japan), deuterium chloride solution (DCl, 35 wt.% in D_2O, Aldrich) and sodium deuteroxide solution (NaOD, 40 wt.% in D_2O, Aldrich) were used as received without further purification. HPLC-grade solvents such as tetrahydrofuran (THF), methanol (MeOH), dimethylformamide (DMF), and dichloromethane (DCM) were purchased from Kanto, Japan. Deionized pure water (>18.2 MΩ) was prepared by an Organo/ELGA purelab system.

3.2.2 Synthesis and Purification of $Au_{25}(PyET)_{18}$ NCs

Solutions of $HAuCl_4$ (6.7 mM, stock solution) and 4-PyET (100.0 mM, stock solution) were separately prepared with THF and MeOH. In a typical synthesis of Au_{25}(4-PyET)$_{18}$ NCs, 8 mL of the 4-PyET solution was added dropwise into 24 mL of the

$HAuCl_4$ solution (noted the ratio of THF to MeOH was 3:1 by volume, and the ratio of 4-PyET to Au was 5:1 by mole) under stirring. The mixture changed into a light reddish turbid suspension, and then into a white turbid suspension during the addition of 4-PyET. After stirring overnight, white residues were found to stick to the inner wall of the flask (Figure S3.1a, Supporting Information). The white residues could be redispersed completely by sonication for 1 min (Figure S3.1b) to form a turbid suspension again. Then, 1.6 mL of the freshly prepared $NaBH_4$ aqueous solution (1.6 mmol, 10:1 molar ratio of $NaBH_4$ to Au, prepared by dissolving 189.2 mg of $NaBH_4$ in 5 mL of cold pure water) was rapidly added to the suspension under vigorous stirring. The color of the suspension immediately turned black, indicating the formation of Au_m NCs. After approximately 1 h of vigorous stirring, the color became slight brownish (Figure S3.1c). The stirring rate was decreased to 500 rpm and the etching process was allowed to continue for at least 48 h. During the long-time etching process, the solution color slowly changed to dark brown, which suggested that the crude polydisperse Au_m NCs were converted to monodisperse $Au_{25}(4\text{-PyET})_{18}$ NCs (Figure S3.1d).

To determine the optimized preparation of $Au_{25}(4\text{-PyET})_{18}$, I also obtained results for different volume ratios of THF to MeOH (including 0:1, 1:7, 1:3, 1:1, 7:1, and 1:0) and molar ratios of $HAuCl_4$ to 4-PyET (including 1:20, 1:10, 1:3, 1:1) as well as $HAuCl_4$ to $NaBH_4$ (including 1:50, 1:20, 1:5, and 1:2). The $Au_{25}(2\text{-PyET})_{18}$ NCs were prepared though the same synthetic strategy except that the concentrations of $HAuCl_4$ and 2-PyET solutions were changed into 1.7 mM and 25.0 mM, respectively, and the etching time was set at 10 h.

The crude sample was cleaned first by centrifugation to remove any solids. Then,

under stirring, 2 mL of aqueous HCl (375.0 mM) was rapidly added to the crude sample and the brownish precipitation was collected by centrifugation. The as-collected solid was washed by THF twice and then redissolved in 8 mL of MeOH. The insoluble particles were removed by centrifugation. In 32 mL of the aqueous NaOH solution (200.0 mM), 8 mL of the obtained Au_{25}-containing MeOH solution was added and the Au_{25} NCs then precipitated in water. Finally, the brown solid collected by centrifugation was washed by water thrice to remove impurities and polydisperse Au clusters ($[Au(PyET)]_m$). This final product, $[Au_{25}(4\text{-}PyET)_{18}]^{-}\cdot Na^{+}$ or $[Au_{25}(2\text{-}PyET)_{18}]^{-}\cdot Na^{+}$, was stored in dry form or in a DMF solution.

In addition, for comparison, $[Au_{25}(PET)_{18}]^{-}\cdot TOA^{+}$ NCs were prepared based on a method previously reported by Murray's group.[41] UV-vis absorption and negative-mode ESI-MS characterization results obtained for the $Au_{25}(PET)_{18}$ NCs are presented in Figure S3.2.

3.2.3 Crystallization and X-ray Crystallographic Determination of $Au_{25}(PyET)_{18}$ NCs

Recrystallization of $Au_{25}(PyET)_{18}$ was carried out by a vapor diffusion method. Fully deprotonated $Au_{25}(4\text{-}PyET)_{18}$ NCs were dispersed in DMF at a concentration of ~10.0 mg/mL in a 5-mL vial without a seal. The 5-mL vial containing the sample was placed in the middle of a separate 50-mL vial. Then, diethyl ether (non-solvent of NCs) was introduced into the 50-mL vial. After tightly sealing the 50-mL vial, it was kept in a refrigerator at 4 °C. After approximately 5–7 days, black belt-shaped crystals were successfully obtained and analyzed by X-ray diffraction (Figure S3.3). For comparison, $Au_{25}(PET)_{18}$ crystals were also prepared based on the previous work by Jin's group.[42] Details acquired on the crystal structure and refinement are shown in

Tables S3.1 and S3.2.

3.2.4 Protonation Reaction on $Au_{25}(PyET)_{18}$ NCs

In 3 mL aliquots of MeOH, each containing 100 μg/mL of $Au_{25}(PyET)_{18}$ NCs, 4.8, 9.6, 14.4, and 28.8 μL of the HCl–MeOH solution (500 mM) were added separately. Each batch was stirred at 300 rpm for 30 s and then subjected to UV-vis absorption characterization in a quartz cuvette with a 10-mm optical path. The reversible protonation–deprotonation process was studied in this part of the experiment by adding 9.6 μL of HCl solution and subsequently 14.4 μL of the NaOH–MeOH solution (500 mM). In NMR monitoring of the protonation, 1.0 mg of $Au_{25}(PyET)_{18}$ NCs was dissolved in 0.6 mL of methanol-d_4, and then 16 μL aliquot of the DCl-D_2O solution (50 mM) was injected step-by-step and immediately analyzed by ^{1}H-NMR. The masses for the free PyET titrations were set equal to those of PyET ligands on the surface of $Au_{25}(PyET)_{18}$ NCs (1.0 mg). The reversible protonation–deprotonation process under NMR investigation was conducted by adding 96 μL of the DCl-D_2O solution and subsequently 144 μL of the NaOD-D_2O solution (50 mM).

3.2.5 Characterization

UV-vis absorption spectra were recorded using a JASCO V-630 spectrophotometer. Electrospray-ionization mass spectrometry (ESI-MS) was performed using a Bruker DaltonicsmicrOTOF-HS mass spectrometer. The purified sample dissolved in methanol (~100 μg/mL) was directly infused at 4 mL·min^{-1}. The nebulizer pressure was set to 1.5 bar, and the sheath gas flow was set to 4.0 L/min. The dry temperature was maintained at 120 °C. The electrospray emitter potential was held at –4500 V (in the negative mode) and 4500 V (in the positive mode). The capillary exit, skimmer 1,

hexapole 1, and skimmer 2 voltages were 200, 50, 25, and 28 V, respectively. The lens 1 transfer and lens 1 pre plus storage were set at 160 and 30 μs, respectively. Thermogravimetric analysis (TGA) was undertaken on a Shimadzu DTG-60H instrument in a N_2 atmosphere (flow rate: ~100 mL min^{-1}). The obtained pure $[Au_{25}(PyET)_{18}]^{-}\cdot Na^{+}$ was put into an alumina cell, and the temperature was increased to 600 °C at a heating rate of 5 °C min^{-1}. ^{1}H-NMR and COSY analyses were performed on a JMTC-400/54/SS (JEOL) spectrometer operating at 400 MHz.

3.3 Results and discussions

3.3.1 Synthesis and Characterization of $Au_{25}(PyET)_{18}$ NCs

Synthesis of $Au_{25}(PyET)_{18}$ NCs was carried out using a technique similar to the typical synthetic strategy for preparing Au_{25} NCs[41–43] with the exception of using a THF–MeOH mixed solvent instead of the commonly used THF,[21,24,32,36–38,41,42] MeOH,[43,44] or H_2O.[13,14,31] PyET shows good solubility in H_2O and MeOH but is only slightly soluble in THF. I first attempted a series of syntheses in the single solvent H_2O, MeOH, or THF. It was seen under $NaBH_4$ injection that the use of MeOH formed Au nanoparticles immediately and H_2O led to the formation of polydisperse Au_m NCs, but failed to achieve size-focusing of Au_{25} NCs in the subsequent etching process (Figure S3.4). In contrast, the use of THF could facilitate the growth of monodisperse Au_{25} NCs but its low solubility limited the production of NCs. Based on this, I proposed use of the mixed solvent, and THF : MeOH in a volume ratio of 3:1 was found to be perform the best in terms of the kinetically controlled growth of $Au_{25}(PyET)_{18}$ NCs (Figure S3.5). Although PyET is different from PET by substitution of only one CH group by N, the solubility properties of Au_{25} NCs by the

two species were significantly different. I therefore developed a new purification strategy for $Au_{25}(PyET)_{18}$ NCs based on the protonation states of the pendant PyET ligands, as described in the Experimental Section.

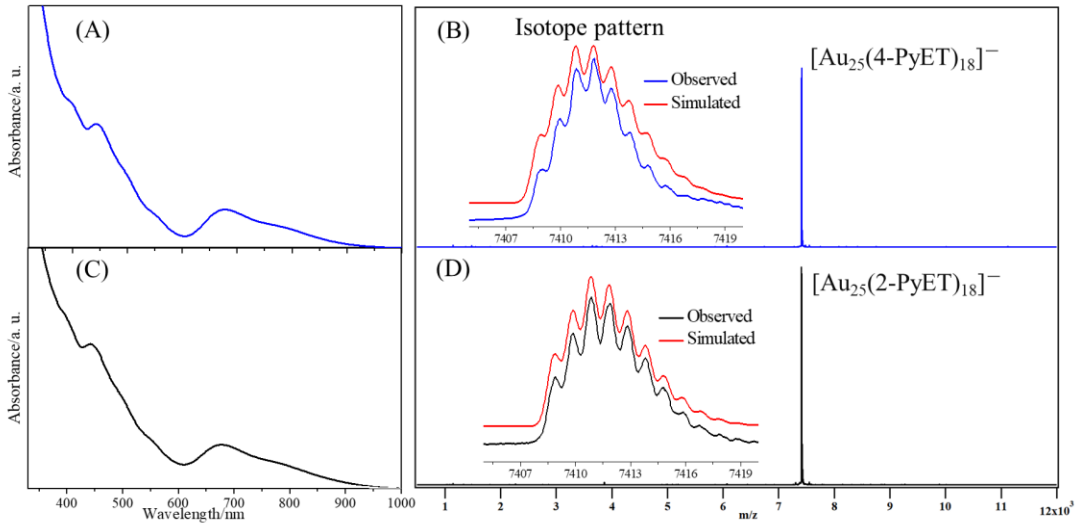

Figure 3.1 UV-vis absorption and negative-mode ESI mass spectra of purified $Au_{25}(PyET)_{18}$ NCs: (A, B) $[Au_{25}(4\text{-}PyET)_{18}]^-$ and (C, D) $[Au_{25}(2\text{-}PyET)_{18}]^-$ (The insets show corresponding isotope patterns for the observed and simulated spectra).

As shown in Figure 3.1, the UV-vis absorption spectra of the as-purified products both showed three distinct absorption bands at ~670, 450, and 400 nm and two weak absorption bands at ~560 and 780 nm (Figures 3.1A and C), which represent the typical spectroscopic fingerprints of SR-protected Au_{25} NCs with a core charge of −1 (Figure S2a).[35–43] Negative-mode ESI-MS of the purified products showed only one peak at *m/z* ~7411.97, corresponding to $[Au_{25}(PyET)_{18}]^-$, for both 4-PyET and 2-PyET. The charge state (−1) of Au_{25} NCs was confirmed by the characteristic peak separations of *m/z* ~1.00 and the molecular formula of $Au_{25}(PyET)_{18}$ was validated by matching the observed isotopic patterns with the simulated ones (Figures 3.1B and D). Moreover, the positive-mode ESI-MS of both $Au_{25}(4\text{-}PyET)_{18}$ and $Au_{25}(2\text{-}PyET)_{18}$

NCs detected predominant peaks of $[Au_{25}(PyET)_{18}Na_x]^{x-1}$ (Figure S3.6), suggesting the counterions of Au_{25} NCs should be Na^+ cations, which may coordinate strongly to pendant Py-groups via the N-atom's long pair of electrons. TGA (Figure S3.7) revealed weight losses of ~33.9% and ~33.7% for $[Au_{25}(4\text{-}PyET)_{18}]^{-}\cdot Na^+$ and $[Au_{25}(2\text{-}PyET)_{18}]^{-}\cdot Na^+$, respectively, which are both very close to the theoretical loss of 33.8%. The yields of the final $Au_{25}(4\text{-}PyET)_{18}$ and $Au_{25}(2\text{-}PyET)_{18}$ NCs were calculated to be ~30% and ~35%, respectively, on the basis of Au atom content.

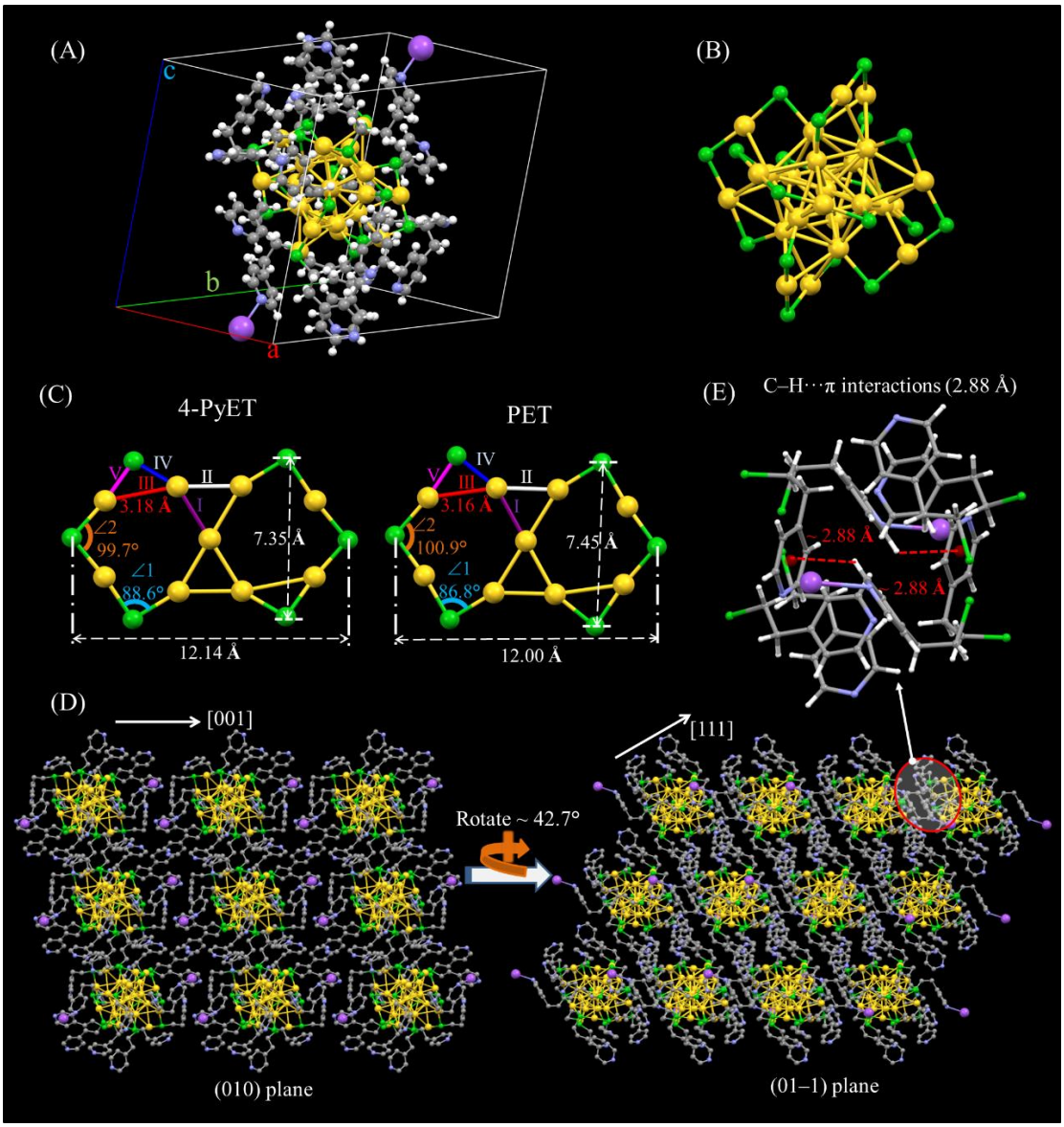

Figure 3.2 X-ray atomic structure of the $[Au_{25}(4\text{-}PyET)_{18}]^{-}\cdot Na^+$ NC: (A) overall

structure—one disordered 4-PyET ligand and solvent molecules are removed for clarity; (B) $Au_{25}S_{18}$ skeleton of $[Au_{25}(4\text{-PyET})_{18}]^{-}$; (C) Au_2S_3 staple motifs along σ_h planes of Au_{25} NCs capped by 4-PyET and PET ligands. Bond types: I, purple, core Au–core surface Au; II, white, core surface Au–core surface Au; III, red, core surface Au–motif Au; IV, blue, core surface Au–motif S; V: magenta, motif Au–motif S. Bond angles: ∠1, light blue, ∠Au-S-Au—12 S atoms connected to one stapled gold atom and one gold atom vertex; ∠2: orange, ∠Au-S-Au—6 S atoms connected to two stapled gold atoms. (D) Views of 3×3×3 superlattice along (010) and (01–1) planes; H atoms are omitted for clarity. (E) C–H···π interactions between adjacent layers; ligands are shown in wireframe mode for clarity. Legend: yellow, Au; green, S; grey, C; blue, N; white, H; magenta, Na.

3.3.2 X-Ray Crystal Structure of $Au_{25}(PyET)_{18}$ NCs

Single-crystal X-ray diffractometry (SC-XRD) measurements were acquired for $[Au_{25}(4\text{-PyET})_{18}]^{-}\cdot Na^{+}$ NCs (Figure S3.3, Table S3.1 and S3.2). Figure 3.2A depicts the overall crystal structure of the entire clusters, which is consistent with the ESI-MS formula (Figures 3.1 and S3.6), TG profile (Figure S3.7) and EDX measurement (Figure 3.3). Notably, the Na^{+} cations and core anion showed $Na^{+}\cdots$"N" ($-C_5H_5N$) interactions (2.59 Å), similar to metal ion complexation.

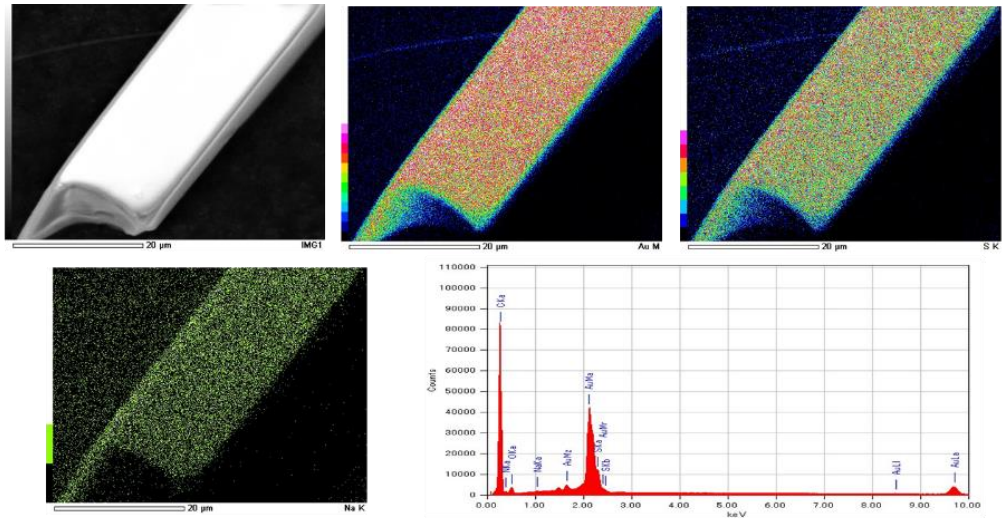

Element	Norm. At. %	Norm. At. % calculated	At. ratio	At. ratio calculated
Au	59.8	56.8	25.0	25
S	38.2	40.9	16.0	18
Na	2.0	2.3	0.83	1

Figure 3.3 Results of the EDX-measurement of $[Au_{25}(4\text{-PyET})_{18}]^{-}\cdot Na^{+}$ crystal. It showed an elemental ratio of Au : S : Na = 59.8 : 38.2 : 2.0, which is close to the calculated ratio for $[Au_{25}(4\text{-PyET})_{18}]^{-}\cdot Na^{+}$: 56.8 : 40.9 : 2.3.

The internal structure of $[Au_{25}(4\text{-PyET})_{18}]^{-}$ resembled that of previously reported $[Au_{25}(PET)_{18}]^{-}$(as suggested by Figure S3.8).[42,46] It showed an icosahedral Au_{13} kernel that was capped by six pairs of $Au_2(4\text{-PyET})_3$ staple motifs to constitute an overall core–shell configuration (Figure 3.2B). As shown in Figure 3.2C, the Au–Au distances in the Au_{13} core (bonds I and II) and the Au–S distances from the surface Au_2S_3 motifs (bonds IV and V) were almost identical regardless of the capped 4-PyET and PET ligands (Table S3.3), which could be rationalized by their analogous structures. However, the average core surface Au–motif Au distances (bond III, 3.18 Å) in $[Au_{25}(4\text{-PyET})_{18}]^{-}$ was slightly longer than that in $[Au_{25}(PET)_{18}]^{-}$ (3.16 Å). In addition, the two types of ∠Au–S–Au angles in Au_2S_3 motifs showed obvious

distinctions (∠1: 88.6° for 4-PyET against 86.8° for PET; ∠2: 99.7° for 4-PyET against 100.9° for PET). The changes led to an apparent extension of the exterior ligand shell along the σ_h planes in Au_{25}(4-PyET)$_{18}$ NCs, as suggested by the increased diameter of the core structure (9.84 Å for 4-PyET against 9.78 Å for PET; see Table S3.3 and Figure S3.9) and the expanded average distances of the paired topmost S–S (12.14 Å for 4-PyET against 12.00 Å for PET) and squeezed average distances of the paired proximal S–S (7.35 Å for 4-PyET against 7.45 Å for PET) in the Au_2(4-PyET)$_3$ motifs. It seems reasonable to conclude that these changes were in response to the alternation of counterions from TOA^+ to Na^+. The smaller Na^+ cation should offer negligible steric effects to the atomic arrangement, resulting in a more relaxed ligand shell than that neutralized by the bulky TOA^+ cation.

More interestingly, [Au_{25}(4-PyET)$_{18}$]$^-$·Na^+ clusters adopted a closest packing, and a very unique layered stacking sequence was found for its single crystal, as presented in Figure 3.2D. The ionic interactions between the Au_{25}^- core and Na^+ cations generated two zones within adjacent unit cells (along the [001] direction), similar to that in the [Au_{25}(PET)$_{18}$]$^-$·TOA^+ crystal (Figure S3.10).[42] Moreover, along the (010) plane, after every [Au_{25}(4-PyET)$_{18}$]$^-$·Na^+ species rotated clockwise (42.7°) along the b axis, the arrangement of clusters in single crystals represented that of a layered structure in the [111] direction. Intramolecularly and owing to the symmetry of overall structure (Figure 3.2A), the ligand shell also shows an inversion symmetry. The surface ligands could be divided into two groups, one of the paired Na^+-binding ligands and other sixteen of almost identical ligands that form a “ring” capping the core of cluster, as shown in Figure 3.4. Notably, the Na^+-binding ethylpyridyl thiolate substituents feature the inclination to enter its adjacent layers. As shown in Figure 3.2E and S3.11,

these layers are bonded to each other through the crosslinks of Na^{+}-binding ligands only through the C–H···π interactions (2.88 Å). Such weak bonding may result in the spacings between the ionic portions of the molecular system that is probably indicative of the crystal morphology being belt-like (Figure S3.5).

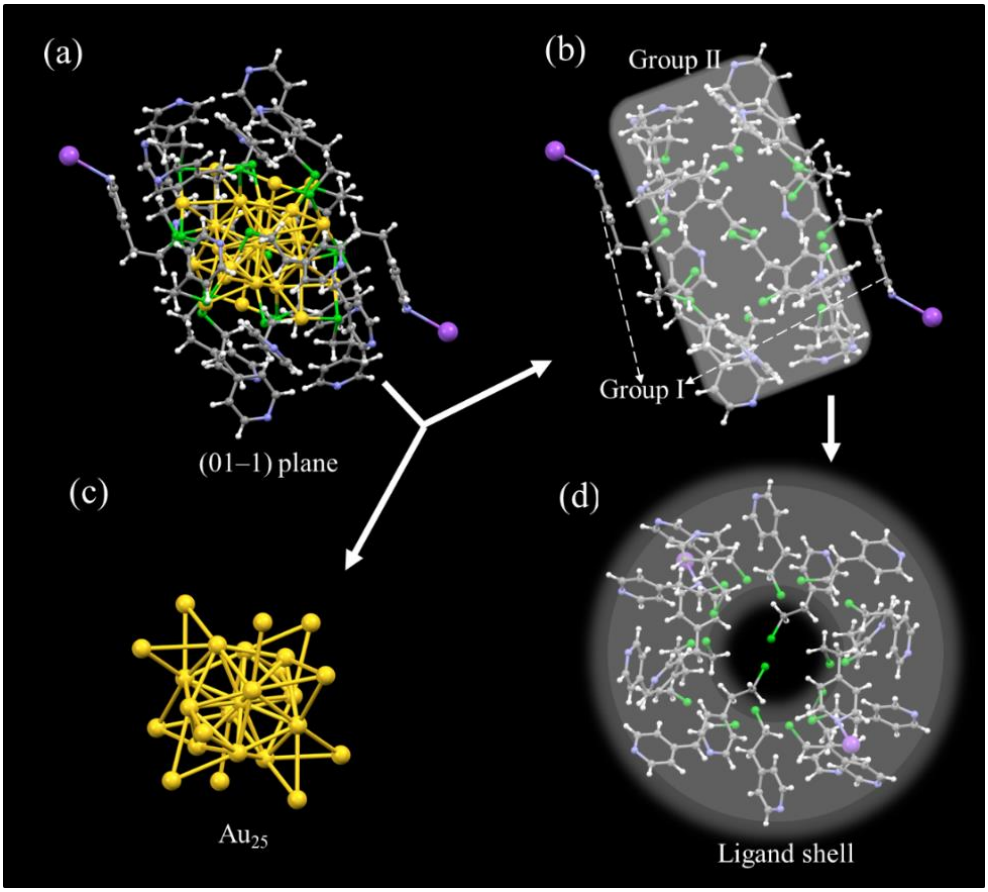

Figure 3.4 Crystal structure of $[Au_{25}(4\text{-PyET})_{18}]^{-}$ cluster: (a) the overall structure in (01–1) plane, (b) the ligand shell consisted by 18 ethylpyridyl thiolate substituents and 2 Na atoms, (c) Au_{25} consisted by Au_{13} core plus exterior 12 Au atoms, and (d) the view of ligand shell along the layered direction. Legend: yellow, Au; green, S; grey, C; blue, N; white, H; magenta, Na. It shows the ligand shell could be divided into two groups: (I) a pair of Na+-binding ethylpyridyl thiolate substituents, and (II) the other 16 ethylpyridyl thiolate substituents that forms a "ring" capping the core of cluster.

Unfortunately, I could not yet obtain the single crystal of $[Au_{25}(2\text{-PyET})_{18}]^{-}\cdot Na^{+}$ NCs. When the Au_{25} NCs were capped by 2-PyET ligands, the asymmetry of the ortho-substituted Py-group and absence of the aforementioned crosslinks between the adjacent layers probably hindered the crystallization of $[Au_{25}(2\text{-PyET})_{18}]^{-}\cdot Na^{+}$ NCs. However, based on the close similarity in optical (Figure 3.1) and NMR spectra (*vide infra*), $Au_{25}(2\text{-PyET})_{18}$ should have a similar geometric structure to that shown in Figure 3.2B.

3.3.3 Surface Protonation of $Au_{25}(PyET)_{18}$ NCs

Protonation of the Py-group gives rise to the acidic form $-C_5H_4NH^{+}$. In the case of $Au_{25}(PyET)_{18}$ NCs, the pendant Py moiety, peripherally exposed to the solution, should also show the protonation characteristics, as depicted by reaction (1). In the $[Au_{25}(4\text{-PyET})_{18}]^{-}$–MeOH solution, different amounts of the HCl–MeOH solution (500 mM) were added (see the Experimental section) and the process was first monitored using UV-vis absorption (Figure 3.5). The intensities of the peaks at ~400 and 560 nm showed a slight increase whereas the peaks at ~450, 670, and 780 nm showed a slight decrease in intensity on protonation. Such absorption changes were also observed when the $Au_{25}(2\text{-PyET})_{18}$ clusters were treated with H^{+} except that the amount of HCl required for complete protonation of $[Au_{25}(2\text{-PyET})_{18}]^{-}$ clusters (9.6 μL, Figure S3.14) was lower than that for $[Au_{25}(4\text{-PyET})_{18}]^{-}$ clusters (14.4 μL, Figure 3.2). In addition, $[Au_{25}(PyET)_{18-x}(PyET\cdot H^{+})_x]^{x-1}$ (x = 2−4, Figure S3.13) was detected in the $Au_{25}(4\text{-PyET})_{18}$ sample when HCl was added. These spectral changes reveal that $Au_{25}(PyET)_{18}$ NCs can conjugate with H^{+} through the pendant Py moiety, similar to the pyridine molecule.

$$Au_{25}(PyET)_{18} + x\ H^{+} \leftrightharpoons Au_{25}(PyET)_{18-x}(PyET\cdot H^{+})_x\ (0 \leq x \leq 18) \qquad (1)$$

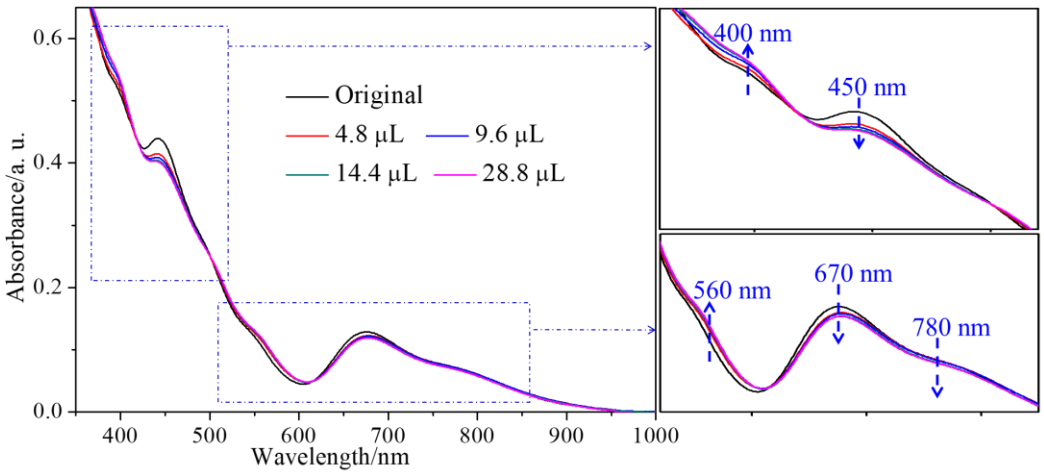

Figure 3.5 UV-vis absorption results obtained for $Au_{25}(4\text{-PyET})_{18}$ in MeOH on addition of methanolic HCl (500 mM). The red arrows denote isosbestic points and the blue arrows denote changes during the protonation.

Inspired by the ^{1}H-NMR titration of heterocyclic bases,[47] I further monitored the protonation reaction in $Au_{25}(PyET)_{18}$ NCs by NMR chemical shifts. The NMR titration results acquired for the free 4-PyET and 2-PyET are shown in Figures S3.14−3.16 and Table S3.4. As shown in Figure S3.16, the proton signals of the Py moiety shifted more upfield upon titration by DCl. The H^+-binding affinity of free 4-PyET was weaker than that of free 2-PyET, as indicated by their critical H^+ concentrations (~6.6 × 10^{-3} M for 4-PyET against ~4.8 × 10^{-3} M for 2-PyET for complete protonation; Table 3.1, entries 1–2). These data demonstrate that not only the NMR shifts but also H^+-binding activities are affected by the relative position of the N center in Py-groups. Below, I discuss the ^{1}H-NMR titration of two types of PyET-capped Au_{25} NCs.

Table 3.1 Critical D^+ concentrations and molar ratios of PyET to D^+ when PyETs were fully protonated in methanol. The data collected are shown in Figures 3.5 and S3.16.[a]

Species	Critical DCl amount (μL)	Critical D^+ concentration (M)
Free 4-PyET	~ 92	~ 6.6×10^{-3}
Free 2-PyET	~ 64	~ 4.8×10^{-3}
Au_{25}(4-PyET)$_{18}$	~ 150	~ 10.1×10^{-3}
Au_{25}(2-PyET)$_{18}$	~ 130	~ 8.9×10^{-3}

[a]*The masses for titrations of free PyET ligands were same as the corresponding PyET on Au_{25}(PyET)$_{18}$ surfaces.*

As discussed above, the structure of the Au_{25}(PyET)$_{18}$ NCs consisted of an icosahedral Au_{13} kernel and six Au_2(PyET)$_3$ motifs (Figure 3.2).Therefore, there were two different chemical environments for the 18 PyET ligands, i.e., the inner ligands and outer ligands that were present in a ratio of 2:1 (Figure 3.6A).[48,49] This structure could also be confirmed by the ^{1}H-^{1}H COSY spectra of the methylene moieties (α-CH_2, β-CH_2) of the pendant PyET ligands, as shown in Figures S3.17 and S3.18. ^{1}H-NMR titration of Au_{25}(PyET)$_{18}$ was conducted by adding a 16 μL aliquot of DCl-D_2O (50 mM) into 0.6 mL of methanol-d_4 containing 1.0 mg of Au_{25} NCs. Here, we focused on the region of the Py moiety ($-C_5H_4N$) in the NMR spectra, as shown in Figures 3.6B and C (see the full ranges in Figure S3.19). Under DCl titration, the proton peaks in the $-C_5H_4N\cdots H^+$ group shifted further upfield compared to those of the original NCs in both 4-PyET- and 2-PyET-capped NCs (see the detailed assignments in Table S3.5), similar to those of the free PyET (Figure S3.14). These

results further verified the protonation process via reaction (1): thus, ^{1}H-NMR could be used to visually detect the process.

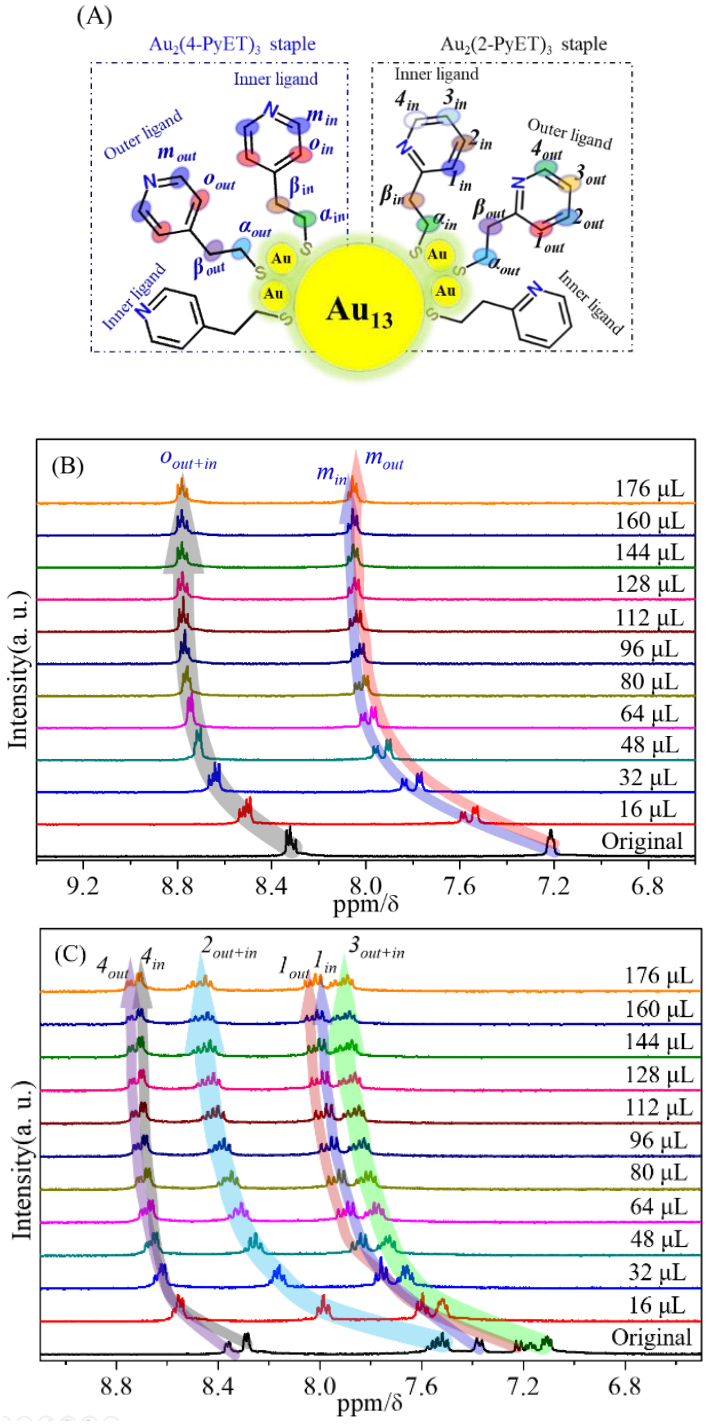

Figure 3.6 Schematic (A) of the dimeric staples (Au_2PyET_3) on $Au_{25}(PyET)_{18}$ surface; ^{1}H-NMR spectra of the Py protons in (B) $Au_{25}(4\text{-}PyET)_{18}$; (C) $Au_{25}(2\text{-}PyET)_{18}$ on addition of DCl-D_2O (50 mM), acquired in methanol-d_4.

The chemical shifts (δ) of pendant Py protons are summarized in Figure 3.7, which shows that the peak changes depended on the degree of protonation, same as the heterocyclic bases.[45] It is worth noting that the D^+-binding affinity for Au_{25}(4-PyET)$_{18}$ NCs (critical D^+ concentration: ~10.1×10^{-3} M; Table 3.1, entry 3) is weaker than that for Au_{25}(2-PyET)$_{18}$ NCs (~8.9×10^{-3} M; Table 3.1, entry 4). This corresponds well to the trend noted in the binding affinities between the free PyET species and HCl amounts of complete protonation in UV-vis monitoring (14.4 μL for Au_{25}(4-PyET)$_{18}$ against 9.6 μL for Au_{25}(2-PyET)$_{18}$; Figures 3.3 and S3.12). Moreover, the H^+-binding affinities for Au_{25} NCs were clearly weaker than those of free PyET, which is understandable since the Au_{25} NCs resembled a more rigid macromolecule than the free PyET.[50] In addition, the protons of outer ligands exhibited faster changes than the inner ones, which is ascribed to them being more easily accessible to the external environment.

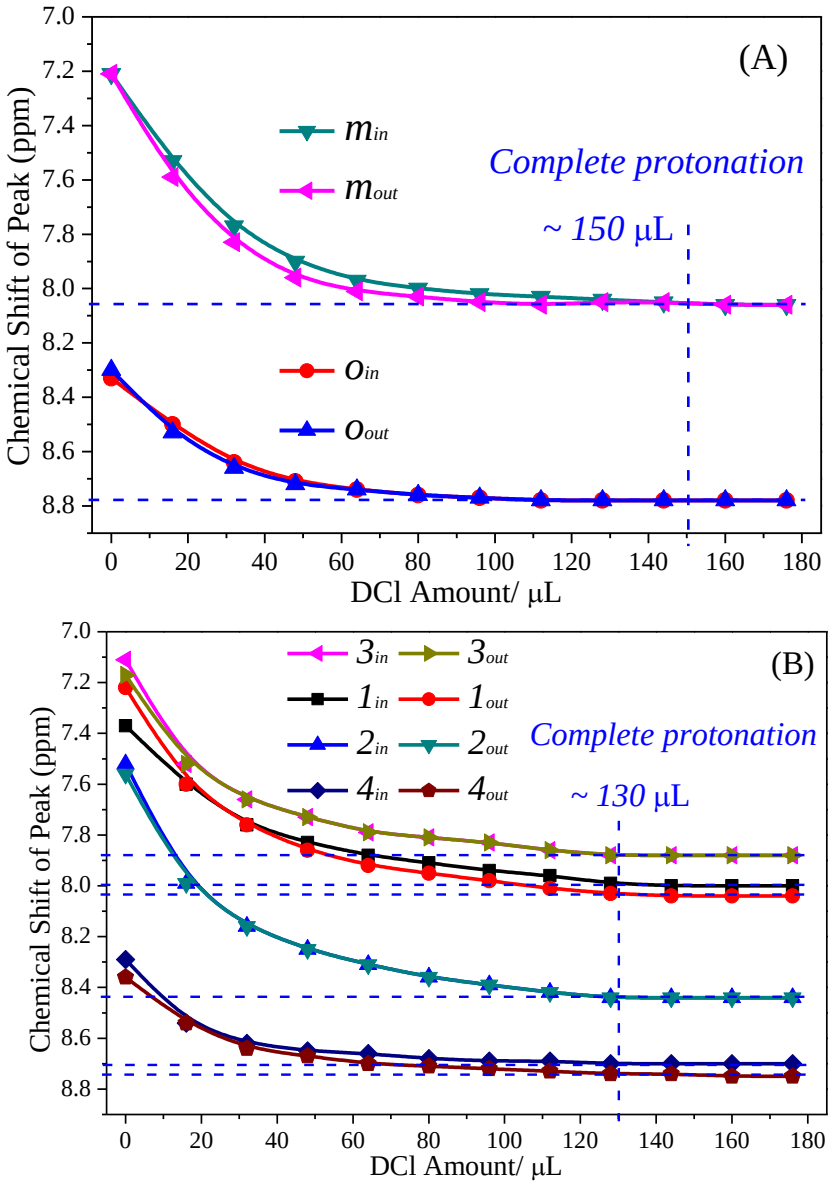

Figure 3.7 ^{1}H-NMR chemical shifts in ppm for Py protons in (A) Au_{25}(4-PyET)$_{18}$ and (B) Au_{25}(2-PyET)$_{18}$ as a function of amount of DCl.

Finally, the UV-vis absorption and ^{1}H-NMR changes observed for the Au_{25}(PyET)$_{18}$ NCs were found to be completely reversible when the spectra of the protonated NCs reverted to their original patterns upon neutralization of the solution on the addition of a base such as NaOH or NaOD, as shown in Figure S3.20. Furthermore, depending on the protonation–deprotonation equilibrium, the Au_{25}(PyET)$_{18}$ NCs unexpectedly

showed tunable solubility in aqueous and some organic solvents, as summarized in Table S3.6. As an example, as demonstrated in Figure 3.8, deprotonated Au_{25}(2-PyET)$_{18}$ NCs were soluble in DCM but insoluble in H_2O; on the addition of aqueous HCl, the protonated NCs transferred to the H_2O phase. When further aqueous NaOH was added, it deprotonated the Py moiety and resulted in reversible transfer to the DCM phase.

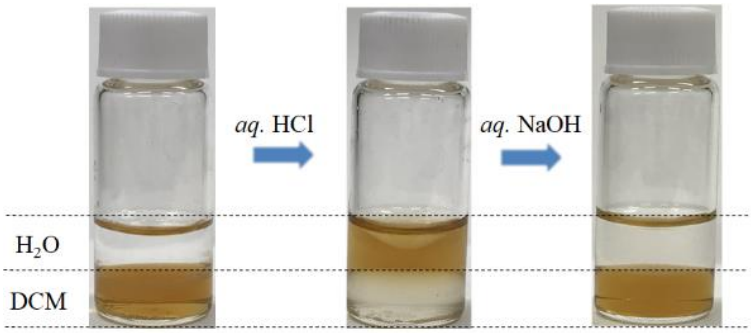

Figure 3.8 Transfer noted for Au_{25}(2-PyET)$_{18}$ NCs between aqueous and organic (DCM, dichloromethane) media through protonation–deprotonation process.

3.4 Conclusions

High-purity $Au_{25}(SCH_2CH_2Py)_{18}$ NCs protected by a basic pyridyl–thiolate ligand were successfully synthesized for the first time. ESI-MS, single-crystal XRD, and ^{1}H-^{1}H COSY characterization indicated that the $[Au_{25}(PyET)_{18}]^-\cdot Na^+$ NCs possessed a typical core–shell configuration but the Na^+ counterion resulted in apparent extension of the exterior ligand shell and a layered crystallographic arrangement in the $[Au_{25}$(4-PyET)$_{18}]^-\cdot Na^+$ crystal. UV-vis absorption and ^{1}H-NMR results verified that Au_{25}(PyET)$_{18}$ NCs can conjugate to H^+ through the pendant Py moiety, similar to a heterocyclic base. The H^+-binding affinity of Au_{25}(2-PyET)$_{18}$ NCs was higher than that of Au_{25}(4-PyET)$_{18}$ NCs, and both showed significantly lower H^+-binding affinity

than their corresponding free PyET thiols. On controlling the H^+ involvement, $Au_{25}(PyET)_{18}$ NCs showed reversible solubility in aqueous and some organic solvents. This paper, therefore, proposes a new family of basic Au_{25} nanomolecules that may also behave like proteins, which envisions the possibility to analyze them using modern standard techniques utilized in molecular biology developed steadily over more than a half-century.

3.5 References

(1) Jin, R.; Zeng, C.; Zhou, M.; Chen, Y. Atomically Precise Colloidal Metal Nanoclusters and Nanoparticles: Fundamentals and Opportunities. *Chem. Rev.* **2016**, *116*, 10346–10413.

(2) Chakraborty, I.; Pradeep, T. Atomically Precise Clusters of Noble Metals: Emerging Link between Atoms and Nanoparticles. *Chem. Rev.* **2017**, *117*, 8208–8271.

(3) Hossain, S.; Niihori, Y.; Nair, L. V.; Kumar, B.; Kurashige, W.; Negishi, Y. Alloy Clusters: Precise Synthesis and Mixing Effects. *Acc. Chem. Res.* **2018**, *51*, 3114–3124.

(4) Cook, A. W.; Hayton, T. W. Case Studies in Nanocluster Synthesis and Characterization: Challenges and Opportunities. *Acc. Chem. Res.* **2018**, *51*, 2456–2464.

(5) Tsukuda, T.; Hakkinen, H. *Protected Metal Clusters: From Fundamental to Applications*; Elsevier: Amsterdam, **2015**.

(6) Li, G.; Jin, R. Atomically Precise Gold Nanoclusters as New Model Catalysts. *Acc. Chem. Res.* **2013**, *46*, 1749–1758.

(7) Wan, X. K.; Wang, J. Q.; Nan, Z. A.; Wang, Q. M. Ligand Effects in Catalysis by Atomically Precise Gold Nanoclusters. *Sci. Adv.* **2017**, *3*, e1701823.

(8) Li, G.; Abroshan, H.; Liu, C.; Zhuo, S.; Li, Z.; Xie, Y.; Kim, H. J.; Rosi, N. L.; Jin, R. Tailoring the Electronic and Catalytic Properties of Au_{25} Nanoclusters via Ligand Engineering. *ACS Nano* **2016**, *10*, 7998–8005.

(9) Guan, G.; Zhang, S. Y.; Cai, Y.; Liu, S.; Bharathi, M. S.; Low, M.; Yu, Y.; Xie, J.; Zheng, Y.; Zhang, Y. W., Han, M. Y. Convenient Purification of Gold Clusters by

Co-Precipitation for Improved Sensing of Hydrogen Peroxide, Mercury Ions and Pesticides. *Chem. Commun.* **2014**, *50*, 5703–5705.

(10) Shen, R., Liu, P., Zhang, Y., Yu, Z., Chen, X., Zhou, L., Nie, B.; Żaczek, A.; Chen, J; Liu, J. Sensitive Detection of Single-cell Secreted H_2O_2 by Integrating a Microfluidic Droplet Sensor and Au Nanoclusters. *Anal. Chem.* **2018**, *90*, 4478–4484.

(11) Teng, Y.; Jia, X.; Li, J.; Wang, E. Ratiometric Fluorescence Detection of Tyrosinase Activity and Dopamine using Thiolate-protected Gold Nanoclusters. *Anal. Chem.* **2015**, *87*, 4897–4902.

(12) Polavarapu, L.; Manna, M.; Xu, Q. H. Biocompatible Glutathione Capped Gold Clusters as One−and Two−PhotonExcitation Fluorescence Contrast Agents for Live Cells Imaging. *Nanoscale* **2011**, *3*, 429–434.

(13) Zheng, K.; Setyawati, M. I.; Leong, D. T.; Xie, J. Surface Ligand Chemistry of Gold Nanoclusters Determines Their Antimicrobial Ability. *Chem. Mater.* **2018**, 30, 2800–2808.

(14) Zheng, K.; Setyawati, M. I.; Leong, D. T.; Xie, J. Antimicrobial Gold Nanoclusters. *ACS Nano* **2017**, 11, 6904–6910.

(15) Chen, Y.; Zeng, C.; Kauffman, D. R.; Jin, R. Tuning the Magic Size of Atomically Precise Gold Nanoclusters via Isomeric Methylbenzenethiols. *Nano Lett.* **2015**, *15*, 3603–3609.

(16) Zeng, C.; Li, T.; Das, A.; Rosi, N. L.; Jin, R. Chiral Structure of Thiolate-Protected 28-Gold-Atom Nanocluster Determined by X-ray Crystallography. *J. Am. Chem. Soc.* **2013**, *135*, 10011–10013.

(17) Zeng, C.; Liu, C.; Pei, Y.; Jin, R. Thiol Ligand-Induced Transformation of $Au_{38}(SC_2H_4Ph)_{24}$ to $Au_{36}(SPh\text{-}t\text{-}Bu)_{24}$. *ACS Nano* **2013**, *7*, 6138–6145.

(18) Zeng, C.; Chen, Y.; Kirschbaum, K.; Appavoo, K.; Sfeir, M. Y.; Jin, R.

Structural Patterns at All Scales in a Nonmetallic Chiral $Au_{133}(SR)_{52}$ Nanoparticle. *Sci. Adv.* **2015**, *1*, e1500045.

(19) Yan, J.; Teo, B. K.; Zheng, N. Surface Chemistry of Atomically Precise Coinage–Metal Nanoclusters: From Structural Control to Surface Reactivity and Catalysis. *Acc. Chem. Res.* **2018**, *51*, 3084–3093.

(20) Higaki, T.; Li, Q.; Zhou, M.; Zhao, S.; Li, Y., Li, S.; Jin, R. Toward the Tailoring Chemistry of Metal Nanoclusters for Enhancing Functionalities. *Acc. Chem. Res.* **2018**, *51*, 2764–2773.

(21) Ackerson, C. J.; Jadzinsky, P. D.; Kornberg, R. D. Thiolate Ligands for Synthesis of Water-Soluble Gold Clusters. *J. Am. Chem. Soc.* **2005**, 127, 6550–6551.

(22) Knoppe, S.; Bürgi, T. Chirality in Thiolate-protected Gold Clusters. *Acc. Chem. Res.* **2014**, *47*, 1318–1326.

(23) Wu, Z.; Gayathri, C.; Gil, R. R.; Jin, R. Probing the Structure and Charge State of Glutathione-Capped $Au_{25}(SG)_{18}$ Clusters by NMR and Mass Spectrometry. *J. Am. Chem. Soc.* **2009**, *131*, 6535–6542.

(24) Yang, H.; Wang, Y.; Lei, J.; Shi, L.; Wu, X.; Makinen, V.; Lin, S.; Tang, Z.; He, J.; Hakkinen, H.; Zheng, L.; Zheng, N. Ligand-Stabilized $Au_{13}Cu_x$ (x = 2, 4, 8) Bimetallic Nanoclusters: Ligand Engineering to Control the Exposure of Metal Sites. *J. Am. Chem. Soc.* **2013**, *135*, 9568–9571.

(25) Yan, J. Z.; Zhang, J.; Chen, X. M.; Malola, S.; Zhou, B.; Selenius, E.; Zhang, X. M.; Yuan, P.; Deng, G. C.; Liu, K. L.; Su, H. F.; Teo, B. K.; Hakkinen, H.; Zheng, L. S.; Zheng, N. F. Thiol-Stabilized Atomically Precise, Superatomic Silver Nanoparticles for CatalyzingCycloisomerization of Alkynyl Amines. *Natl. Sci. Rev.* **2018**, *5*, 694–702.

(26) Wu, Z., Jin, R. On the Ligand's Role in the Fluorescence of Gold Nanoclusters. *Nano Lett.* **2010**, *10*, 2568–2573.

(27) Yuan, X.; Goswami, N.; Chen, W.; Yao, Q.; Xie, J. Insights into the Effect of Surface Ligands on the Optical Properties of Thiolated Au_{25} Nanoclusters. *Chem. Commun.* **2016**, *52*, 5234–5237.

(28) Kang, X.; Zhu, M. Tailoring the Photoluminescence of Atomically Precise Nanoclusters. *Chem. Soc. Rev*. **2019**, *48*, 2422–2457.

(29) Lavenn, C.; Demessence, A.; Tuel, A. Atomically Well-defined $Au_{25}(SR)_{17/18}$ Nanoclusters Deposited on Silica Supports for the Aerobic Epoxidation of Trans-stilbene. *Catal. Today* **2014**, *235*, 72–78.

(30) Ackerson, C. J.; Jadzinsky, P. D.; Jensen, G. J.; Kornberg, R. D. Rigid, Specific, and Discrete Gold Nanoparticle/antibody Conjugates. *J. Am. Chem. Soc.* **2006**, *128*, 2635–2640.

(31) Yuan, X.; Zhang, B.; Luo, Z.; Yao, Q.; Leong, D. T.; Yan, N.; Xie, J. Balancing the Rate of Cluster Growth and Etching for Gram-scale Synthesis of Thiolate-protected Au_{25} Nanoclusters with Atomic Precision. *Angew. Chem., Int. Ed.* **2014**, *53*, 4623–4627.

(32) Lavenn, C.; Albrieux, F.; Bergeret, G.; Chiriac, R.; Delichere, P.; Tuel, A.; Demessence, A. Functionalized Gold Magic Clusters: $Au_{25}(SPhNH_2)_{17}$. *Nanoscale* **2012**. *4*, 7334–7337.

(33) Hoque, M. M.; Black, D. M.; Mayer, K. M.; Dass, A.; Whetten, R. L. The Base Side of Noble Metal Clusters: Efficient Route to Captamino-Gold, $Au_n(-S(CH_2)_2N(CH_3)_2)_p$, n= 25–144. *J. Phys. Chem. Lett.* **2019**, *10*, 3307–3311;

(34) Hoque, M. M.; Dass, A.; Mayer, K. M.; Whetten, R. L. Protein-like Large Gold Clusters Based on the ω-Amino-Thiolate DMAET: Precision Thermal and

Reaction Control Leads to Selective Formation of Cationic Gold Clusters in the Critical Size Range, n= 130–144 Au Atoms. *J. Phys. Chem. C* **2019**, 123, 14871–14879.

(35) Brust, M.; Walker, M.; Bethell, D.; Schiffrin, D. J.; Whyman, R. Synthesis of Thiol-Derivatised Gold Nanoparticles in a Two-phase Liquid-Liquid System. *J. Chem. Soc., Chem. Commun.* **1994**, 7, 801–802.

(36) Ishida, Y.; Narita, K.; Yonezawa, T.; Whetten, R. L. Fully Cationized Gold Clusters: Synthesis of $Au_{25}(SR^{+})_{18}$. *J. Phys. Chem. Lett.* **2016**, *7*, 3718–3722.

(37) Ishida, Y.; Huang, Y. L.; Yonezawa, T.; Narita, K. Charge Neutralization Strategy: A Novel Synthetic Approach to Fully Cationized Thiolate−Protected $Au_{25}(SR^{+})_{18}$ Clusters with Atomic Precision. *ChemNanoMat* **2017**, *3*, 298−302.

(38) Huang, Z.; Ishida, Y.; Narita, K; Yonezawa, T. Kinetics of Cationic-Ligand-Exchange Reactions in Au_{25} Nanoclusters. *J. Phys. Chem. C* **2018**, *122*, 18142−18150.

(39) Ishida, Y.; Corpuz, R. D.; Yonezawa, T. Matrix Sputtering Method: A Novel Physical Approach for Photoluminescent Noble Metal Nanoclusters. *Acc. Chem. Res.* **2017**, *50*, 2986–2995.

(40) Kumara, C.; Hoque, M. M.; Zuo, X.; Cullen, D. A.; Whetten, R. L.; Dass, A., Isolation of a 300 kDa, Au∼1400 Gold Compound, the Standard 3.6 nm Capstone to a Series of Plasmonic Nanocrystals Protected by Aliphatic-like Thiolates. *J. Phys. Chem. Lett.* **2018,** *9*, 6825–6832.

(41) Parker, J. F.; Weaver, J. E.; McCallum, F.; Fields−Zinna, C. A.; Murray, R. W. Synthesis of Monodisperse $[Oct_4N^{+}][Au_{25}(SR)_{18}^{-}]$ Nanoparticles, with Some Mechanistic Observations. *Langmuir* **2010**, *26*, 13650−13654.

(42) Zhu, M.; Aikens, C. M.; Hollander, F. J.; Schatz, G. C.; Jin, R. Correlating the Crystal Structure of a Thiol-Protected Au_{25} Cluster and Optical Properties. *J. Am. Chem. Soc.* **2008**, *130*, 5883−5885.

(43) Kumar, S.; Jin, R. Water-soluble $Au_{25}(Capt)_{18}$ Nanoclusters: Synthesis, Thermal Stability, and Optical Properties. *Nanoscale* **2012**, *4*, 4222−4227.

(44) Negishi, Y.; Nobusada, K.; Tsukuda, T. Glutathione-protected Gold Clusters Revisited: Bridging the Gap between Gold (I)−thiolate Vomplexes and Thiolate-protected Gold Nanocrystals. *J. Am. Chem. Soc.* **2005**, *127*, 5261−5270.

(45) Hancock, R. D. The Pyridyl Group in Ligand Design for Selective Metal Ion Complexation and Sensing. *Chem. Soc. Rev.* **2013**, *42*, 1500−1524.

(46) Heaven, M. W.; Dass, A.; White, P. S.; Holt, K. M.; Murray, R. W. Crystal Structure of the Gold Nanoparticle $[N(C_8H_{17})_4][Au_{25}(SCH_2CH_2Ph)_{18}]$. *J. Am. Chem. Soc.* **2008**, *130*, 3754−3755.

(47) Gift, A. D.; Stewart, S. M.; KweteBokashanga, P. Experimental Determination of pK_a Values by Use of NMR Chemical Shifts, Revisited. *J. Chem. Educ.* **2012**, *89*, 1458−1460.

(48)Venzo, A.; Antonello, S.; Gascón, J. A.; Guryanov, I.; Leapman, R. D.; Perera, N. V.; Sousa, A; Zamuner, M.; Zanella, A.; Maran, F. Effect of the Charge State (z= −1, 0, + 1) on the Nuclear Magnetic Resonance of Monodisperse $Au_{25}[S(CH_2)_2Ph]_{18}^z$ Clusters. *Anal. Chem.* **2011**, *83*, 6355−6362

(49) Qian, H.; Zhu, M.; Gayathri, C.; Gil, R. R.; Jin, R. Chirality in Gold Nanoclusters Probed by NMR Spectroscopy. *ACS Nano* **2011**, *5*, 8935−8942.

(50) Koivisto, J.; Chen, X.; Donnini, S.; Lahtinen, T.; Häkkinen, H.; Groenhof, G.; Pettersson, M. Acid–Base Properties and Surface Charge Distribution of the Water-Soluble Au_{102}(*p*MBA)$_{44}$ Nanocluster. *J. Phys. Chem. C* **2016**, *120*, 10041−10050.

Appendix II: Supporting Information

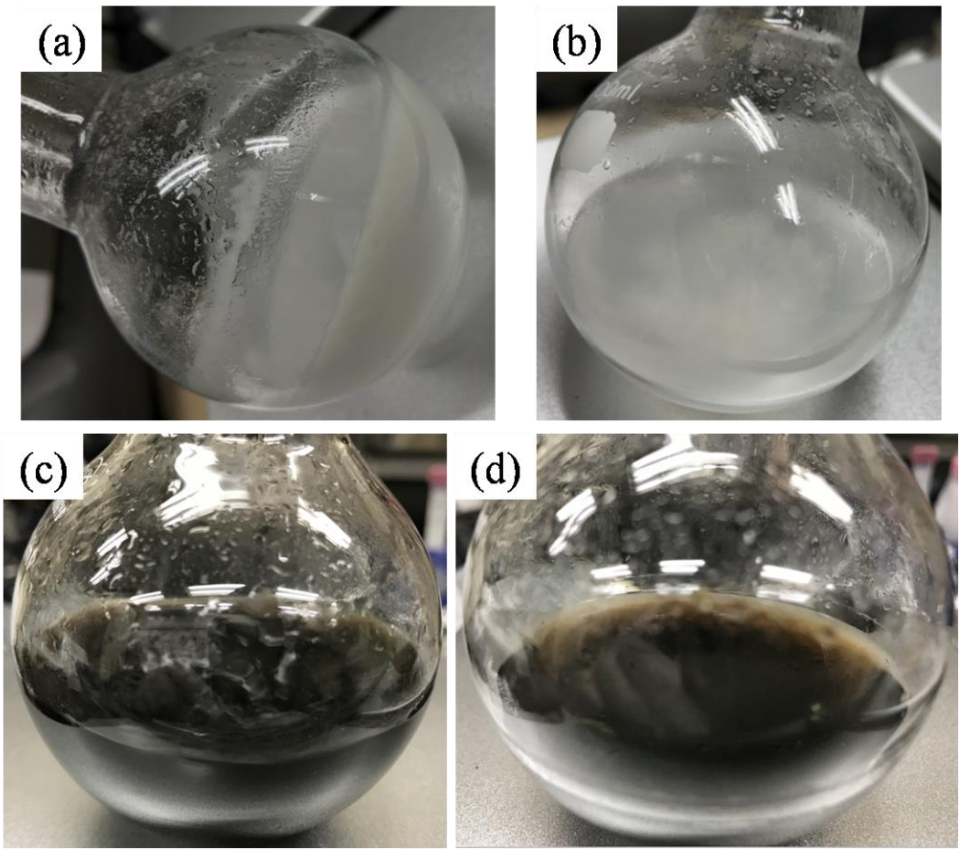

Figure S3.1 Pictures on the $Au_{25}(4\text{-PyET})_{18}$ synthesis process: (a) after overnight stirring for forming Au(I)-4-PyET precursor; (b) after sonication; (c) after 1 h etching; (d) after 48 h etching.

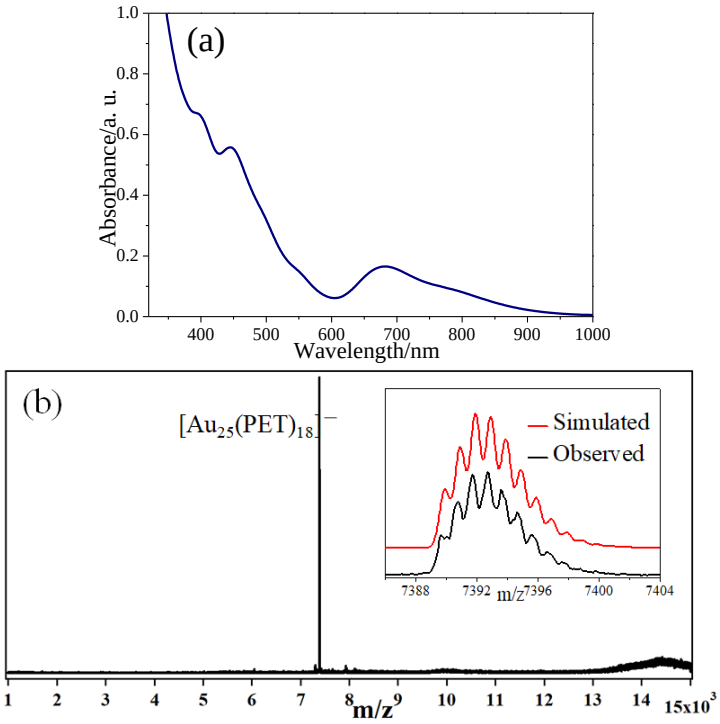

Figure S3.2 UV-vis absorption (a) and negative-mode ESI mass spectra (b) of the $Au_{25}(PET)_{18}$ NCs.

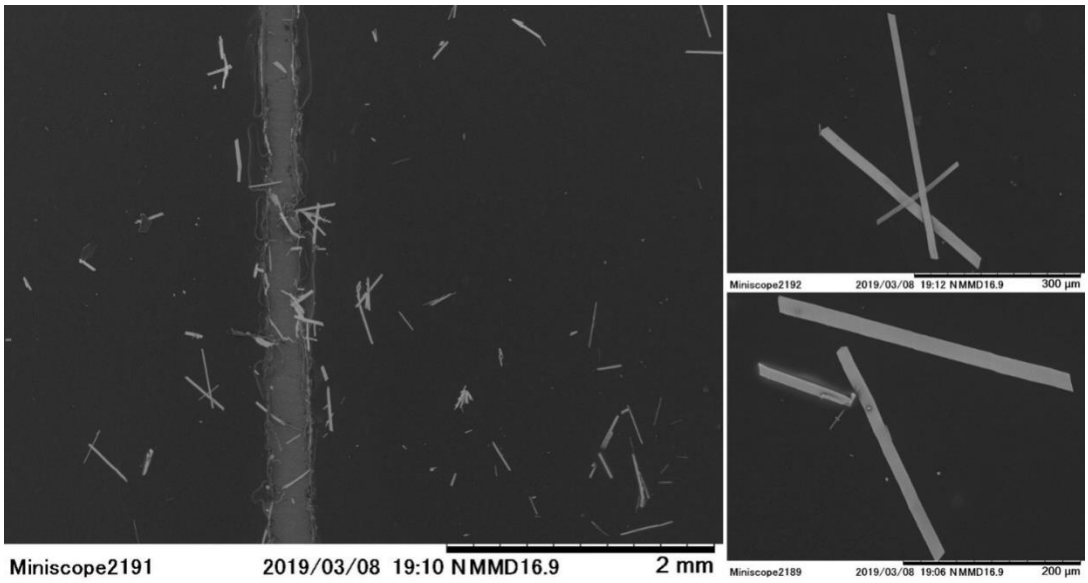

Figure S3.3 SEM images of the $[Au_{25}(4\text{-}PyET)_{18}]^{-}\cdot Na^{+}$ crystals.

Table S3.1 Crystal data for Au_{25} NCs.

	$[Au_{25}(4\text{-}PyET)_{18}]^{-}\cdot Na^{+}$	**$[Au_{25}(PET)_{18}]^{-}\cdot TOA^{+}$**
Identification code	data_190405_a	data_190407_a
Empirical formula	$C_{132}H_{158}Au_{25}N_{20}NaS_{18}O_8$[a]	$C_{176}H_{162}Au_{25}NS_{18}$
Formula weight	7677.11	7792.41
Temperature/K	93(2)	93(2)
Crystal system	triclinic	triclinic
Space group	P-1	P-1
a/Å	14.4996(2)	16.0981(2)
b/Å	17.7915(3)	17.3143(3)
c/Å	19.0270(4)	18.5804(3)
α/°	85.449(2)	106.300(1)
β/°	77.874(1)	105.488(1)
γ/°	68.233(1)	90.953(1)
Volume/Å^3	4456.71(14)	4766.66(13)
Z	2	2
D_{calc}	2.848	2.715
m/mm^{-1}	20.743	19.389
F(000)	3412.0	3488.0
Crystal color, habit	black, belt	black, needle
Crystal size/mm^3	0.005×0.02×0.1	0.05×0.1×0.2

[a]*Solvent molecules (DMF: $(CH_3)_2NC(O)H$×2; H_2O×6: with H atoms omitting) are involved in the lattice spaces of $[Au_{25}(4\text{-}PyET)_{18}]^{-}\cdot Na^{+}$ crystals.*

Table S3.2 Intensity measurements and structure refinements for Au_{25} NCs.

	$[Au_{25}(4\text{-}PyET)_{18}]^{-}\cdot Na^{+}$	**$[Au_{25}(PET)_{18}]^{-}\cdot TOA^{+}$**
Device	Rigaku VariMax Saturn	
Radiation	Mo Kα (λ = 0.71075)	
Data collection	RIGAKU CrystalClear	
2 range for data collection/°	2.092 to 29.999	1.7840 to 31.0780
Index ranges	-20 ≤ h ≤ 20, -25 ≤ k ≤ 19, -26 ≤ l ≤ 26	-22 ≤ h ≤ 22, -24 ≤ k ≤ 23, -21 ≤ l ≤ 25
Reflections collected	42372	45441
Independent reflection	23712 [R_{int}= 0.0227,R_{sigma}= 0.0330]	25390 [R_{int}= 0.0412, R_{sigma}= 0.0571]
Data/restraints/parameters	23712/430/1047	25390/1579/1094
Goodness-of-fit on F2	1.0447	1.0240
Final *R* indexes [I>=2σ (I)]	*R1* = 0.0299, *wR2* = 0.0739	*R1* = 0.0381, *wR2* = 0.0888
Final *R* indexes [all data]	*R1* = 0.0375, wR_2= 0.0779	*R1* = 0.0551, wR_2= 0.1056
Absorption corrections	multi-scan, 0.22536 to 1.00000	multi-scan, 0.56344 to 1.00000

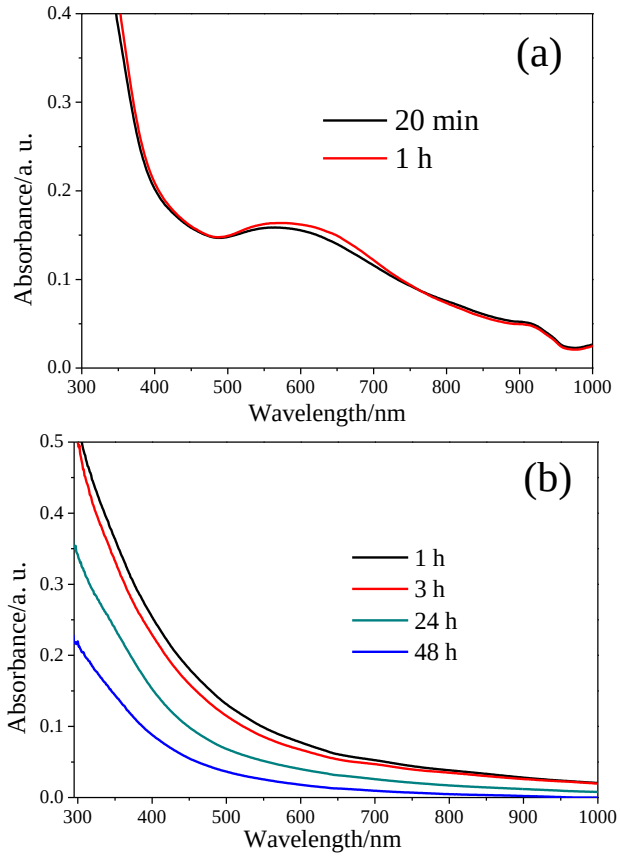

Figure S3.4 UV-vis absorption monitoring of the etching process of 4-PyET-protected Au_m NCs in: (a) H_2O solvent; (b) MeOH solvent (the molar ratios of $HAuCl_4$ to 4-PyET and $HAuCl_4$ to $NaBH_4$ were set at 1:5 and 1:10, respectively).

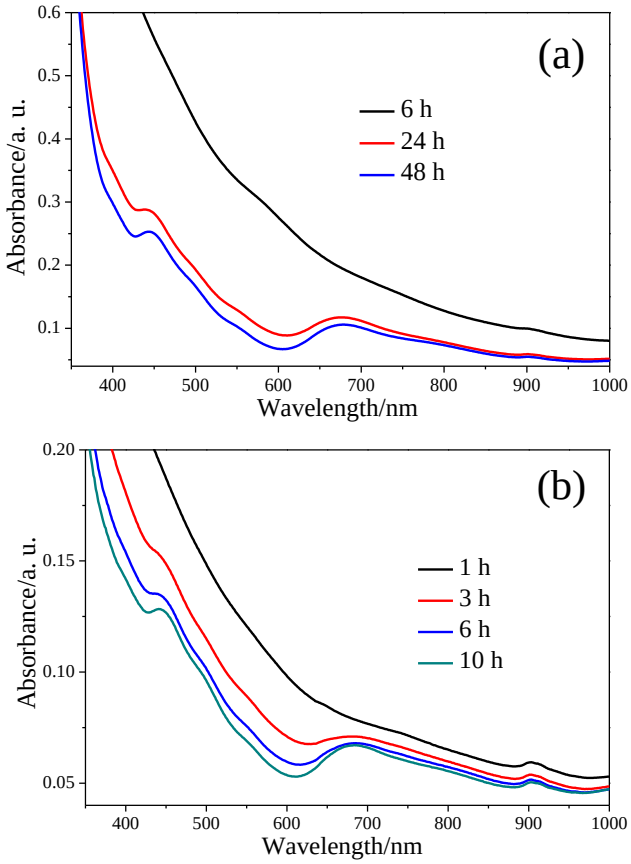

Figure S3.5 UV-vis absorption spectra of the crude samples in etching process: (a) Au_{25}(4-PyET)$_{18}$; (b) Au_{25}(2-PyET)$_{18}$.

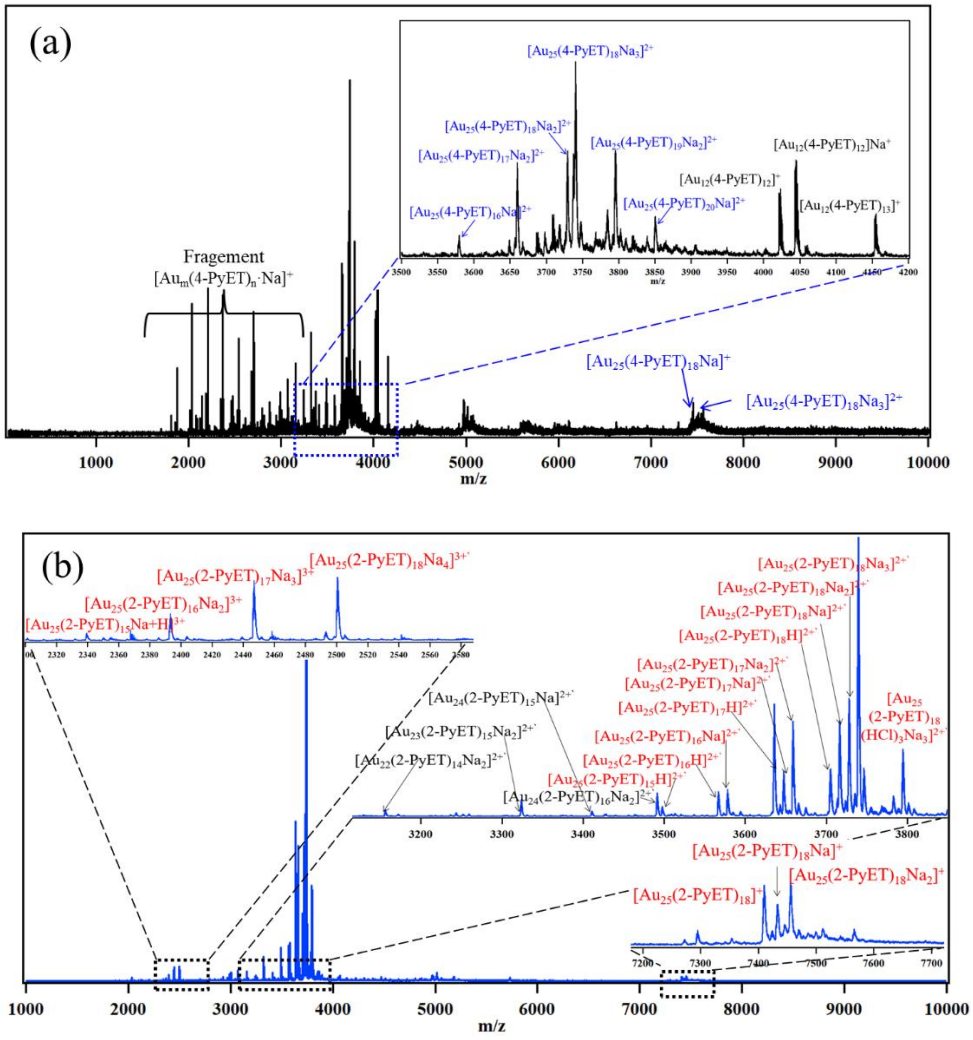

Figure S3.6 Positive-mode ESI mass spectra of purified $Au_{25}(PyET)_{18}$ NCs: (a) $[Au_{25}(4\text{-}PyET)_{18}]^{-}$; (b) $[Au_{25}(2\text{-}PyET)_{18}]^{-}$. The positive-mode ESI-MS indicated that the counterions of $Au_{25}(PyET)_{18}$ are Na^{+} cation.

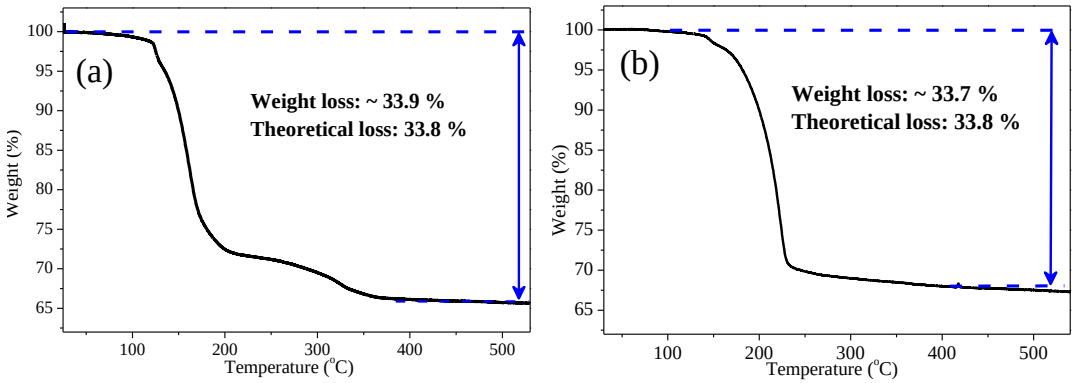

Figure S3.7 TGA profile of the obtained Au_{25}NCs: (a) $Au_{25}(4\text{-PyET})_{18}$: (b) $Au_{25}(2\text{-PyET})_{18}$. Theoretical weight loss of $[Au_{25}(PyET)_{18}]^{-}\cdot Na^{+}$ is 33.8%.

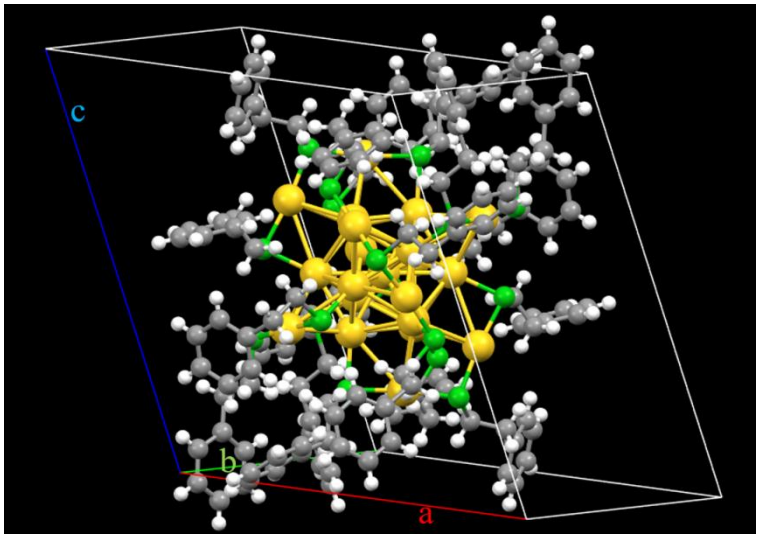

Figure S3.8 The crystal structure of the $[Au_{25}(PET)_{18}]^{-}\cdot TOA^{+}$ NCs (Legend: yellow, Au; green, S; grey, C; blue, N; white, H; magenta, the TOA^{+} counterion is omitted for clarity).

Table S3.3 Comparisons of crystallographic data, bond lengths and angles in $[Au_{25}(SR)_{18}]^-$ crystals.

NCs		**$[Au_{25}(4\text{-PyET})_{18}]^-\cdot Na^+$**	**$[Au_{25}(PET)_{18}]^-\cdot TOA^+$**	**$[Au_{25}(PET)_{18}]^-\cdot TOA^+$**	**$[Au_{25}(PET)_{18}]^-\cdot TOA^+$**
Reference		This work	This work	*J. Am. Chem. Soc.* **2008**, *130*, 3754	*J. Am. Chem. Soc.* **2008**, *130*, 5883
***a, b, c* (Å)**		14.4996(2) 17.7915(3) 19.0270(4)	16.0981(2) 17.3143(3) 18.5804(3)	16.1114(5) 17.3313(6) 18.5810(6)	16.156(3) 17.388(3) 18.641(3)
***α, β, γ* (°)**		85.449(2) 77.874(1) 68.233(1)	106.300(1) 105.488(1) 90.953(1)	106.269(2) 105.494(2) 90.959(2)	106.359(3) 105.492(2) 90.897(3)
***V* (Å^3)**		4456.71(14)	4766.66(13)	4776.1(3)	4818.6(14)
Diameter (Å)[a]		9.84(4)	9.78(4)	9.79(4)	9.79(3)
Bond length[b] **(Å)**	**I**	2.76–2.79 Avg. 2.78	2.77–2.78 Avg. 2.78	2.77–2.80 Avg. 2.79	2.77–2.79 Avg. 2.78
	II	2.79–3.02 Avg. 2.92	2.79–2.97 Avg. 2.92	2.80–2.99 Avg. 2.93	2.80–2.97 Avg. 2.92
	III	3.05–3.33 Avg. 3.18	3.06–3.28 Avg. 3.16	3.03–3.24 Avg. 3.16	3.02–3.24 Avg. 3.16
	IV	2.37–2.39 Avg. 2.38	2.36–2.38 Avg. 2.37	2.37–2.40 Avg. 2.38	2.37–2.44 Avg. 2.39
	V	2.29–2.32 Avg. 2.30	2.30–2.33 Avg. 2.31	2.30–2.33 Avg. 2.31	2.23–2.32 Avg. 2.30
Bond angle[c] **(°)**	**∠1**	88.6 (10)	86.8 (9)	86.7 (8)	87.0 (9)
	∠2	99.7(7)	100.9 (4)	101.2 (6)	100.9 (5)

[a]*The diameter of core structure of Au_{25} NCs were measured by using the average distances between the paired outermost gold atoms, see the illustration in Figure S9;*

[b, c]*The types of bonds and bond angles were illustrated in Figure 2C. Depictions of bonds types and bond angles in $Au_{25}(SR)_{18}$ NCs: Bond I: purple, core Au—core surface Au; Bond II: white, core surface Au—core surface Au; Bond III: red, core surface Au—motif Au; Bond IV: blue, core surface Au—motif S; Bond V: magenta, motif Au—motif S. Angle ∠1: light blue, ∠Au-S-Au, 12 S atoms that are connected to one stapled gold atom and one vertex gold*

atom ; Angle ∠2: orange, ∠Au-S-Au, 6 S atoms that connected to two stapled golds.

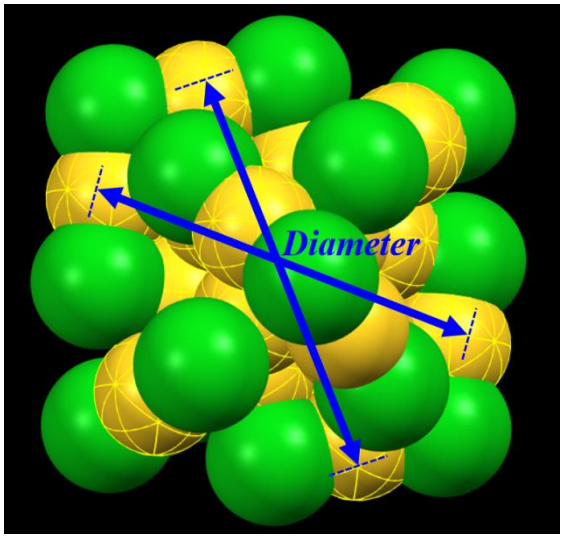

Figure S3.9 Illustration of the diameter of core structure in $Au_{25}(SR)_{18}$ NCs, the centroids of Au atoms were used to measure the distances between the six paired outermost Au atoms (Legend: yellow, Au; green, S; pyridyl-ethyl groups omitted for clarity).

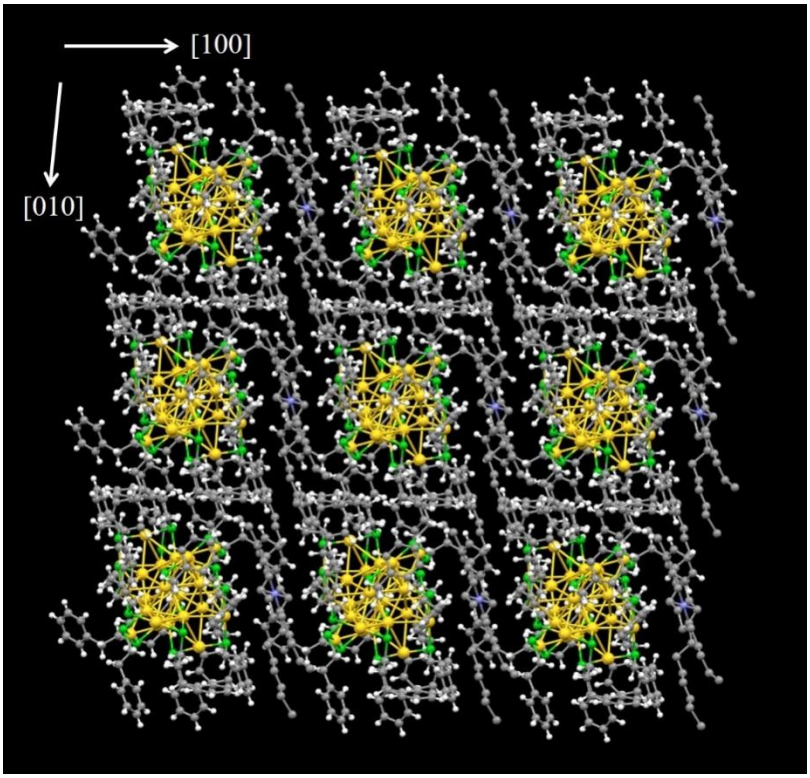

Figure S3.10 The view along the (001) plane of 3×3×3 superlattice in $[Au_{25}(PET)_{18}]^{-}\cdot TOA^{+}$ crystal, one disordered TOA^{+} is removed for clarity (yellow, Au; green, S; grey, C; blue, N; white, H).

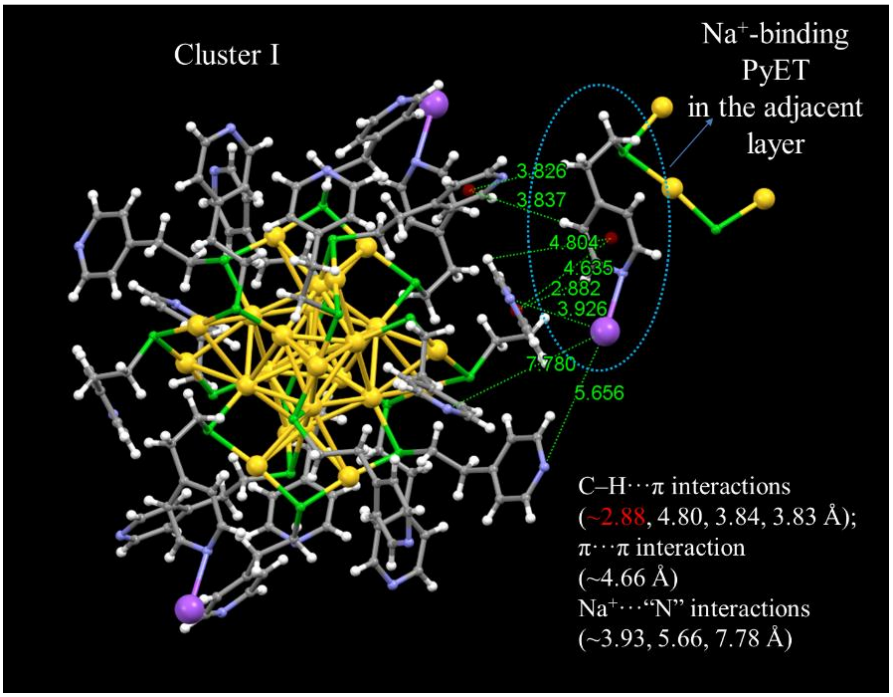

Figure S3.11 The interactions between the adjacent layers in $[Au_{25}(4\text{-PyET})_{18}]^{-}\cdot Na^{+}$. Legend: green, S; grey, C; blue, N; white, H; magenta, Na. It shows that except one C–H···π interaction (~2.88 Å) in the Na^{+}-binding ethylpyridyl thiolate substituents PyETs (which enter its itsadjacent layer), the other C–H···π distances, π···π distances and Na^{+}···"N" distances are close to or larger than the sum of van der Waal radii (~3.46 Å).

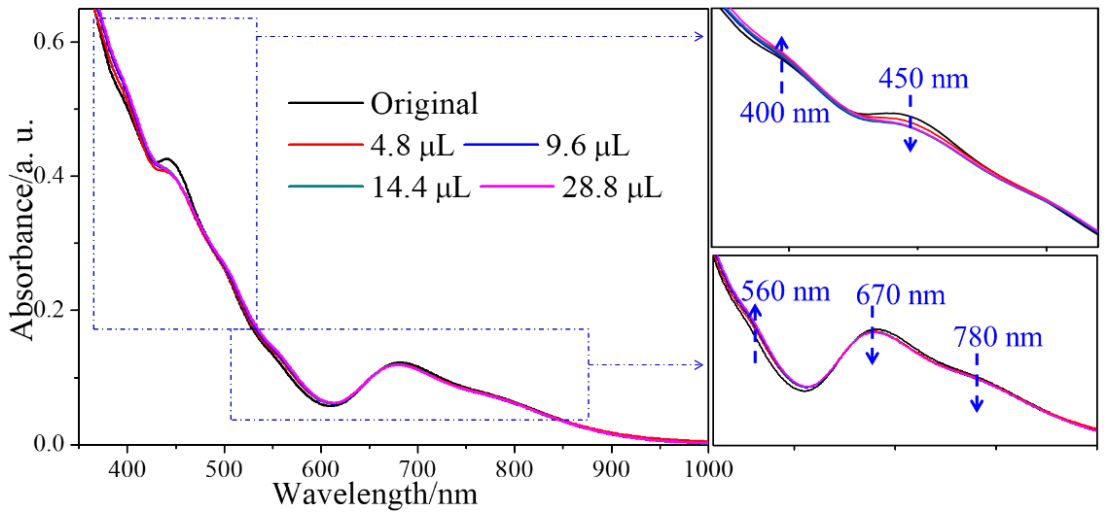

Figure S3.12 UV-vis absorption spectra Au_{25}(2-PyET)$_{18}$ with the addition of HCl (methanol, 500 mM). The red arrows denote the isosbestic points, and the blue arrows denote the change during the protonation.

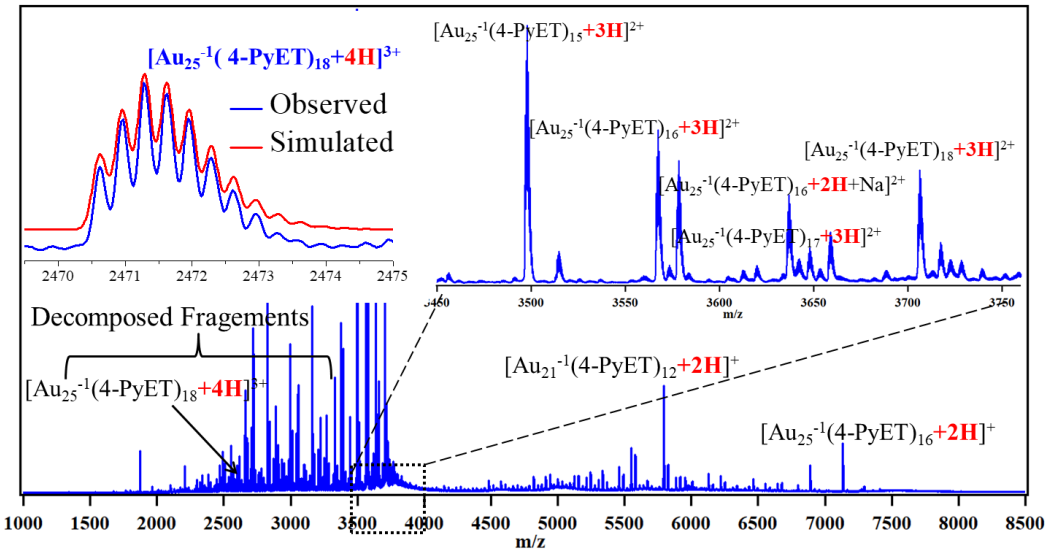

Figure S3.13 Positive-mode ESI mass spectrum of the Au_{25}(4-PyET)$_{18}$ NCs with the addition of HCl-methanol solution.

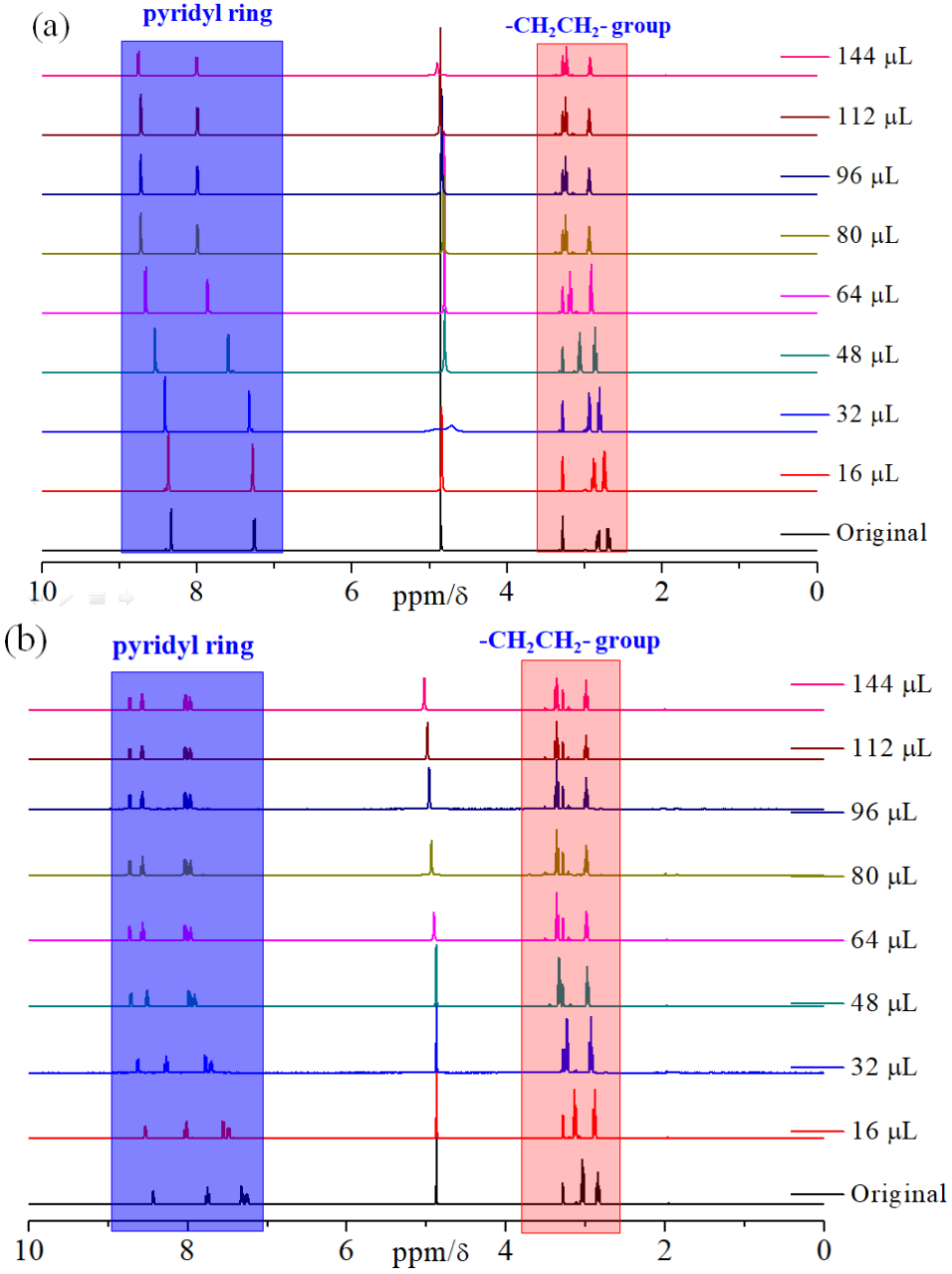

Figure S3.14 ^{1}H-NMR spectra of (a) 4-PyET, (b) 2-PyET upon titration of DCl-D_2O (50 mM), acquired in methanol-d_4.

The peak assignments were verified by their corresponding ^{1}H-^{1}H COSY spectra (Figure S3.15). In the original 4-PyET (the 4-PyET·HCl was first neutralized by NaOD and then the titration was conducted, Figure S14a), the ^{1}H signals at ~7.26 ppm (doublet, 2H) and ~ 8.34 ppm (doublet, 2H) are from the *o*-position (*othor*- to the N center) and *m*-position (*meta*- to the N center) of pyridyl group respectively, ~2.70

ppm (triplet, 2H) corresponding to the α-CH_2 group (closest to the −SH group), ~2.83 ppm (triplet, 2H) to the β-CH_2 group (second closest to −SH). The same peak assignments of the original 2-PyET (Figure S3.14b) could be summarized as: α-CH_2 group (triplet, 2H): ~3.04 ppm; β-CH_2 group (triplet, 2H): ~2.84 ppm; *1*-CH: ~7.32 ppm (doublet, 1H); *2*-CH: ~7.75ppm (triplet, 1H); *3*-CH; ~7.25 ppm (triplet, 1H): *4*-CH: ~8.43 ppm (doublet, 1H). The peak assignments upon the DCl titrations were shown in Table S4 and Figure S3.16.

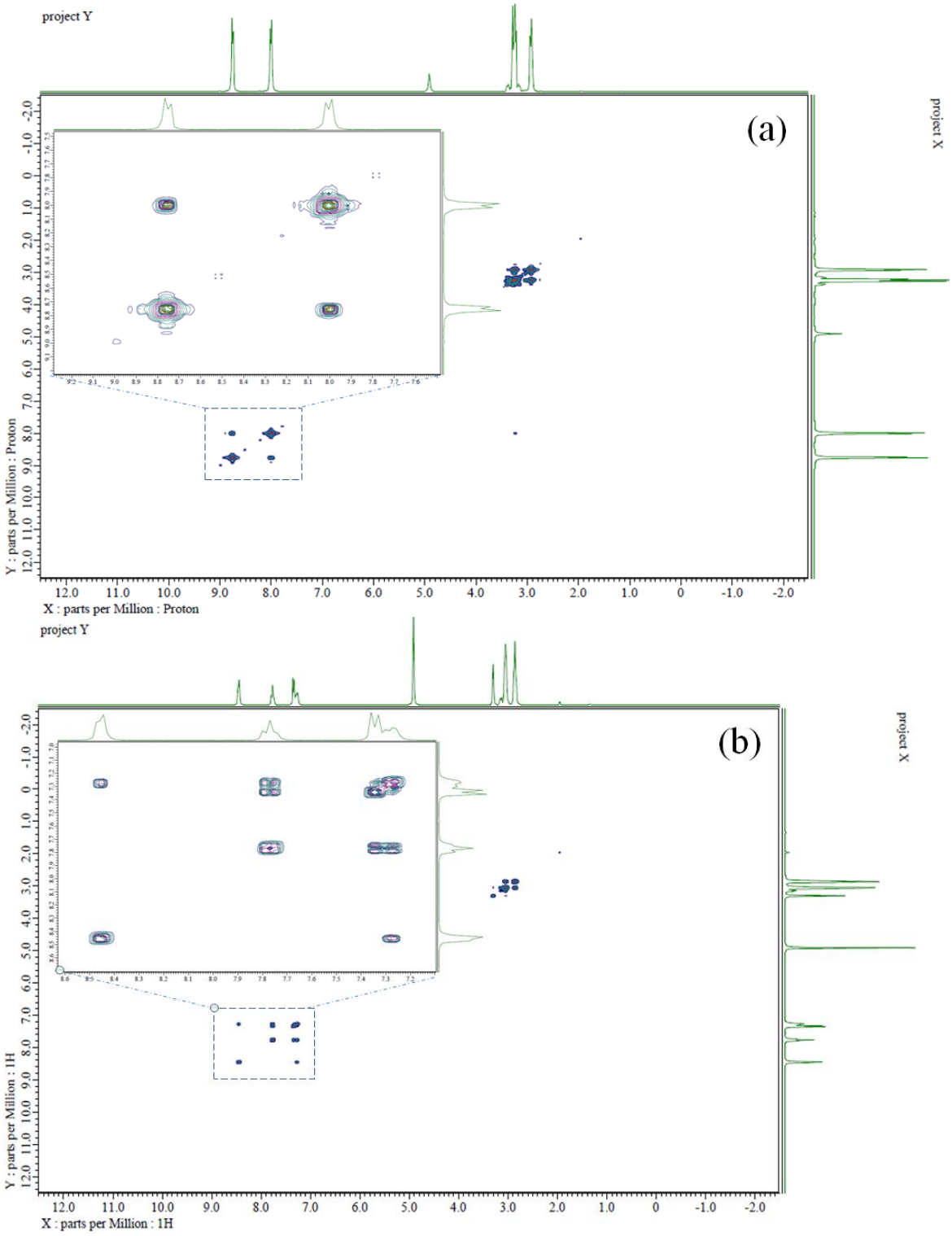

Figure S3.15 ^{1}H-^{1}H COSY spectra of the original (a) 4-PyET·HCl; (b) 2-PyET acquired in methanol-d_4.

Table S3.4 ^{1}H-NMR chemical shifts (δ) of (a) 4-PyET; (b) 2-PyET upon titration of DCl-D_2O (50 mM) in Figure S14.

(a) 4-PyET				
DCl amount	***α-CH_2***	***β-CH_2***	***o-CH***	***m-CH***
Original	2.83	2.70	7.26	8.34
16 μL	2.88	2.74	7.28	8.37
32 μL	2.94	2.81	7.42	8.45
48 μL	3.07	2.86	7.60	8.54
64 μL	3.19	2.91	7.87	8.67
80 μL	3.24	2.94	7.99	8.72
96 μL	3.24	2.94	8.00	8.73
112 μL	3.24	2.94	8.00	8.73
144 μL	3.24	2.94	8.00	8.73

(b) 2-PyET						
DCl amount	***α-CH_2***	***β-CH_2***	***1-CH***	***2-CH***	***3-CH***	***4-CH***
Original	3.04	2.84	7.32	7.75	7.25	8.43
16 μL	3.13	2.89	7.55	8.02	7.48	8.53
32 μL	3.23	2.93	7.77	8.27	7.70	8.62
48 μL	3.33	2.97	7.98	8.51	7.91	8.71
64 μL	3.36	2.99	8.02	8.57	7.96	8.73
80 μL	3.36	2.99	8.02	8.57	7.96	8.73
96 μL	3.36	2.99	8.02	8.57	7.96	8.73
112 μL	3.36	2.99	8.02	8.57	7.96	8.73
144 μL	3.36	2.99	8.02	8.57	7.96	8.73

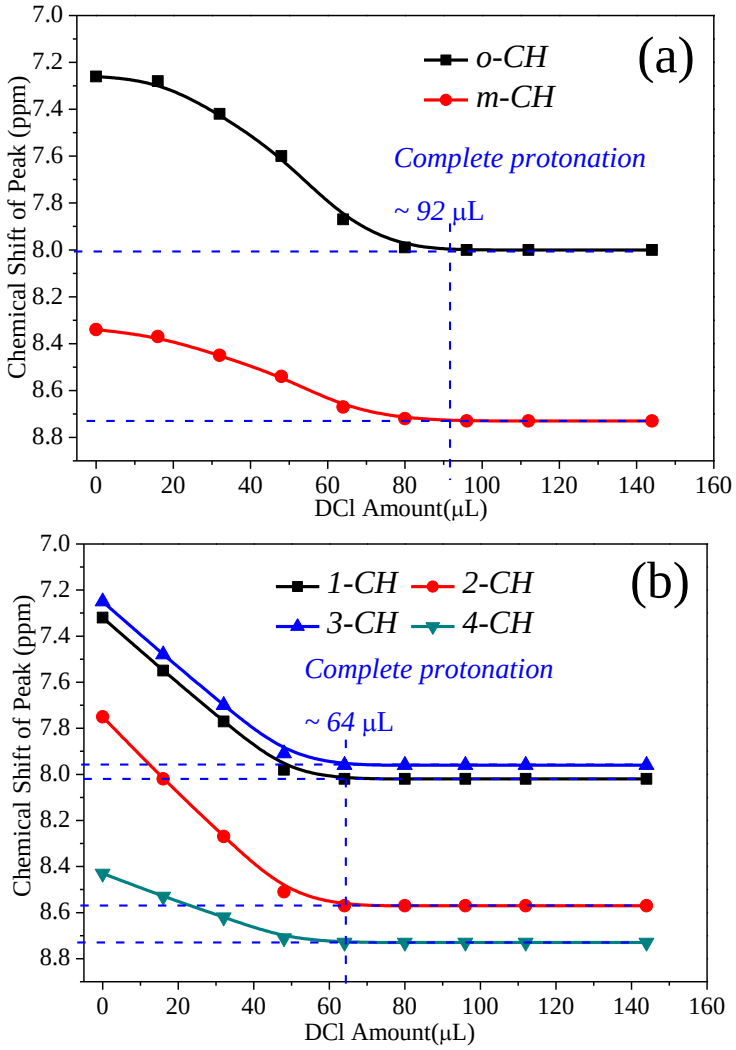

Figure S3.16 ^{1}H-NMR chemical shifts in ppm for Py protons in (a) 4-PyET and (b) 2-PyET as a function of amount of DCl.

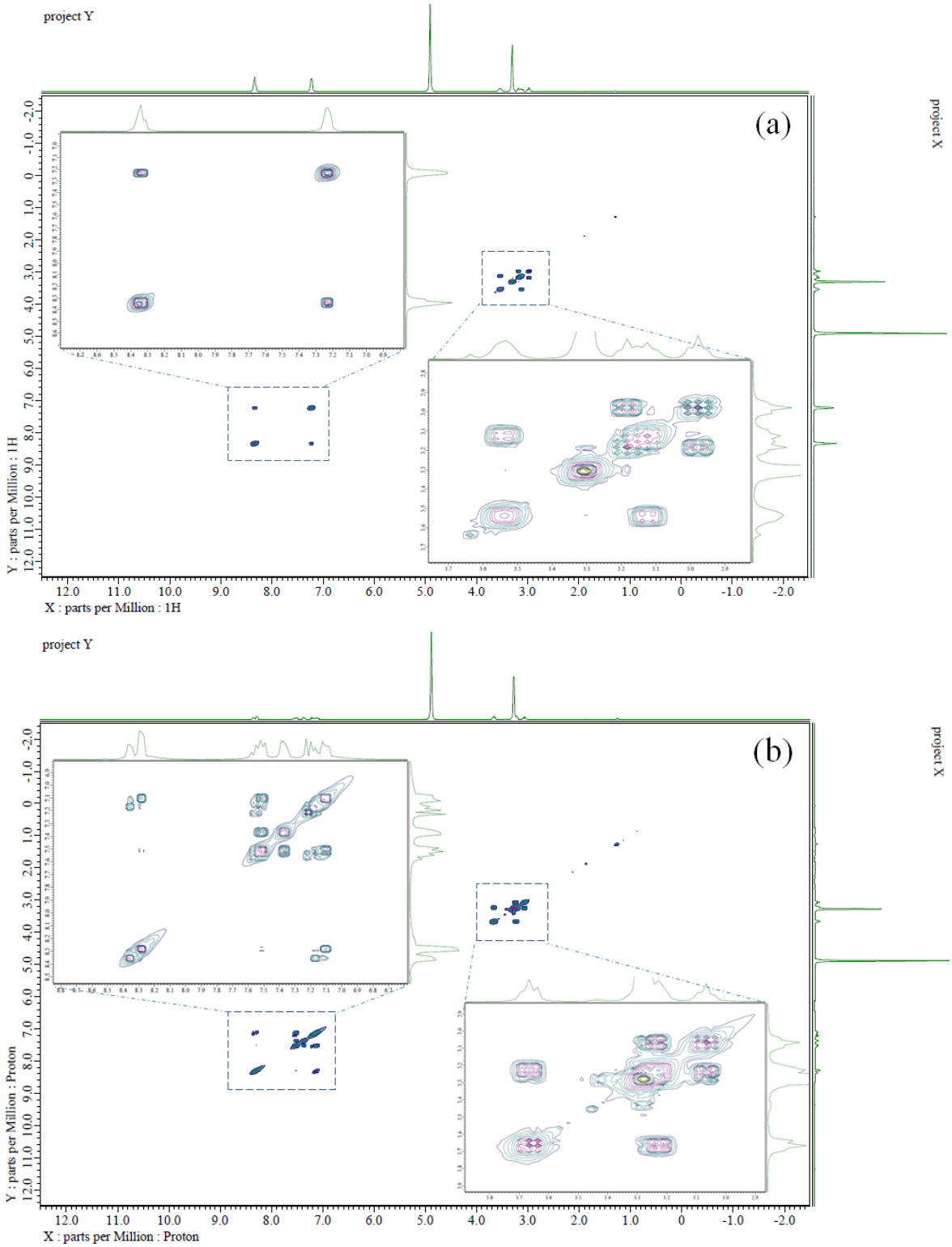

Figure S3.17 Full range ^{1}H-^{1}H COSY spectra of the original (a) Au_{25}(4-PyET)$_{18}$; (b) Au_{25}(2-PyET)$_{18}$, acquired in methanol-d_4.

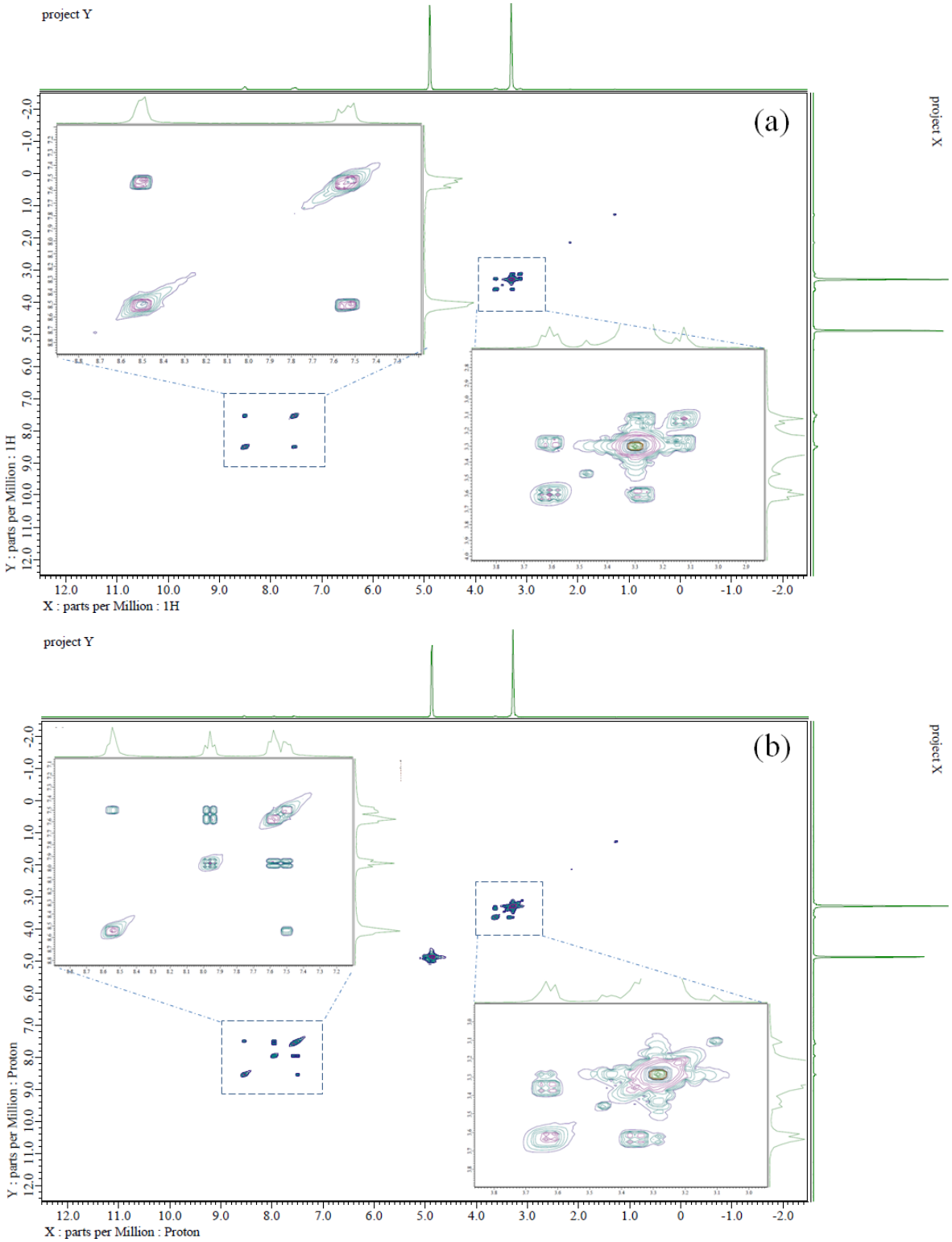

Figure S3.18 Full range ^{1}H-^{1}H COSY spectra of the protonated (a) Au_{25}(4-PyET)$_{18}$; (b) Au_{25}(2-PyET)$_{18}$, acquired in methanol-d_4 (1.0 mg of Au_{25}(PyET)$_{18}$ NCs was dissolved in 0.6 mL of methanol-d_4, and then 16 μL of DCl-D_2O solution (50 mM) was added for protonation.).

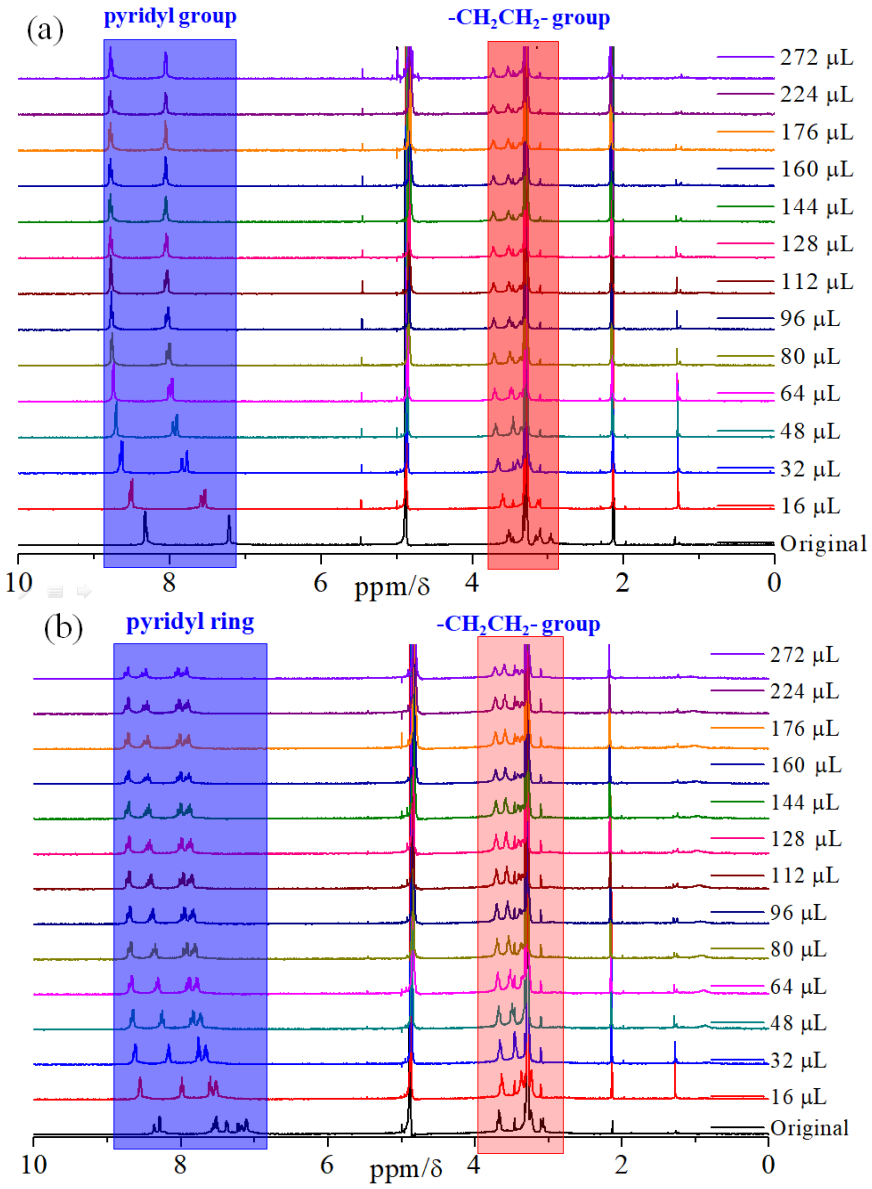

Figure S3.19 ^{1}H-NMR spectra of (a) $Au_{25}(4\text{-PyET})_{18}$, (b) $Au_{25}(2\text{-PyET})_{18}$ upon titration of DCl-D_2O (50 mM), acquired in methanol-d_4.

Table S3.5 ^{1}H-NMR chemical shifts (δ) of (a) $Au_{25}(4\text{-PyET})_{18}$; (b) $Au_{25}(2\text{-PyET})_{18}$ with the protonation of the surface pyridyl rings in Figure S3.14.

(a) $Au_{25}(4\text{-PyET})_{18}$								
DCl amount	***α*-CH$_2$**		***β*-CH$_2$**		***o*-CH**		***m*-CH**	
	Inner	*Outer*	*Inner*	*Outer*	*Inner*	*Outer*	*Inner*	*Outer*
Original	3.52	3.16	3.16	2.96	8.33	8.30	7.21	7.21
16 μL	3.60	n. d.[a]	n. d.	n. d.	8.50	8.53	7.53	7.59
32 μL	3.66	n. d.	n. d.	n. d.	8.64	8.66	7.77	7.83
48 μL	3.68	n. d.	3.46	n. d.	8.71	8.72	7.90	7.96
64 μL	3.70	n. d.	3.47	n. d.	8.74	8.74	7.97	8.01
80 μL	3.71	3.37[b]	3.50	n. d.	8.76	8.76	8.00	8.03
96 μL	3.71	3.37[b]	3.51	n. d.	8.77	8.77	8.02	8.05
112 μL	3.72	3.37[b]	3.52	n. d.	8.78	8.78	8.03	8.06
128 μL	3.72	3.37[b]	3.52	n. d.	8.78	8.78	8.04	8.06
144 μL	3.72	3.37[b]	3.52	n. d.	8.78	8.78	8.05	8.06
160 μL	3.72	3.37[b]	3.52	n. d.	8.78	8.78	8.06	8.06
176 μL	3.72	3.37[b]	3.52	n. d.	8.78	8.78	8.06	8.06
224 μL	3.72	3.37[b]	3.52	n. d.	8.78	8.78	8.06	8.06
272 μL	3.72	3.37[b]	3.52	n. d.	8.78	8.78	8.06	8.06

(b) Au_{25}(2-PyET)$_{18}$												
DCl amount	***α*-CH$_2$**		***β*-CH$_2$**		***1*-CH**		***2*-CH**[c]		***3*-CH**[c]		***4*-CH**	
	Inner	*Outer*	*Inner*	*Outer*	*Inner*	*Outer*	*Inner*	*Outer*	*Inner*	*Outer*	*Inner*	*Outer*
Original	3.62	3.26[b]	3.26[b]	3.09	7.37	7.22	7.52	7.56	7.11	7.17	8.29	8.36
16 μL	3.64	3.37[b]	n. d.	3.23b	7.60[a]	7.60[a]	7.99	7.99	7.52	7.52	8.54[a]	8.54[a]
32 μL	3.66	3.45[b]	n. d.	n. d.	7.76[a]	7.76[a]	8.16	8.16	7.66	7.66	8.62	8.64
48 μL	3.67	3.49[b]	n. d.	n. d.	7.83	7.86	8.25	8.25	7.73	7.73	8.65	8.67
64 μL	3.69	3.52[b]	n. d.	n. d.	7.88	7.92	8.31	8.31	7.79	7.79	8.66	8.70
80 μL	3.70	3.54[b]	n. d.	3.36[b]	7.91	7.95	8.36	8.36	7.81	7.81	8.68	8.71
96 μL	3.70	3.55[b]	n. d.	3.38[b]	7.94	7.98	8.39	8.39	7.83	7.83	8.69	8.72
112 μL	3.71	3.56	n. d.	3.39[b]	7.96	8.01	8.42	8.42	7.86	7.86	8.69	8.73
128 μL	3.71	3.57	n. d.	3.40[b]	7.99	8.03	8.44	8.44	7.88	7.88	8.7	8.74
144 μL	3.71	3.58	n. d.	3.41[b]	8.00	8.04	8.44	8.44	7.88	7.88	8.7	8.74
160 μL	3.71	3.58	n. d.	3.41[b]	8.00	8.04	8.44	8.44	7.88	7.88	8.7	8.75
176 μL	3.71	3.58	n. d.	3.41[b]	8.00	8.04	8.44	8.44	7.88	7.88	8.7	8.75
224 μL	3.71	3.58	n. d.	3.41[b]	8.00	8.04	8.44	8.44	7.88	7.88	8.71	8.75
272 μL	3.71	3.58	n. d.	3.41[b]	8.00	8.04	8.44	8.44	7.88	7.88	8.71	8.75

[a]n. d.= not determined because the overlaps with the solvent signals; [b] partially overlaps with solvent signals; [c]hard to assign the inner and outer sites separately.

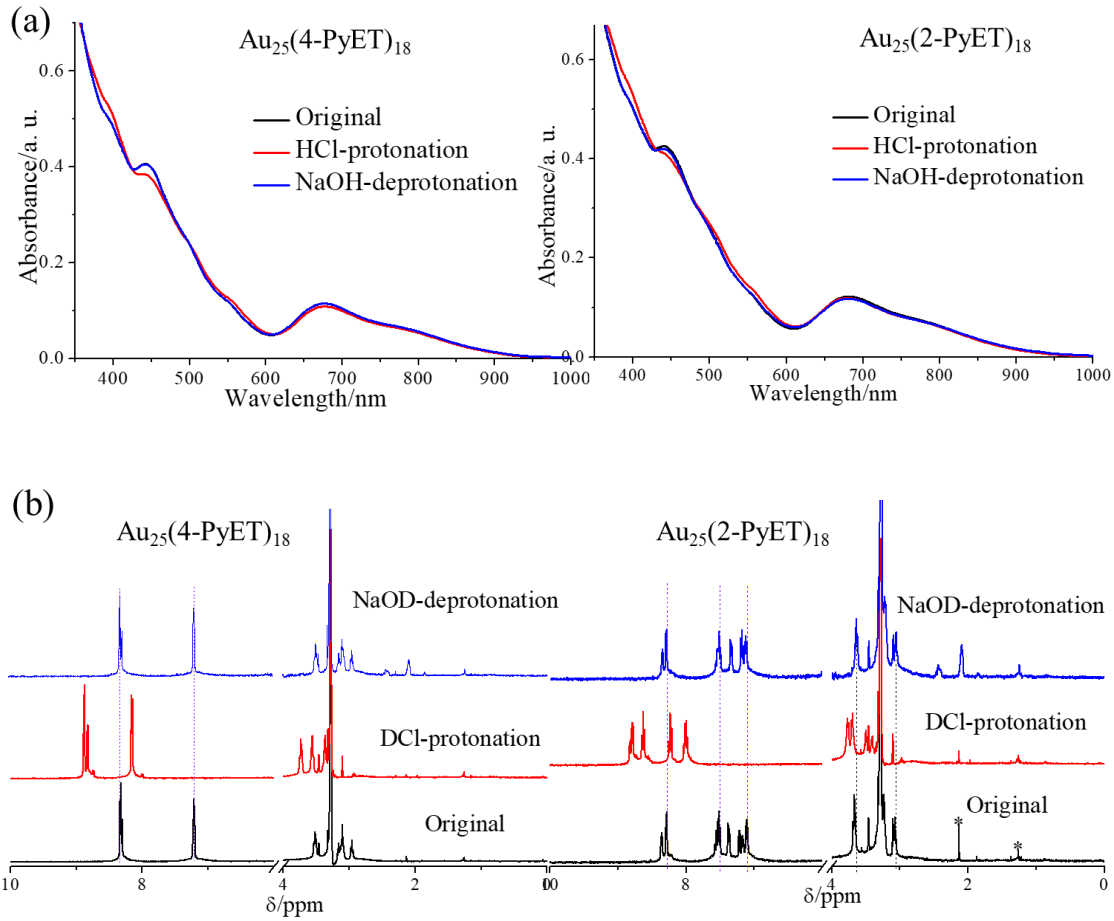

Figure S3.20 Reversible protonation reaction on $Au_{25}(PyET)_{18}$ NCs: (a) UV-vis absorption; and (b) ^{1}H-NMR spectra.

Table S3.6 Solubility of $Au_{25}(PET)_{18}$, and $Au_{25}(PyET)_{18}$ NCs in protonated and deprotonated states.

Solvent	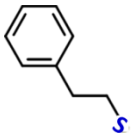	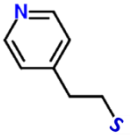	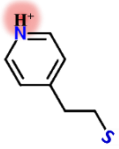	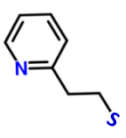	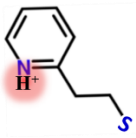
H_2O	I	I	$S^{+\,a}$	I	$S^{+\,a}$
Alcohol	I	S^{+}	S^{+}	S^{+}	S^{+}
DMF	S^{+}	S^{+}	S^{+}	S^{+}	S^{+}
THF	S^{+}	S^{-}	$I^{\,a}$	S	$I^{\,a}$
THF-MeOH (Vol., 3:1)	I	S^{+}	$I^{\,a}$	S^{+}	$I^{\,a}$
Toluene	S^{+}	I	$S^{\,b}$	I	$S^{\,b}$
DCM	S^{+}	I	$S^{\,b}$	S	S^{-b}
MeCN	S	S^{-}	$S^{a,b}$	S^{-}	$S^{a,b}$
Acetone	S	S^{-}	$S^{a,b}$	S^{-}	$S^{a,b}$
Hexane	I	I	$I^{\,b}$	I	$I^{\,b}$
Ether	I	I	$I^{\,b}$	I	$I^{\,b}$

[a]Aq. HCl (375 mM, 20 µL) was added for protonation; [b]Acetic acid (20 µL) was added for protonation; [c]Solubility: $S^{+} > S > S^{-}$, Insoluble: I; [d]In each batch, ~ 1.0 mg of Au_{25} NCs was tested in 1.0 mL of the solvent.

Chapter 4

Proton-Induced Resonances on Photoluminescence of Pyridyl-Thiolated Au_{25} Nanoclusters

Abstract

Engineering surface ligands on metal nanoclusters (NCs) with preservation of the structural template is of great role for enhancing their practical utility. This chapter investigates the photoluminescence properties on $Au_{25}(PyET)_{18}$ and $Au_{25}(4\text{-}PyET)_{18}$, in which the PyET ligands have only one element different to PET. The results show that PyET ligand with electron-rich pydidyl-group could significantly enhance the PL emission of Au_{25} NCs. The ligand-to-metal electron transfer is responsible for the PL enhancement on $Au_{25}(PyET)_{18}$ NCs. In addition, upon involvement of the proton (H^+), the protonated PyET would reduce the electron-donation, and the emission responses of PyET-capped Au_{25} NCs were found to be correlated with the resonance-coupled structure of PyET ligands.

4.1 Introduction

Thiolated metal nanoclusters ($Au_m(SR)_n$ NCs) with atomically-precise structures have provided the opportunities for in-depth understanding their origin of physicochemical properties,[1–5] which made their potential uses in catalysis,[6–8] sensing,[9–11] and bioapplications,[12–14] as examples. Especially in the last case, the photoluminescence (PL) of NCs show a great potential in a range of fields owing to their ultrasmall sizes

(<~2 nm), easy modification, good biocompatibility, etc.

However, the low photoluminescence quantum yields hamper the practical application. How and why can the NCs photoluminescence be enhanced constitutes a core issue for the current research of photoluminescent NCs, which has received the extensive attention in the past years.[15] Among various annotations to this fundamental issue, one major opinion is that the surface ligands can greatly influence the photoluminescence at least by charge transfer from the ligands to the metal parts of the NCs through the Au-S bonds, which had been proposed by Whetten,[16,17] Aikens,[18] Jin,[19,20] and Bakr[21] et al. For example, Jin et al.[19] reported the ligand effect on the PL of $Au_{25}(SR)_{18}$ NCs. The PL intensity follows the order $[Au_{25}(SG)_{18}]^-$ >> $[Au_{25}(PET)_{18}]^-$ > $[Au_{25}(SC_{12}H_{25})_{18}]^-$ > $[Au_{25}(SC_6H_{13})_{18}]^-$. Because all $Au_{25}(SR)_{18}$ NCs share a typical Au_{13}/Au_{12} core-shell structure regardless of the SR ligands, it indicated the ligand effect play an important role on the PL of metal NCs. In addition, when the $Au_{25}(SG)_{18}$ NCs were ligand-exchanged with a long-chain peptide nucleic acid (PNA, containing many electron-rich N and O atoms), its PL intensity could be enhanced by 1.8 times. Based on this, they proposed that to use SR ligands with the strong electron donation capability or electron-rich atoms and groups can enhance the PL performance of metal NCs. Wu et al.[22] also investigated the PL intensities of $MAg_{24}(SR)_{18}$ NCs, which follow a sequence of $PdAg_{24}(SR)_{18}$ < $Ag_{25}(SR)_{18}$ < $PtAg_{24}(SR)_{18}$ < $AuAg_{24}(SR)_{18}$. Such a sequence is in good agreement with the order of the electron affinity of Au_{13} core, which also hinted that the charge transfer of delocalized electrons contributes to the emission intensity of metal NCs.

The heterocyclic aromatic substituent, pyridyl, which is structurally analogous to phenyl with one CH group in the six-membered ring replaced by a N atom, features a

basic lone pair of electrons, which does not overlap with the aromatic π-system ring, consequently pyridyl-group should be electron-rich. In 2013, Konishi et al.[23] reported the site-specific introduction of organic functionality on the [core+exo]-type Au_8 NCs, stabilized by four diphosphine (dppp = $Ph_2P(CH_2)_3PPh_2$) and two acetylide ligands. The results indicated the pyridylethynyl (C≡CPy)-modified NCs showed protonation-induced absorption and PL responses, which were critically dependent on the relative N position of the Py atom. Especially, the PL of the 3-pyridyl isomer was negligibly affected by the protonation event, which was in contrast to the significant quenching observed for the 2- and 4-pyridyl isomers. Recently, they[24] also demonstrated that the electronic coupling with the π-resonance contributors of the attached pyridylthiolate ligands (SPy) on such Au_8 NCs. The π-stack formation in the peripheral aromatic ring environment, which was induced by local chemical events at the ligand moiety, could lead to the increase of emission efficiency.

Scheme 4.1 Crystal structure of $Au_{25}(SR)_{18}$NCs (yellow, kernel Au atoms; blue, staple Au atoms; magenta, S atoms) and PET, 4-PyET, 2-PyET thiols used in this work.

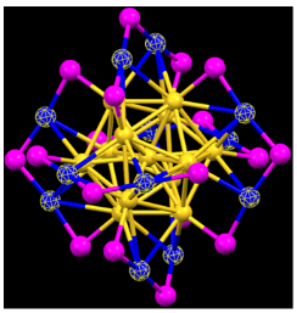

$Au_{25}S_{18}$

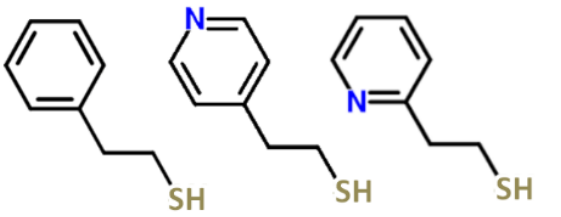

PET 4-P*ET 2-P*ET

In present work, on the basis of my recent successful work[25] (Chapter Three) for the basic Au_{25} NCs capped by pyridyl ethanethiolate ligands (−SCH_2CH_2Py, 4-PyET or

2-PyET, Scheme 1), the PL performance of such Py-attached NCs was investigated. First, I compared the PL properties of the $Au_{25}(PyET)_{18}$ NCs with the typical $Au_{25}(PET)_{18}$(−SCH_2CH_2Ph, PET, Scheme 4.1), showing the PL of $Au_{25}(PyET)_{18}$ was enhanced with the introduction of the electron-rich Py-group. I also investigated the PL responses of the PyET-capped NCs to the pronated case ($PyET{\cdot}H^+$), and indicated that the PL emission energies were critically dependent on the π-resonance structure of the pendant Py moiety. To the best of my knowledge, this is the first research focusing on the protonation effect on the thiolated metal NCs, which allows the inspection of the pendant ligand environments through the systematic studies for NCs with the variable SR ligands.

4.2 Experimental section

4.2.1 Chemicals

Hydrogen tetrachloroaurate (III) ($HAuCl_4{\cdot}4H_2O$, > 99.99%, Wako Pure Chemical Industries, Ltd), 2-(4-pyridinyl)ethanethiol hydrochloride (4-PyET·HCl, $C_7H_{10}ClNS$, > 97%, Tokyo Chemical Industry Co., Ltd), 2-pyridyl ethylmercaptan (2-P*ET, C_7H_9NS, Toronto Research Chemical Inc.), 2-phenylethanethiol (PET, 99%, Wako Pure Chemical Industries, Ltd), tetra-*n*-octylammonium bromide (TOABr, > 98%, Wako Pure Chemical Industries, Ltd), sodium borohydride ($NaBH_4$, 99%, Wako Pure Chemical Industries, Ltd), sodium hydroxide (NaOH, > 97%, Junsei Chemical Co., Ltd), hydrochloric acid (HCl, 35%~37%, Kanto Chemical Co., Ltd), hydrogen chloride-methanol solution (HCl-MeOH, ~ 1.25 M, Aldrich). HPLC-grade solvents such as tetrahydrofuran (THF) and methanol (MeOH) were purchased from Kanto

Chemical. Deionized pure water (> 18.2 MΩ) was prepared by an Organo/ELGA purelab system.

4.2.2 Synthesis and Purification of $Au_{25}(SR)_{18}$ NCs

The syntheses and purifications of $Au_{25}(PyET)_{18}$ were following my recent works.[25] In brief, 8 mL of 4-PyET solution (MeOH, 100 mM) was added dropwise into 24 mL of $HAuCl_4$ solution (6.7 mM). The mixture changed into light reddish cloudy suspension and then into white cloudy suspension during 4-PyET dropping. After overnight stirring, 1.6 mL of the fresh-made $NaBH_4$ solution (1.6 mmol, prepared by dissolving 189.2 mg of $NaBH_4$ in 5 mL of cold pure water) was rapidly added to the suspension under vigorous stirring. The color of the solution immediately turned black after addition of $NaBH_4$. Finally, the stirring speed was slowed down to 500 rpm and the etching process was allowed to continue for at least 48 hours. Over the long time of etching process, the solution color would become dark brown slowly, suggesting the initial polydisperse Au_m NCs were finally converted to monodisperse $Au_{25}(4\text{-PyET})_{18}$. The crude samples were purified based on the protonated states of the pendant Py moiety on Au_{25} NCs, which endows NCs with the tunable solubility in water and some organic solvents. This final product, $[Au_{25}(4\text{-PyET})_{18}]^{-}\cdot Na^{+}$ or $[Au_{25}(2\text{-PyET})_{18}]^{-}\cdot Na^{+}$ was stored in dry form or DMF solution. The detail characterizations for the NCs are shown in Figure S4.1. In addition, for comparison, $[Au_{25}(PET)_{18}]^{-}\cdot TOA^{+}$ NCs were prepared based on that previously reported by the group of Murray.[26] The UV-vis absorption and negative-mode ESI-MS characterizations of the $Au_{25}(PET)_{18}$ NCs are presented in Figure S4.2.

4.2.3 Protonation Reaction on $Au_{25}(SR)_{18}$ NCs.

In each 3 mL MeOH with 100 μg/mL of $Au_{25}(PyET)_{18}$ NCs, 4.8, 9.6, 14.4 and 28.8 μL of HCl-MeOH solution (500 mM) were added separately. Each batch was stirred at 300 rpm for 30 seconds and then conducted by PL tests and lifetime measurements using a quartz cuvette with a 10-mm optical path. The reversible protonation-deprotonation process of PL measurements were carried out with adding 9.6 μL of HCl solution and subsequently 14.4 μL of NaOH-MeOH solution (500 mM). For comparison, the $Au_{25}(PET)_{18}$ was also treated as same to the above cases.

4.2.4 Characterization.

UV-vis absorption spectra of samples were recorded using a JASCO V-630 spectrophotometer. Photoluminescent measurements were conducted using a JASCO FP-6600 spectrofluorometer. Time-resolved PL lifetime measurements were measured using a time-correlated single photon counting technique after excitation at 365 nm with a diode laser excitation, and the measurements were carried out in an Edinburgh F900S spectrofluorimeter. Electrospray-ionization mass spectrometry (ESI-MS) was performed using a Bruker DaltonicsmicrOTOF-HS mass spectrometer. The purified sample, dissolved in methanol (~100 μg/mL), was directly infused at 4 $mL \cdot min^{-1}$. The nebulizer pressure was set to 1.5 bar, and the sheath gas was set to 4.0 L/min. The dry temperature was kept at 120°C. The electrospray emitter potential was held at –4500 V (negative mode) and 4500 V (positive mode). The capillary exit, skimmer 1, hexapole 1, skimmer 2 voltage settings were 200, 50, 25, and 28 V, respectively. The lens 1 transfer and lens 1 pre puls storage were set at 160, and 30 μs, respectively.

4.3 Results and discussions

4.3.1 Photoluminescence of $Au_{25}(SR)_{18}$ NCs

The UV-vis absorbance spectra of Au_{25}(4-PyET)$_{18}$, Au_{25}(2-PyET)$_{18}$, $Au_{25}(PET)_{18}$ (100 μg/mL) are shown in Figure S4.3. Although the shapes of absorption peaks present differences among these three NCs, the almost same absorbance at ~ 670 nm, primarily arising from the Au_{13} kernel in $Au_{25}(SR)_{18}$,[27] verified the almost same numbers of Au_{25} NCs in the samples for PL measurements. As shown in Figure S4.4, the excitation spectra of $Au_{25}(SR)_{18}$ all shows two board peaks at ~ 365 and ~ 624 nm, which both emit the maximal PL at ~ 719 nm. Because under 624 nm excitation, the weak broad PL peaks (~ 719 nm) would overlap with the strong incident wavelength (624 nm), it was hard to compare the PL emissions among the as-measured samples. So here, the PL test were all carried out under the excitation wavelength at 365 nm.

Under the same conditions, the PL tests of $Au_{25}(PET)_{18}$ and $Au_{25}(PyET)_{18}$ NCs (noting that the counterion was tetra-*n*-octylammonium TOA^+ for the former, and Na^+ for the latter) were conducted and compared, as shown in Figure 4.1. The $Au_{25}(PET)_{18}$ was found to exhibit weak emission at ~719 nm under the 365 nm excitation. By contrast, the emission wavelength (~719 nm) of Au_{25}(4-PyET)$_{18}$ or Au_{25}(2-PyET)$_{18}$ remained constant whereas the PL intensities showed the definite enhancements. The fluorescence intensity follows the order Au_{25}(4-PyET)$_{18}$ > Au_{25}(2-PyET)$_{18}$ > $Au_{25}(PET)_{18}$. Especially in the Au_{25}(4-PyET)$_{18}$, which was ~6-fold greater than that of the $Au_{25}(PET)_{18}$. Notably, use of difference solvents required a collection by the refractive index of two solvents (for MeOH and toluene, 1.329 and 1.49, respectively), however it is clear that the PL of PyET cases are stronger than that of PET. Since the

$Au_{25}(SR)_{18}$ NCs have the common structure, an icosahedral Au_{13} core that is capped by three pairs of $Au_2(SR)_3$ staple motifs (Scheme 4.1), the above observation indicated that the surface ligands play an important role in the PL emission, that is, SR ligands with pyridyl-group can enhance the PL of Au_{25} NCs over that with phenyl-group.

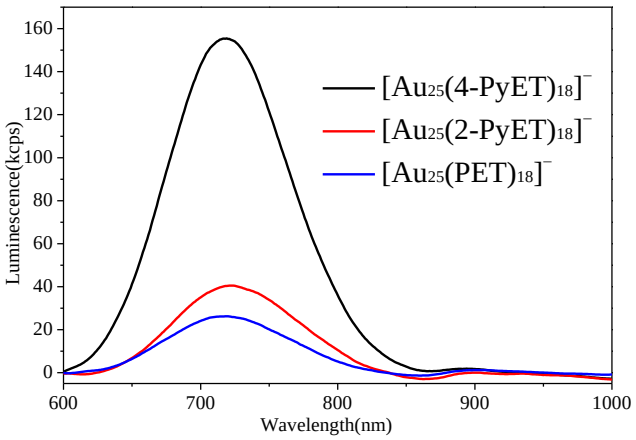

Figure 4.1 Photoluminescence spectra of (a) $Au_{25}(SR)_{18}$ with different aromatic rings (PET, 4-PyET and 2-PyET). (Solvents: toluene for PET case, and MeOH for PyET cases; excitation: 365 nm; solution concentration: 100 μg/mL).

4.3.2 Proton-Resonance on Photoluminescence of $Au_{25}(SR)_{18}$ NCs

Protonation of Py-group gives to its acid form, $-C_5H_4NH^+$. In $Au_{25}(PyET)_{18}$ NCs, the surface Py moiety is peripherally exposed to the solution, they also holds the protonation characteristics, as depicted in my recent work.[25] It showed that the peak intensities at 400 and 560 nm had a slight increase whereas the peaks at 450, 670 and 780 nm showed a slight decrease along the H^+ addition. However, as shown in Figure 2, a notable decrease in the PL emission of $Au_{25}(PyET)_{18}$ was observed under the addition of HCl (~75% decrease for $Au_{25}(4\text{-}PyET)_{18}$, and ~17% decrease for $Au_{25}(2\text{-}PyET)_{18}$; with 28.8 μL HCl), whereas no distinct emission quenching in the case of

$Au_{25}(PET)_{18}$ (Figure S4.5). Noting that the PL emissions on $Au_{25}(PyET)_{18}$ are reversible upon the deprotonation by NaOH. (Figure S4.6) These results indicated that its emission intensities were correlated with the protonation states of surface Py-group.

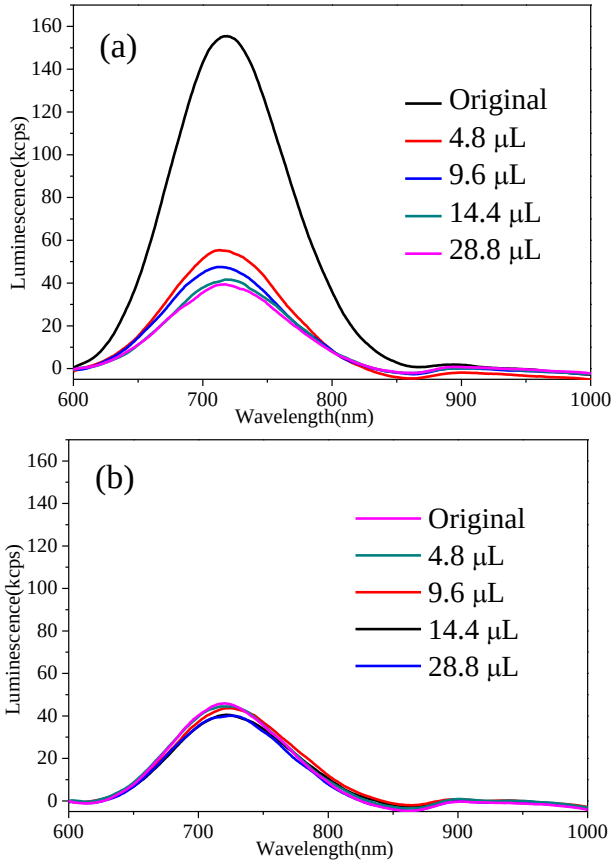

Figure 4.2 Photoluminescence spectra of $Au_{25}(4\text{-}PyET)_{18}$ (a), and $Au_{25}(2\text{-}PyET)_{18}$ (b) upon the addition of HCl (methanol, 500 mM). (Solvents: toluene for PET case, and MeOH for PyET cases; excitation: 365 nm; solution concentration: 100 μg/mL)

4.3.3 The Mechanism of Photoluminescence on $Au_{25}(SR)_{18}$ NCs

As reported previously,[11,12,15–20,22–24] the electronic and steric characteristics of surface ligands have been demonstrated to profoundly affect both the electronic/geometric structures of the NCs and their optical performance. On the basis of above optical absorptions, the above three Au_{25} NCs were believed to share a common Au_{13}/Au_{12}

core-shell structure regardless of surface aromatic group (Scheme 4.1). It should be mentioned that the geometric structure of $Au_{25}(PyET)_{18}$ NCs might have a slight distortion, caused by the surface charge anisotropy[28] when the positive charges (H^+) were distributed on the surface of Au_{25} NCs. This could be indicative of the absorption changes along with the protonation degree of both $Au_{25}(PyET)_{18}$ NCs. However, the PL of these three Au_{25} NCs, primarily arising from its core-based orbitals,[29]shows the definite differences in emission intensity (Figure 4.2) but no obvious change in emission wavelength (~719 nm) while there were only slight structural distortions among them. Thus, it is believed that the geometric structure should not mainly account for the origin of the enhanced PL emissions between PET and PyET, and the emission quenching during protonation process.

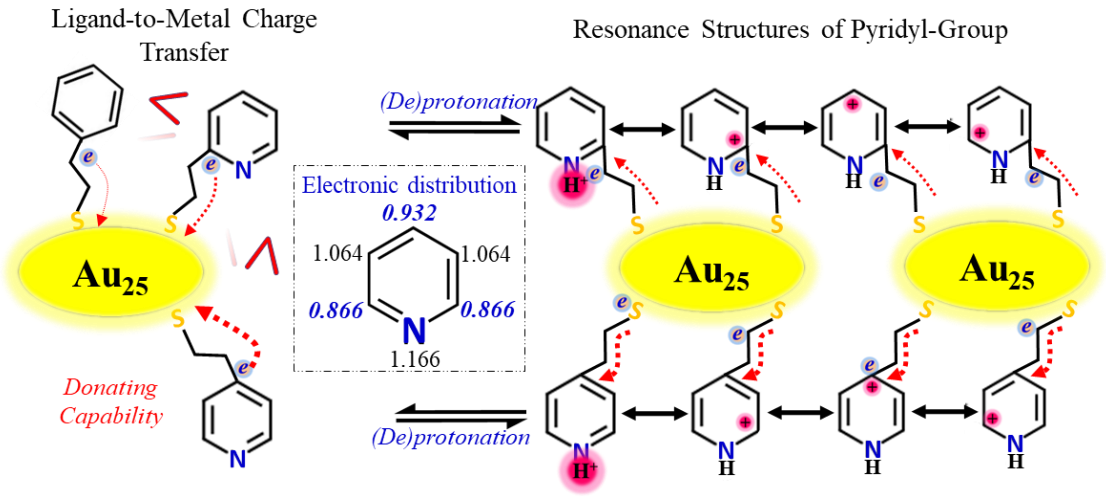

Figure 4.3 Schematic illustration of the enhanced PL emissions on $Au_{25}(PyET)_{18}$ NCs.

The pyridyl-group contains the π-system ring and nitrogen lone pair of electrons, which make PyET ligands electron-rich and owning the stronger electron donating capability than PET ligand. So the ligand-to-metal charge transfer[15,19] should be responsible for the PL enhancement on $Au_{25}(PyET)_{18}$ NCs, as presented in Figure 4.3.

Under the excitation, the pyridyl-group pushes more electrons to the S atom and hence affects the Au_{25} core via the S-Au bonds.[19] Noting that the PL increase of Au_{25}(2-PyET)$_{18}$ (~1.6-fold) was lower than that of Au_{25}(4-PyET)$_{18}$ (~6-fold), which was possibly attributed to the different relative electronic distributions in the *para*- (0.932) and *othor*- (0.866) position (relative to the N atom) of pyridine.[30] The *para*-substituted $-(CH_2)_2S-$ group might be given more electrons from pyridyl ring,[24] and resulted in the higher PL emission in Au_{25}(4-PyET)$_{18}$ NCs. This mechanism could be verified by the emission quenching during protonation process. Because the resonance structures of the pyridyl group, the positive charge (H^+), gained by protonation, could move either within the pyridyl ring or to methylene groups, it would produce a pronounced perturbation effect and significantly suppress the ligand-to-metal electron transfer in Au_{25}(4-PyET)$_{18}$.[23,24] By contrast, since only a few electrons of surface 2-PyET participated in the PL emission of NCs, the perturbation effect by protonation was not obvious in Au_{25}(2-PyET)$_{18}$.

4.4. Conclusions

In summary, even only one element difference between Au_{25}(PyET)$_{18}$ and Au_{25}(PET)$_{18}$ NCs, it plays a major role in the PL efficiency. Pydidyl group on NCs surface could donate more electrons to Au_{25} core, resulting in the enhanced PL emissions of Au_{25}(PyET)$_{18}$ NCs. Upon protonation, the resonance-coupled structure of PyET ligands, caused by H^+, would hinder the electron donation and quench the emission of Au_{25} NCs. Overall, the electronic factors of the surface organic ligand moiety are able to cause perturbation effects on the optical/electronic properties of ligand-protected NCs, offering versatile toolboxes for the fine tuning of their

electronic properties towards designing NCs.

4.5 References

(1) Jin, R.; Zeng, C.; Zhou, M.; Chen, Y. Atomically Precise Colloidal Metal Nanoclusters and Nanoparticles: Fundamentals and Opportunities. *Chem. Rev.* **2016**, *116*, 10346–10413.

(2) Chakraborty, I.; Pradeep, T. Atomically Precise Clusters of Noble Metals: Emerging Link between Atoms and Nanoparticles. *Chem. Rev.* **2017**, *117*, 8208–8271.

(3) Hossain, S.; Niihori, Y.; Nair, L. V.; Kumar, B.; Kurashige, W.; Negishi, Y. Alloy Clusters: Precise Synthesis and Mixing Effects. *Acc. Chem. Res.* **2018**, *51*, 3114–3124.

(4) Cook, A. W.; Hayton, T. W. Case Studies in Nanocluster Synthesis and Characterization: Challenges and Opportunities. *Acc. Chem. Res.* **2018**, *51*, 2456–2464.

(5) Tsukuda, T.; Hakkinen, H. *Protected Metal Clusters: From Fundamental to Applications*; Elsevier: Amsterdam, **2015**.

(6) Li, G.; Jin, R. Atomically Precise Gold Nanoclusters as New Model Catalysts. *Acc. Chem. Res.* **2013**, *46*, 1749–1758.

(7) Wan, X. K.; Wang, J. Q.; Nan, Z. A.; Wang, Q. M. Ligand effects in catalysis by atomically precise gold nanoclusters. *Sci. Adv.* **2017**, *3*, e1701823.

(8) Yan, J.; Teo, B. K.; Zheng, N. Surface Chemistry of Atomically Precise Coinage–Metal Nanoclusters: From Structural Control to Surface Reactivity and Catalysis. *Acc. Chem. Res.* **2018**, *51*, 3084–3093.

(9) Guan, G.; Zhang, S. Y.; Cai, Y.; Liu, S.; Bharathi, M. S.; Low, M.; Yu, Y.; Xie,

J.; Zheng, Y.; Zhang, Y. W., Han, M. Y. Convenient Purification of Gold Clusters by Co-Precipitation for Improved Sensing of Hydrogen Peroxide, Mercury Ions and Pesticides. *Chem. Commun.* **2014**, *50*, 5703–5705.

(10) Shen, R.; Liu, P.; Zhang, Y.; Yu, Z.; Chen, X.; Zhou, L.; Nie, B; Żaczek, A.; Chen, J; Liu, J. Sensitive Detection of Single-cell Secreted H_2O_2 by Integrating a Microfluidic Droplet Sensor and Au Nanoclusters. *Anal. Chem.* **2018**, *90*, 4478–4484.

(11) Teng, Y.; Jia, X.; Li, J.; Wang, E. Ratiometric Fluorescence Detection of Tyrosinase Activity and Dopamine using Thiolate-protected Gold Nanoclusters. *Anal. Chem.* **2015**, *87*, 4897–4902.

(12) Polavarapu, L.; Manna, M.; Xu, Q. H. Biocompatible Glutathione Capped Gold Clusters as One−and Two−Photon Excitation Fluorescence Contrast Agents for Live Cells Imaging. *Nanoscale* **2011**, *3*, 429–434.

(13) Zheng, K.; Setyawati, M. I.; Leong, D. T.; Xie, J. Surface Ligand Chemistry of Gold Nanoclusters Determines Their Antimicrobial Ability. *Chem. Mater.* **2018**, *30*, 2800–2808.

(14) Zheng, K.; Setyawati, M. I.; Leong, D. T.; Xie, J. Antimicrobial Gold Nanoclusters. *ACS Nano* **2017**, *11*, 6904–6910.

(15) Kang, X.; Zhu, M. Tailoring the photoluminescence of atomically precise nanoclusters. *Chem. Soc. Rev.* **2019**, *48*, 2422–2457.

(16) Bigioni, T. P.; Whetten, R. L.; Dag, O. Near-infrared Luminescence from Small Gold Nanocrystals. *J. Phys. Chem. B* **2000**, *104*, 6983−6986.

(17) Link, S.; Beeby, A.; FitzGerald, S.; El-Sayed, M. A.; Schaaff, T. G.; Whetten, R. L. Visible to Infrared Luminescence from a 28-Atom Gold Cluster. *J. Phys. Chem. B* **2002**, *106*, 3410−3415.

(18) Aikens, C. M. Origin of Discrete Optical Absorption Spectra of $M_{25}(SH)_{18}^-$

Nanoparticles (M = Au, Ag). *J. Phys. Chem. C* **2008**, *112*, 19797−19800.

(19) Wu, Z.; Jin, R. On the Ligand's Role in the Fluorescence of Gold Nanoclusters. *Nano Lett.* **2010**, *10*, 2568−2573.

(20) Qian, H.; Sfeir, M. Y.; Jin, R. Ultrafast Relaxation Dynamics of $[Au_{25}(SR)_{18}]^q$ Nanoclusters: Effects of Charge State. *J. Phys. Chem. C* **2010**, *114*, 19935−19940.

(21) AbdulHalim, L. G.; Bootharaju, M. S.; Tang, Q.; Del Gobbo, S.; AbdulHalim, R. G.; Eddaoudi, M.; Jiang, D. E.; Bakr, O. M. $Ag_{29}(BDT)_{12}(TPP)_4$: A Tetravalent Nanocluster. *J. Am. Chem. Soc.* **2015**, *137*, 11970−11975.

(22) Liu, X.; Yuan, J.; Yao, C.; Chen, J.; Li, L.; Bao, X.; Yang, J.; Wu, Z. Crystal and solution photoluminescence of $MAg_{24}(SR)_{18}$ (M= Ag/Pd/Pt/Au) nanoclusters and some implications for the photoluminescence mechanisms. *J. Phys. Chem. C* **2017**, *121*, 13848−13853.

(23) Kobayashi, N.; Kamei, Y.; Shichibu, Y.; Konishi, K. Protonation-induced Chromism of Pyridylethynyl-Appended [core+exo]-Type Au_8 Clusters. Resonance-coupled Electronic Perturbation through π-Conjugated Group. *J. Am. Chem. Soc.* **2013**, *135*, 16078−16081.

(24) Iwasaki, M.; Kobayashi, N.; Shichibu, Y.; Konishi, K. Facile Modulation of Optical Properties of Octagold Clusters through the Control of Ligand-mediated Interactions. *Phys. Chem. Chem. Phys.* **2016**, *18*, 19433−19439.

(25) Huang, Z.; Ishida, Y.; Yonezawa, T. Basic $[Au_{25}(SCH_2CH_2Py)_{18}]^-\cdot Na^+$ Clusters: Synthesis, Layered Crystallographic Arrangement, and Unique Surface Protonation. *Angew. Chem., Int. Ed.* **2019**, *58*, 13411−13415.

(26) Parker, J. F.; Weaver, J. E.; McCallum, F.; Fields−Zinna, C. A.; Murray, R. W. Synthesis of Monodisperse $[Oct_4N^+][Au_{25}(SR)_{18}^-]$ Nanoparticles, with Some Mechanistic Observations. *Langmuir* **2010**, *26*, 13650−13654.

(27) Zhu, M.; Aikens, C. M.; Hollander, F. J.; Schatz, G. C.; Jin, R. Correlating the Crystal Structure of a Thiol-Protected Au_{25} Cluster and Optical Properties. *J. Am. Chem. Soc.* **2008**, *130*, 5883−5885.

(28) Yuan, X.; Goswami, N.; Chen, W.; Yao, Q.; Xie, J. Insights into the Effect of Surface Ligands on the Optical Properties of Thiolated Au_{25} Nanoclusters. *Chem. Commun.* **2016**, *52*, 5234–5237.

(29) Weerawardene, K. D. M.; Aikens, C. M. Theoretical Insights into the Origin of Photoluminescence of $Au_{25}(SR)_{18}^-$ Nanoparticles. *J. Am. Chem. Soc.* **2016**, *138*, 11202−11210.

(30) Reddy, M. L. P.; Bejoymohandas, K. S. Evolution of 2,3′-Bipyridine Class of Cyclometalating Ligands as Efficient Phosphorescent Iridium (III) Emitters for Applications in Organic Light Emitting Diodes. *J. Photoch. Photobio. C* **2016**, *29*, 29−47.

Appendix III: Supporting Information

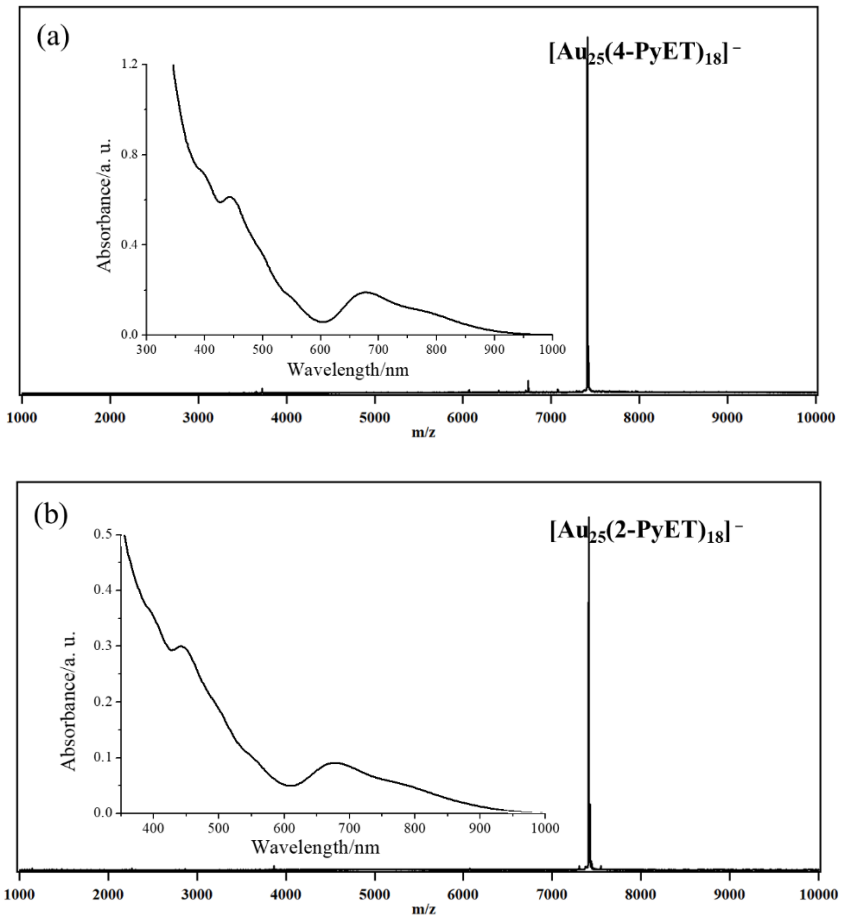

Figure S4.1 UV-vis absorption and negative-mode ESI mass spectra of the Au_{25}(4-PyET)$_{18}$ (a), and Au_{25}(2-PyET)$_{18}$ (b) NCs.

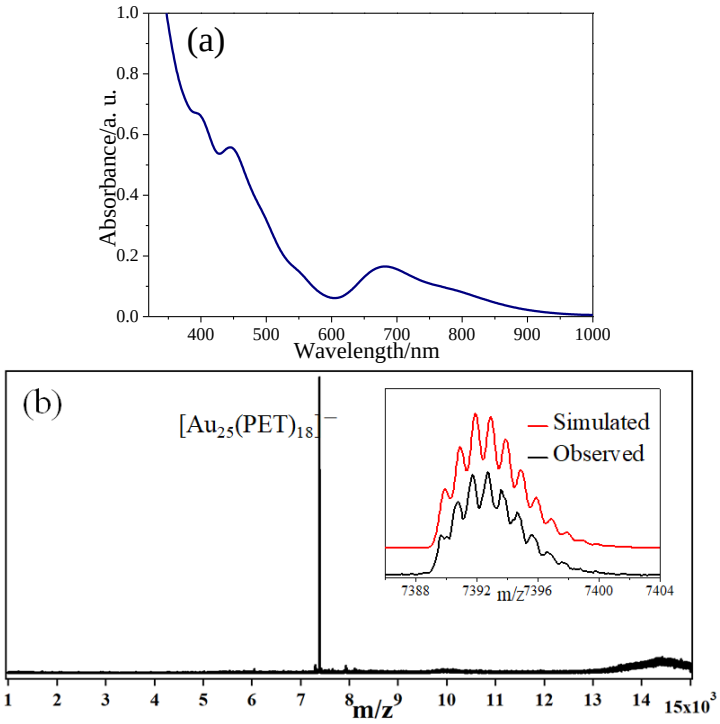

Figure S4.2 UV-vis absorption (a), and negative-mode ESI mass spectra (b) of the $Au_{25}(PET)_{18}$ NCs.

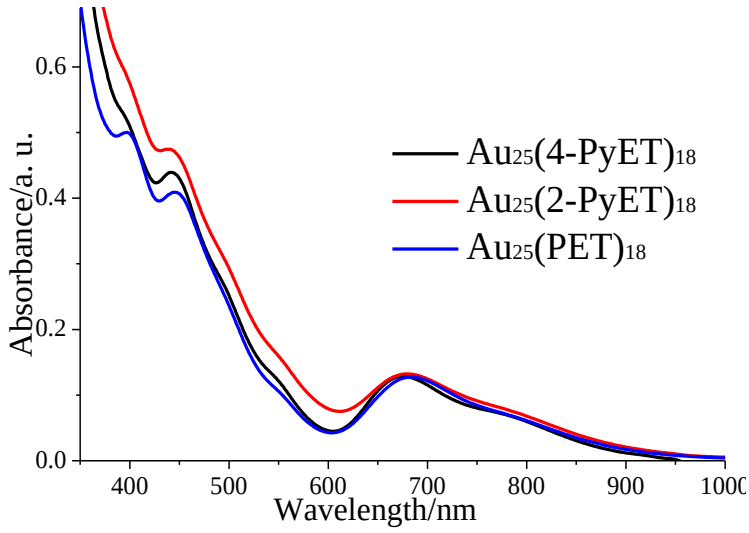

Figure S4.3 UV-vis absorption spectra of $[Au_{25}(4\text{-}PyET)_{18}]^-$, $[Au_{25}(2\text{-}PyET)_{18}]^-$ and $[Au_{25}(PET)_{18}]^-$ in 10-mm quartz cuvette with the concentration of 100 μg/mL.

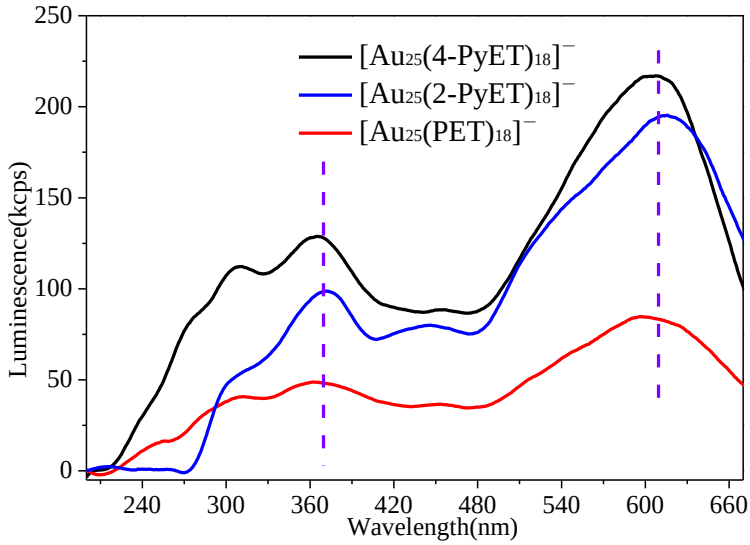

Figure S4.4 Excitation spectra of $[Au_{25}(SR)_{18}]^-$ with different aromatic rings (PET, 4-PyET and 2-PyET). The excitation spectra were measured at λ_{max} = 719 nm.

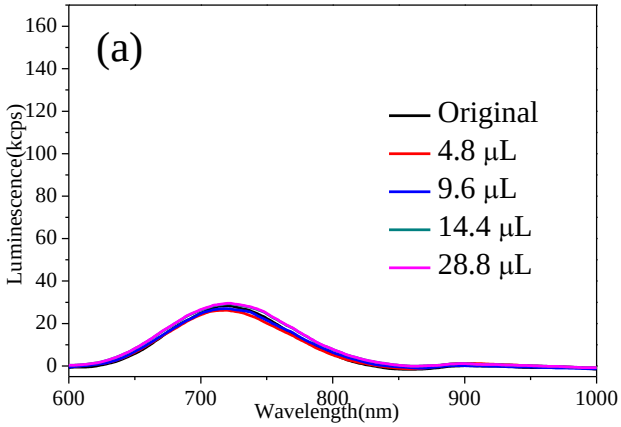

Figure S4.5 Photoluminescence spectra of $Au_{25}(PET)_{18}$ upon the addition of HCl (methanol, 500 mM) (Solvent: toluene; excitation: 365 nm; solution concentration: 100 μg/mL)

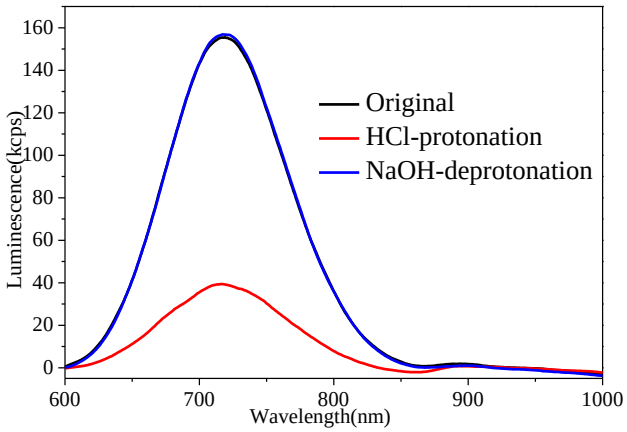

Figure S4.6 Reversible protonation reaction of the photoluminescence ((λ_{ex} = 365 nm) on Au_{25}(4-PyET)$_{18}$NCs.

Chapter 5

Menshutkin Reaction on Noble Metal Clusters: A Facile Route to Cationized $Au_{25}(SR)_{18}$ Cluster

Abstract

Interfacial surface chemistry on atomically-precise metal clusters is rarely reported, but can provide a new platform for the functionalization of clusters toward enhancing their practical utility. This chapter firstly reports the Menshutkin reactionon $Au_{25}(SCH_2CH_2Py)_{18}$ cluster through the reaction of surface pyridyl (Py) moieties with the dimethyl sulfate, which resulted in the formation of consistently-cationized Au_{25} clusters, i.e., $Au_{25}(4\text{-PyET}{-}CH_3^+)_x(4\text{-PyET})_{18-x}$. A two-step of Menshutkin reaction was conducted, and its process was monitored by UV-vis absorption, ESI-MS and ^{1}H-NMR. The results showed that the surface Py moieties amenable to be methylated into $Py{-}CH_3^+$ can easily achieve the cationization modification of PyET-capped Au_{25} clusters, which opens a facile route to allow the post-assembly of positive charges to metal clusters via surface modification.

5.1 Introduction

Thiolate-protected gold clusters ($Au_m(SR)_n$ cluster) with well-defined compositions have provided their potential uses in catalysis,[1–3] sensing,[4–6] and bioapplications,[7–9] as examples. The surface SR ligands have attracted great recent interest because: (i) the substituent R group affect the magic size (stable number of metal atoms) and

structures of as-prepared clusters,[9–13] and (ii) The pendant R-group on the cluster surface is exposed to solutions and other phases, and therefore its molecular chemistry determines the molecular-like characteristics of clusters to some extent,[14,15] such as the hydrophobicity/hydrophilicity,[16] chirality,[17,18] catalytic activity,[2,19,20] optical properties,[21–23] and interactions with the hosts.[8,9,24,25] Accordingly, R-group on metal clusters holds the key role for rational design of their functional properties and applications.

Among various applications, physicochemical properties of surface ligands of metal clusters are crucial in determining their biological fate and their subsequent uses as nanomedicine. In the biological applications of the conventional Au nanoparticles (differentiating from the atomically-precise clusters), positively-charged moieties are incorporated on the surface to cater the long-held belief that these moieties would yield intimate interactions with the negatively-charged contents.[26–30] Based on this, the R-group bearing positive charge should also show good affinity of clusters to biomaterials. However, to the best of my knowledge, except one work by Xie's group that tuning the ratio of −COOH to $-NH_2$ groups for the antimicrobial ability of Au_{25}cluster, there is no other application research on the cationic Au clusters.[8] It is reasonable to speculate that the infrequent synthetic works (especially with high yield and purity) for cationized Au clusters is the bottleneck in this field.

The syntheses of Au clusters have been reported with using amino-terminated SR ligands, $HSPhNH_2$, $HSCH_2CH_2NH_2$ and $HS(CH_2)_2N(CH_3)_2$.[31–34] In my recent work,[35] high-purity $Au_{25}(PyET)_{18}$ clusters (PyET, $-SCH_2CH_2Py$) were successfully synthesized for the first time. Similar to the $-NH_2$ group, the protonation reaction can result in Py-termini being cationic in acidic condition, whereas it arises one problem

that both $-NH_2$ and −Py group are neutral in alkaline case. Such phenomenon counts on the synthesis of metal clusters by using the consistently-cationized SR ligands. From this, Ishida *et al*. directly synthesized Au_{25} and Au_{144} clusters utilizing a SR ligand with the pendant quaternary-ammonium group $-[N(CH_3)_3]^+$ that is positively-charged in any conditions. [36–38]

Scheme 5.1 Menshutkin reaction on the surface of $Au_{25}(PyET)_{18}$ clusters.

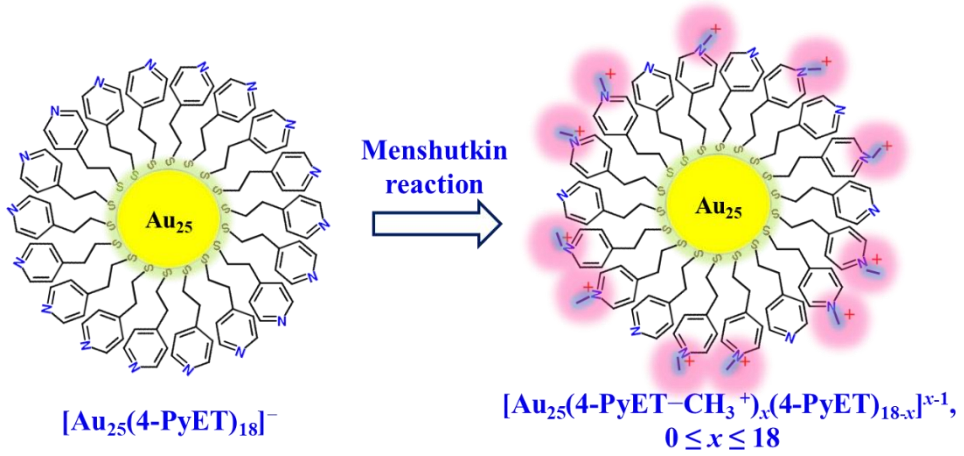

Menshutkin reaction, a bimolecular nucleophilic substitution (S_N2) reaction first described by Nikolai Menshutkin in 1890,[39] is a common method to quaternary ammonium salt ($-[N(CH_3)_3]^+$) by reaction with an alkylating agent, which involves developing of charge separation along the reaction pathway. In present work, on the basis of my recent successful work[35] (Chapter Three) for the Au_{25} clusters capped by $-SCH_2CH_2Py$ ligands, I investigated the Menshutkin reaction, $-SCH_2CH_2Py + H_3C-R = -[SCH_2CH_2Py-CH_3]^+ + R^-$, on the Au_{25} clusters surface (Scheme 5.1).A two-step Menshutkin reaction was monitored by UV-vis absorption and ESI-MS characterizations, and ^{1}H-NMR was used to further confirm the formation of $-Py-CH_3^+$ moiety on cluster surface.

5.2 Experimental section

5.2.1 Chemicals

Hydrogen tetrachloroaurate (III) ($HAuCl_4 \cdot 4H_2O$, > 99.99%, Wako Pure Chemical Industries, Ltd), 2-(4-pyridinyl)ethanethiol hydrochloride (4-PyET·HCl, $C_7H_{10}ClNS$, > 97%, Tokyo Chemical Industry Co., Ltd), sodium borohydride ($NaBH_4$, 99%, Wako Pure Chemical Industries, Ltd), sodium hydroxide (NaOH, > 97%, Junsei Chemical Co., Ltd), hydrochloric acid (HCl, 35%~37%, Kanto Chemical Co., Ltd), dimethyl sulfate (Me_2SO_4, $C_2H_6O_4S$, > 98%, Tokyo Chemical Industry Co., Ltd). HPLC-grade solvents such as tetrahydrofuran (THF), methanol (MeOH), *N*,*N*-dimethylformamide (DMF), diethyl ether and dichloromethane (DCM) were purchased from Kanto Chemical. Deionized pure water (> 18.2 MΩ) was prepared by an Organo/ELGA purelab system.

5.2.2 Synthesis of Au_{25}(4-PyET)$_{18}$ Cluster

The synthesis of $Au_{25}(4\text{-PyET})_{18}$ were following my recent works.[35] In brief, 8 mL of 4-PyET solution (MeOH, 100 mM) was added dropwise into 24 mL of $HAuCl_4$ solution (THF, 6.7 mM; 4-PyET : Au = 5:1 in molar ratio). The mixture changed into light reddish cloudy suspension, and then into white cloudy suspension during 4-PyET dropping. After overnight stirring, 1.6 mL of the fresh-made $NaBH_4$ solution (1.6 mmol, $NaBH_4$:Au = 5:1 in molar ratio; prepared by dissolving 189.2 mg of $NaBH_4$ in 5 mL of cold pure water) was rapidly added to the suspension under vigorous stirring. The color of the solution immediately turned black after addition of $NaBH_4$. Finally, the etching process was allowed to continue for at least 48 hours. Over the long time of etching process, the solution color would become dark brown

slowly, suggesting the formation of monodisperse Au_{25}(4-PyET)$_{18}$. The crude samples were purified based on the protonated states of the pendant Py moiety on Au_{25} cluster. The detail characterizations for the Au_{25}(4-PyET)$_{18}$cluster are shown in Figure S5.1.

5.2.3 Menshutkin Reaction on Au_{25}(4-PyET)$_{18}$ Cluster

Two-step Menshutkin reaction was investigated in Au_{25}(4-PyET)$_{18}$ cluster. First-step: in 1 mL DMF solvent with 1 mg/mL of Au_{25}(4-PyET)$_{18}$ cluster (~2.4 μmol), liquid Me_2SO_4 (23 μL, ~240 μmol) were added in the mole ratio of Me_2SO_4:4-PyET = 100:1. The mixture was stirred at 500 rpm for different reaction time (5 min, 30 min, 1 h, 2h, 4h and 6 h), and then conducted by UV-vis absorption using a quartz cuvette with a 10-mm optical path. Each batch was first precipitated by dimethyl ether (3 mL), and then washed by DCM (3 mL) twice. The collected samples were vacuum-dried at room temperature for further characterizations.

Second-step: the above collected sample (2 h reaction) was redissolved in 1 mL DMF, and another 23 μL of Me_2SO_4 was added for difference reaction time, as same to the case of first-step. Each batch was tested by UV-vis spectra, and then purified for further characterizations.

5.2.4 Characterization

UV-vis absorption spectra of samples were recorded using a JASCO V-630 spectrophotometer. Photoluminescent measurements were conducted using a JASCO FP-6600 spectrofluorometer. Electrospray-ionization mass spectrometry (ESI-MS) was performed using a Bruker DaltonicsmicrOTOF-HS mass spectrometer. The purified sample, dissolved in methanol (~100 μg/mL), was directly infused at 4 $mL \cdot min^{-1}$. The nebulizer pressure was set to 1.5 bar, and the sheath gas was set to 4.0 L/min. The dry temperature was kept at 120°C. The electrospray emitter potential was

held at –4500 V (negative mode) and 4500 V (positive mode). The capillary exit, skimmer 1, hexapole 1, skimmer 2 voltage settings were 200, 50, 25, and 28 V, respectively. The lens 1 transfer and lens 1 pre puls storage were set at 160, and 30 μs, respectively. ^{1}H-NMR analyses were performed on a JMTC-400/54/SS (JEOL) spectrometer operating at 400 MHz.

5.3 Results and discussion

5.3.1 First-Step Menshutkin Reaction

In 1.0 mL Au_{25}(4-PyET)$_{18}$-DMF solution (1.0 mg/mL), dimethyl sulfate (Me_2SO_4, 23 μL, which is 100 times as high as the mole ratio of surface 4-PyET ligands) was added, and the process was firstly monitored by UV-vis absorption spectroscopy. As presented in Figure 5.1a, the characteristic absorption peaks of Au_{25} cluster at ~400 and 560 nm had a slight increase, whereas the peaks at ~450, 670 and 780 nm showed a slight decrease in 60 min reaction. Interestingly, such absorption changes were also observed when the Au_{25}(4-PyET)$_{18}$ cluster was treated with H^+, in which a reversible protonation of Py-group gives its positive form, $-C_5H_4NH^+$. These results indicate that the geometric structure of Au_{25}(4-PyET)$_{18}$ cluster might have a slight distortion, caused by the surface charge anisotropy[22,35] when the positive charges (H^+ or $[N-CH_3]^+$ in present work) were distributed on the surface of Au_{25} cluster. This indicated that the surface 4-PyET ligands were methylated on Py-group through the Menshutkin reaction (Scheme 5.1). Further increasing the reaction to 120 min and 240 min, the absorption peaks show the negligible change, suggesting the good stability of the methylated (or cationized) Au_{25} clusters.

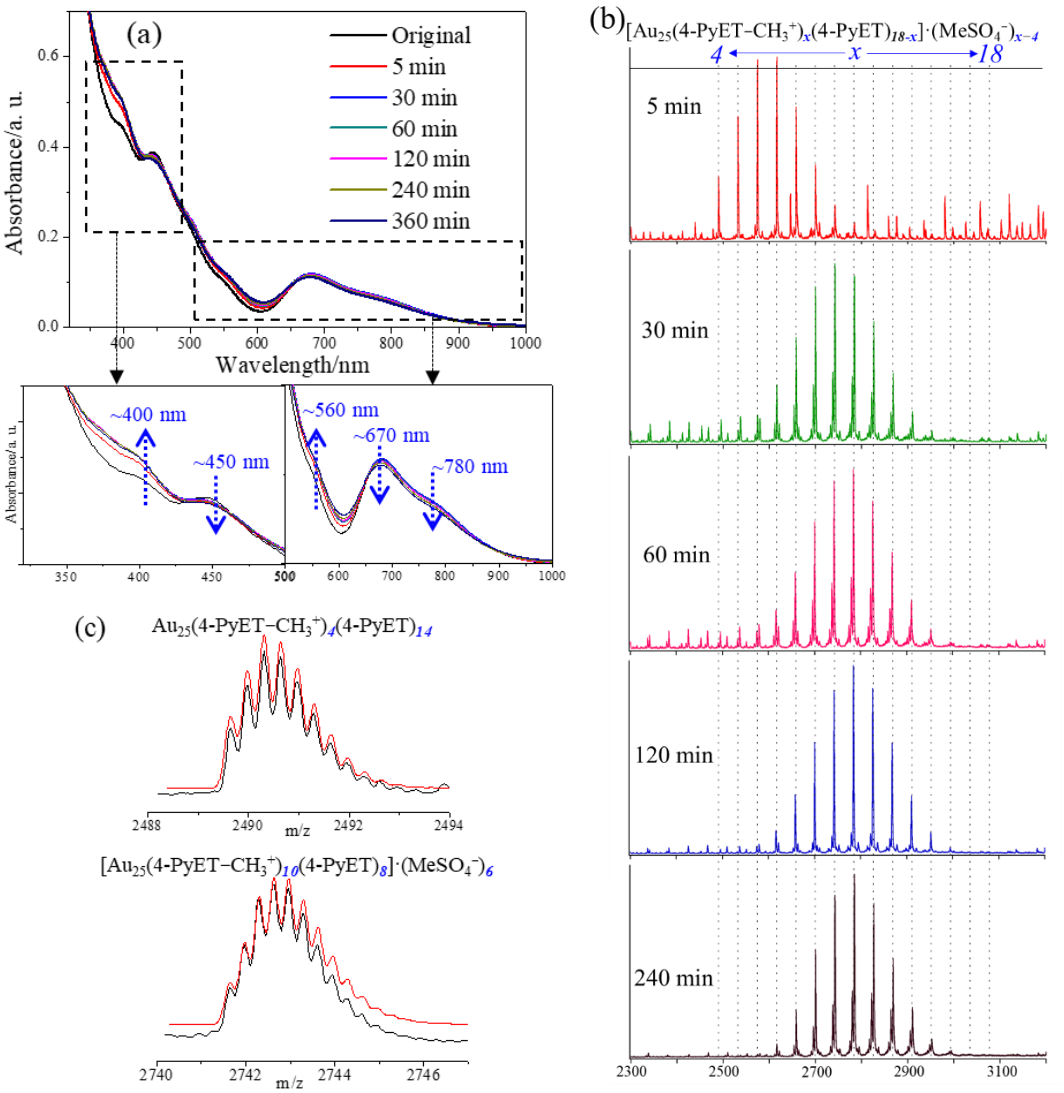

Figure 5.1 (a) UV−vis absorption, (b) positive-mode ESI mass spectra of group III (2300−3200 m/z) of samples collected at different times during first-step Menshutkin reaction, and (c) expanded high-resolution ESI mass spectra (black) and simulated isotope patterns (red) of two representative peaks (x = 4 and 10, see the others in Figure S5.6).

After reaction in different times, each batch of sample (1.0 mL) was collected and purified for ESI-MS characterization. Figure S5.2, as an example, presents the UV-vis absorption of the purified samples before and after 120 min reaction. The almost identical peaks indicated the purification process could completely collect the

cationized clusters. Since the initial $[Au_{25}(4\text{-PyET})_{18}]^-$ is negatively charged, I first monitored the time course of the Menshutkin reaction by negative-mode ESI-MS. As shown in Figure S5.1, only one peak located at ~7411.97 *m/z* was observed in the spectrum of the initial compound, which corresponds to the starting $[Au_{25}(4\text{-PyET})_{18}]^-$. Following the Menshukin reaction, only after 5 min reaction, the starting$[Au_{25}(4\text{-PyET})_{18}]^-$ clusters disappeared, instead of the resulting cationized clusters, $[Au_{25}(4\text{-PyET}{-}CH_3^+)_x(4\text{-PyET})_{18-x}(MeSO_4^-)_{x+1}]^{2-}$ ($2 \leq x \leq 17$, Figure S5.3 and Table S5.1), were observed by negative-mode ESI-MS. This indicated that all initial Au_{25}clusters had been consumed in a very short time of 5 min.

Figure 5.1b displays positive-mode ESI-MS of the sample after Menshutkin reaction of different time (5, 30, 60 120 and 240 min). The full spectrum in Figure S4a displays prominent groups of peaks for +2 (group II, 3500–4700 *m/z*, Figure S5.5a), +2 (group III, 2300–3200 *m/z*, Figure 5.1b), and +3 (group IV, 1800–2300 *m/z*, Figure S5.5b) charged states; the corresponding detailed assignments and isotope patterns are presented in Table S5.2–4 and Figure S5.6, respectively. Figure 5.1b, as an example, shows the *x* value of the cationized Au_{25} clusters with +3 charge state. The cationized Au_{25} clusters, $[Au_{25}(4\text{-PyET}{-}CH_3^+)_x(4\text{-PyET})_{18-x}(MeSO_4^-)_y]^{3+}$ ($4 \leq x \leq 18$, $y = x–1$) were successfully characterized by positive-mode ESI-MS. After 5 min reaction, the *x* was distributed between 4 and 12. When increasing the reaction time to 30, 60 and 120 min, *x* values were observed to increase: x = 4–15, 5–16, and 7–16, respectively, suggesting the extent of Menshutkin reaction would proceed along the reaction time. Further prolonging the reaction time to 240 min, the *x* value still ranges from 7 to 16. Expanded ESI mass spectra of the two representative peaks, $Au_{25}(4\text{-PyET}{-}CH_3^+)_4(4\text{-PyET})_{14}$ (x = 4) and $[Au_{25}(4\text{-PyET}{-}CH_3^+)_{10}(4\text{-PyET})_8]\cdot(MeSO_4^-)_6$ (x = 10), are

presented in Figure 5.1c, along with the simulated isotope patterns (red); the observed isotope patterns (black) are well matched to those simulated. The expanded ESI mass spectra of the remaining observed peaks are summarized in Figure S5.6 in the Supporting Information. Based on these, it can be concluded that through Menshutkin reaction, the surface 4-PyET of Au_{25} clusters can be easily methylated into cationic 4-PyET$-CH_3^+$, which is a facile way to the cationized Au_{25} clusters.

5.3.2 Second-Step Menshutkin Reaction

Based on above reaction, one problem arises that, since the partially-methylated Au_{25} have a good stability (Figure 5.1a), is it possible to further kinetically promote the Menshutkin reaction, aiming to achieve the completely-methylated Au_{25}(4-PyET$-CH_3^+)_{18}$ clusters? Thus, inspired by the ligand-exchange reaction, in which two-step reaction was often used to completely exchange the surface ligands,[40,41] I carried out a second-step Menshutkin reaction by using the sample after 120 min first-step reaction. The purified product was redissolved in 1.0 mL DMF, and same amount of Me_2SO_4 (23 μL) was included for reaction. The reaction process was also monitored by UV-vis absorption and ESI-MS spectra, as shown in Figure 5.2.

Figure 5.2a shows the characteristic Au_{25} cluster absorption peaks located at 400, 450, 670, and 780 nm decreased in intensity with prolonged reaction time. I did not observe any precipitation during reaction; consequently, the observed decrease in absorbance is indicative of the decomposition of the Au_{25} clusters. This observation is different from the first-step reaction (Figure 5.1a), where absorbances were almost maintained for 240 min reactions. These results indicated that the Au_{25} clusters became unstable during the second-step Menshukin reaction, especially for reaction times in excess of 60 min.

Figure 5.2b displays positive-mode ESI mass spectra of the sample (group III, 2300–3200 *m/z,* see the full spectrum in Figure S5.4b) during the second-step Menshutkin reaction. The cationized Au_{25} clusters, $[Au_{25}(4\text{-PyET}{-}CH_3^+)_x(4\text{-PyET})_{18-x}(MeSO_4^-)_y]^{x-y-1}$ ($0 \leq x \leq 18$, $y < x$), shows the x value of 8 to 18 in 5 min, which is higher than that of 7–16 in 120 min of first-step reaction. However, further prolonging the reaction time to 30, 60, 120 and 240 min, the x value range did not show the significant change, and the $[Au_{25}(4\text{-PyET}{-}CH_3^+)_{14}(4\text{-PyET})_4(MeSO_4^-)_{10}]^{3+}$ is the most-abundant species. The observed spectra for the completely-methylated cluster, $[Au_{25}(4\text{-PyET}{-}CH_3^+)_{18}]\cdot(MeSO_4^-)_{14}$ (x = 18) and most-abundant one, $[Au_{25}(4\text{-PyET}{-}CH_3^+)_{14}(4\text{-PyET})_4]\cdot(MeSO_4^-)_{10}$ (x = 14) are well matched with their simulated isotope patterns shown in Figure 5.2c (the remaining expanded spectra are displayed in Figure S5.6). Noting the reaction times in excess of 60 min resulted in spectra that contained peaks corresponding to fragments that arise from the missing of $-CH_3^+$ groups in cationizedAu_{25} clusters, were observed in the spectra of these samples at 60–240 min, as shown in the inset of Figure 5.2b.

Unfortunately, although the weak peaks, corresponding to the completely-methylated $Au_{25}(4\text{-PyET}{-}CH_3^+)_{18}$ species (indicated by red circles), could be detected by mass spectroscopy, the most abundant species were still the cationized Au_{25} clusters with x = 13 or 14. In the present work, we were not able to achieve a complete Menshutkin reaction on Au_{25} clusters. Instead, the second-step methylation of surface 4-PyET ligands will strongly decrease the stability of Au_{25} clusters. The reason for it might be similar to my lab's previous reports[36,37] on the synthesis of the fully-cationic $Au_{25}(SR^+)_{18}$ cluster and cationic-ligand-exchange reaction[42] using the cationic thiol. When the positive charges ($N{-}CH_3^+$) highly accumulate on Au_{25} cluster surface, the

Coulombic repulsions among $N{-}CH_3^+$ moieties decrease the stability of clusters, especially after most of surface 4-PyET ligands had been methylated, making the Menshutkin reaction difficult to further proceed until complete.

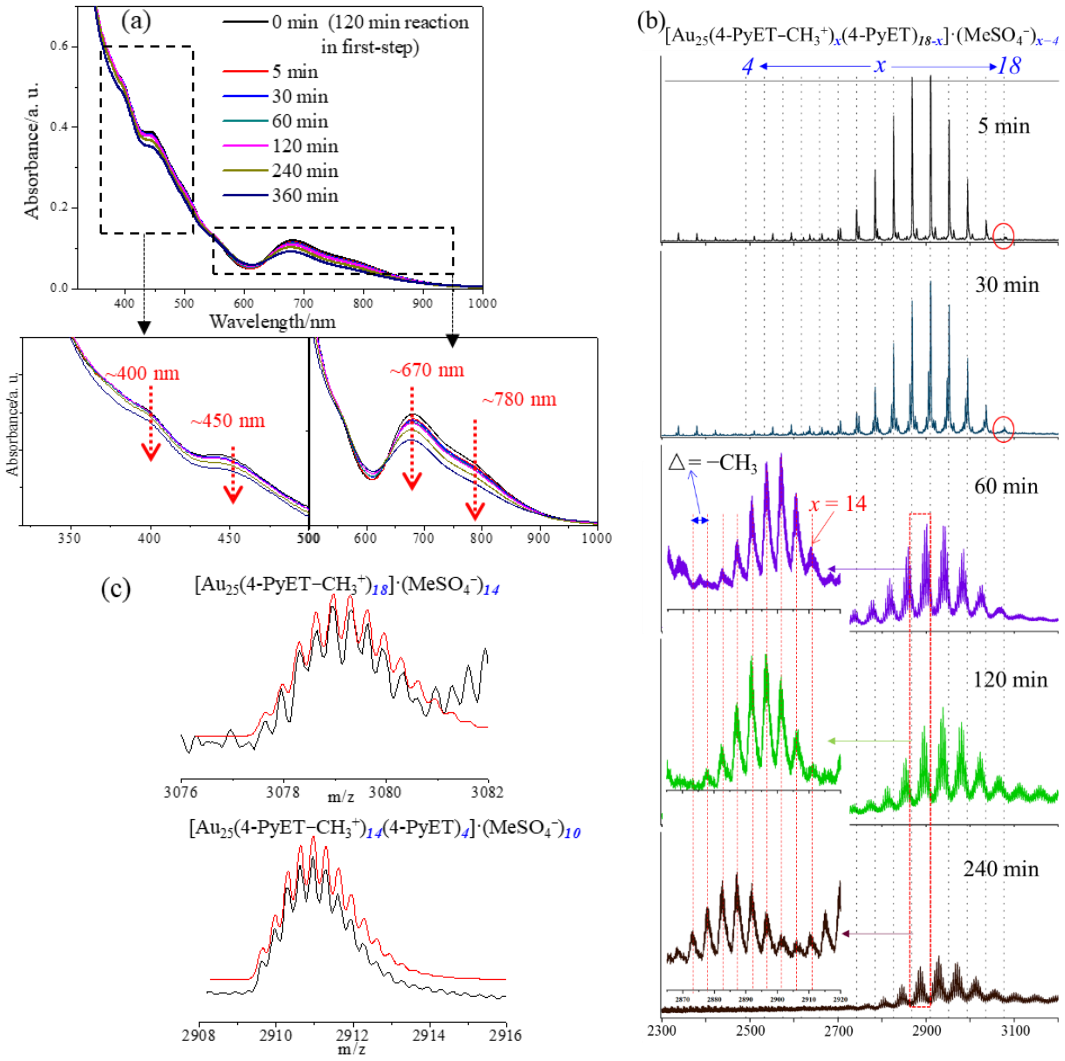

Figure 5.2 (a) UV−vis absorption, (b) positive-mode ESI mass spectra of group III (2300−3200 m/z) of samples collected at different times during second-step Menshutkin reaction. The purified sample after first-step 120 min reaction was used as the starting sample of second-step reaction, and (c) expanded high-resolution ESI mass spectra (black) and simulated isotope patterns (red) of representative peaks (x = 18 and 14, see the others in Figure S5.6).

5.3.3 ^{1}H-NMR Spectroscopy

From above ESI-MS results, the Au_{25}(4-PyET−CH_3^+)$_x$(4-PyET)$_{18-x}$ ($6 \leq x \leq 18$) species were mainly detected with attaching the $MeSO_4^-$ ions, it is questionable that the surface 4-PyET was probably not be methylated, the Me_2SO_4 molecules directly combined the Au_{25} clusters, and resulting in the uniformly-spaced peaks in Figure 5.1b and 5.2b. In order to further confirm the formation of methylated 4-PyET−CH_3^+ ligands on cluster surface, ^{1}H-NMR was carried out for the original Au_{25}(4-PyET)$_{18}$ cluster, samples of first-step (2 h) and second-step (2 h) Menshutkin reaction, and pure Me_2SO_4, as presented in Figure 5.3. The structure of the $Au_{25}(SR)_{18}$ clusters is consisted of an icosahedral Au_{13} kernel and six $Au_2(PyET)_3$ motifs. Therefore, there are two different chemical environments for the 18 4-PyET ligands, i.e., the inner ligands and outer ligands that are present in a ratio of 2:1.[43,44] In present work, I did not achieve the complete methylation, and the as-obtained products are the mixtures of Au_{25}(4-PyET−CH_3^+)$_x$(4-PyET)$_{18-x}$ species. Thus, it should be hard to accurately distinguish the inner/outer ligands. However, after the comparisons of the ^{1}H-NMR data, the following results could be also obtained: 1) the ^{1}H signal of pure Me_2SO_4 at ~3.92 ppm is from the −CH_3 group, which does not occur in the sample of first-step or second-step reaction, suggesting the successful purification to remove Me_2SO_4 molecules in final products. 2) Two strong signals at ~4.36 and 3.62 ppm, respectively corresponding to the −CH_3 groups in 4-PyET−CH_3^+ ligand and counterion $MeSO_4^-$, were detected with the integrals that very close to 1:1 (Figure S5.6). 3) The proton peaks of surface ligands (*m*-CH_2, *o*-CH_2, α-CH_2 and β-CH_2) of the methylated samples were found to shift more downfield than the original cluster, being indicative of the characteristic feature of methylation of pyridyl groups.[45,46]

These results are clearly indicative of the occurrence of Menshutkin reaction, that is, the formation of 4-PyET−CH_3^+ ligands on Au_{25} cluster surface.

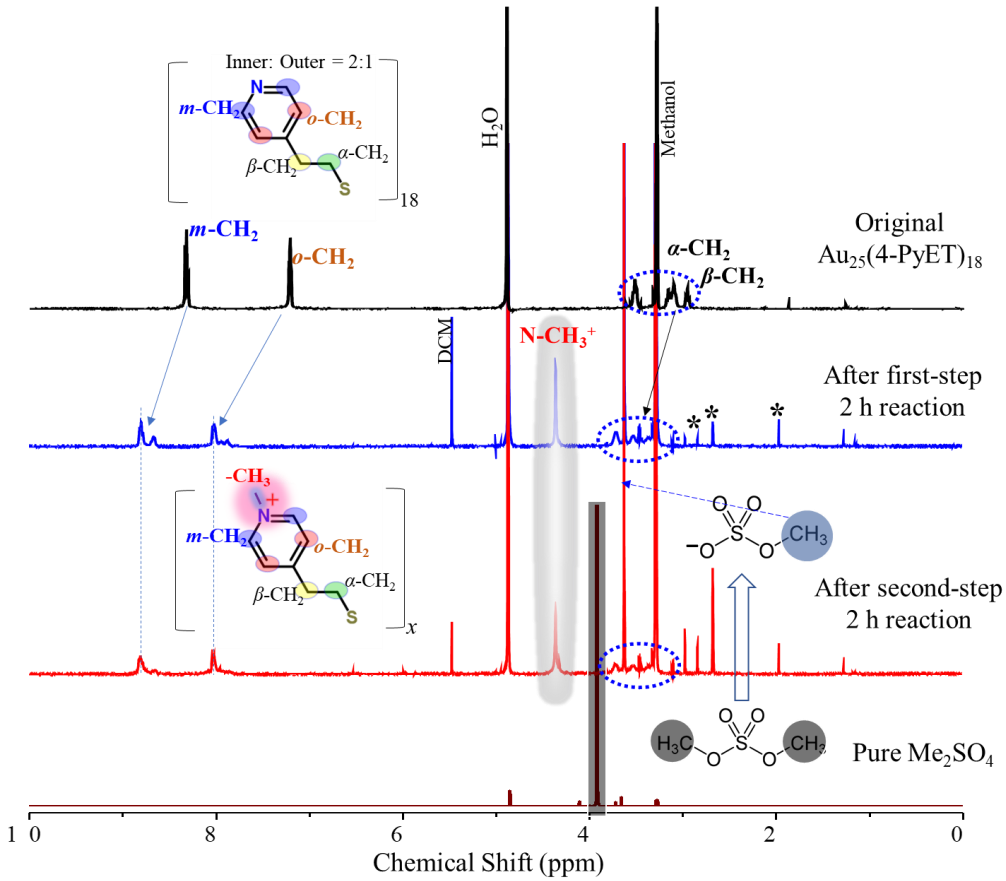

Figure 5.3 ^{1}H-NMR of the original $Au_{25}(4\text{-PyET})_{18}$ cluster, samples of first-step (2 h) and second-step Menshutkin reaction (2 h), and pure Me_2SO_4 in methanol-d_4 at 400 MHz. (* represents the unassigned impurities.)

5.4 Conclusion

In summary, this report describes the Menshutkin reaction of surface 4-PyET ligands on $Au_{25}(4\text{-PyET})_{18}$ clusters. A two-step of reaction process was designed and investigated by UV-vis absorption, ESI-MS and ^{1}H-NMR. The results reveal that the first-step reaction could methylate the 4-PyET ligands, resulting in the formation of

the cationized Au_{25}(4-PyET−CH_3^+)$_x$(4-PyET)$_{18-x}$ clusters showing the good stability. By contract, the second-step reaction had a small boosting on the methylation of the left 4-PyET, whereas the as-obtained Au_{25} clusters became unstable because of the accumulation of positive moieties (N−CH_3^+). The incorporation of a reactive Py group amenable to be methylated can easily transform the neutral PyET-capped metal clusters into the cationized ones, which not only provide a new idea to the cationization modification of metal clusters, but also renders them the starting point for diversifying R-groups of clusters though *in-situ* modification of them.

5.5 References

(1) Li, G.; Jin, R. Atomically Precise Gold Nanoclusters as New Model Catalysts. *Acc. Chem. Res.* **2013**, *46*, 1749–1758.

(2) Wan, X. K.; Wang, J. Q.; Nan, Z. A.; Wang, Q. M. Ligand effects in catalysis by atomically precise gold nanoclusters. *Sci. Adv.* **2017**, *3*, e1701823.

(3) Yan, J.; Teo, B. K.; Zheng, N. Surface Chemistry of Atomically Precise Coinage–Metal Nanoclusters: From Structural Control to Surface Reactivity and Catalysis. *Acc. Chem. Res.* **2018**, *51*, 3084–3093.

(4) Guan, G.; Zhang, S. Y.; Cai, Y.; Liu, S.; Bharathi, M. S.; Low, M.; Yu, Y.; Xie, J.; Zheng, Y.; Zhang, Y. W., Han, M. Y. Convenient Purification of Gold Clusters by Co-Precipitation for Improved Sensing of Hydrogen Peroxide, Mercury Ions and Pesticides. *Chem. Commun.* **2014**, *50*, 5703–5705.

(5) Shen, R., Liu, P., Zhang, Y., Yu, Z., Chen, X., Zhou, L., Nie, B; Żaczek, A.; Chen, J; Liu, J. Sensitive Detection of Single-cell Secreted H_2O_2 by Integrating a Microfluidic Droplet Sensor and Au Nanoclusters. *Anal. Chem.* **2018**, *90*, 4478–4484.

(6) Teng, Y.; Jia, X.; Li, J.; Wang, E. Ratiometric Fluorescence Detection of Tyrosinase Activity and Dopamine using Thiolate-protected Gold Nanoclusters. *Anal. Chem.* **2015**, *87*, 4897–4902.

(7) Polavarapu, L.; Manna, M.; Xu, Q. H. Biocompatible Glutathione Capped Gold Clusters as One−and Two−Photon Excitation Fluorescence Contrast Agents for Live Cells Imaging. *Nanoscale* **2011**, *3*, 429–434.

(8) Zheng, K.; Setyawati, M. I.; Leong, D. T.; Xie, J. Surface Ligand Chemistry of Gold Nanoclusters Determines Their Antimicrobial Ability. *Chem. Mater.* **2018**, *30*, 2800–2808.

(9) Zheng, K.; Setyawati, M. I.; Leong, D. T.; Xie, J. Antimicrobial Gold Nanoclusters. *ACS Nano* **2017**, 11, 6904–6910.

(10) Chen, Y.; Zeng, C.; Kauffman, D. R.; Jin, R. Tuning the Magic Size of Atomically Precise Gold Nanoclusters via Isomeric Methylbenzenethiols. *Nano Lett.* **2015**, *15*, 3603–3609.

(11) Zeng, C.; Li, T.; Das, A.; Rosi, N. L.; Jin, R. Chiral Structure of Thiolate-Protected 28-Gold-Atom Nanocluster Determined by X-ray Crystallography. *J. Am. Chem. Soc.* **2013**, *135*, 10011–10013.

(12) Zeng, C.; Liu, C.; Pei, Y.; Jin, R. Thiol Ligand-Induced Transformation of $Au_{38}(SC_2H_4Ph)_{24}$ to $Au_{36}(SPh\text{-}t\text{-}Bu)_{24}$. *ACS Nano* **2013**, *7*, 6138–6145.

(13) Zeng, C.; Chen, Y.; Kirschbaum, K.; Appavoo, K.; Sfeir, M. Y.; Jin, R. Structural Patterns at All Scales in a Nonmetallic Chiral $Au_{133}(SR)_{52}$ Nanoparticle. *Sci. Adv.* **2015**, *1*, e1500045.

(14) Yan, J.; Teo, B. K.; Zheng, N. Surface Chemistry of Atomically Precise Coinage–Metal Nanoclusters: From Structural Control to Surface Reactivity and Catalysis. *Acc. Chem. Res.* **2018**, *51*, 3084–3093.

(15) Higaki, T.; Li, Q.; Zhou, M.; Zhao, S.; Li, Y., Li, S.; Jin, R. Toward the Tailoring Chemistry of Metal Nanoclusters for Enhancing Functionalities. *Acc. Chem. Res.* **2018**, *51*, 2764–2773.

(16) Ackerson, C. J.; Jadzinsky, P. D.; Kornberg, R. D. Thiolate Ligands for Synthesis of Water-Soluble Gold Clusters. *J. Am. Chem. Soc.* **2005**, *127*, 6550–6551.

(17) Knoppe, S.; Bürgi, T. Chirality in Thiolate-protected Gold Clusters. *Acc. Chem. Res.* **2014**, *47*, 1318–1326.

(18) Wu, Z.; Gayathri, C.; Gil, R. R.; Jin, R. Probing the Structure and Charge State of Glutathione-Capped $Au_{25}(SG)_{18}$ Clusters by NMR and Mass Spectrometry. *J. Am.*

Chem. Soc. **2009**, *131*, 6535–6542.

(19) Yang, H.; Wang, Y.; Lei, J.; Shi, L.; Wu, X.; Makinen, V.; Lin, S.; Tang, Z.; He, J.; Hakkinen, H.; Zheng, L.; Zheng, N. Ligand-Stabilized $Au_{13}Cu_x$ (x = 2, 4, 8) Bimetallic Nanoclusters: Ligand Engineering to Control the Exposure of Metal Sites. *J. Am. Chem. Soc.* **2013**, *135*, 9568–9571.

(20) Yan, J. Z.; Zhang, J.; Chen, X. M.; Malola, S.; Zhou, B.; Selenius, E.; Zhang, X. M.; Yuan, P.; Deng, G. C.; Liu, K. L.; Su, H. F.; Teo, B. K.; Hakkinen, H.; Zheng, L. S.; Zheng, N. F. Thiol-Stabilized Atomically Precise, Superatomic Silver Nanoparticles for Catalyzing Cycloisomerization of Alkynyl Amines. *Natl. Sci. Rev.* **2018**, *5*, 694–702.

(21) Wu, Z.; Jin, R. On the Ligand's Role in the Fluorescence of Gold Nanoclusters. *Nano Lett.* **2010**, *10*, 2568–2573.

(22) Yuan, X.; Goswami, N.; Chen, W.; Yao, Q.; Xie, J. Insights into the Effect of Surface Ligands on the Optical Properties of Thiolated Au_{25} Nanoclusters. *Chem. Commun.* **2016**, *52*, 5234–5237.

(23) Kang, X.; Zhu, M. Tailoring the Photoluminescence of Atomically Precise Nanoclusters. *Chem. Soc. Rev*. **2019**, *48*, 2422–2457.

(24) Lavenn, C.; Demessence, A.; Tuel, A. Atomically Well-defined $Au_{25}(SR)_{17/18}$ Nanoclusters Deposited on Silica Supports for the Aerobic Epoxidation of Trans-stilbene. *Catal. Today* **2014**, *235*, 72–78.

(25) Ackerson, C. J.; Jadzinsky, P. D.; Jensen, G. J.; Kornberg, R. D. Rigid, Specific, and Discrete Gold Nanoparticle/antibody Conjugates. *J. Am. Chem. Soc.* **2006**, *128*, 2635–2640.

(26) Nel, A. E.; Mädler, L.; Velegol, D.; Xia, T.; Hoek, E. M.; Somasundaran, P.; Klaessig, F.; Castranova, V.; Thompson, M. Understanding biophysicochemical interactions at the nano–bio interface. *Nat. Mater.* **2009**, *8*, 543−557.

(27) Walkey, C. D.; Chan, W. C. Understanding and controlling the interaction of nanomaterials with proteins in a physiological environment. *Chem. Soc. Rev.* **2012**, *41*, 2780−2799.

(28) Petros, R. A.; DeSimone, J. M. Strategies in the design of nanoparticles for therapeutic applications. *Nat. Rev. Drug Discovery* **2010**, *9*, 615−627.

(29) Lundqvist, M.; Stigler, J.; Elia, G.; Lynch, I.; Cedervall, T.; Dawson,K. A. Nanoparticle size and surface properties determine the protein corona with possible implications for biological impacts.*Proc. Natl. Acad. Sci.* **2008**, *105*, 14265−14270.

(30) Le Ouay, B.; Stellacci, F. Antibacterial activity of silver nanoparticles: a surface science insight. *Nano Today* **2015**, *10*, 339−354.

(31) Yuan, X.; Zhang, B.; Luo, Z.; Yao, Q.; Leong, D. T.; Yan, N.; Xie, J. Balancing the Rate of Cluster Growth and Etching for Gram-scale Synthesis of Thiolate-protected Au_{25} Nanoclusters with Atomic Precision. *Angew. Chem., Int. Ed.* **2014**, *53*, 4623–4627.

(32) Lavenn, C.; Albrieux, F.; Bergeret, G.; Chiriac, R.; Delichere, P.; Tuel, A.; Demessence, A. Functionalized Gold Magic Clusters: $Au_{25}(SPhNH_2)_{17}$. *Nanoscale* **2012**, *4*, 7334–7337.

(33) Hoque, M. M.; Black, D. M.; Mayer, K. M.; Dass, A.; Whetten, R. L. The Base Side of Noble Metal Clusters: Efficient Route to Captamino-Gold, $Au_n(–S(CH_2)_2N(CH_3)_2)_p$, n= 25–144. *J. Phys. Chem.* Lett. **2019**, *10*, 3307–3311;

(34) Hoque, M. M.; Dass, A.; Mayer, K. M.; Whetten, R. L. Protein-like Large Gold Clusters Based on the ω-Amino-Thiolate DMAET: Precision Thermal and

Reaction Control Leads to Selective Formation of Cationic Gold Clusters in the Critical Size Range, n= 130–144 Au Atoms. *J. Phys. Chem. C* **2019**, *123*, 14871–14879.

(35) Huang, Z.; Ishida, Y.; Yonezawa, T. Basic $[Au_{25}(SCH_2CH_2Py)_{18}]^{-}\cdot Na^{+}$ Clusters: Synthesis, Layered Crystallographic Arrangement, and Unique Surface Protonation. *Angew. Chem., Int. Ed.* **2019**, *58*, 13411−13415.

(36) Ishida, Y.; Narita, K.; Yonezawa, T.; Whetten, R. L. Fully Cationized Gold Clusters: Synthesis of $Au_{25}(SR^{+})_{18}$. *J. Phys. Chem. Lett.* **2016**, *7*, 3718–3722.

(37) Ishida, Y.; Huang, Y. L.; Yonezawa, T.; Narita, K. Charge Neutralization Strategy: A Novel Synthetic Approach to Fully Cationized Thiolate−Protected $Au_{25}(SR^{+})_{18}$ Clusters with Atomic Precision. *ChemNanoMat* **2017**, *3*, 298−302.

(38) Narita, K; Ishida, Y.; Yonezawa, T; Huang, Z. Super Polycationic Molecular Compounds: $Au_{144}(SR^{+})_{60}$ Clusters. *J. Phys. Chem. C* **2019**, *123*, 21768−21773.

(39) Menschutkin, N. BeiträgezurKenntnis der Affinitätskoeffizienten der Alkylhaloide und der organischen Amine. *Z. Phys. Chem.* **1890**, *5*, 589−600.

(40) Kurashige, W.; Niihori, Y.; Sharma, S.; Negishi, Y. Precise synthesis, functionalization and application of thiolate-protected gold clusters. *Coordin. Chem. Rev.* **2016**, *320*, 238−250.

(41) Kurashige, W.; Yamazoe, S.; Kanehira, K.; Tsukuda, T.; Negishi, Y. Selenolate-protected Au_{38} nanoclusters: Isolation and structural characterization. *J. Phys. Chem. Lett.* **2013**, *4*, 3181−3185.

(42) Huang, Z.; Ishida, Y.; Narita, K; Yonezawa, T. Kinetics of Cationic-Ligand-Exchange Reactions in Au_{25} Nanoclusters. *J. Phys. Chem. C* **2018**, *122*, 18142−18150.

(43) Venzo, A.; Antonello, S.; Gascón, J. A.; Guryanov, I.; Leapman, R. D.; Perera, N. V.; Sousa, A; Zamuner, M.; Zanella, A.; Maran, F. Effect of the Charge State (z= −

1, 0, + 1) on the Nuclear Magnetic Resonance of Monodisperse $Au_{25}[S(CH_2)_2Ph]_{18}^z$ Clusters. *Anal. Chem.* **2011**, *83*, 6355−6362

(44) Qian, H.; Zhu, M.; Gayathri, C.; Gil, R. R.; Jin, R. Chirality in Gold Nanoclusters Probed by NMR Spectroscopy. *ACS Nano* **2011**, *5*, 8935−8942.

(45) Heemstra, J. M.; Moore, J. S. Folding-promoted methylation of a helical DMAP analogue. *J. Am. Chem. Soc.* **2004**, *126*, 1648−1649.

(46) Zhou, Z.; Hauke, C. E.; Song, B.; Li, X.; Stang, P. J.; Cook, T. R. Understanding the Effects of Coordination and Self-Assembly on an Emissive Phenothiazine. *J. Am. Chem. Soc.* **2019**, *141*, 3717−3722.

Appendix IV: Supporting Information

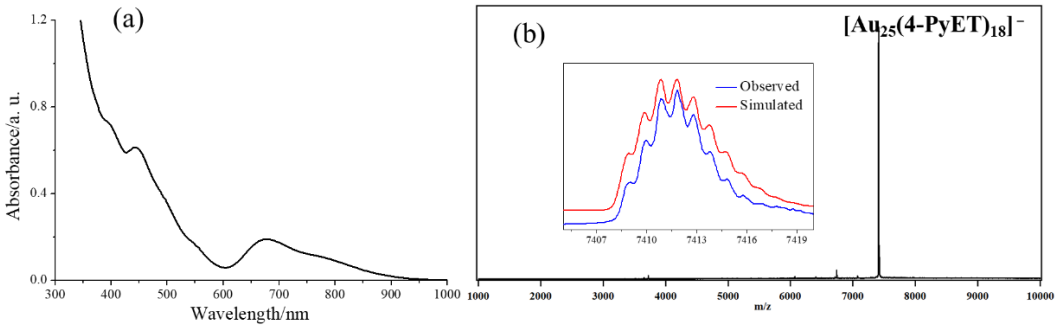

Figure S5.1 (a) UV-vis absorption and (b) negative-mode ESI mass spectra of the original $Au_{25}(4\text{-PyET})_{18}$ clusters. The inset of Figure S1b shows the observed and simulated isotope patterns of $[Au_{25}(4\text{-PyET})_{18}]^{-}$.

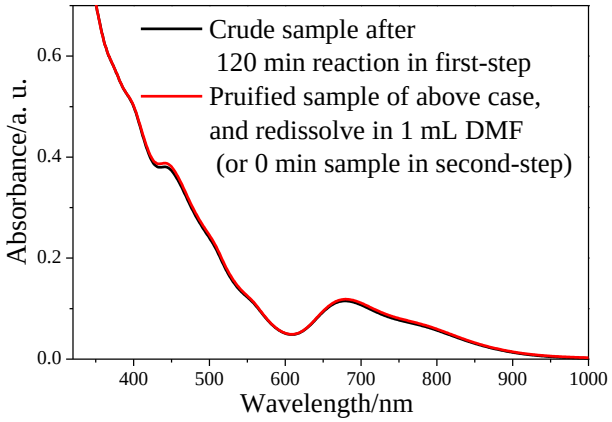

Figure S5.2 UV-vis absorption spectra of before and after purification after 120 min Menshutkin reaction in first-step. Noting that the concentration of starting $Au_{25}(4\text{-PyET})_{18}$ was 1.0 mg/mL (DMF), and after 120 min reaction, 1.0 mL of such sample was purified, and then redissolved in 1.0 mL DMF for UV-vis absorption check.

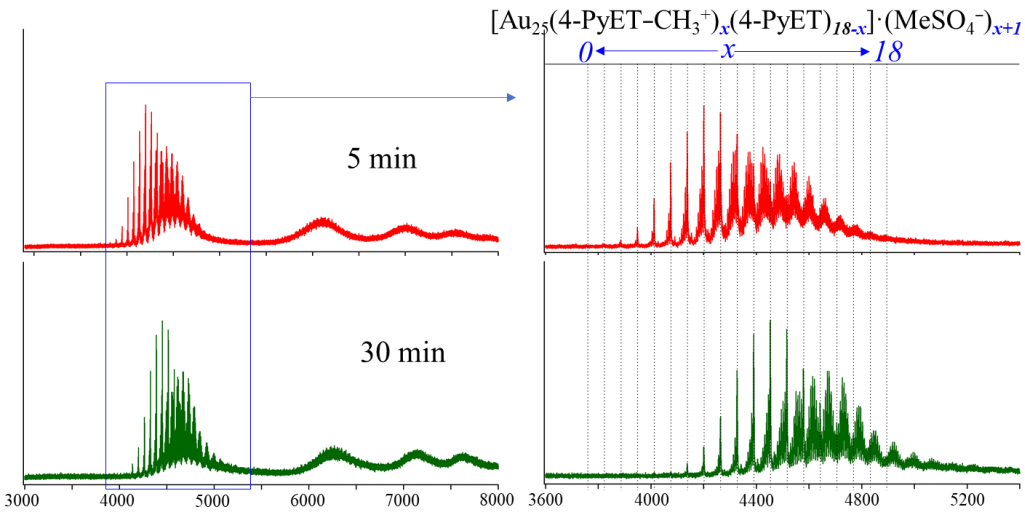

Figure S5.3 Negative-mode ESI mass spectra of samples collected at 5 and 30 min during the first-step Menshutkin reaction.

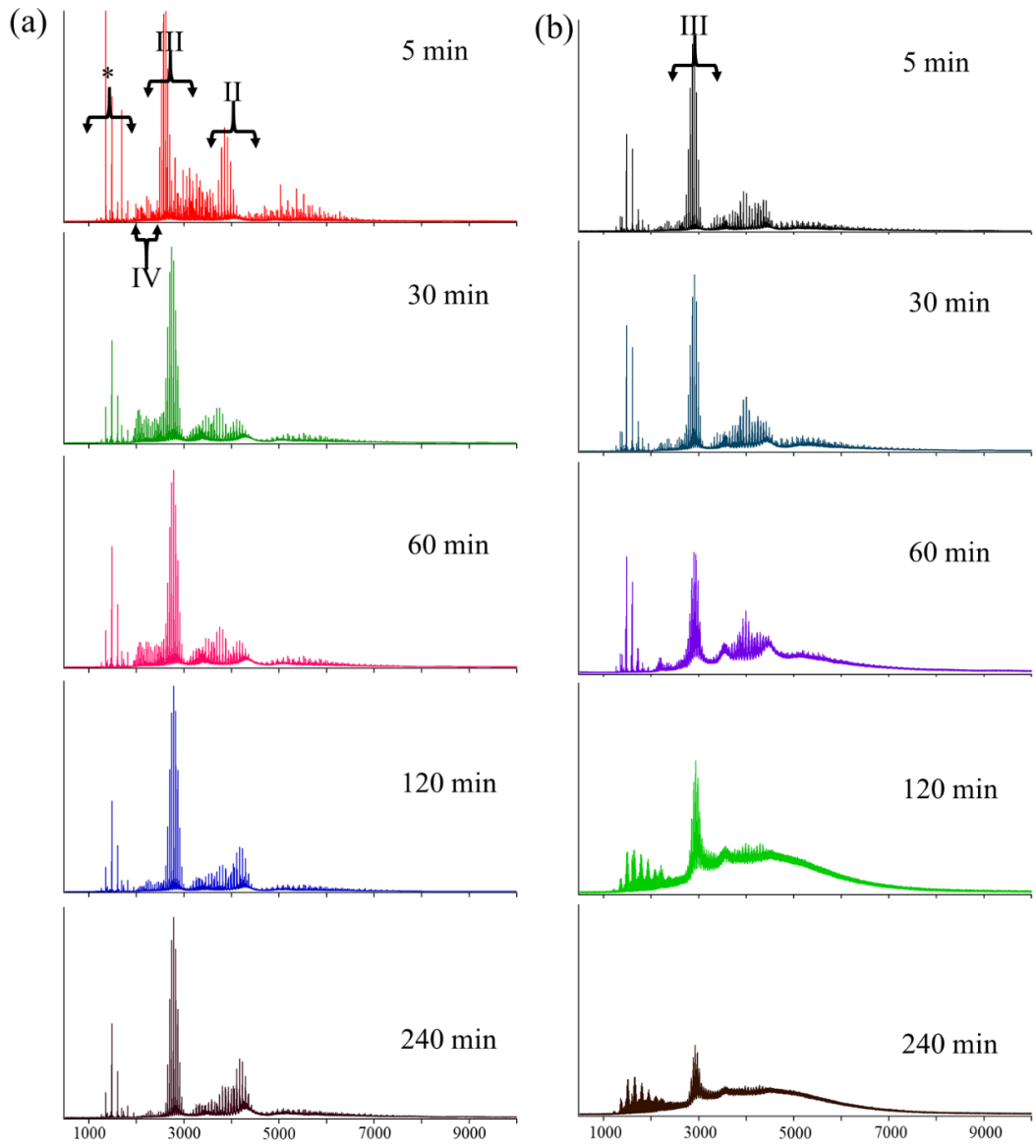

Figure S5.4 Positive-mode ESI mass spectra (a) of samples collected at different times (5, 30, 60, 120 and 240 min) during Menshutkin reaction: (a) first-step reaction; (b) second-step reaction.

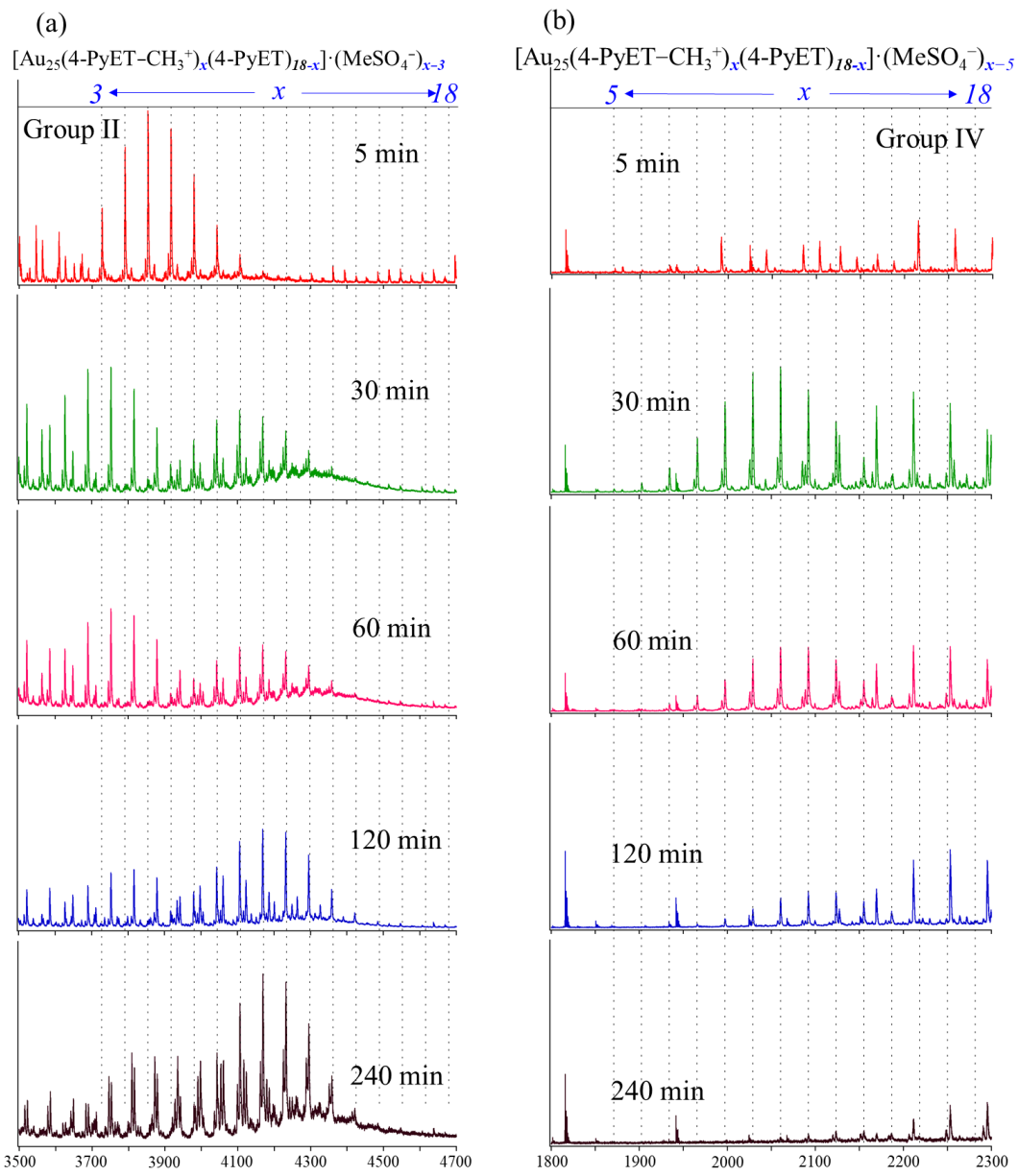

Figure S5.5 Expanded spectra of the regions indicated in Figure S5.3a: (a) Group II with +2 charge (3500−4700 m/z), and (b) Group IV with +4 charge (1800−2300 m/z).

In negative-mode ESI-MS, Au_{25} cluster species with −2 charge (Group −2) shown in Figure S5.3

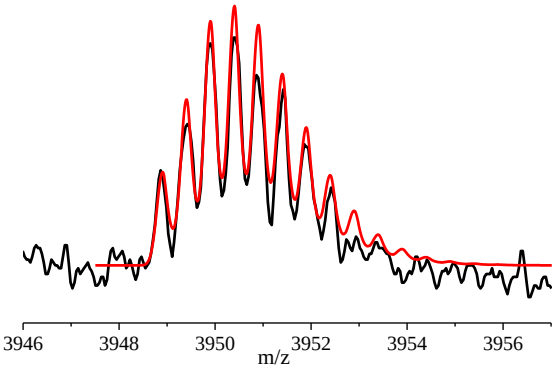

x = 3, $[Au_{25}(4\text{-PyET}{-}CH_3^+)_3(4\text{-PyET})_{15}]\cdot(MeSO_4^-)_4$

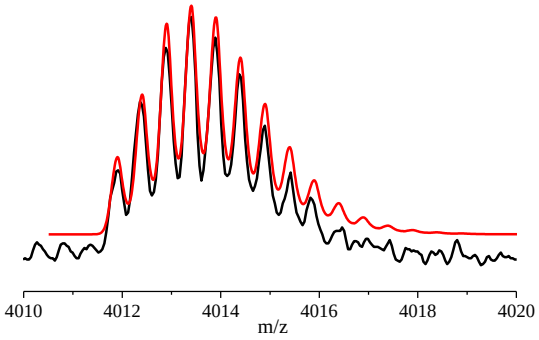

x = 4, $[Au_{25}(4\text{-PyET}{-}CH_3^+)_4(4\text{-PyET})_{14}]\cdot(MeSO_4^-)_5$

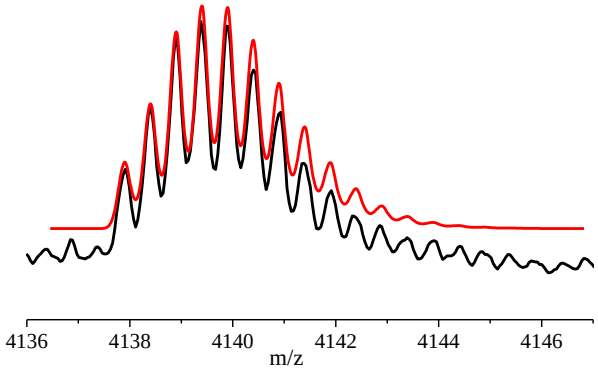

x = 5, $[Au_{25}(4\text{-PyET}{-}CH_3^+)_5(4\text{-PyET})_{13}]\cdot(MeSO_4^-)_6$

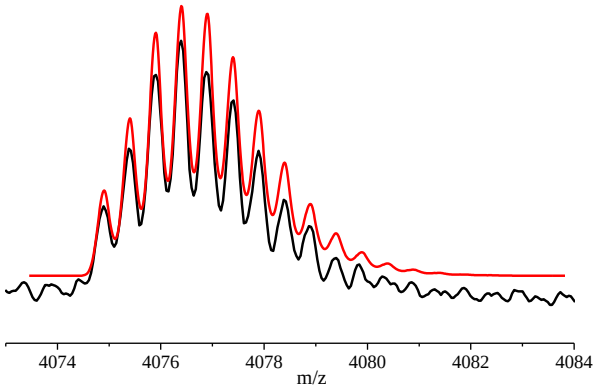

x = 6, $[Au_{25}(4\text{-PyET}{-}CH_3^+)_6(4\text{-PyET})_{12}]\cdot(MeSO_4^-)_7$

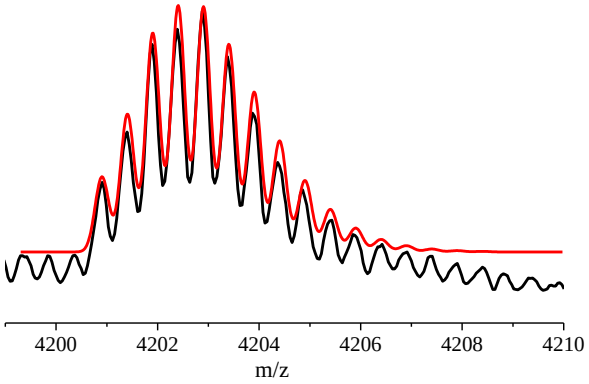

x = 7, $[Au_{25}(4\text{-PyET}{-}CH_3^+)_7(4\text{-PyET})_{11}]\cdot(MeSO_4^-)_8$

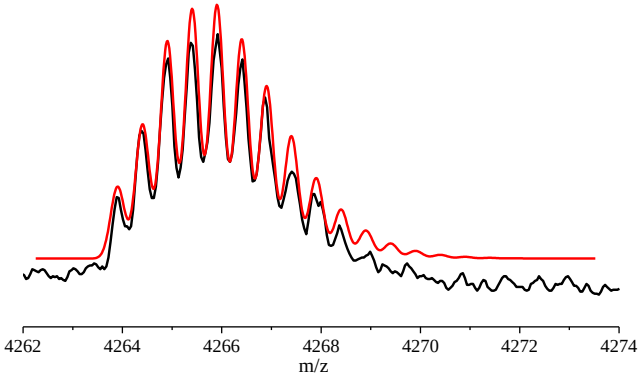

x = 8, $[Au_{25}(4\text{-PyET}{-}CH_3^+)_8(4\text{-PyET})_{10}]\cdot(MeSO_4^-)_9$

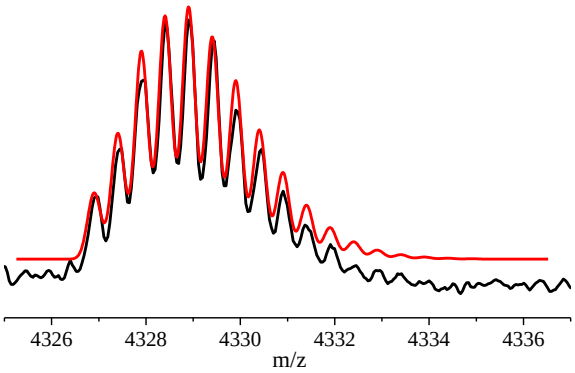

x = 9, $[Au_{25}(4\text{-PyET}{-}CH_3^+)_9(4\text{-PyET})_9]\cdot(MeSO_4^-)_{10}$

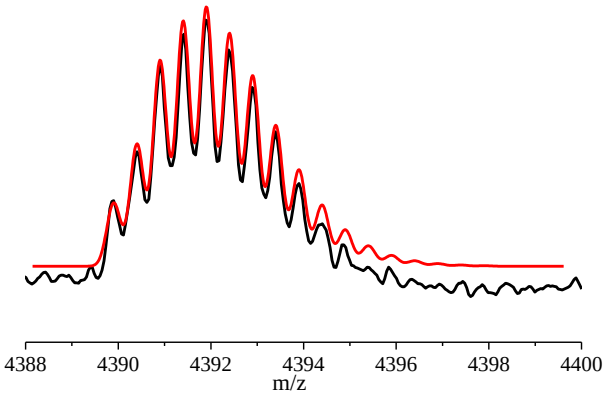

x = 10, $[Au_{25}(4\text{-PyET}{-}CH_3^+)_{10}(4\text{-PyET})_8]\cdot(MeSO_4^-)_{11}$

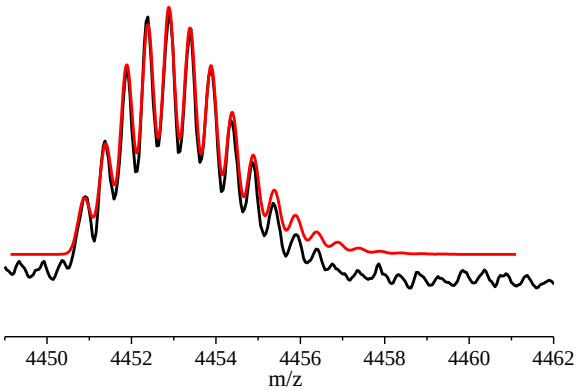

x = 11, $[Au_{25}(4\text{-PyET}{-}CH_3^+)_{11}(4\text{-PyET})_7]\cdot(MeSO_4^-)_{12}$

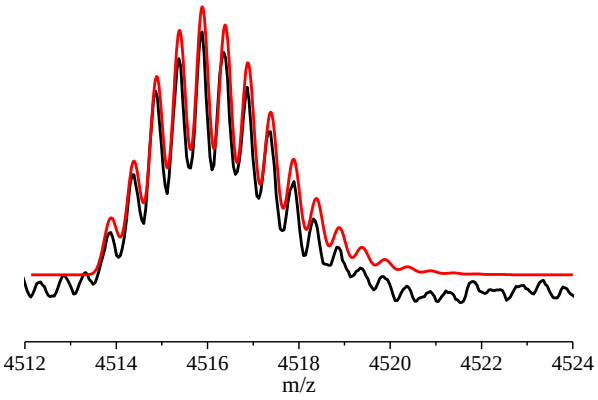

x = 12, $[Au_{25}(4\text{-PyET}{-}CH_3^+)_{12}(4\text{-PyET})_6]\cdot(MeSO_4^-)_{13}$

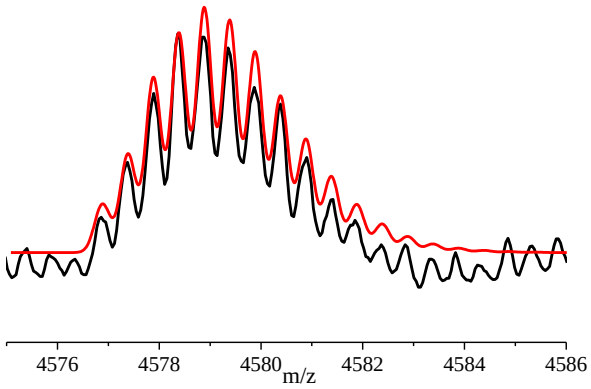

x = 13, $[Au_{25}(4\text{-PyET}{-}CH_3^+)_{13}(4\text{-PyET})_5]\cdot(MeSO_4^-)_{14}$

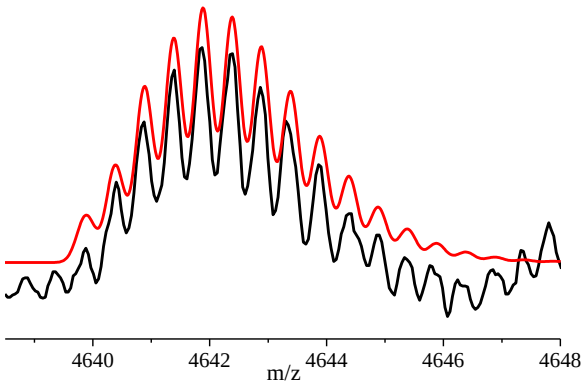

x = 14, $[Au_{25}(4\text{-PyET}{-}CH_3^+)_{14}(4\text{-PyET})_4]\cdot(MeSO_4^-)_{15}$

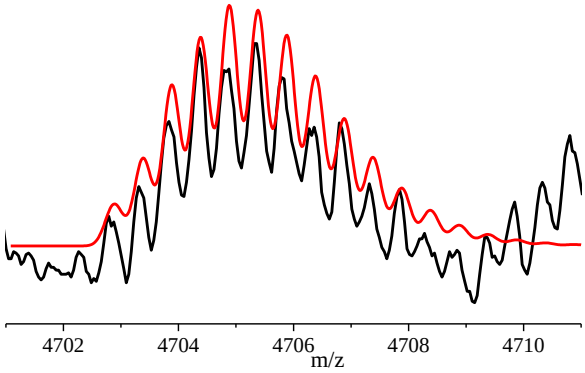

x = 15, $[Au_{25}(4\text{-PyET}{-}CH_3^+)_{15}(4\text{-PyET})_3]\cdot(MeSO_4^-)_{11}$

In positive-mode ESI-MS, Au_{25} cluster species with +2 charge (Group II) shown in Figure S5a

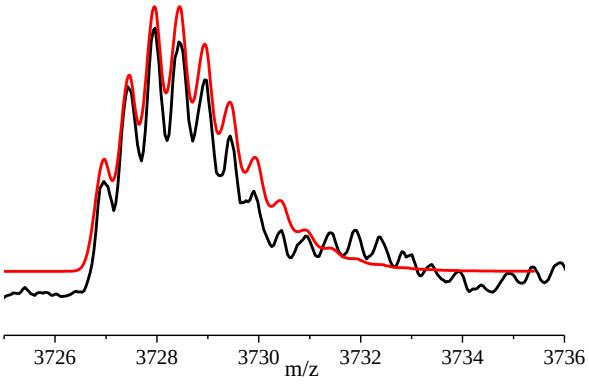

x = 3, $Au_{25}(4\text{-PyET}{-}CH_3^+)_3(4\text{-PyET})_{15}$

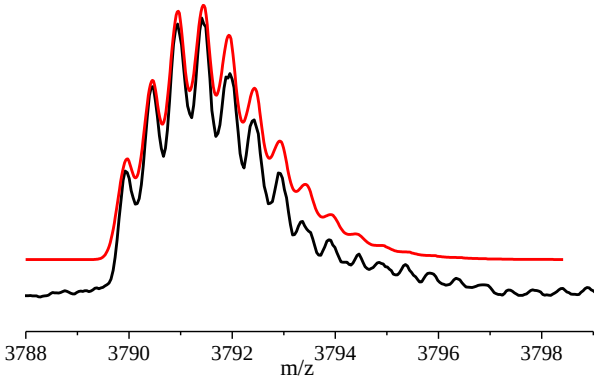

x = 4, $[Au_{25}(4\text{-PyET}{-}CH_3^+)_4(4\text{-PyET})_{14}]\cdot MeSO_4^-$

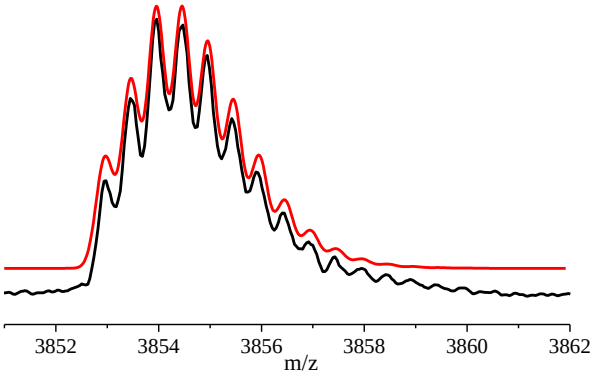

x = 5, $[Au_{25}(4\text{-PyET}{-}CH_3^+)_5(4\text{-PyET})_{13}]\cdot(MeSO_4^-)_2$

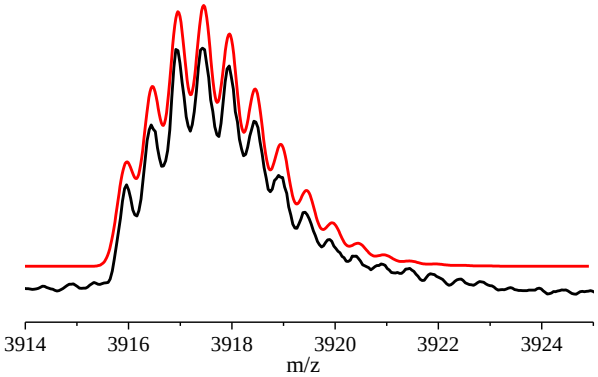

x = 6, $[Au_{25}(4\text{-PyET}{-}CH_3^+)_6(4\text{-PyET})_{12}]\cdot(MeSO_4^-)_3$

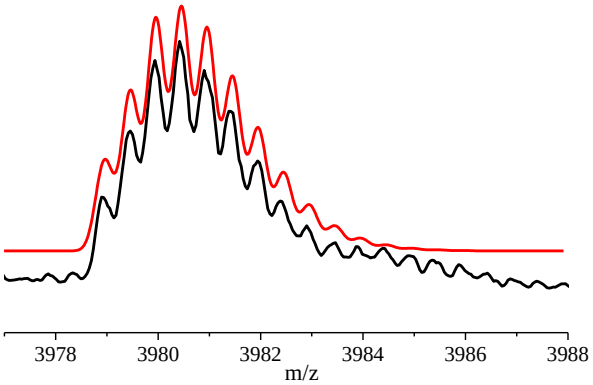

x = 7, $[Au_{25}(4\text{-PyET}{-}CH_3^+)_7(4\text{-PyET})_{11}]\cdot(MeSO_4^-)_4$

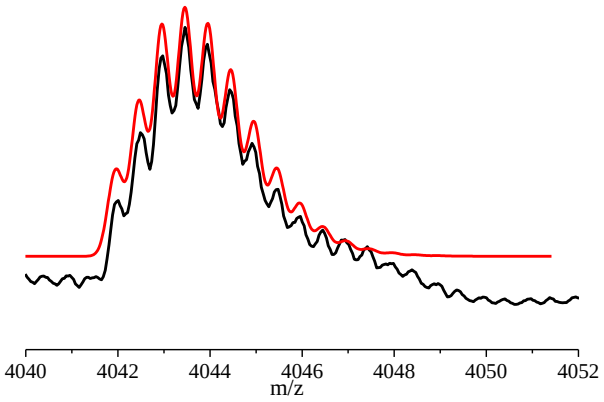

x = 8, $[Au_{25}(4\text{-PyET}{-}CH_3^+)_8(4\text{-PyET})_{10}]\cdot(MeSO_4^-)_5$

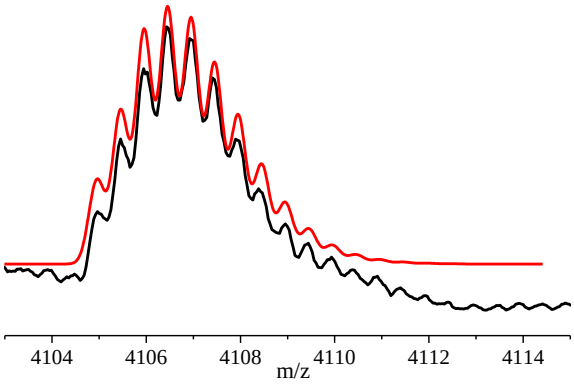

x = 9, $[Au_{25}(4\text{-PyET}{-}CH_3^+)_9(4\text{-PyET})_9]\cdot(MeSO_4^-)_6$

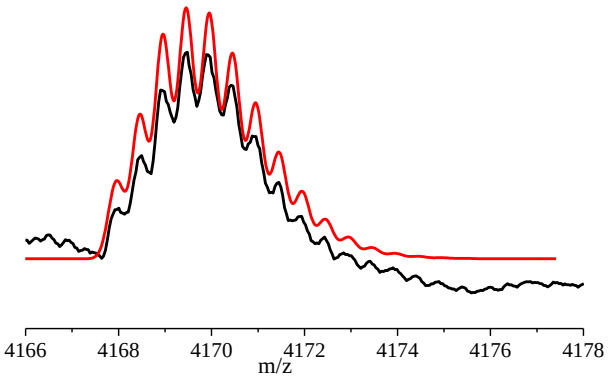

x = 10, $[Au_{25}(4\text{-PyET}{-}CH_3^+)_{10}(4\text{-PyET})_8]\cdot(MeSO_4^-)_7$

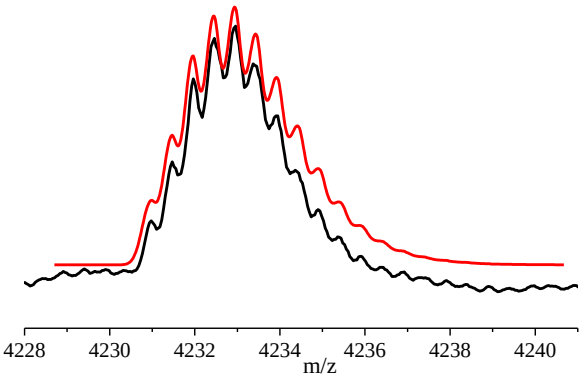

x = 11, $[Au_{25}(4\text{-PyET}{-}CH_3^+)_{11}(4\text{-PyET})_7]\cdot(MeSO_4^-)_8$

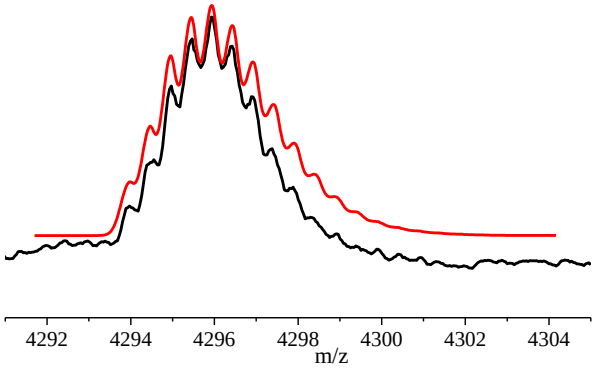

x = 12, $[Au_{25}(4\text{-PyET}{-}CH_3^+)_{12}(4\text{-PyET})_6]\cdot(MeSO_4^-)_9$

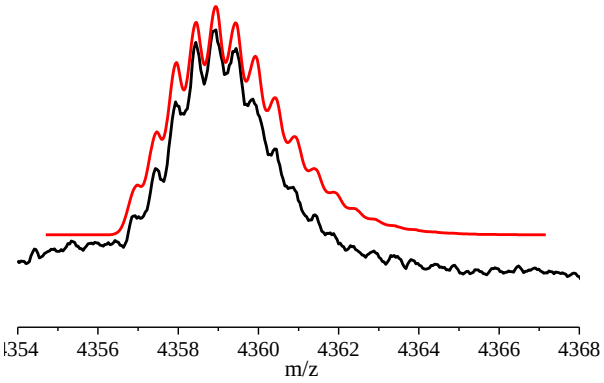

x = 13, $[Au_{25}(4\text{-PyET}{-}CH_3^+)_{13}(4\text{-PyET})_5]\cdot(MeSO_4^-)_{10}$

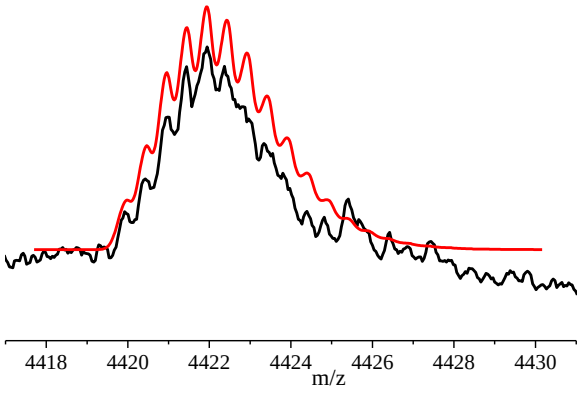

x = 14, $[Au_{25}(4\text{-PyET}{-}CH_3^+)_{14}(4\text{-PyET})_4]\cdot(MeSO_4^-)_{11}$

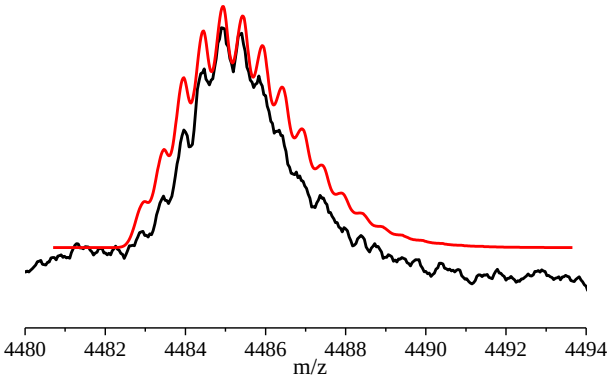

x = 15, $[Au_{25}(4\text{-PyET}{-}CH_3^+)_{15}(4\text{-PyET})_3]\cdot(MeSO_4^-)_{12}$

In positive-mode ESI-MS, Au_{25} cluster species with +3 charge (Group III) shown in Figure 5.2 and 5.3

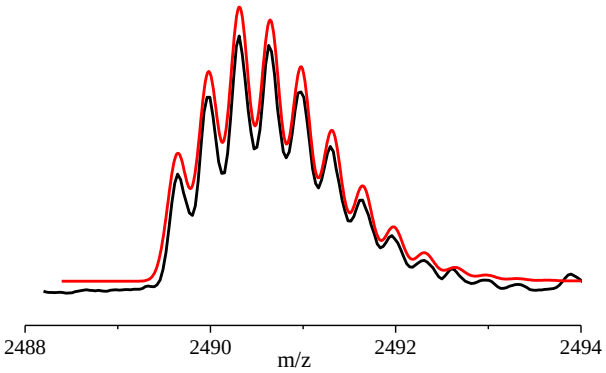

x = 4, $Au_{25}(4\text{-PyET}{-}CH_3^+)_4(4\text{-PyET})_{14}$

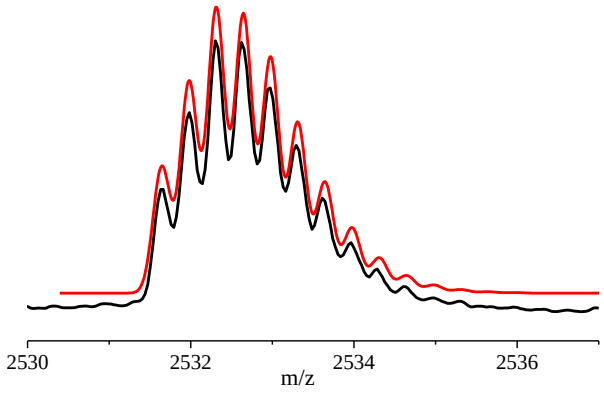

x = 5, $[Au_{25}(4\text{-PyET}{-}CH_3^+)_5(4\text{-PyET})_{13}]\cdot MeSO_4^-$

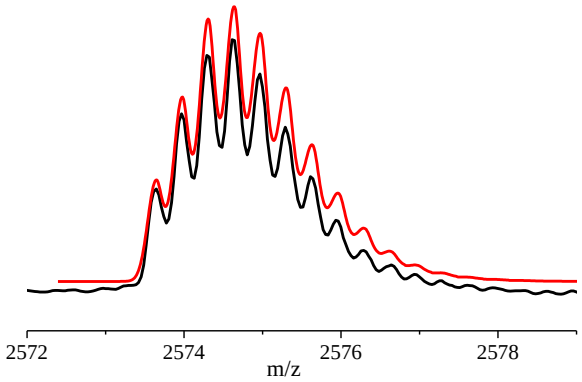

x = 6, $[Au_{25}(4\text{-PyET}{-}CH_3^+)_6(4\text{-PyET})_{12}]\cdot(MeSO_4^-)_2$

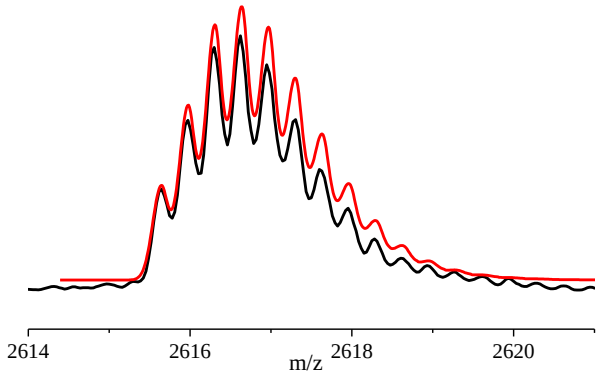

x = 7, $[Au_{25}(4\text{-PyET}{-}CH_3^+)_7(4\text{-PyET})_{11}]\cdot(MeSO_4^-)_3$

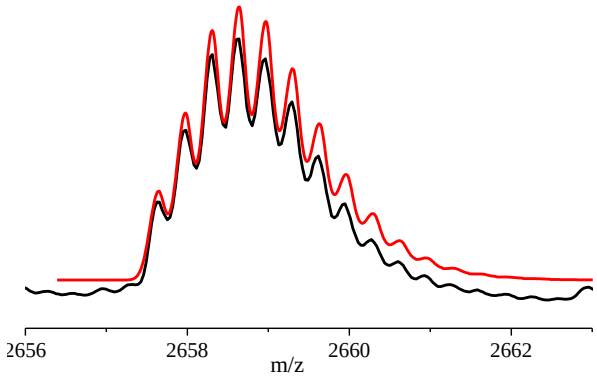

x = 8, $[Au_{25}(4\text{-PyET}{-}CH_3^+)_8(4\text{-PyET})_{10}]\cdot(MeSO_4^-)_4$

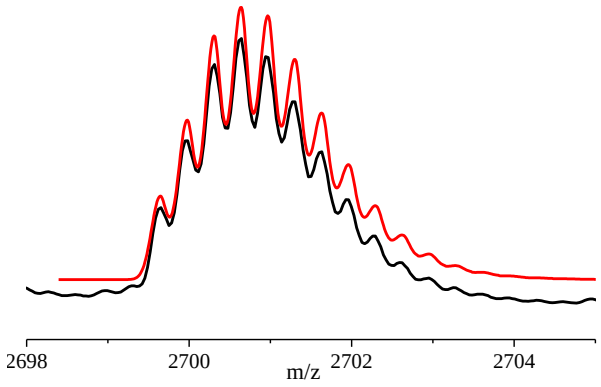

x = 9, $[Au_{25}(4\text{-PyET}{-}CH_3^+)_9(4\text{-PyET})_9]\cdot(MeSO_4^-)_5$

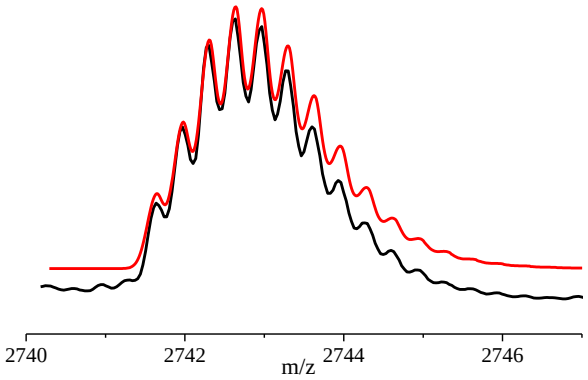

x = 10, $[Au_{25}(4\text{-PyET}{-}CH_3^+)_{10}(4\text{-PyET})_8]\cdot(MeSO_4^-)_6$

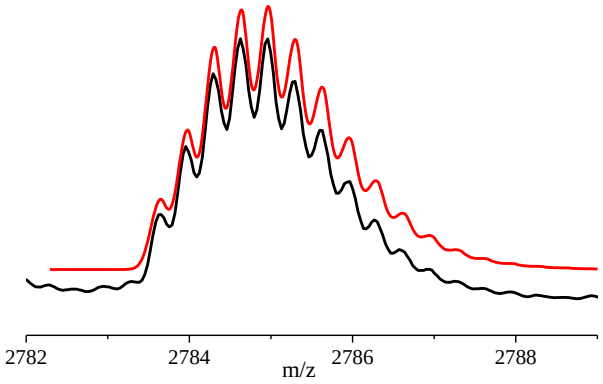

x = 11, $[Au_{25}(4\text{-PyET}{-}CH_3^+)_{11}(4\text{-PyET})_7]\cdot(MeSO_4^-)_7$

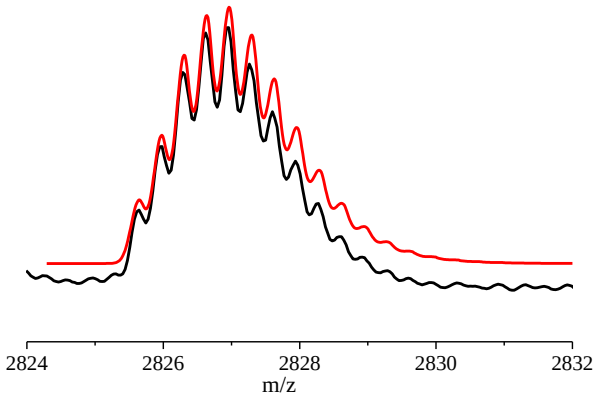

x = 12, $[Au_{25}(4\text{-PyET}{-}CH_3^+)_{12}(4\text{-PyET})_6]\cdot(MeSO_4^-)_8$

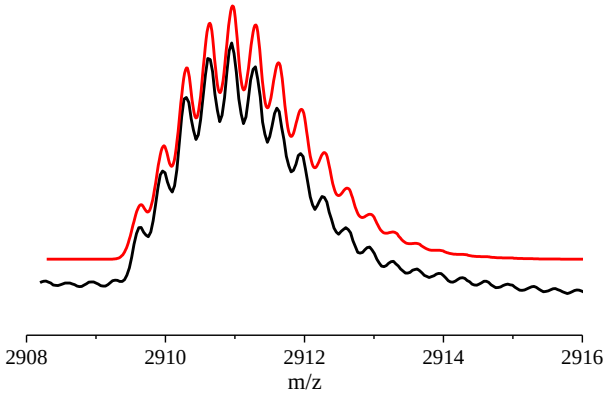

x = 13, $[Au_{25}(4\text{-PyET}{-}CH_3^+)_{13}(4\text{-PyET})_{15}]\cdot(MeSO_4^-)_9$

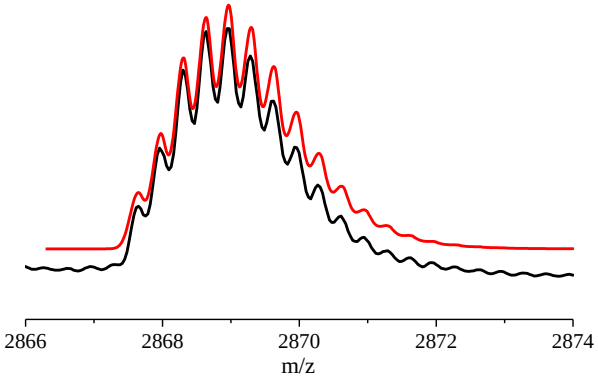

x = 14, $[Au_{25}(4\text{-PyET}{-}CH_3^+)_{14}(4\text{-PyET})_4]\cdot(MeSO_4^-)_{10}$

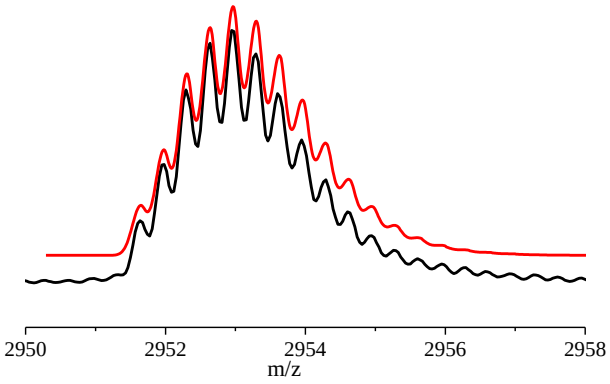

x = 15, $[Au_{25}(4\text{-PyET}{-}CH_3^+)_{15}(4\text{-PyET})_3]\cdot(MeSO_4^-)_{11}$

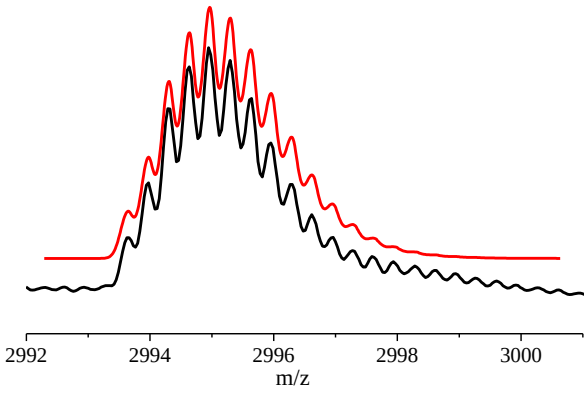

x = 16, $[Au_{25}(4\text{-PyET}{-}CH_3^+)_{16}(4\text{-PyET})_2]\cdot(MeSO_4^-)_{12}$

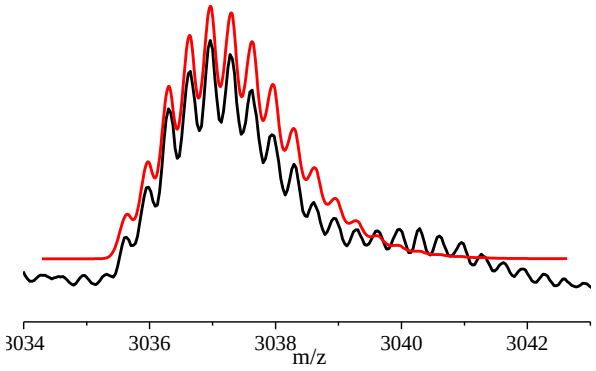

x = 17, $[Au_{25}(4\text{-PyET}{-}CH_3^+)_{17}(4\text{-PyET})]\cdot(MeSO_4^-)_{13}$

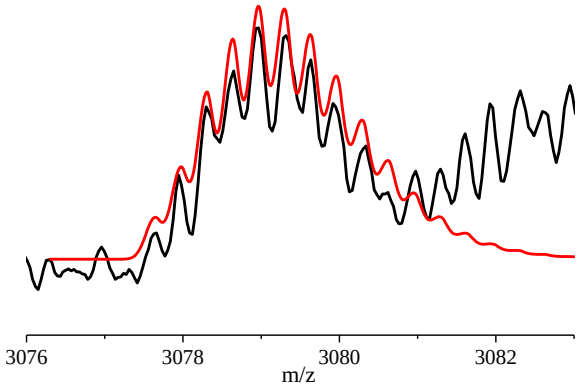

x = 18, $[Au_{25}(4\text{-PyET}{-}CH_3^+)_{18}]\cdot(MeSO_4^-)_{14}$

In positive-mode ESI-MS, Au_{25} cluster species with +4 charge (Group IV) shown in Figure S5b

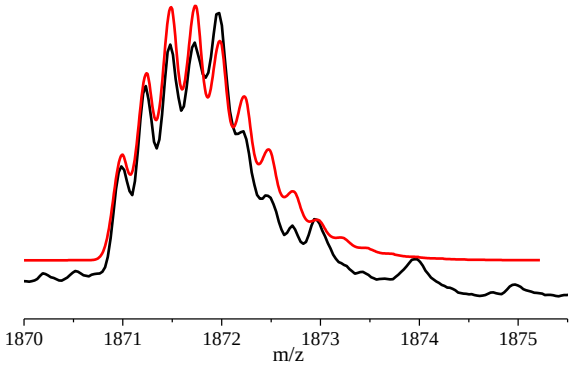

x = 5, $Au_{25}(4\text{-PyET}{-}CH_3^+)_5(4\text{-PyET})_{13}$

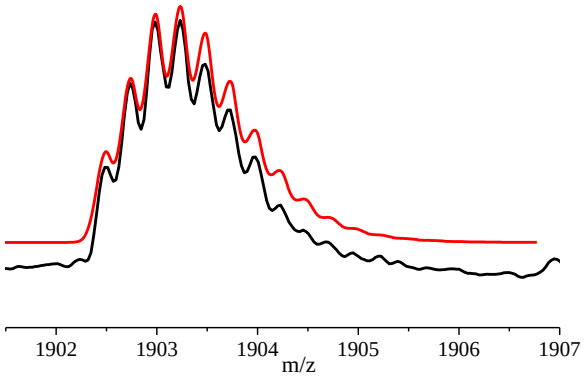

x = 6, $[Au_{25}(4\text{-PyET}{-}CH_3^+)_6(4\text{-PyET})_{12}]\cdot MeSO_4^-$

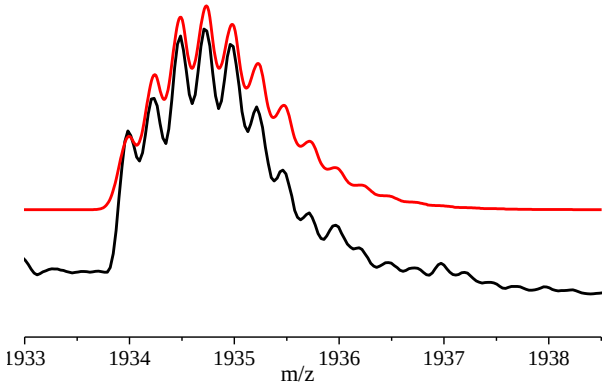

x = 7, $[Au_{25}(4\text{-PyET}{-}CH_3^+)_7(4\text{-PyET})_{11}]\cdot(MeSO_4^-)_2$

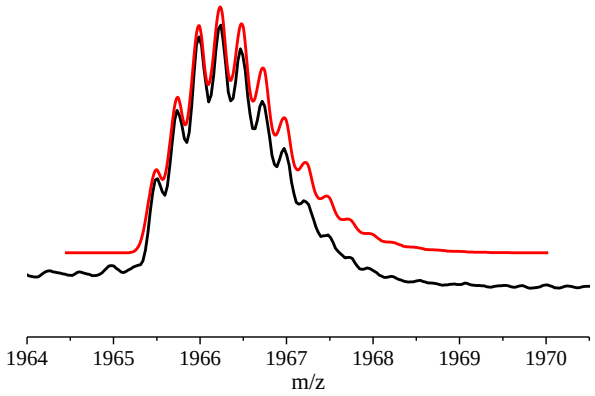

x = 8, $[Au_{25}(4\text{-PyET}{-}CH_3^+)_8(4\text{-PyET})_{10}]\cdot(MeSO_4^-)_3$

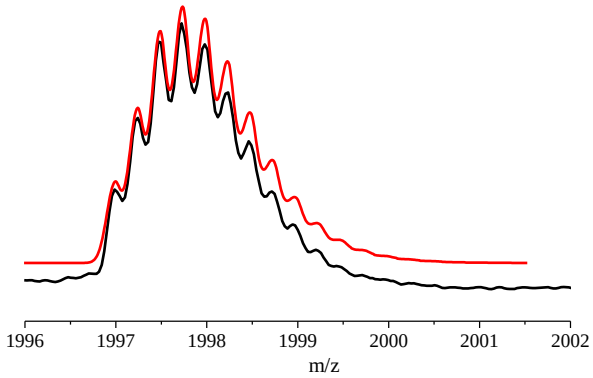

x = 9, $[Au_{25}(4\text{-PyET}{-}CH_3^+)_9(4\text{-PyET})_9]\cdot(MeSO_4^-)_4$

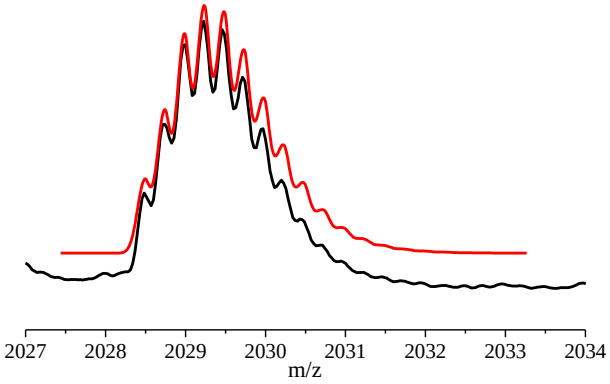

x = 10, $[Au_{25}(4\text{-PyET}{-}CH_3^+)_{10}(4\text{-PyET})_8]\cdot(MeSO_4^-)_5$

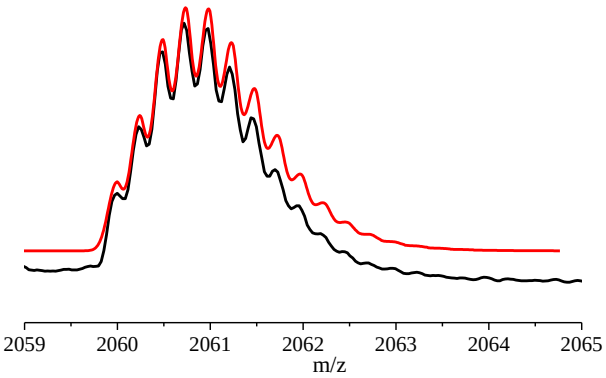

x = 11, $[Au_{25}(4\text{-PyET}{-}CH_3^+)_{11}(4\text{-PyET})_7]\cdot(MeSO_4^-)_6$

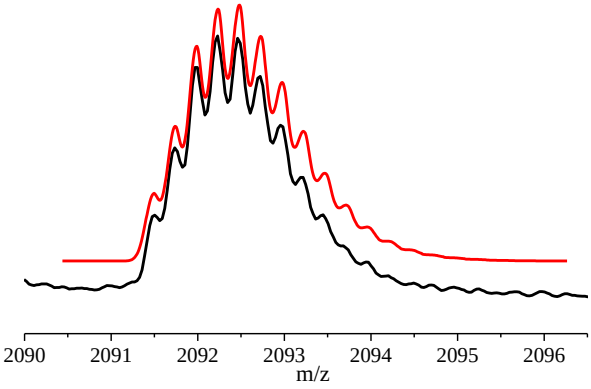

x = 12, $[Au_{25}(4\text{-PyET}{-}CH_3^+)_{12}(4\text{-PyET})_6]\cdot(MeSO_4^-)_7$

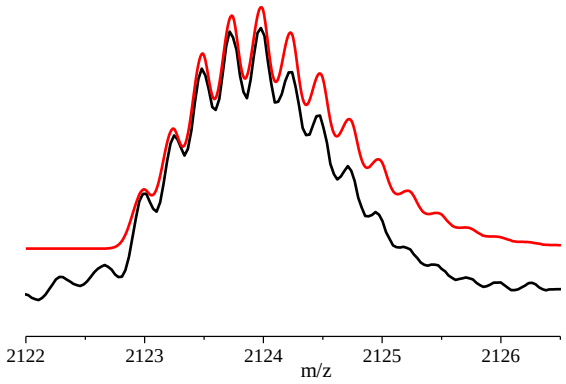

x = 13, $[Au_{25}(4\text{-PyET}{-}CH_3^+)_{13}(4\text{-PyET})_5]\cdot(MeSO_4^-)_8$

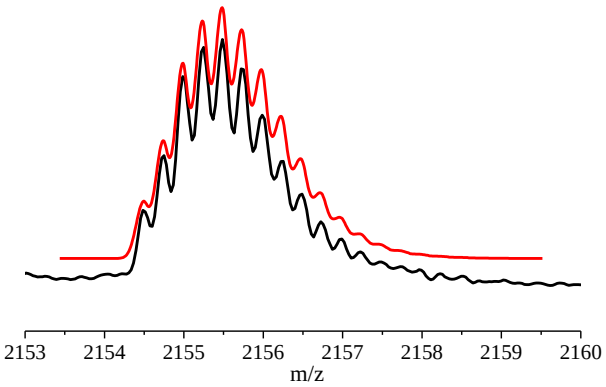

x = 14, $[Au_{25}(4\text{-PyET}{-}CH_3^+)_{14}(4\text{-PyET})_4]\cdot(MeSO_4^-)_9$

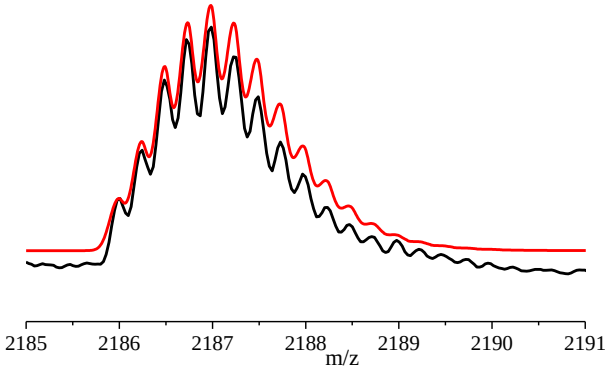

x = 15, $[Au_{25}(4\text{-PyET}{-}CH_3^+)_{15}(4\text{-PyET})_3]\cdot(MeSO_4^-)_{10}$

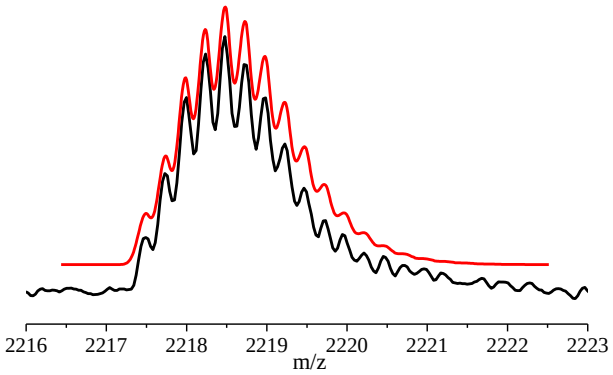

x = 16, $[Au_{25}(4\text{-PyET}{-}CH_3^+)_{16}(4\text{-PyET})_2]\cdot(MeSO_4^-)_{11}$

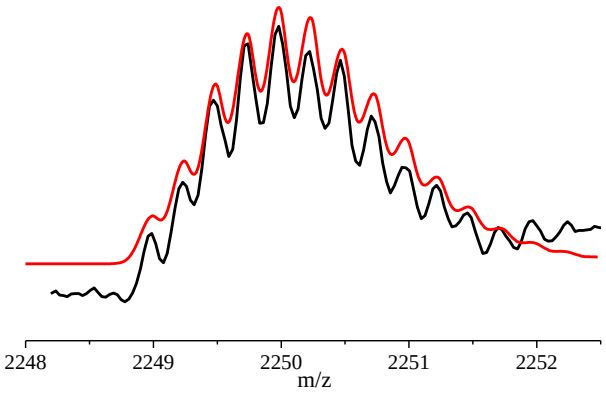

x = 17, $[Au_{25}(4\text{-PyET}{-}CH_3^+)_{17}(4\text{-PyET})]\cdot(MeSO_4^-)_{12}$

Figure S5.6. Isotope patterns of the cationized Au_{25} clusters obtained in Figure 5.2, 5.3, S5.3, S5.4 and S5.5. When one cluster has same observed peaks at different

reaction time, the strongest one was chosen as a representative example. The expanded high-resolution ESI mass spectrum (black) and the simulated isotope pattern (red).

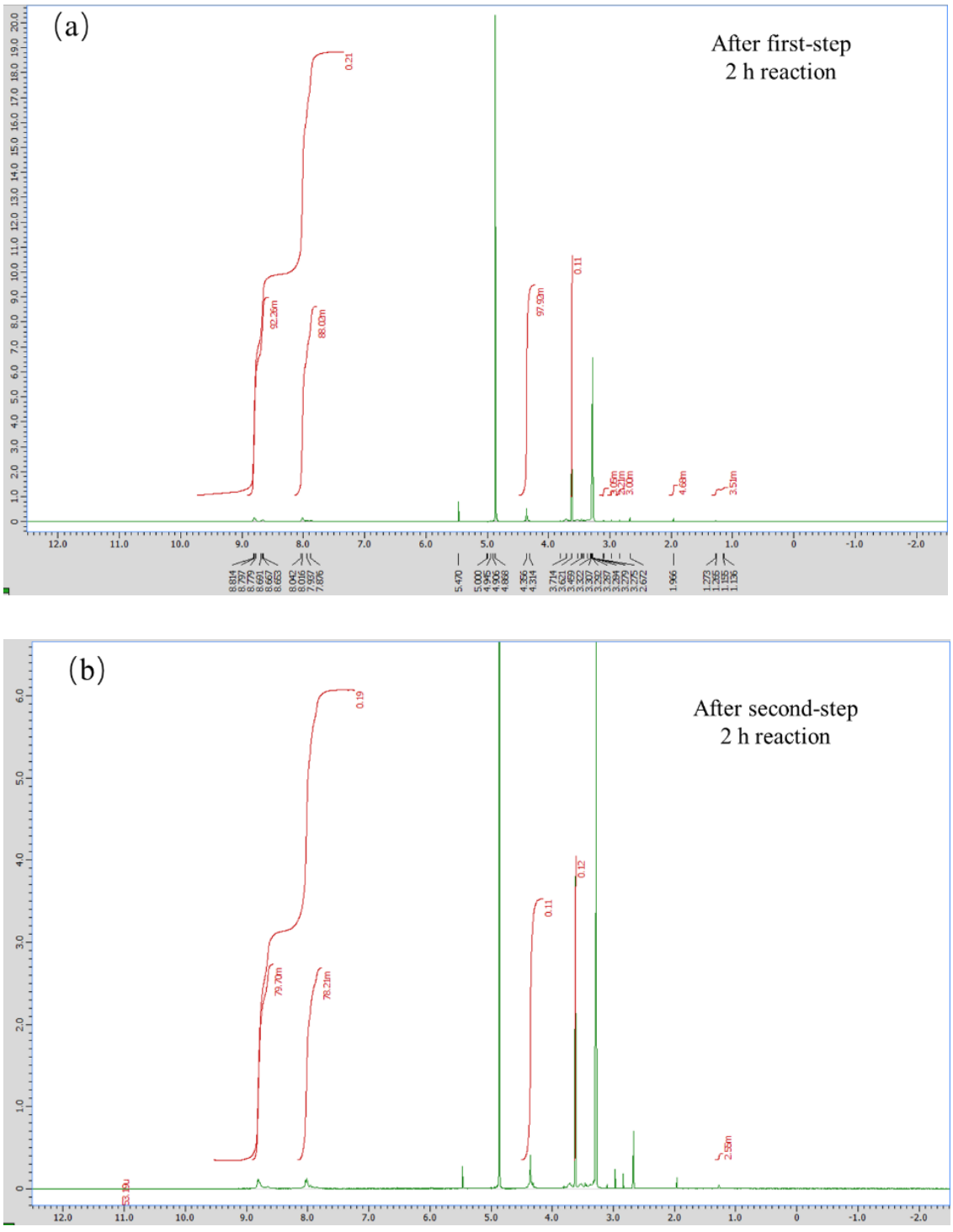

Figure S5.7 ^{1}H-NMR Integral data of $Au_{25}(4\text{-PyET}{-}CH_3^+)_x(4\text{-PyET})_{18-x}$ species in samples after (a) first-step 2 h reaction, and (b) second-step 2 h reaction in methanol-*d*$_4$ at 400 MHz.

Table S5.1 Formula weights of structural assignments of Group (−2 charge) in Figure S5.3.

x	Group, −2 charge	F. W.	m/z
0	$Au_{25}(4\text{-PyET})_{18}\cdot MeSO_4^-$	7523.07	3761.54
1	$[Au_{25}(4\text{-PyET}{-}CH_3^+)(4\text{-PyET})_{17}]\cdot(MeSO_4^-)_2$	7649.20	3824.60
2	$[Au_{25}(4\text{-PyET}{-}CH_3^+)_2(4\text{-PyET})_{16}]\cdot(MeSO_4^-)_3$	7775.33	3887.67
3	$[Au_{25}(4\text{-PyET}{-}CH_3^+)_3(4\text{-PyET})_{15}]\cdot(MeSO_4^-)_4$	7901.46	3950.73
4	$[Au_{25}(4\text{-PyET}{-}CH_3^+)_4(4\text{-PyET})_{14}]\cdot(MeSO_4^-)_5$	8027.59	4013.80
5	$[Au_{25}(4\text{-PyET}{-}CH_3^+)_5(4\text{-PyET})_{13}]\cdot(MeSO_4^-)_6$	8153.72	4076.86
6	$[Au_{25}(4\text{-PyET}{-}CH_3^+)_6(4\text{-PyET})_{12}]\cdot(MeSO_4^-)_7$	8279.85	4139.93
7	$[Au_{25}(4\text{-PyET}{-}CH_3^+)_7(4\text{-PyET})_{11}]\cdot(MeSO_4^-)_8$	8405.98	4202.99
8	$[Au_{25}(4\text{-PyET}{-}CH_3^+)_8(4\text{-PyET})_{10}]\cdot(MeSO_4^-)_9$	8532.11	4266.06
9	$[Au_{25}(4\text{-PyET}{-}CH_3^+)_9(4\text{-PyET})_9]\cdot(MeSO_4)_{10}$	8658.24	4329.12
10	$[Au_{25}(4\text{-PyET}{-}CH_3^+)_{10}(4\text{-PyET})_8]\cdot(MeSO4^-)_{11}$	8784.37	4392.19
11	$[Au_{25}(4\text{-PyET}{-}CH_3^+)_{11}(4\text{-PyET})_7]\cdot(MeSO4^-)_{12}$	8910.5	4455.25
12	$[Au_{25}(4\text{-PyET}{-}CH_3^+)_{12}(4\text{-PyET})_6]\cdot(MeSO4^-)_{13}$	9036.63	4518.32
13	$[Au_{25}(4\text{-PyET}{-}CH_3^+)_{13}(4\text{-PyET})_5]\cdot(MeSO4^-)_{14}$	9162.76	4581.38
14	$[Au_{25}(4\text{-PyET}{-}CH_3^+)_{14}(4\text{-PyET})_4]\cdot(MeSO4^-)_{15}$	9288.89	4644.45
15	$[Au_{25}(4\text{-PyET}{-}CH_3^+)_{15}(4\text{-PyET})_3]\cdot(MeSO4^-)_{16}$	9415.02	4707.51
16	$[Au_{25}(4\text{-PyET}{-}CH_3^+)_{16}(4\text{-PyET})_2]\cdot(MeSO4^-)_{17}$	9541.15	4770.58
17	$[Au_{25}(4\text{-PyET}{-}CH_3^+)_{17}(4\text{-PyET})]\cdot(MeSO4^-)_{18}$	9667.28	4833.64
18	$[Au_{25}(4\text{-PyET}{-}CH_3^+)_{18}]\cdot(MeSO_4^-)_{19}$	9793.41	4896.71

Table S5.2 Formula weights of structural assignments of Group II (+2 charge) in Figure S5.5a.

x	**Group II, +2 charge**	**F.W.**	**m/z**
3	$Au_{25}(4\text{-PyET}{-}CH_3^+)_3(4\text{-PyET})_{15}$	7457.07	3728.54
4	$[Au_{25}(4\text{-PyET}{-}CH_3^+)_4(4\text{-PyET})_{14}]\cdot MeSO_4^-$	7583.20	3791.60
5	$[Au_{25}(4\text{-PyET}{-}CH_3^+)_5(4\text{-PyET})_{13}]\cdot(MeSO_4^-)_2$	7709.33	3854.67
6	$[Au_{25}(4\text{-PyET}{-}CH_3^+)_6(4\text{-PyET})_{12}]\cdot(MeSO_4^-)_3$	7835.46	3917.73
7	$[Au_{25}(4\text{-PyET}{-}CH_3^+)_7(4\text{-PyET})_{11}]\cdot(MeSO_4^-)_4$	7961.59	3980.80
8	$[Au_{25}(4\text{-PyET}{-}CH_3^+)_8(4\text{-PyET})_{10}]\cdot(MeSO_4^-)_5$	8087.72	4043.86
9	$[Au_{25}(4\text{-PyET}{-}CH_3^+)_9(4\text{-PyET})_9]\cdot(MeSO_4^-)_6$	8213.85	4106.93
10	$[Au_{25}(4\text{-PyET}{-}CH_3^+)_{10}(4\text{-PyET})_8]\cdot(MeSO_4^-)_7$	8339.98	4169.99
11	$[Au_{25}(4\text{-PyET}{-}CH_3^+)_{11}(4\text{-PyET})_7]\cdot(MeSO_4^-)_8$	8466.11	4233.06
12	$[Au_{25}(4\text{-PyET}{-}CH_3^+)_{12}(4\text{-PyET})_6]\cdot(MeSO_4^-)_9$	8592.24	4296.12
13	$[Au_{25}(4\text{-PyET}{-}CH_3^+)_{13}(4\text{-PyET})_5]\cdot(MeSO_4^-)_{10}$	8718.37	4359.19
14	$[Au_{25}(4\text{-PyET}{-}CH_3^+)_{14}(4\text{-PyET})_4]\cdot(MeSO_4^-)_{11}$	8844.50	4422.25
15	$[Au_{25}(4\text{-PyET}{-}CH_3^+)_{15}(4\text{-PyET})_3]\cdot(MeSO_4^-)_{12}$	8970.63	4485.32
16	$[Au_{25}(4\text{-PyET}{-}CH_3^+)_{16}(4\text{-PyET})_2]\cdot(MeSO_4^-)_{13}$	9096.76	4548.38
17	$[Au_{25}(4\text{-PyET}{-}CH_3^+)_{17}(4\text{-PyET})]\cdot(MeSO_4^-)_{14}$	9222.89	4611.45
18	$[Au_{25}(4\text{-PyET}{-}CH_3^+)_{18}]\cdot(MeSO_4^-)_{15}$	9349.02	4674.51

Table S5.3 Formula weights of structural assignments of Group III (+3 charge) in Figure 5.2.

x	**Group III, +3 charge**	**F.W.**	**m/z**
4	$Au_{25}(4\text{-PyET}{-}CH_3^+)_4(4\text{-PyET})_{14}$	7472.10	2490.70
5	$[Au_{25}(4\text{-PyET}{-}CH_3^+)_5(4\text{-PyET})_{13}]\cdot MeSO_4^-$	7598.23	2532.74
6	$[Au_{25}(4\text{-PyET}{-}CH_3^+)_6(4\text{-PyET})_{12}]\cdot(MeSO_4^-)_2$	7724.36	2574.79
7	$[Au_{25}(4\text{-PyET}{-}CH_3^+)_7(4\text{-PyET})_{11}]\cdot(MeSO_4^-)_3$	7850.49	2616.83
8	$[Au_{25}(4\text{-PyET}{-}CH_3^+)_8(4\text{-PyET})_{10}]\cdot(MeSO_4^-)_4$	7976.62	2658.87
9	$[Au_{25}(4\text{-PyET}{-}CH_3^+)_9(4\text{-PyET})_9]\cdot(MeSO_4^-)_5$	8102.75	2700.92
10	$[Au_{25}(4\text{-PyET}{-}CH_3^+)_{10}(4\text{-PyET})_8]\cdot(MeSO_4^-)_6$	8228.88	2742.96
11	$[Au_{25}(4\text{-PyET}{-}CH_3^+)_{11}(4\text{-PyET})_7]\cdot(MeSO_4^-)_7$	8355.01	2785.00
12	$[Au_{25}(4\text{-PyET}{-}CH_3^+)_{12}(4\text{-PyET})_6]\cdot(MeSO_4^-)_8$	8481.14	2827.05
13	$[Au_{25}(4\text{-PyET}{-}CH_3^+)_{13}(4\text{-PyET})_5]\cdot(MeSO_4^-)_9$	8607.27	2869.09
14	$[Au_{25}(4\text{-PyET}{-}CH_3^+)_{14}(4\text{-PyET})_4]\cdot(MeSO_4^-)_{10}$	8733.40	2911.13
15	$[Au_{25}(4\text{-PyET}{-}CH_3^+)_{15}(4\text{-PyET})_3]\cdot(MeSO_4^-{}_{11}$	8859.53	2953.18
16	$[Au_{25}(4\text{-PyET}{-}CH_3^+)_{16}(4\text{-PyET})_2]\cdot(MeSO_4^-)_{12}$	8985.66	2995.22
17	$[Au_{25}(4\text{-PyET}{-}CH_3^+)_{17}(4\text{-PyET})]\cdot(MeSO_4^-)_{13}$	9111.79	3037.26
18	$[Au_{25}(4\text{-PyET}{-}CH_3^+)_{18}]\cdot(MeSO_4^-)_{14}$	9237.92	3079.31

Table S5.4 Formula weights of structural assignments of Group IV (+4 charge) in Figure S5.5b.

x	**Group IV, +4 charge**	**F.W.**	**m/z**
5	$Au_{25}(4\text{-PyET}{-}CH_3^+)_5(4\text{-PyET})_{13}$	7487.13	1871.78
6	$[Au_{25}(4\text{-PyET}{-}CH_3^+)_6(4\text{-PyET})_{12}]\cdot MeSO_4^-$	7613.26	1903.32
7	$[Au_{25}(4\text{-PyET}{-}CH_3^+)_7(4\text{-PyET})_{11}]\cdot(MeSO_4^-)_2$	7739.39	1934.85
8	$[Au_{25}(4\text{-PyET}{-}CH_3^+)_8(4\text{-PyET})_{10}]\cdot(MeSO_4^-)_3$	7865.52	1966.38
9	$[Au_{25}(4\text{-PyET}{-}CH_3^+)_9(4\text{-PyET})_9]\cdot(MeSO_4^-)_4$	7991.65	1997.91
10	$[Au_{25}(4\text{-PyET}{-}CH_3^+)_{10}(4\text{-PyET})_8]\cdot(MeSO_4^-)_5$	8117.78	2029.45
11	$[Au_{25}(4\text{-PyET}{-}CH_3^+)_{11}(4\text{-PyET})_7]\cdot(MeSO_4^-)_6$	8243.91	2060.98
12	$[Au_{25}(4\text{-PyET}{-}CH_3^+)_{12}(4\text{-PyET})_6]\cdot(MeSO_4^-)_7$	8370.04	2092.51
13	$[Au_{25}(4\text{-PyET}{-}CH_3^+)_{13}(4\text{-PyET})_5]\cdot(MeSO_4^-)_8$	8496.17	2124.04
14	$[Au_{25}(4\text{-PyET}{-}CH_3^+)_{14}(4\text{-PyET})_4]\cdot(MeSO_4^-)_9$	8622.30	2155.58
15	$[Au_{25}(4\text{-PyET}{-}CH_3^+)_{15}(4\text{-PyET})_3]\cdot(MeSO_4^-)_{10}$	8748.43	2187.11
16	$[Au_{25}(4\text{-PyET}{-}CH_3^+)_{16}(4\text{-PyET})_2]\cdot(MeSO_4^-)_{11}$	8874.56	2218.64
17	$[Au_{25}(4\text{-PyET}{-}CH_3^+)_{17}(4\text{-PyET})]\cdot(MeSO_4^-)_{12}$	9000.69	2250.17
18	$[Au_{25}(4\text{-PyET}{-}CH_3^+)_{18}]\cdot(MeSO_4^-)_{13}$	9126.82	2281.71

Chapter 6

Conclusions

Surface chemistry on cationic-ligands-protected metal clusters of atomically-precision is rarely reported, but providing a new platform for the functionalization of clusters toward enhancing their practical utility. In this thesis, taking the $Au_{25}(SR)_{18}$ cluster as the example, three interfacial surface reactions: ligand-exchange, protonation and Menshutkin reactions, have been investigated on the cationic-ligands-protected noble metal clusters. The key results and conclusions can be summarized as follows:

Chapter Two demonstrates the kinetics of the cationic-ligand-exchange reactions of Au_{25} nanoclusters, which is different from a typical neutral-thiol-to-neutral-thiol ligand exchange, is strongly dependent on how the SR^+ ligands interact with each other during the ligand-exchange process. There are two main factors that determine the unique reaction kinetics, namely Coulombic repulsions (i) between the attached SR^+ ligands and free ligands in solution that hinder further ligand exchange, and (ii) among the surface SR^+ ligands on the thiolate monolayer, which promotes the thermal decomposition of the nanocluster. It is believed that this contribution is theoretically and practically relevant because it benefits the precise and controlled functionalization of gold nanoclusters, and broadens this exciting area of research for future investigations and applications.

Chapter Three focuses on the first synthesis of high-purity and high-yield Au_{25} clusters protected by the basic pyridyl ethanethiol ($HSCH_2CH_2Py$, 4-PyET and 2-PyET) using a simple one-pot synthetic strategy. Single crystal of $[Au_{25}(4\text{-}PyET)_{18}]^-\cdot Na^+$ was successfully prepared and its structure solved. It reveals a

structure similar to that known for the phenyl ethanethiolate analog, but with pyridyl-N coordination to Na^+, a more relaxed ligand shell, and a profoundly layered arrangement in the solid state. $Au_{25}(PyET)_{18}$ clusters being endowed with a unique (de)protonation equilibria, can conjugate to H^+ through the pendant Py moiety, similar to a heterocyclic base. In addition, the clusters hold the reversible solubility in aqueous and some organic solvents based on the protonation states of the pendant PyET ligands. This work proposes a new family of basic Au_{25} clusters. Considering the remarkable achievements of their "cousin", phenyl ethanethiol (PET) which has been widely applied for noble metal clusters, It is believed that the use of PyET will ignite the spread of synthesizing the basic metal clusters such as $Au_{38}(PyET)_{24}$, $Au_{67}(PyET)_{35}$, $Au_{144}(PyET)_{60}$, $Ag_{25}(PyET)_{18}$, and their intermetallic (alloy) variations and investigating their basic properties and utilizations.

Chapter Four found that even only one element difference between $Au_{25}(PyET)_{18}$ and $Au_{25}(PET)_{18}$ clusters, the Py moieties plays a major role in the PL efficiency. The result indicated that Py groups on cluster surface donate more electrons to Au_{25} core, resulting in the enhanced PL emissions of $Au_{25}(PyET)_{18}$ clusters. The resonance-coupled structure of PyET ligands, caused by proton (H^+), would hinder the electron donation, and quench the emission of Au_{25} NCs. Overall, the electronic factors of the surface organic ligand moiety are able to cause perturbation effects on the optical/electronic properties of ligand-protected clusters.

Chapter Five describes the Menshutkin reaction of surface 4-PyET ligands on $Au_{25}(4\text{-}PyET)_{18}$ clusters. The incorporation of a reactive Py group amenable to be methylated can easily transform the neutral PyET-capped metal clusters into the cationized ones. A two-step of reaction process was designed, and the results reveal

that the first-step reaction could methylate the 4-PyET ligands in a very short time, resulting in the formation of the cationized $Au_{25}(4\text{-PyET}{-}CH_3^+)_x(4\text{-PyET})_{18-x}$ clusters. By contract, the second-step reaction only had a small boosting on the methylation of the left 4-PyET, whereas the as-obtained Au_{25} clusters became unstable because of the accumulation of positive moieties ($N{-}CH_3^+$). This research not only provides a facial route to the cationization modification of metal clusters, but also renders them the starting point for diversifying R-groups of clusters though *in-situ* modification of them.

ACKNOWLEDGEMENTS

This dissertation would have been impossible without the contributions from many people.

Prof. Tetsu Yonezawa, whose wisdom, patience, and guidance cannot be understated. Accepting my PhD application, motivating and instilling confidence in me are highly appreciating. Working in his lab over the last three years has been my great honor.

I want to specifically thank my greatest mentor and collaborator, Assistant Prof. Yohei Ishida, who played vital roles in supporting and challenging me to finish a doctorate in engineering. Great thanks are also given to Dr. Nguyen Thanh Mai for her fruitful discussions, and Mr. Hiroki Tsukamoto for his experimental assistance.

My dear lab members, Dr. Lianlian Deng, Dr. Shilei Zhu, Miss Ikumi Akita, Mr. Kunihiro Narita, Miss Minjia Saw, Miss Chau Yuen Ting Rachel and *etc.*, helped me realize that "research work is hard, but I still enjoyed many happiness with the friends' companies." Being such lucky to meet you here. Thanks, guys!

The list of people who deserve acknowledgements is too lengthy to include, Prof. Tatsufumi Okino (Hokkaido Univ.) for his helps on ESI-MS measurements, Mr. Sato Kimura (Hokkaido Univ.) for his trainings on NMR tests, Dr. Norihito Fukui (Nagoya Univ.) for his generous assistances on single-crystal X-ray diffraction measurements and analyses, and so on. I have been extremely fortunate with the working of teachers, instructors, and friends, who guided me through this meaningful period.

I also would like to acknowledge my country, China, who gave me the CSC scholarship (China Scholarship Council), financially supporting me living in Japan, and my university, Hokudai, who provided the tuition-free. They were the cornerstone for my PhD study.

Finally, with all my heart to my parents, whose teachings inspire me every day, to be a better person, and to be a better worker.

LIST OF PUBLICATIONS

[1] **Huang, Z.**; Ishida, Y.; Narita, K; Yonezawa, T. Kinetics of Cationic-Ligand-Exchange Reactions in Au_{25} Nanoclusters. *J. Phys. Chem. C* **2018**, 122, 18142−18150.

[2] **Huang, Z.**; Ishida, Y.; Yonezawa, T. Basic $[Au_{25}(SCH_2CH_2Py)_{18}]^{-}\cdot Na^{+}$ Clusters: Synthesis, Layered Crystallographic Arrangement, and Unique Surface Protonation. *Angew. Chem. Int. Ed.* **2019**, *58*, 13411−13415.

[3] **Huang, Z.**; Ishida, Y.; Yonezawa, T. Menshutkin Reaction on Noble Metal Clusters: A Facile Route to Cationized $Au_{25}(SR)_{18}$ Cluster. *To be submitted*.

[4] Narita, K; Ishida, Y.; Yonezawa, T; **Huang, Z.** Super Polycationic Molecular Compounds: $Au_{144}(SR^{+})_{60}$ Clusters. *J. Phys. Chem. C* **2019**, 123, 21768−21773.

LIST OF ATTENDED CONFERENCES

No.	Conference	Date and place	Title
1	The Iron and Steel Institute of Japan and The Japan Institute of Metal and Materials, Hokkaido Region Meeting	Jan. 25th -26th, 2018. Sapporo	Atomically Mono-Disperse, Cationized $Au_{25}(SR^{0})_{18-x}(SR^{+})_{x}$ Cluster via Ligand-Exchange Reaction (*Oral*)
2	Heisei 30th Japan Iron and Steel Institute·Japan Institute of Metal (JIM), Hokkaido Region Meeting	Jul. 13th, 2018. Sapporo	Kinetics of Cationic-Ligand-Exchange Reactions in Au_{25} Nanoclusters (*Poster*)
3	The 69th Divisional Meeting of Division of Colloid and Surface Chemistry	Sep. 18th -20th, 2018. Tsukuba	Kinetics of Cationic-Ligand-Exchange Reactions in Au_{25} Nanoclusters (*Poster*)
4	Hokkaido University-National Central University Joint Symposium on Materials Chemistry and Physics, 2018	Nov. 15th-16th, 2018. Sapporo	Synthesis of Cationic-Ligand-Protected Au_{25} Nanoclusters (*Poster*)
5	The CSJ Conference of Hokkaido Branch, 2019	Jan. 22th -23th, 2019. Sapporo	Synthesis of Au_{25} Nanoclusters Protected by Pyridineethanethiol (*Oral*)
6	The 99th CSJ Annual Meeting, 2019	Mar. 14th -18th, 2019. Kobe	Synthesis of Pyridineethanethiol-Protected Au_{25} Nanoclusters (*Oral*)